THÈSE PRÉSENTÉE

POUR OBTENIR LE GRADE DE

DOCTEUR

DE L'UNIVERSITÉ DE BORDEAUX

ÉCOLE DOCTORALE MATHÉMATIQUES ET

INFORMATIQUE

SPÉCIALITÉ: MATHÉMATIQUES APPLIQUÉES ET CALCUL SCIENTIFIQUE

Par **Luis H. Benetti Ramos**

Self-propulsion and fluid-mediated interaction of flapping wings in viscous flows

Sous la direction de : **Olivier Marquet, Michel Bergmann et Angelo Iollo**

Soutenue le 16 décembre 2020 à Meudon, France devant le jury composé de

Michel Bergmann	Chargé de recherche	Institut de Mathématiques de Bordeaux/ INRIA	Directeur de thèse
Uwe Ehrenstein	Professeur	Aix-Marseille Université	Rapporteur
François Gallaire	Professeur associé	École Polytechnique Fédérale de Lausanne	Rapporteur
Angelo Iollo	Professeur	Institut de Mathématiques de Bordeaux/ INRIA	Directeur de thèse
Justin Leontini	Professeur associé	Swinburne University of Technology	Membre du jury
Olivier Marquet	Maître de recherche	ONERA - The French Aerospace Lab	Encadrant de thèse
Sophie Ramananarivo	Maître de conférences	École Polytechnique	Membre du jury
Peter Schmid	Professeur	Imperial College London	Membre du jury

Auto-propulsion et interaction hydrodynamique d'ailes battantes dans des écoulements visqueux

Résumé: Une stratégie de locomotion exploitée par les animaux et dans la conception des dispositifs d'ingénierie est le battement d'ailes. Cette propulsion apparaît grâce à l'évolution de la nature dynamique des écoulements où, suite à l'augmentation de l'inertie et des non-linéarités des écoulements, la locomotion par des battement réciproques dans le temps et la dynamique collective deviennent possibles. Dans ce travail, l'émergence de la propulsion par battement et le rôle des interactions hydrodynamiques passives dans la dynamique collective sont étudiés par des analyses de stabilité du système couplé fluide / aile.

La première partie de la thèse est consacrée à l'étude de l'autopropulsion horizontale d'une aile symétrique en mouvement de battement vertical dans un fluide au repos. Dans un premier temps, nous étudions l'émergence de régimes autopropulsés, en adoptant un rapport de densité et une amplitude de battement fixes tout en faisant varier la fréquence de battement. À basse fréquence de battement, deux états d'autopropulsion sont analysés : un périodique de propulsion unidirectionnelle et un quasi périodique de mouvement de va-et-vient autour d'un point fixe. L'émergence de ces états est expliquée par la stabilité de Floquet fluide-solide des écoulements symétriques non propulsifs. Contrairement aux analyses de stabilité purement hydrodynamiques, l'analyse fluide-solide détermine avec précision l'apparition des états. De plus, elle met en évidence mécanismes linéaires responsables de la propulsion unidirectionnelle et du mouvement de va-et-vient. L'analyse de la moyenne temporelle des force et vitesse des modes permet d'établir un critère d'instabilité physique pour les ailes autopropulsées. Cette analyse est étendue à des fréquences de battement plus élevées. Trois régimes de propulsion unidirectionnelle qui suivent le mouvement de va et vient - sillage dévié quasi périodique, périodique symétrique et périodique dévié - sont étudiés. Des méthodes de bifurcation non linéaire sont utilisées pour étudier leur apparition, révélant que la propulsion avec sillage dévié quasi périodique et périodique apparaît comme des bifurcations locales des solutions propulsives avec sillage périodique symétrique. La transition entre la propulsion avec sillage dévié quasi-périodique et le va-et-vient est finalement comprise comme une bifurcation globale. Cette partie est conclue par une analyse physique de la nature des forces de poussée. En décomposant la poussée en contributions de diffusion et de pression, nous révélons une transition entre un régime de poussée de diffusion et un de pression. Le régime de poussée de diffusion est caractérisé par l'absence de tourbillons et un cisaillement visqueux asymétrique le long de la paroi latérale de l'aile battante. Le régime de poussée de pression se caractérise par un sillage tourbillonnaire et l'augmentation de la pression au bord de fuite qui en résulte.

La deuxième partie est consacrée aux interactions collectives dans la locomotion d'une allée infinie d'ailes battantes confinées dans un canal. Pour comprendre l'impact de l'interaction collective, on fait varier l'écart fixe entre les ailes et la fréquence de battement, maintenant fixe le rapport de densité des ailes, leur amplitude de battement et la hauteur du canal. Deux solutions coexistantes, qui peuvent être soit plus rapides soit plus lentes qu'une seule aile, sont obtenues pour certaines fréquences et écartements. La puissance nécessaire pour imposer le mouvement de battement de l'aile est toujours inférieure lorsque des interactions collectives sont en jeu. L'émergence de ces solutions est étudiée par des simulations avec une vitesse horizontale imposée à l'allée. La force horizontale moyenne agissant sur les ailes révèle l'existence de trois équilibres du système plutôt que deux. L'émergence des états autopropulsés stables est expliquée par le comportement stabilisateur de la force hydrodynamique moyenne dans le temps agissant sur l'allée.

Mots-clés: Interaction fluide-structure, Propulsion, Stabilité de Floquet, Stabilité non-linéaire

Self-propulsion and fluid-mediated interaction of flapping wings in viscous flows

Abstract: A common locomotion strategy exploited by animals and in the conception of engineering devices is the flapping motion of wings. This form of propulsion appears due to an evolution of the flow dynamics. As fluid inertia and nonlinearities become more significant, locomotion through time-reciprocal flapping motions and collective dynamics become possible. In this work, the onset of flapping propulsion and the role played by passive hydrodynamic interactions in collective dynamics are studied through the stability of the coupled fluid/self-propelled wing system.

The first part of this thesis deals with the horizontal self-propulsion of a symmetric heaving foil in a two-dimensional quiescent fluid. The problem is investigated numerically based on the resolution of the coupled fluid-solid system. At first, we investigate the emergence of self-propelled regimes, adopting a fixed density ratio and flapping amplitude while varying the flapping frequency. At low flapping frequencies, two self-propelled states are analysed: a periodic state of unidirectional propulsion and a quasi-periodic state of slow back and forth motion around a fixed point. These states emergence is explained through a fluid-solid Floquet stability analysis of non-propulsive symmetric base-flows. Unlike purely hydrodynamic stability analyses, the fluid-solid analysis accurately determines the states onset. In addition, it highlights linear mechanisms responsible for unidirectional propulsion and the slow direction switching of back and forth motion. A time-averaged analysis of the modes horizontal force and velocity allows to establish a physical instability criterion for self-propelled foils. This analysis is extended to higher flapping frequencies. Three unidirectional propulsive regimes that follow the back & forth one - quasi-periodic deviated, symmetric periodic and deviated periodic wake - are studied. Nonlinear bifurcation methods are used to investigate their onset, revealing that quasi-periodic and periodic deviated wake propulsion appear as local bifurcations of symmetric periodic wake propulsive solutions. The transition between quasi-periodic deviated wake propulsion and back and forth motion is finally understood as a global bifurcation. This part is concluded by a physical analysis of the thrust generation. Decomposing the thrust force into diffusive and pressure contributions we reveal a transition between diffusion and pressure-driven thrust regimes while increasing the flapping frequency. The diffusive thrust regime is characterized by no vortex shedding and an asymmetric viscous shear alongside the lateral wall of the foil. The pressure driven regime features vortex shedding and its resultant trailing edge pressure increase.

The second part of this thesis is dedicated to the collective interactions of an infinite array of heaving wings confined in a channel. To understand the impact of the collective interaction on the array locomotion, the fixed gap between wings and the flapping frequency are varied while maintaining the wings density ratio, their flapping amplitude and the channel height fixed. Two coexisting solutions, that can be either faster or slower than a single wing, are obtained for certain frequencies and gaps. The power input to heave the wing is always inferior when collective interactions are at play. The emergence of the coexisting solutions is studied through unsteady simulations with an imposed horizontal velocity to the array. The time-averaged horizontal force acting on the wings reveals the existence of three rather than two equilibria of the system. The emergence of only two stable self-propelled states is finally explained by the stabilizing/destabilizing behaviour of the time-averaged hydrodynamic force acting on the array.

Keywords: Fluid-structure interactions, Propulsion, Floquet stability, Nonlinear stability

---

18/09/2017 – 10/11/2020
ONERA, The French Aerospace Lab
8, Rue des Vertugadins, F-92190 Meudon, France.
&
Institut de Mathématiques de Bordeaux
UMR 5251 Université de Bordeaux, F-33400 Talence, France.

This PhD was part of the AEROFLEX project (grant agreement n° 638307) that received funding from the European Research Council (ERC) under the European Union Horizon 2020 research and innovation program.

Dedication

For the final version.

Summary

Introduction

"The first time he saw my airplane, for instance (I shall not draw my airplane; that would be much too complicated for me), he asked me:

- What is that object?

- That is not an object. It flies. It is an airplane. It is my airplane.

And I was proud to have him learn that I could fly." [1]

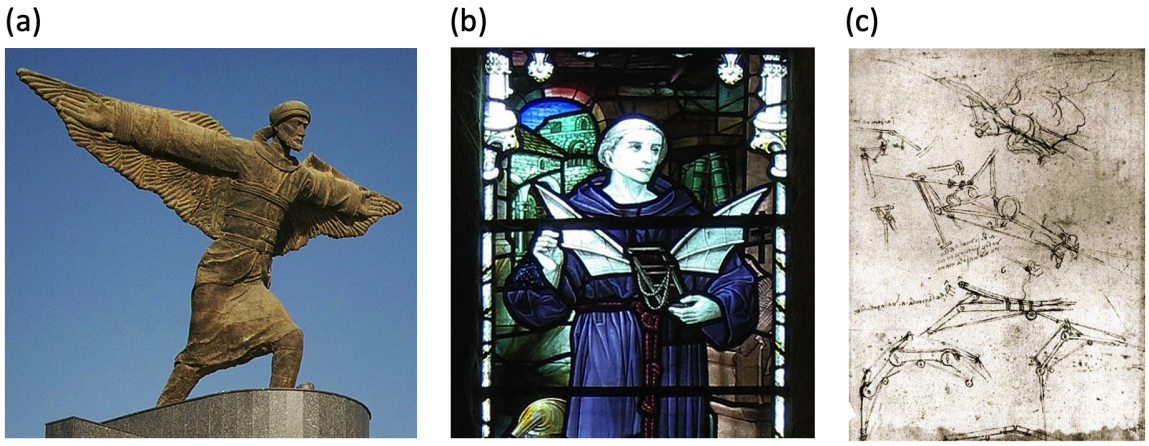

Figure 1: Flapping wing propulsion in human history. (a) Statue of the Andalusian polymath pioneer of aviation Abbas ibn Firnas (810-887) outside Baghdad international airport[A]. (b) Stained glass window portraying Eilmer of Malmesbury (11th century), known for its attempts on gliding flight, at Malmesbury abbey[B]. (c) Leonardo Da Vinci drawings on the conception of a flapping based flying machine[C].

The ability to fly is an ancient human dream. Long was the path followed by the human race until a man could proudly affirm, as Saint-Éxupery to the Little Prince, that he could fly. Although the final chapters of the human aviation history mainly talk about flying machines based on helices or jet propellers, as airplanes and rockets, the first chapters begun with bird and insect inspired flapping wings. This is clearly visible in legends, such as Icarus, or the

[1] Translated from **de Saint-Éxupery, Antoine**, *Le petit prince*, chapitre III (1943)

[A] Extracted from https://en.wikipedia.org/wiki/Abbas_ibn_Firnas, and [B] https://en.wikipedia.org/wiki/Eilmer_of_Malmesbury,[C] Smithsonian National Air and Space Museum, Leonardo da Vinci Codex on the Flight of Birds, 2013 https://airandspace.si.edu/exhibitions/codex/codex.cfm

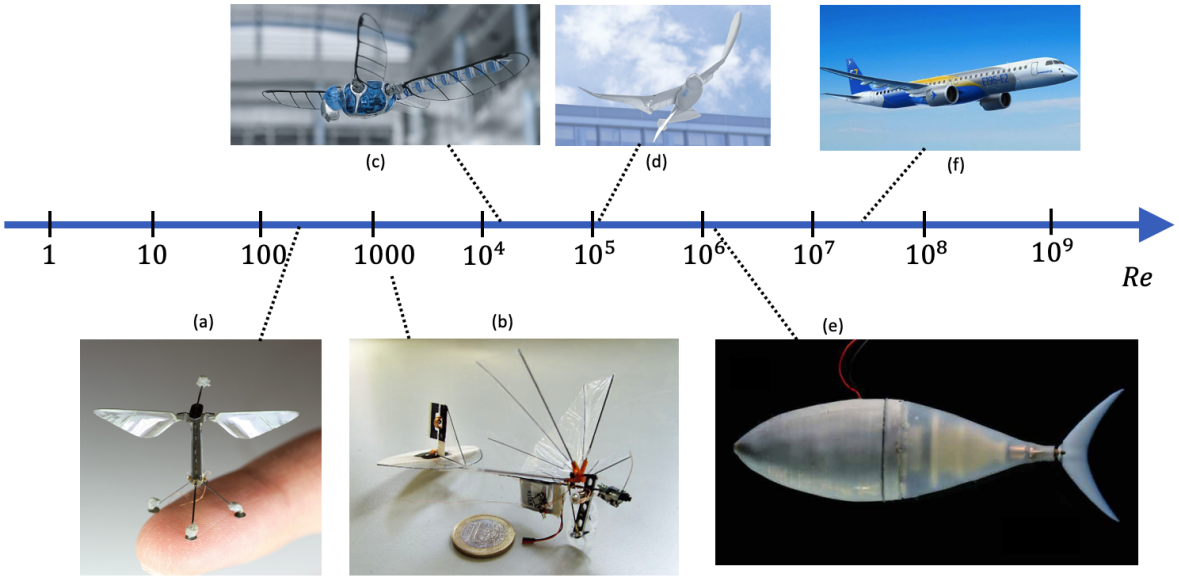

Figure 2: Average Reynolds number range of mankind flying (and one swimming) devices (Calculated based on the references). Flapping wing propulsion micro aerial vehicles (FWMAV) such as (a) Robobee (Chen et al. 2019), (b) Delfly Micro (Deng, Percin, and Van Oudheusden 2015), (c) Festo BionicOpter (Gaissert et al. 2011), (d) Festo SmartBird (Send et al. 2012), the tuna inspired swimming robot (e) Tunabot (Zhu et al. 2019) and (f) commercial jets (Embraer E195-E2).

researches of greek philosophers, as Aristotle. Various historical examples are equally found such as gliding flights with assembled bird feathers or wing-like appendage summed to cliff and roof jumps, as the Andalusian pioneer of aviation Ibn Firnas (figure 1-a) and the Eilmer of Marmesbury (1-b), or the sophisticated human powered flapping mechanisms conceived to mimic bird flight by Leonardo Da Vinci, figure 1(c). At some point, however, flapping wings were replaced through the invention of thermal machines during the industrial revolutions. Hot air balloons, zeppelins and airplanes were the human inventions that first crossed the skies, with Alberto Santos Dumont's *14-bis* documenting the first non-assisted public airplane flight in Paris, 1906.

Despite this latter adoption of different propulsion strategies, flapping wings regained a great territory in the past years. Possible applications are wave and wind energy harvesting (Young, Lai, and Platzer 2014) or the design of artificial swimming and flying machines, see figure 2 and (Ramananarivo, Godoy-Diana, and Thiria 2013; Ristroph and Childress 2014). These applications aim to benefit from flapping propulsion energetic efficiency, maneuvering capabilities (Wu 2010) and its wide range of characteristic body lengths and velocities seen for living organisms, generally measured by the Reynolds number as in figure 3. Several concepts of flapping propulsion based micro-aerial vehicles (MAVs) and artificial swimmers have thus spawned in recent years. Examples of prototypes are insect-like 2(a,b) or seagull and dragonfly 2(c,d) inspired aerial vehicles and tuna inspired swimming robots 2(e), spawning a Reynolds range of $O(100 - 10^6)$. Although already large, this range has not even reached the superior and inferior Reynolds bounds of living organisms, that surpass $O(100 - 10^6)$, where

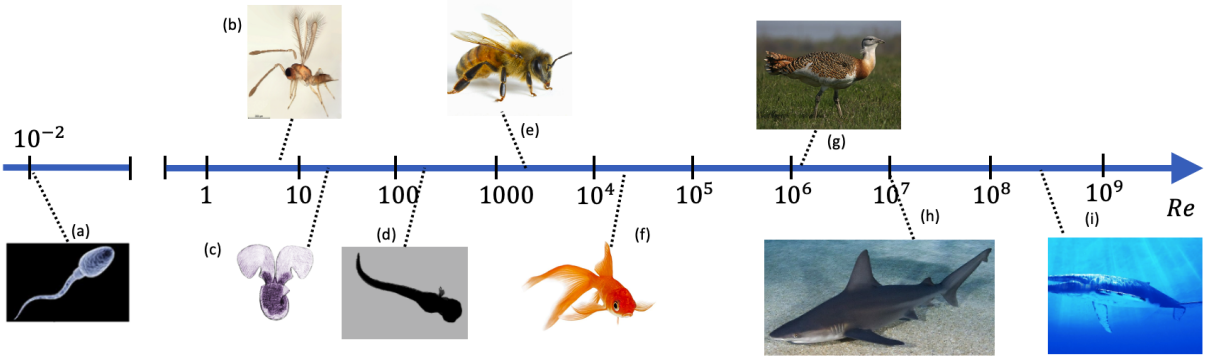

Figure 3: Living organisms Reynolds number range (calculated and averaged based on the indicated references). Flagelary, (a) human sperm (Sane 2003), and flapping propulsion, (b) fairyfly (Santhanakrishnan et al. 2018), (c) sea butterfly (Murphy et al. 2016), (d) zebrafish larvae (Muller 2004), (e) honeybee (Dudley and Ellington 1990), (f) goldfish (Gazzola, Argentina, and Mahadevan 2014b), (g) bustard (Kessler et al. 2013), (h) sharks and (i) whales (Gazzola, Argentina, and Mahadevan 2014b). In the case of flapping propulsion (b-i) swimming and flying organisms are resp. in bottom and top.

birds, fish, bees and zebrafish larvae 3(d-g) are found, attaining very large or unity Reynolds, where resp. whales 3(i) of $Re \approx 10^8$ and sea butterflies or fairyflies 3(b,c) still exploit this locomotion strategy. In fact, to achieve these small scales, flapping wings might be a better option than fixed wing and turbine powered design, a strategy that face challenges in terms of lift production and flight stability in small Reynolds numbers (Mueller 2001; Mueller and Delaurier 2003). Applications of flapping wing devices are found in military (surveillance and detection), agricultural (pollination and spread of pesticides), and even recreational activities (film, photographing and replacing fireworks). As the current designs performance remains far inferior than their biological counterparts (Karásek et al. 2019), a great deal of research is still necessary to better understand intrinsic mechanisms of flapping propulsion. The present work represents an effort towards a better understanding of certain flapping wing propulsion fundamental aspects and tools to simulate their dynamics.

Research surrounding flapping propulsion date back from the works of Gray (1933) about the swimming of animals (eels) or the linearized theories of oscillating airfoils of Garrick (1936). Researches are normally very interdisciplinary encompassing physics, mathematics, computer science and biology. In the case treated in this thesis, aquatic and aerial locomotion, flapping propulsion deals with the interaction of a moving structure and a surrounding fluid and is a typical *fluid-structure interaction* (FSI) problem (Païdoussis, Price, and De Langre 2010). The movement of the flapping appendage both accelerate the surrounding fluid and has its energy dissipated through viscosity. In return, fluid forces act on the body, accelerating it and originating movement. Although the description of the interaction between the moving body and the fluid is a very complex problem, simplified models are one way to assess and understand some flapping propulsion mechanisms. For example, the whole body can be simplified up to studying only the self-propelled motion of a foil like appendage, ignoring the body non-thrust producing part. The coupled dynamics can be equally simplified. Earlier works, for instance, sought to model the surrounding fluid flow as added forces to the solid dynamics through the-

oretical derivations (Garrick 1936; Lighthill 1971) of inviscid flows or correlations obtained from experimental works (Taylor 1952). To assess the surrounding flow dynamics, computational and experimental methods can be exploited, the former presenting the great advantage of not requiring numerical and theoretical models to deal with the problem. Along the years experimental investigations have been used to measure flapping wings forces (Triantafyllou, Triantafyllou, and Grosenbaugh 1993), to assess their self-propelled dynamics (Vandenberghe, Zhang, and Childress 2004; Ramananarivo, Godoy-Diana, and Thiria 2010) and even that of real animals (Beal et al. 2006). Advances in visualization techniques allowed even very accurate descriptions of the surrounding flow interacting with the moving object through bubble evaporation (Vandenberghe, Zhang, and Childress 2004) or particle-image velocimetry (PIV) (Moored et al. 2012). Advances in computer performances and methods handling moving interfaces allow nowadays simulations to attain also great levels of complexity, i.e. three-dimensional fish swimming (Li et al. 2019). Very refined theoretical methods are employed to couple fluid and solid dynamics, such as non-inertial frames of reference (Mougin and Magnaudet 2003), domain decomposition (Ehrenstein 2019), penalization (Bergmann and Iollo 2011; Gazzola et al. 2011), sharp interface immersed boundary (Griffith and Leontini 2017) or arbitrary Lagrangian Eulerian (ALE) methods (Pfister, Marquet, and Carini 2019). Recent advances in numerical methods are even capable of reconstructing fish swimming movements captured from images through optimal transport (Bergmann and Iollo 2016) to feed simulations input. A great benefit from numerical methods, which will be explored in thesis is their capability to attain unstable scenarios that can be used to study transitions in the system dynamics.

In addition to the complexity of simulating fluid-solid coupled problems, flapping wing propulsion faces a very large control parameters space. The nature of the surrounding environment and the solid body itself, the applied kinematics, the geometry of the body and its self-propelled regime are all variables that can be explored. This variety can be exemplified by the numerous choices of characteristic scales. For example, non-dimensional numbers used to characterize flapping propulsion can be constructed based on characteristic scales as the wing size L, flapping frequency and amplitude f and A, the towed or cruise self-propelled velocity U, resulting in the construction of parameters as

$$\beta = \frac{fL^2}{\nu},\ \beta_A = \frac{fAL}{\nu},\ Re = \frac{UL}{\nu},\ St = \frac{fA}{U}\left(\text{or } \frac{fL}{U}\right),$$

the Stokes number β, its flapping amplitude based version β_A (or similarly to both the Swimming number (Gazzola, Argentina, and Mahadevan 2014a) that uses the angular instead of linear frequency), the Reynolds number Re and the Strouhal number St. Stokes and Reynolds number are choices to characterize the balance between inertia and viscosity in the surrounding flow, β and Re differing in the choice of the self-propelled or flapping velocity as characteristic velocity scales, and the Strouhal the balance between horizontal and oscillating velocities. In addition to these, other parameters should be introduced to analyse the solid elasticity, the fluid-solid density ratio, body stream and span-wise ratio, non-dimensional flapping amplitude and many other physical phenomena existent in this seemingly simple (but not) and beautiful problem.

A wide range of these physical phenomena has been explored in the literature. For example, authors investigated the existence of an optimal Strouhal number based on the flapping

frequency and amplitude where thrust is maximized (Triantafyllou, Triantafyllou, and Grosenbaugh 1993), and how the interaction of leading and trailing edge vortex affected this efficiency (Lewin and Haj-Hariri 2003). Propulsive efficiency was then linked to the stability of the jet-like time-averaged wake produced behind oscillating profiles (Triantafyllou, Triantafyllou, and Grosenbaugh 1993; Moored et al. 2012; Moored et al. 2014), with a similar attempt with momentum-less wakes behind self-propelled bodies presenting contrasting results (Arbie, Ehrenstein, and Eloy 2016). As flapping wings are generally elastic, the role of flexibility on thrust enhancement (Spagnolie et al. 2010; Bergmann, Iollo, and Mittal 2014) and a link between (structure or couple fluid-solid system) resonance and optimal thrust has been equally addressed (Ramananarivo, Godoy-Diana, and Thiria 2010; Goza, Floryan, and Rowley 2020). The dynamics when deformation are imposed by muscles rather than passive or piloted by group interactions have been equally investigated (Bergmann and Iollo 2011; Becker et al. 2015). A particular point concerning links between efficiency, animal size and flapping movements, evident in figure 3 is the fact not all self-propelled living organisms exploit flapping wing propulsion. Apparently, this locomotion strategy cannot attain certain scales, and determining those is of utter importance to establish application limits.

The onset of flapping propulsion

As flapping propulsion based devices tend towards applications in smaller scales, for example figure 2(a), a fundamental question is the critical size above which this strategy remains efficient. Organisms in very small scales whose Reynolds numbers attain $Re << 1$, such as human sperm figure 3(a), explore indeed different locomotion strategies (see Lauga (2011) for a review) as ciliar and flagelar propulsion. These strategies are marked by imposed movements which are non time-reciprocal (where the half-strokes are not identical under time-reversal) and in the direction of propulsion. Flapping propulsion, on the other hand, adopts oscillations perpendicular to the direction of travel that can be time-reciprocal. The switch of strategies is related to the evolution of the flow nature. In low Reynolds, the flow is dominated by diffusion having both a linear and time-less character. As stated by Purcell (1977) in the so-called scallop theorem, a reciprocal appendages motion, as the one used by a scallop in high Reynolds, is not capable of generating net locomotion along a cycle under such conditions. Due to the lack of inertia, the velocity which the scallop opens and closes its shell does not affect the force. Added to this fact, the linearity of the diffusive flow character implies that time-reciprocal half-strokes achieve opposite sign forces of same intensity, resulting in a zero displacement. In larger scales, where inertia comes to play, locomotion through flapping time-reciprocal motions become possible. An emblematic observation of the emergence of flapping propulsion concerns the *Clione Antartica*, sketched in figure 4(a), studied by Childress and Dudley (2004). This animal disposes of a hybrid strategy composed both of ciliary and flapping propulsion. While the first is always employed, the flapping of wings is exclusively performed by the animal when its velocity increase above a certain level of $Re \sim 5$, leading to the idea of a critical onset above which flapping propulsion based on reciprocal motions emerge.

To test this hypothesis Vandenberghe, Zhang, and Childress (2004) designed an experiment where flapping locomotion could emerge exclusively from flow rather than motion asymmetry. Although motion asymmetry is substantially exploited by living animals (i.e. Weis-Fogh

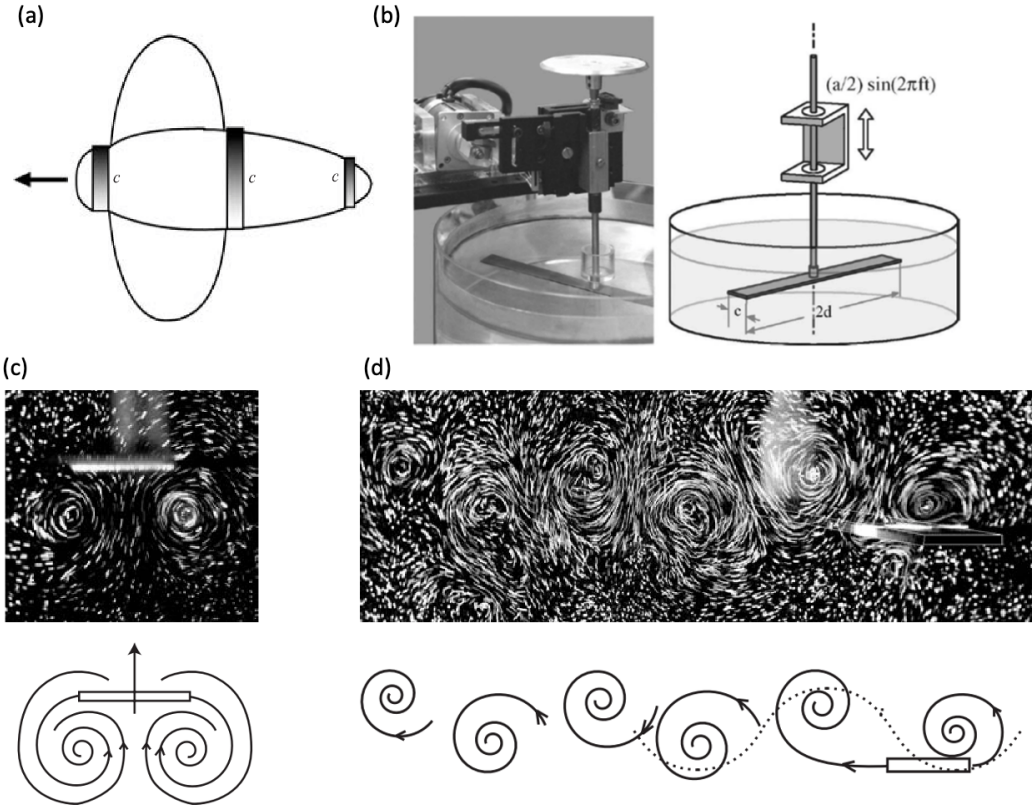

Figure 4: (a) Sketch from (Childress and Dudley 2004) of the mollusc *Clione antarctica* of typical length 6mm, that indicates the mollusc wings, three bands of cilia and its direction of locomotion. (b) Experimental setup of (Vandenberghe, Zhang, and Childress 2004): a rigid rectangular flat wing heaved sinusoidally in the vertical direction and free to rotate in a cylindrical water tank filled with quiescent water. (c,d) Visualization of the flow structures applying a DC potential difference between the wing and the flow, that induces the production of bubbles at the foil surface. (c) Visualization and sketch of a left-right spatial symmetric flow and (d) of a propulsive state featuring a reverse Von-Kármán wake. (b-d) extracted from (Vandenberghe, Zhang, and Childress 2004).

(1973)), the idea of this experiment was to differentiate a regime where fluid inertia and nonlinearities would become important enough allowing time-reciprocal flapping motion to generate net locomotion. The experimental setup, shown in figure 4(b), consists of a flat horizontal rectangular plate immersed in a cylindrical tank filled with quiescent water. The foil is attached to a shaft that is vertically flapped with a sinusoidal motion, while the foil all-together with the shaft are authorized to rotate around the vertical axis. While maintaining a fixed flapping amplitude and increasing the frequency, Vandenberghe, Zhang, and Childress (2004) were capable of visualizing two distinct regimes. For small frequencies (non-dimensional Stokes numbers), the flow produced by the flapping foil is left-right symmetric (figure 4-c). As the flow is symmetric no locomotion is achieved. The forces exerted on the left and right side of the foil are identical and of opposite sign (Elston, Sheridan, and Blackburn 2004). However, for a sufficiently large frequency, above a critical amplitude-based Stokes number of $\beta_A \sim 500$ [2],

[2]Note that as the amplitude based Stokes number is a control parameter, it is here preferred than the Reynolds

(a)

(b)

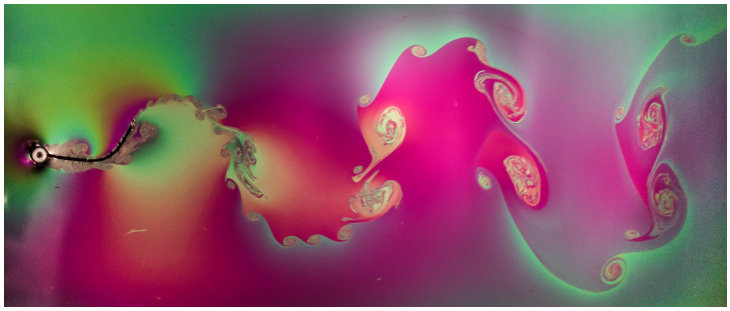

Figure 5: Examples of purely hydrodynamic and coupled fluid solid instabilities in a soap-film flow experiment (Pfister et al. 2020). (a) Von-Kármán vortex wake behind a fixed circular cylinder. (b) Interaction of this vortex shedding with a flexible filament (a silk thread in the experiment) attached behind the cylinder. Incoming flow is oriented towards the right.

the flow symmetry is broken and horizontal forces are generated. The foil achieves locomotion and eventually settles down in a cruise regime of constant time-averaged velocity. Thrust producing reversed Von-Kármán wakes (Triantafyllou, Triantafyllou, and Gopalkrishnan 1991) are observed for these propulsive regimes, as shown in figure 4(d). It appears it exists, indeed, a critical scale where fluid inertia and nonlinearities allow time-reciprocal flapping movements to generate locomotion. But how can we understand and predict the onset of propulsive solutions departing from balanced left-right symmetric ones?

The onset as a hydrodynamic or fluid-solid instability

A promising path to understand how dynamical systems transitions is the concept of *stability*. Hydrodynamic stability (Schmid and Henningson 2001), that deals with flow stability, has been an interest topic since the nineteenth century experiments of Reynolds about transition to turbulence in pipe flows. In recent years, advancements in numerical techniques and performance allowed the field to regain territory. The notion of stability can be understood through the faith of small or moderate perturbations imposed to a dynamic system equilibrium. A stable system is one where perturbation decays and the system returns eventually to its previous state. In an unstable system, however, these same perturbations grow in time, eventually leading the system to a different equilibrium. A simple example of hydrodynamic instability is the transition to vortex shedding behind a cylinder [3] for low Reynolds number flows. While for small Reynolds

number to establish the onset, as the Reynolds is an output of the self-propelled regime.

[3] What would aliens say about this amount of cylinder studies if they ever find Earth and we will no longer be here to explain? They will probably think mankind worshiped them (Iollo 2019).

numbers the flow is steady, unsteady vortex structures start to detach from the cylinder above $Re \sim 47$ (Sipp and Lebedev 2007) originating a Von-Kármán vortex wake as the one visualized in figure 5(a). At this critical Reynolds, perturbations applied to a steady equilibrium, similar to the one observed for smaller Re, will grow exponentially until saturating at a new unsteady state. This critical Re and the amplified structures that generate the vortex shedding are predicted by linear stability analyses.

In the case of the flapping foil locomotion, the studied base solution is periodic, not steady as the cylinder case. Rather than investigating the growth in an infinite time horizon as the cylinder flow, the growth of a perturbation over a period should be investigated. If the system is unstable, perturbations will grow progressively shifting the system away from its periodic equilibrium, changing the periodic cycle and possibly even its frequency. Floquet stability analysis (Floquet 1883) is the mathematical foundation that deals with the stability of periodic systems. It has been first employed in hydrodynamics by Barkley and Henderson (1996) to investigate the onset of three-dimensionality in the wake of circular cylinder. For flapping objects, Floquet stability has successfully been employed (Elston, Sheridan, and Blackburn 2004) to determine the onset of two and three-dimensional asymmetries around non-propelled vertically heaving cylinders. As the emergence of flapping propulsion is also connected to flow symmetry breaking, this same *purely-hydrodynamic* Floquet stability analysis has been employed to study its onset (Deng and Caulfield 2016; Deng et al. 2017; Deng and Caulfield 2018a). This attempt, however, presented disagreements between the stability analysis and the self-propelled results, with the onset not being correctly predicted.

Although flow symmetry breaking appears to be an essential ingredient of the flapping propulsion onset, the problem is an intimately fluid-solid coupled one. Ignoring the feedback mechanisms existing between the solid movement and the fluid flow could result in disagreements between stability and self-propelled predictions. This difference can be illustrated in the case of an elastic filament clamped behind a rigid cylinder. Without the filament, the cylinder displays the purely hydrodynamic instability that generates the Von Kármán vortex street, figure 5(a). As the filament is included, the vortex shedding is altered, figure 5(b). The cylinder vortex shedding excites the filament deformation that in return modifies the mechanism of vortex shedding, resulting in a much different pattern than the purely hydrodynamic system. As we see the lines connecting the vortices shed and the filament trailing edge, we can imagine how this pattern would be different if the elastic filament would not be allowed to deform. This illustrative example leaves the impression that the emergence of a non-zero horizontal velocity and foil movement must be an essential ingredient of the stability of self-propelled systems. As past works (Tchoufag, Fabre, and Magnaudet 2014) took this coupling into account for the study of *steady* base solutions, **this work will extend the inherent fluid-solid coupling to the stability analysis of periodic solutions, perturbing not only the symmetric base-flow but also the foil horizontal velocity.** The idea is to use this analysis to predict the onset of flapping propulsion and linear mechanisms that lead to the emergence of self-propelled regimes from non-propulsive solutions.

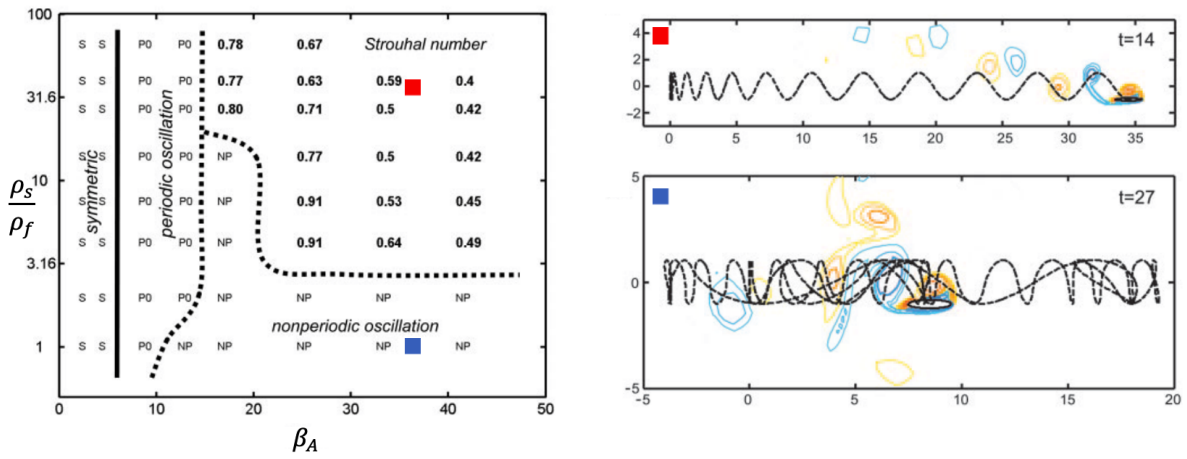

Figure 6: Evolution of the self-propelled regimes in the plan density ratio and flapping amplitude based Stokes number (ρ_s/ρ_f x β_A) in the case of a two-dimensional elliptical foil of thickness-to-chord aspect ratio 0.1. Adapted from (Alben and Shelley 2005). Symmetric zones correspond to no locomotion. Oscillations to back & forth movement around a fixed point, and "Strouhal number" to coherent forward locomotion with a certain velocity that determines the St. Red and blue squares represent a forward and a non-periodic back & forth self-propelled solutions.

Self-propelled dynamics beyond the onset

Beyond the onset of flapping propulsion new self-propelled regimes and transitions await. As the amplitude and frequency of the flapping movement increases, unsteady flow effects become more important. The horizontal velocity normally increases and so do the aerodynamics charges the self-propelled object experience. The light materials (Faux et al. 2018) generally employed for flapping wing micro-aerial vehicles result in an enhancement of the coupling between solid acceleration and these fluid forces. The self-propelled dynamics evolve to complex scenarios, as seen in figure 6, that can be both beneficial or detrimental to locomotion, for example deviated wake and back & forth movements. Periodic or chaotic non-coherent back & forth movements are detrimental states of frequency much smaller than the flapping one where the self-propelled wing looses control of its trajectory oscillating back & forth around a fixed point. As these detrimental regimes are found both in nature, sea butterflies (Murphy et al. 2016), and numerical examples, two-dimensional elliptical foils (Alben and Shelley 2005), it is essential to predict their range. Back & forth movements appear to be surrounded by non-propulsive and coherent forward propulsive solutions. Inside unidirectional locomotion, certain frequencies and amplitudes achieve an enhanced velocity thanks to the wake deviation behind the flapping foil. This phenomenon, already observed for non-propelled foils (Godoy-Diana et al. 2009), is known to enhance the thrust (Jallas, Marquet, and Fabre 2017) of the flapping wing and could probably be exploited to increase the energetic efficiency of self-propelled devices.

As the onset of flapping propulsion, an essential question is how to predict these transitions to avoid or achieve them e.g. through control of the flapping amplitude and frequencies. However, the transitions that take place beyond the onset of flapping propulsion are more complex to follow than the transition between non-propelled and propelled states. The most

straightforward manner is to study the evolution in time of the system under different control parameters, for example by time marching a numerical simulation. This approach was followed by many numerical studies, for example Alben and Shelley (2005) density ratio and amplitude based Stokes plan of self-propelled regimes of two-dimensional ellipses shown in figure 6. This plan shows that for a fixed density ratio, rising the Stokes numbers (flapping frequencies) results in a transition between back & forth periodic oscillations around a mean position to unidirectional propulsive solutions with different Strouhal numbers. For a fixed Stokes number, while small density ratios tend to encourage non-periodic oscillations, the increase of the foil density, corroborated also by Lu and Liao (2006), has a stabilizing effect that allow flapping wings to achieve unidirectional locomotion.

Although this time-marching approach has the benefit of generality, it lacks theoretical explanations and practical efficiency. The *a priori* fastidious study of a wide range of parameters, going through long transient evolution, generates a great amount of unexploited work or data, and more efficient methods could be developed. On the theoretical side, this natural time evolution does not allow to calculate some unstable states, an option that opens the possibility to assess linear or nonlinear mechanisms leading to the regimes transition. To obtain quicker estimations of stable self-propelled regimes and explain the different dynamics beyond the onset, purely hydrodynamic Floquet stability analyses have been also explored. In the case of a three-dimensional self-propelled ellipsoid, Deng et al. (2016) and Deng and Caulfield (2018a) have tried to link snaking and stair-step back & forth and unidirectional propulsive regimes to the nonlinear combination of Floquet unstable modes obtained for the axi-symmetric flow around a non-propelled heaving ellipsoid. They associated, for certain frequencies, non-coherent and coherent regimes to the existence of higher and unitary azimuthal unstable modes. However, the prediction of the regimes onset or a general robust comparison within a greater parameters range was not performed.

To improve this understanding, **the self-propelled dynamics and transitions beyond the onset are revisited in this work, in the case of a two-dimensional self-propelled heaving foil, through nonlinear bifurcation methods and fluid-solid Floquet stability**. Our strategy consists at considering the fluid-solid coupling both at base-solution and perturbation level, different than purely hydrodynamics analyses. Alternatively to time marching methods, *harmonic balance methods*, recently applied in the context of flapping airfoils (Gopinath and Jameson 2005) and turbomachinery (Gopinath et al. 2007), are used to directly calculate self-propelled base solutions. Using the imposed heaving movement inherent periodicity, these methods convert a time-dependent problem into a system of equations that together determine the periodic solution spectral content (Fourier coefficients). In this work, the time-domain variant time-spectral method (TSM) will be applied in the context of self-propelled flapping wings. These methods present not only the advantage of directly assessing cruise regimes, but they also allow to determine unstable periodic solutions. In this manner, TSM and continuation methods, as pseudo arc-length continuation (Govaerts 2000), allow to investigate the nonlinear transition between non-coherent back & forth motion and unidirectional propulsion by following the faith of the periodic propulsive solution. Followed then by a fluid-solid Floquet stability analysis, the stability of these solutions is evaluated to predict the dynamics beyond the onset.

On the physical origins of thrust forces

In addition to predicting self-propelled dynamics, another matter of great concern for the conception of flapping devices is the physical origin of thrust forces generated by the wing motion. As these forces allow to trigger and sustain motion during respectively transient and cruise regimes, thus the emergence and control of self-propelled regimes, it is essential to understand how the wing geometry and its flapping motion affect thrust forces. Since they are generated by the dynamic response of the surrounding medium to the moving appendage, in our case generally a fluid, the forces greatly vary according to the balance between inertia and viscosity of the surrounding flow. In the case of oscillatory and undulatory propulsion (Smits 2019), theoretical models (Eloy 2013) give an example of the numerous existing force physical natures. Key components are for example those of reaction of the solid to fluid acceleration (reactive forces) (Lighthill 1971; Candelier, Boyer, and Leroyer 2011), forces that resist against the flapping motion (Taylor 1952), and forces that actuate in the swimming direction as skin drag, which has additional components when compared to a static object due to the boundary layer thinning while flapping (Ehrenstein and Eloy 2013), and pressure drag, which in flapping swimmers is increased by the roll-up of vortices in the lateral edge (Raspa et al. 2014). For high Reynolds numbers, the thrust of oscillatory and undulatory self-propelled bodies (Smits 2019) is mainly generated by inertial components with forces that resist against the body movement playing a secondary thrust or drag role (Eloy 2013).

Recent studies have however reconsidered, encouraged by the relatively low transverse Reynolds numbers found in intermediary (horizontal velocity based) Reynolds numbers, the role of forces that resist against the body flapping motion (motion perpendicular to the swimming direction). They revealed that these forces might rise up to greater proportion and even drive in some cases the thrust generated by flapping foils in the swimming direction. For undulatory swimmers, the inclusion of this perpendicular damping in the structural equations is capable of generating propagating waves, an anguilliform kinematic, in passively deforming elastic bodies (Ramananarivo, Godoy-Diana, and Thiria 2014) contributing to propulsive efficiency. Due to the body curvature projection of these perpendicular forces in the swimming direction, resistive forces can contribute to thrust, being identified as key components (up to 90 percent of the thrust) (Piñeirua, Godoy-Diana, and Thiria 2015) of low aspect ratio anguilliform swimmers. Fluid acceleration becomes, again, a dominant thrust source as the flapping swimmers become less elongated or carangiform, like a beam first mode of vibration, kinematics are adopted. Another path towards intermediary regimes, where both resistive and inertial forces contribute to thrust, can be precisely the self-propelled dynamics of heaving foils near the onset of flapping propulsion. In this case, studies of bodies as ellipses and ellipsoids in respectively two and three-dimensional flows (Alben and Shelley 2005; Deng and Caulfield 2018a) have noticed that resistive forces of viscous nature are at the origin of the thrust generation during transient regimes, particularly in the early phases where the foil velocity becomes non-zero. In this transient phase, the foil is accelerated along its flapping period with viscous and pressure forces actuating together as thrust sources. However, once a cruise regime is achieved (and thus the foil is no longer accelerated along a flapping period) the time-averaged viscous and pressure forces should mutually compensate each other, viscous forces were observed to fall into an usual drag role with pressure driving the thrust forces in cruise regime. **In this work we will revisit this problem investigating either a cruise regime where thrust is driven by viscous forces exist.** To distinguish thrust sources in cruise regimes, we employ a time-averaged analysis of

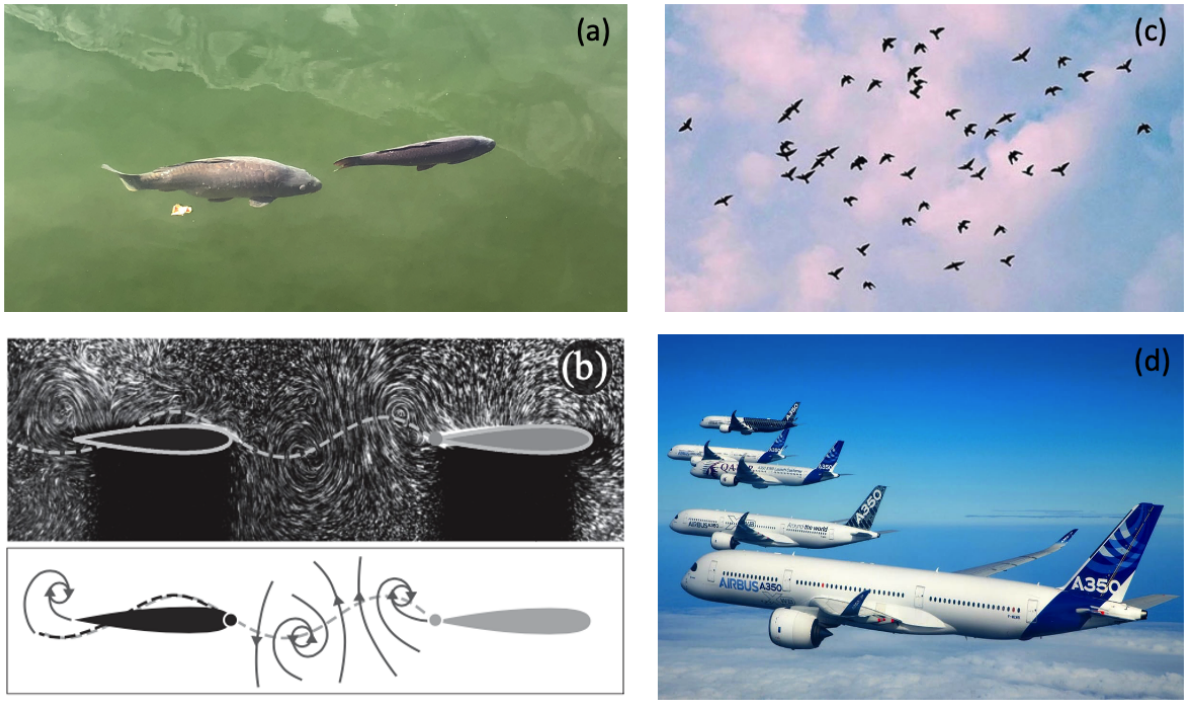

Figure 7: Examples of fluid-mediated interaction of self-propelled objects. (a) Two fish closely swimming together in the lake of Fontainebleau (photo took by the author). (b) Ramananarivo et al. (2016) experiment of two simultaneously heaving NACA profiles separated by a non-fixed gap. (c) Flock of birds in the sky of Palaiseau. (d) Airbus airplanes flying in formation(AirBus fello'fly project).

diffusive and pressure contributions to horizontal forces. As they mutually compensate when periodic cruise regimes are attained, a distinction can be made between overall thrust and drug contributions along a flapping period. For posterior conception of flapping based devices, the effect of control parameters as the foil flapping frequency, amplitude and its aspect and density ratio over the physical origin of the thrust is equally addressed. As studies have long associated thrust production to wake patterns (Triantafyllou, Triantafyllou, and Grosenbaugh 1993; Zhang 2017; Andersen et al. 2017), we extend this analysis to associate different wakes to their thrust physical nature.

Fluid-mediated collective interactions

The previous commented works evaluate the propulsion of a flapping wing in an ideal environment where the surrounding fluid is quiescent. An essential point to be dealt within flapping wing locomotion is how the self-propelled dynamics are influenced under the presence of natural turbulence (Engels et al. 2016), solid walls (Quinn, Lauder, and Smits 2014) or the proximity of other self-propelled organisms. As illustrated in figure 7(a,c), living organisms are known to collectively interact, resulting in agglomerates as bird flocks and fish schools. Those collective formations have long interested researchers due to their promising energetic benefits (Portugal et al. 2014). Energy efficiency, and its correlated atmosphere pollution, are very actual topics of aerial traffic. For example, the AirBus fello'fly project, 7(d), intends to benefit

from placing airplanes in cruise altitude in the nearby wake of neighbouring airplanes ($\approx$ 3 km of horizontal distance between airplanes) to reduce fuel consumption and drop CO2 emissions. How would this collective interaction come at play in the case of flapping and not steady wings? As collective dynamics are already envisaged in the case of low Reynolds numbers, for example in drug delivery applications with active squirmers delivering and interacting with a particle (Reigh et al. 2017), would it also be possible to exploit collective interaction in higher Reynolds numbers where flapping wings are found?

Recent studies show that understanding fluid mediated interactions are essential to conceive collective interaction of flapping wings (Filella et al. 2018). Fish are known to dispose of specific mechanisms as the lateral line (Liao and Akanyeti 2017) to sense the surrounding flow thus adapting their trajectory to intercept vortex (Liao, Beal, and Lauder 2003). From a fluid dynamics point of view it has been also long conjectured (Lighthill 1975) that collective dynamics might arise spontaneously and exclusively from passive hydrodynamic interaction between different flapping wings. This option is particularly interesting for engineering devices since it does not require additional sensing and control strategies. Recent theoretical, experimental and numerical works have consistently verified the Lighthill conjecture for coordinated (Ramananarivo et al. 2016; Peng, Huang, and Lu 2018a) and uncoordinated (Newbolt, Zhang, and Ristroph 2019; Lin et al. 2019) schools of two or many flapping tandem wings as well as other lattices (Oza, Ristroph, and Shelley 2019). These works reveal that coherent ordering and stable collective formations can effectively arise without the need for control strategies. Energetic advantages, such as velocity increase or decrease of the power input necessary to impose the flapping motion have been observed (Becker et al. 2015; Ramananarivo et al. 2016; Lin et al. 2019), indicating a true interest for collective dynamics in artificial devices. However, the dependency of the final configuration on initial conditions remains an open question necessary to tame this phenomenon for applications.

Ramananarivo et al. (2016) showed (figure 7-b) in the case of two tandem self-propelled wings that successive stable states exist, inferring these states are successively linked. The attraction to different stable states is explained by the stabilizing hydrodynamic force that acts like a spring when the follower wing is driven away from its stable position. Concerning the interaction between wing and the incoming wake, the stable states appear to be linked to constructive wake-flapping body interactions as the ones observed in the experiments of Becker et al. (2015) where the gap between wings was fixed. In these two cases, bifurcations are observed with respect to the flapping frequency or the initial position of the foil. **In this work we will investigate if transitions in the collective self-propelled dynamics should be interpreted as instabilities of the coupled fluid-solid system.** We try to enlarge to the formation of collective "patterns" in fluid-solid systems the known role of hydrodynamic instabilities in pattern formations (Gallaire and Brun 2017).

Organization of the present manuscript

To answer the questions raised during this "short" introduction, this dissertation is decomposed in two distinct parts, each dealing with a specific configuration. The first chapters of the parts are

always dedicated to theoretical and numerical methods, being then followed by their application in physical studies.

The **part I** of this thesis is dedicated to the horizontal self-propulsion of a symmetric heaving foil in a quiescent fluid.

The **chapter 1** introduces the theoretical and numerical framework used throughout this part of the thesis. The adoption of a non-inertial frame of reference in the Navier-Stokes equations, coupled to the foil horizontal dynamics is first discussed. Numerical methods for solving the unsteady nonlinear problem are then presented, followed by their validation. Using a semi-implicit time-advancing scheme second order accurate, the unsteady solver is practically implemented using finite-elements within the programming language FreeFEM. Based on the intrinsic periodicity of the imposed heaving movement specific methods for periodic solutions are then introduced. The first to be introduced is the time-spectral method (TSM). This time-domain harmonic balance method exploit the time-periodicity of the system to solve directly for the periodic cruise regime of self-propelled foils. The previous semi-implicit time scheme is then replaced by a spectral approximation of the time derivative that couples several instants along a flapping period. The resulting nonlinear system is solved by a Newton method. The iterative method with its parallel implementation and preconditionning strategy used to tackle the large scale discrete linear problem is then introduced and validated. Floquet stability analysis for self-propelled foils is finally presented. The fluid-solid coupling is introduced in this analysis using the same strategy of the unsteady nonlinear method. The Arnoldi method in a serial implementation with the modified Gram-Schmidt algorithm used for the orthogonalization process is presented to compute the Floquet modes and exponents. The method is validated in a purely-hydrodynamic Floquet analysis and cross-validated with the exponential growth of perturbations in the unsteady nonlinear simulations.

The self-propelled dynamics at low flapping frequencies (Stokes number) at a fixed flapping amplitude are addressed in **chapter 2**. Using unsteady nonlinear simulations two self-propelled regimes are analysed: a periodic regime of unidirectional motion and another quasi-periodic one of slow back & forth motion around a mean horizontal position. The emergence of this regimes is explained through a fluid-solid Floquet stability analysis of non-propulsive solutions. While it is shown that this analysis captures the onset of the self-propelled regimes, linear mechanisms leading to unidirectional and back & forth motion and physical instability criteria are also exposed.

The study of the self-propelled regimes is then extended to higher flapping frequencies in **chapter 3**. Unsteady nonlinear simulations reveal the existence of three additional unidirectional propulsive self-propelled regimes that appear beyond quasi-periodic back & forth motion: A deviated wake quasi-periodic, a symmetric wake periodic and a deviated wake periodic propulsive regime. To study their onset time-spectral method coupled to a pseudo arc-length are used to follow symmetric periodic wake propulsive solutions beyond their natural range. Fluid-solid Floquet stability analysis of these propulsive solutions are then employed to study as local bifurcations the transition between deviated wake quasi periodic and symmetric periodic wake as well as symmetric and deviated wake periodic solutions. The transition between back & forth and deviated wake quasi-periodic propulsive regimes is finally studied as a global bifurcation of the self-propelled system.

The last chapter of part I, **chapter 4**, is devoted to a physical analysis of the thrust produced by the flapping foil. Thrust regimes driven by diffusion and pressure are reported and the evolution of these regimes with different flapping frequencies and amplitudes as well as foil thickness-to-chord aspect ratio is studied.

Collective interactions rather than a single heaving foil are then studied in the **part II**, considering the horizontal self-propulsion of an infinite array of heaving wings confined in a channel surrounded by a quiescent fluid.

The first chapter of this part, **chapter 5**, is consecrated to theoretical and numerical methods. As the configuration is confined by walls, the non-inertial frame of reference introduced in §1 cannot be exploited to take into account the wing heaving motion. A fictitious domain formulation with distributed Lagrange multipliers is then introduced. Using a implicit linearized second-order accurate temporal discretization, the unsteady solver is again pratically implemented using finite-elements within the programming language FreeFEM. The unsteady solver is finally validated.

The final chapter of this thesis, **chapter 6**, deals with the effect of the collective hydrodynamic interaction over the infinite array of heaving wing confined within a channel. The co-existence of two different self-propelled solutions of the array, one faster and one slower than a non-interacting wing, is investigated. Imposing the array horizontal velocity, the existence of an additional unstable *quasi*-self-propelled solution is studied. Energetic aspects and the stabilizing and destabilizing role of the hydrodynamic interactions is depicted.

Finally, concluding remarks assemble the results obtained throughout the two parts of the thesis. Insights are offered on different perspectives such as the study of three dimensional fluid solid instabilities of self-propelled foils, adjoint fluid-solid Floquet modes and collectively interacting self-propelled system.

Communications

The present work has lead to different past and foreseen communications, that are hereby listed

Journal articles

- L. Benetti Ramos, O. Marquet, M. Bergmann, A. Iollo, *Fluid-solid Floquet stability analysis of self-propelled heaving foils*, accepted for publication in Journal of Fluid Mechanics (2020).

- L. Benetti Ramos, O. Marquet, M. Bergmann, *Transition between diffusion and pressure driven thrust of self-propelled heaving foils*, in preparation for Journal of Fluid Mechanics (2020).

- L. Benetti Ramos, O. Marquet, M. Bergmann, A. Iollo, *Local and global bifurcation of self-propelled heaving foils at high flapping frequencies*, in preparation for Journal of Fluid Mechanics.

Conferences

- L. Benetti Ramos, O. Marquet, M. Bergmann, A. Iollo, *Symmetry breaking and self-propulsion of heaving foils*, 8th International Symposium on Bifurcations and Instabilities in Fluid Dynamics, Limerick - Ireland (2019).

- L. Benetti Ramos, O. Marquet, M. Bergmann, A. Iollo, *Interaction hydrodynamique d'une allée infinie d'ailes battantes dans un écoulement visqueux*, Journée de la Fédération Francilienne de Mécanique - ondes et vibrations en milieux complexes, Paris - France (2020).

- L. Benetti Ramos, O. Marquet, M. Bergmann, A. Iollo, *Stabilizing and destabilizing hydrodynamic interaction in a self-propelled infinite array of flapping wings in a viscous flow*, International Congress of Theoretical and Applied Mechanics - ICTAM 2020/2021, Milan - Italy (2021).

Part I

Dynamics of a self-propelled flapping wing in a viscous flow

Part I introduction

Description of the self-propelled configuration

We investigate the horizontally constrained locomotion of a vertically flapping foil of density ρ_s immersed in an initially quiescent fluid of density ρ_f and viscosity ν. The adopted foil is similar to the one used in the experimental studies of Vandenberghe, Zhang, and Childress (2004) and Vandenberghe, Childress, and Zhang (2006). Its shape, rectangular with rounded edges, is characterized by the thickness h^* and chord c^* with the rounded corners diameter equal to the foil thickness. The periodic displacement imposed along the vertical axis e_y is

$$y_g^*(t) = -A^* \cos(2\pi f^* t^*), \tag{1}$$

where the superscript * is used to indicate dimensional variables. A^* is the maximal vertical amplitude and f^* is the flapping frequency, and $T^* = 1/f^*$ is the flapping period. The foil is free to move along the horizontal axis e_x as a result of hydrodynamic forces acting on the solid-fluid interface Γ_w. This rigid-body fluid-structure interaction is characterized by four non-dimensional parameters, namely the frequency-based Stokes number β, the non-dimensional amplitude A, the solid-fluid density ratio ρ and the non-dimensional thickness h, defined respectively as

$$\beta = \frac{f^*(c^*)^2}{\nu},\ A = \frac{A^*}{c^*},\ \rho = \frac{\rho_s}{\rho_f} \text{ and } h = \frac{h^*}{c^*}. \tag{2}$$

These parameters are obtained by choosing the chord c^* as characteristic length scale, the fluid density ρ_f as characteristic mass scale and the flapping period $1/f^*$ as characteristic time. In the following, all variables are thus made non-dimensional using these scales. Note that the non-dimensional flapping period T is thus equal to 1 whatever the values of the Stokes number β, which is the only parameter or variable containing the dependency to the dimensional frequency f^*. Other choices of characteristic scale are also possible and made in the literature. For instance, Alben and Shelley (2005) used the flapping velocity $A^* f^*$ as characteristic velocity, thus introducing the frequency Reynolds number $Re_f = A^* f^* c/\nu = A\beta$ instead of the Stokes number.

In this study the foil geometry, flapping amplitude and frequency influence will be investigated. A discussion of the influence of these two parameters can be found in Zhang et al. (2009) and Deng and Caulfield (2016). The influence of the Stokes number β will be a current topic along chapters 2 and 3, where the aspect ratio and amplitude will be fixed to $h = 1/20$ and $A = 0.5$. These parameters are adopted to have an aspect ratio similar to Vandenberghe, Zhang, and Childress (2004) and the same flapping amplitude of Alben and Shelley (2005). The effect

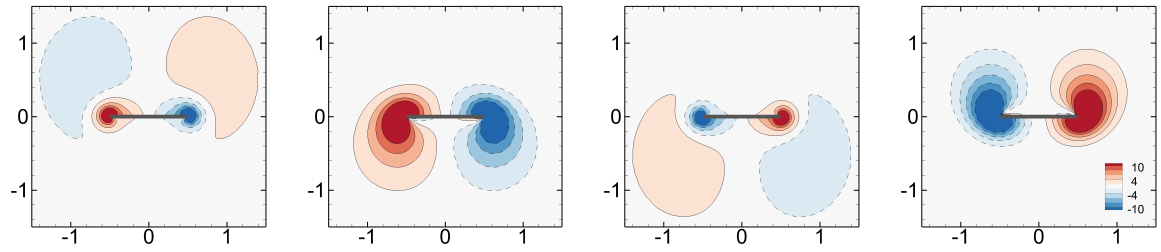

(a) t_0 (b) $t_0 + 1/4$ (c) $t_0 + 1/2$ (d) $t_0 + 3/4$

Figure 8: Symmetric solution for $\beta = 2$. The vorticity field is depicted in the non-inertial frame of reference (x, y) (a-d) for four equally-spaced instant of the unitary period. The initial time t_0 corresponds to the lowest vertical position of the foil.

of the density ratio ρ will be also invoked in chapters 2 and 4. In this last chapter, effects of the aspect ratio, flapping amplitude and frequency will also be discussed.

Spatial and spatio-temporal symmetries of the problem

Due to the inherent shape symmetry of the foil and time symmetry of the applied heaving movement, some symmetries are expected in the fluid flow. A typical solution obtained for small values of the Stokes number that retains all problem symmetries, $\beta = 2$ in figure 8, is used here to illustrate these. The flow induced by the flapping foil satisfies the x-reflection spatial symmetry (in a non-inertial frame of reference that moves with the foil center of gravity), i.e.

$$(u, v, p, \omega_z)(x, y, t) = (-u, v, p, -\omega_z)(-x, y, t), \tag{3}$$

and the spatio-temporal symmetry

$$(u, v, p, \omega_z)(x, y, t) = (u, -v, p, -\omega_z)(x, -y, t + T/2), \tag{4}$$

which is the combination of the y-reflection symmetry and the $T/2$ time-reciprocal translation. The vorticity ω_z, used to display the solution, in Figure 8(a-d) at four equally-spaced instants of the period T, is clearly an odd function of the x variable for every time instants. Physically, vortices of equal shape but different sign are shed one each side of the foil during its vertical motion. The spatio-temporal flow symmetry is observed by noting the inversion of the vorticity sign in opposite foil strokes. A direct consequence of the spatial flow symmetry is the absence of instantaneous hydrodynamic forces acting in the horizontal direction, i.e. $F_x(t) = 0$ (Jallas, Marquet, and Fabre 2017). Consequently, the foil is not accelerated in that direction and its velocity remains zero, resulting in non-propulsive solutions.

Part I overview

When the flow symmetries are no longer respected, hydrodynamic forces will act on the foil that will thus accelerate and retrieve cruise regimes. The locomotion regimes, characterized in figure 9(a) through the time-averaged over a flapping period horizontal velocity, are many and

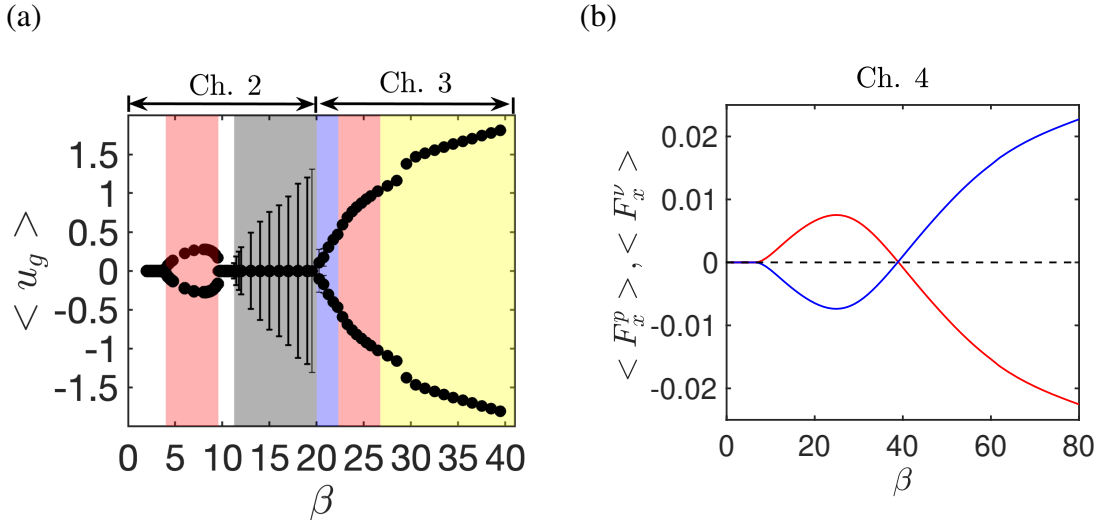

Figure 9: Partition of the contents of Part I along its chapters. The chapters 2 and 3 deal with the transitions betweene self-propelled regimes illustrated here by the background colors in (a) time-averaged horizontal velocity $< u_g >$ evolution with the Stokes number ($A = 0.5$, $h = 0.05$, $\rho = 100$) . The chapter 4 then deals with the thrust produced by these regimes, and more particularly the transition between (b) diffusion and pressure-driven thrust forces with the evolution of β ($A = 0.25$, $h = 0.05$, $\rho = 100$).

so are their thrust producing mechanisms, represented in (9-b) by the time-averaged viscous and pressure force components. The intent of the present part of this thesis is to first study the onset of self-propulsion, the first self-propelled regimes that emerge from non-propulsive solutions, as fluid-solid Floquet instabilities (chapter 2). Transitions occurring at higher flapping frequencies will thus be investigated as local and global bifurcations in chapter 3. This part is finished by a study of the physical mechanisms behind thrust production (chapter 4).

First of all, the next chapter will discuss the theoretical and numerical methods used to perform these aforementioned studies. Without further suspense, we come to it at last![4]

[4]The White, Gandalf (3019 year of the 3rd age).

Chapter 1

Theoretical and numerical methods

This chapter introduces the theoretical and numerical methods used throughout the Part I of this thesis. To study the unsteady dynamics of the self-propelled foil coupled to the fluid flow we introduce the system of equations composed of the Navier-Stokes equations written in a non-inertial frame of reference and Newton's second law. The numerical method used to solve the unsteady problem is detailed and validated. Owing to the inherent time-periodicity of the heaving motion applied to the wing, theoretical and numerical methods for studying periodic solutions are then introduced. The Time Spectral Method, a method that allows to obtain directly a periodic cycle without passing through transient regimes is first presented. This method is followed by Floquet stability analysis. Both methods are specifically detailed for the coupled fluid-solid problem. In the end of this chapter a summary synthesizes how these methods allowed us to explore the studied problem across the different chapters of this part of the thesis.

Contents

1.1 Introduction

One of the most amazing things of watching the flight of birds and the swim of fish is to calmly realize how far in the deep blue horizon or sea these animals can reach with the simple beating of their wings and tails. Nevertheless, what is so pleasing to watch is also one of the greatest challenges of simulating the self-propelled dynamics of flapping foils: handling the movement of an interface that separates two very distinct media - the fluid and the solid ones.

In this part of the thesis we deal with a rigid foil, whose interface does not deform. In this case, an efficient method to get rid of the interface time-dependency is then to adopt a non-inertial frame of reference that follow the foil self-propelled motion. This formulation has been successfully employed in the study of rising and falling bodies in viscous fluids (Mougin and Magnaudet 2002; Jenny, Bouchet, and Dušek 2003; Tchoufag, Fabre, and Magnaudet 2014) as well as the study of non-propelled pitching foils (Jallas, Marquet, and Fabre 2017). This technique will be preferred in this study due to two of its qualities. In one hand, this method is capable of achieving a conforming description of the solid-fluid interface without the numerical burden of arbitrary Lagrangian Eulerian (ALE) methods and their extension domain (Deparis et al. 2016; Pfister, Marquet, and Carini 2019). In addition, large movements of the fluid-solid interface can be handled, as is the case for Immersed Boundary Methods (IBM) (Peskin 1972), Fictitious Domain (FD) (Glowinski et al. 2001) and Penalization Methods (Angot, Bruneau, and Fabrie 1999). It, however, does not have interpolation and non-conformity issues on the fluid-solid interface of these methods. These two issues can add up in numerical errors when integrating forces acting on the solid body (Bergmann and Iollo 2011; Goza et al. 2016).

In the next sections, we will describe how the adoption of this non-inertial frame of reference results in minimal modification of the coupled fluid-solid equations. The numerical method used to solve these equations will thus be introduced and validated. A reader familiar with the concept of non-inertial frames might be capable of jumping these derivations.

Another burden of studying self-propelled flapping foils are its transient dynamics. A long time is consumed from the moment a bird takes off until it reaches a permanent cruise regime. Although transient dynamics might have an inherent physical interest, they result in a large amount of unused data when only permanent regimes under different control conditions are sought. In addition, even tough a periodic flapping is imposed to the foil, sometimes non-periodic self-propelled dynamics might emerge. In these cases, it is particularly interesting to assess if an unstable periodic solution exists. Linear mechanisms responsible for non-periodic behavior emergence can be thus studied. However, unsteady approaches, that mimic natural time evolution, are normally not capable of remaining in these unstable cycles.

For these two reasons, *Harmonic Balance Methods* (HBM) will be explored to seek the periodic solution (cruise regime) of a self-propelled foil under the form of a Fourier series. More particularly their time domain variation, the Time-Spectral Method (TSM) (Gopinath and Jameson 2005), will be employed in this work. These methods use the intrinsic periodicity of a dynamical system to calculate directly their limit cycle, establishing the harmonic content of the periodic solution rather than undergoing the transitory and saturation process of unsteady simulations. The HBM/TSM then transforms an unsteady equation into a (coupled) system of equations that determine the amplitude of the Fourier coefficients of the unknown periodic solution. These approaches have been successfully adopted in recent studies of electrical circuits (Gilmore and Steer 1991), flapping airfoils (Gopinath and Jameson 2005), turbomachines (Hall,

Thomas, and Clark 2002; Weide, Gopinath, and Jameson 2005; Gopinath et al. 2007), shape optimization of turbines in unsteady flows (Rubino et al. 2018) and in the transition mechanisms of boundary layers (Rigas, Sipp, and Colonius 2020).

In this chapter the TSM formulation will be introduced to study the self-propelled dynamics of a foil coupled to a viscous fluid. The numerical method, its validation and performance will be presented. The numerical method used to tackle the coupled equations will be equally presented. The greatest challenge of numerically solving the HBM or TSM methods lies in the switch between time iterating a single equation and solving at once coupled equations: the numerical problem to solve grows proportionally to the spectral content of the truncated Fourier series. As a result, even when two-dimensional or small spatial discretizations are used, a great number of degrees of freedoms need to be solved. An efficient and robust solver for such large-scale problem is still an ongoing field of research. Originally, the coupled equations were solved through an approach much similar to time advancing schemes through explicit (Weide, Gopinath, and Jameson 2005) or implicit (Sicot, Puigt, and Montagnac 2008) pseudo-time-stepping. However, these approaches presented severe time-step restrictions as the system looses diagonal dominance with the increase of the number of harmonics and the off-diagonal physical frequency. To overcome this issue, iterative methods were sought as alternative. Instead of time-step restrictions, these methods require an efficient preconditionning strategy to achieve a reasonable efficiency. Robust strategies for the TSM are still an ongoing research topic (Mundis and Mavriplis 2013; Mundis and Mavriplis 2017) and preconditionners robust to the number of harmonics were only recently presented by Mundis and Mavriplis (2017). In this work, we contribute to this search presenting an alternative (easy to implement) preconditionning strategy, also robust to the number of harmonics. The strategy is based on the inversion of the easily diagonizable (Schmid, De Pando, and Peake 2017) circulant matrix block of the TSM Jacobian, also presented by Moulin (2020) in the case of flutter bifurcations.

The choice of the TSM variant is based in two factors. First the presence of nonlinearities result in a fastidious analytic derivation of harmonic coupling in the HBM mathematical formulation. This derivation should be increased for every variation of the resolved number of harmonics. In the case of the time-domain version, this coupling is handled by a time-differential matrix that is easily calculated through Fourier coefficients, not producing any modification of the governing equations. In a second step, this choice was based on the possibility of adopting an immersed boundary method rather than the non-inertial frame. The time-dependency of the fluid-solid interface is a problem for the harmonic balance method. In the HBM, the time-dependent Eulerian description of solid domains generate a time-averaged and harmonic domain occupied by the solid. This can be avoided by the time-domain version where the immersed boundary is not a problem. For a given instant the position of the interface is or known or its variation can be derived using transpiration methods (Fernandez and Le Tallec 2003).

In the case of following the behaviour of unstable self-propelled dynamics, fold or saddle node bifurcations might be problematic. One way of handling this is to introduce numerical continuation techniques as pseudo arc-length methods (Govaerts 2000). This method will be here introduced for the time spectral method for self-propelled foils continuation.

Finally, the last theoretical point discussed in this chapter concerns the evaluation of linear stability of periodic solutions through Floquet analysis (Floquet 1883). In hydrodynamics, Barkley and Henderson (1996) first performed this analysis on a two-dimensional time-periodic wake flow to explain the onset of three-dimensional structures in the wake of a *fixed* circu-

lar cylinder. The Floquet analysis of time-periodic flows generated by flapping bodies has then been considered by Elston, Sheridan, and Blackburn (2004) and Elston, Blackburn, and Sheridan (2006) for two-dimensional oscillating cylinder flows. They successfully explained the emergence of two and three dimensional flow asymmetries observed in experiments and simulations. To investigate the emergence of the self-propelled regimes of flapping foils, Deng and Caulfield (2016), Deng et al. (2016), Deng et al. (2017), and Deng and Caulfield (2018a) first proposed to consider a Floquet analysis for various flapping foil configurations. Based on the observation that flow symmetry breaking occurs prior to the self-propulsion of the foil in temporal simulations, Deng and Caulfield (2016) and Deng and Caulfield (2018a) applied a purely-hydrodynamic analysis, that does not consider a perturbation of the foil speed in the propulsion direction. However, disagreements between the purely-hydrodynamic analysis and self-propelled simulations nonlinear were reported. In the present work, we introduce the so-called fluid-solid Floquet analysis that considers the foil speed as a perturbation variable and takes into account the inherent coupling between the flow perturbation and the rigid motion of the foil at the perturbation level. To our knowledge, is the first time that such a coupled fluid-solid formalism, already employed for steady base solutions (Tchoufag, Fabre, and Magnaudet 2014), is used to investigate the stability of periodic solutions. The strategy to compute Floquet modes is the one proposed by Barkley and Henderson (1996). The stability of an initial perturbation is assessed through numerical integration of the linearized coupled fluid-solid equations over one period. Arnoldi method in a serial implementation with the modified Gram-Schmidt algorithm used for the orthogonalization process is presented to compute the Floquet modes and exponents. The method is validated in a purely-hydrodynamic Floquet analysis and cross-validated with the exponential growth of perturbations in the unsteady nonlinear simulations.

This chapter is organized as follows. The detailed derivation of the unsteady nonlinear equations that govern the coupled fluid-solid system and the numerical method developed to solve them in §1.2. Methods for periodic solutions are then introduced. The time spectral method (TSM) has its mathematical formulation for the fluid- self-propelled foil system as well as the numerical method implemented to solved detailed in §1.3.1. The pseudo arc-length continuation that is usually coupled to it for its numerical continuation is detailed in §1.3.2. The fluid-solid Floquet stability analysis and the Arnoldi method used for the computation of the Floquet exponents and modes are introduced in §1.3.3. A summary of the theoretical and numerical methods that will be used along this part of the thesis is finally presented in §1.4.

1.2 Unsteady nonlinear equations and solver

We first establish the equations governing the self-propelled dynamics of a rigid heaving foil immersed in a two-dimensional quiescent fluid and free to move in the horizontal direction. The configuration studied in this part of the thesis is a rectangular rigid plate with rounded edges that is represented in figure 1.1. A periodic vertical displacement is imposed to the foil

$$y_g = -A\cos(2\pi t),\ v_g = 2\pi A\sin(2\pi t), \tag{1.1}$$

where the variables considered in this section follow the non-dimensional form established in the part I introduction. The foil heaving movement generates a fluid flow that is governed by the Navier-Stokes equations written in the inertial frame of reference (O, e_X, e_Y) of figure 1.1 as

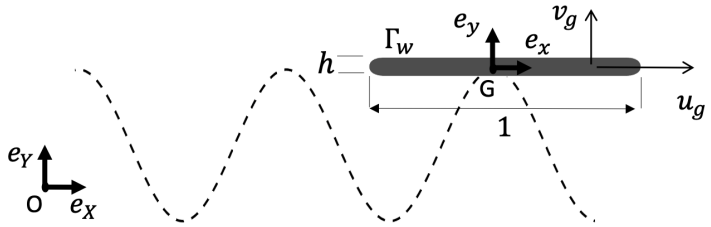

Figure 1.1: Sketch of the foil configuration under sinusoidal vertical motion and horizontal translation with velocity $\mathbf{u}_g$. The foil chord (trailing to leading edge) and its thickness, the frames of reference and the solid/fluid interface Γ_w are indicated.

$$\begin{aligned} \frac{\partial \mathbf{U}}{\partial t} &= -\bar{\boldsymbol{\nabla}}\mathbf{U}\cdot\mathbf{U} - \bar{\boldsymbol{\nabla}}P + \beta^{-1}\bar{\boldsymbol{\Delta}}\mathbf{U} \quad \Omega_f(t), \\ \bar{\boldsymbol{\nabla}}\cdot\mathbf{U} &= 0 \qquad\qquad\qquad\qquad\quad \Omega_f(t), \\ (U,V)(\mathbf{X}_w(t),t) &= (u_g, v_g) \qquad\qquad \Gamma_w(t)\,. \end{aligned} \tag{1.2}$$

where (U, V) represents the absolute fluid velocities, P the pressure and $\bar{(-)}$ spatial operators in the inertial frame of reference. β is the Stokes number (only control parameter of the above equation) and $\Omega_f(t)$ and $\Gamma_w(t)$ are respectively the fluid domain and the foil surface (or the fluid-solid interface). While the vertical velocity v_g is imposed at the foil surface, the horizontal velocity depends on the fluid forces and its time variation is governed by Newton's second law

$$\frac{\mathrm{d}u_g}{\mathrm{d}t} = (\rho S)^{-1} F_x(\mathbf{U}, P)\,. \tag{1.3}$$

The velocity time-variation depends on the non-dimensional mass of the foil ρS ($S = h(1-h) + \pi h^2/$ being its non-dimensional surface) and on the hydrodynamic force acting on the foil surface $\Gamma_w(t)$. This last one depends on the fluid velocity and pressure as

$$F_x(\mathbf{U}, P) = \int_{\Gamma_w(t)} ([-P\mathcal{I} + \beta^{-1}(\bar{\boldsymbol{\nabla}}\mathbf{U} + \bar{\boldsymbol{\nabla}}\mathbf{U}^T)]\cdot\mathbf{n})\cdot\mathbf{e_x}\,\mathrm{d}\Gamma_w\,. \tag{1.4}$$

An evident point in this formulation of the system of equations is that the fluid domain $\Omega_f(t)$ as well as the foil surface $\Gamma_w(t)$ are time dependent. As we can see in Figure 1.2 that illustrates the fluid flow around a flapping foil, the surface occupied by the solid and the fluid vary along the flapping period and so do the position of the foil surface. This fact creates two different burdens: the first one, characteristic of fluid-structure interactions, is the variation of the fluid and solid domain with time. The second one, more specific to self-propelled wings, is the size of the domain if the wing is to be followed. In the next subsection, a non-inertial frame of reference will be adopted to avoid these two problems while maintaining a simple formulation.

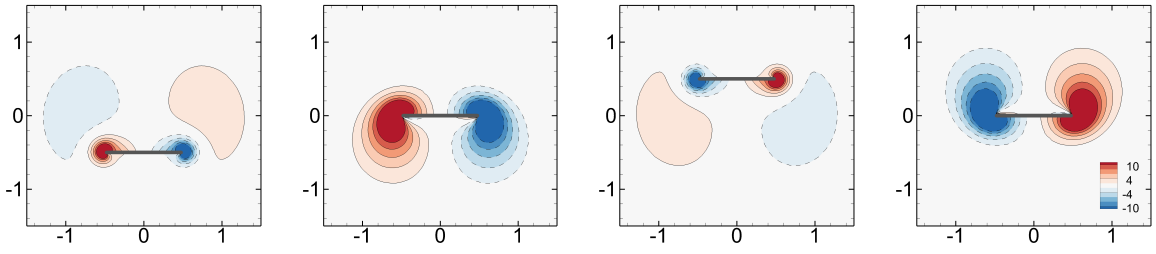

(a) t_0 (b) $t_0 + 1/4$ (c) $t_0 + 1/2$ (d) $t_0 + 3/4$

Figure 1.2: Fluid flow (colors) vorticity field and foil flapping movement (grey) depicted in the laboratory frame of reference (O, X, Y) of Fig. 1.1. (a-d) for four equally-spaced along a flapping period.

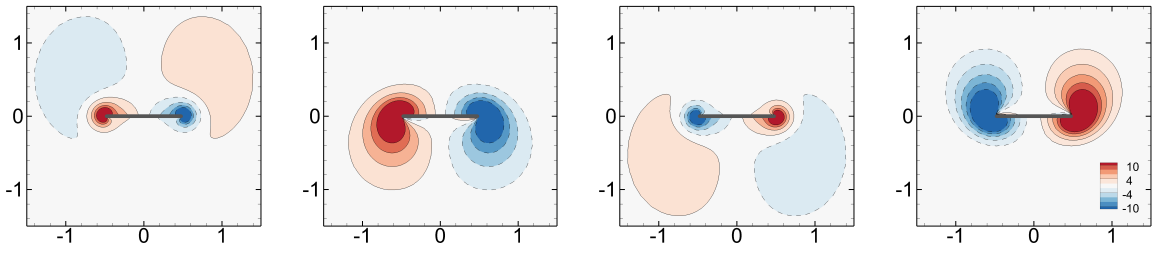

(a) t_0 (b) $t_0 + 1/4$ (c) $t_0 + 1/2$ (d) $t_0 + 3/4$

Figure 1.3: Same as Fig. 1.2 but depicted in the the non-inertial frame of reference (G, x, y) attached to the foil center of gravity.

1.2.1 Governing equations in a non-inertial frame of reference

Since the foil studied in this problem is not elastic, an easy way of circumventing the time-dependency of its frontier is to adopt a non-inertial frame of reference. When the foil is rigid it is always possible to find a frame of reference under which its surface is not a function of time. In this case such a frame of reference is the one that follows the foil vertical flapping motion and its horizontal translation. In Figure 1.3 we adopt the non-inertial frame of reference (G, x, y) of Figure 1.1, which is centered over the foil center of gravity G. The flow depicted in Figure 1.2 is now at a fixed domain and the foil surface is constant in time. We now consider how the adoption of this non-inertial frame of reference affects the governing equations (1.2)-(1.3). We consider the position of an arbitrary point P that belongs either on the surface of the rigid wing (and thus follow its movement) or a point that belongs to the fluid domain and remains at a constant distance of the foil center of gravity G. The position of such a point can be written as

$$X_p(t) = X_g(t) + x_p\,,\; Y_p(t) = Y_g(t) + y_p\,, \tag{1.5}$$

where $\mathbf{X}_p(t) = (X_p(t), Y_p(t))$ and $\mathbf{X}_g(t)$ are the position of the point P and of G at the inertial frame of reference, and $\mathbf{x}_p$ is the position of the point P at the non-inertial frame. Since the point P remains at a constant distance from the foil center of gravity, it is easy to understand that $\mathbf{x}_p$ is time-independent. More particularly, the position $\mathbf{x}$ of any point of a domain that follows the foil in its horizontal and vertical translation can be written as a function of their position in the laboratory frame of reference $\mathbf{X}(t)$ and the foil center of gravity $\mathbf{X}_G(t)$ position as

$$\mathbf{x} = \mathbf{X}(t) - \mathbf{X}_g(t)\,. \tag{1.6}$$

Note that, again, this position x is no longer dependent of time t. This means that the fluid domain Ω and the fluid-solid interface Γ_w are now fixed in time and space, the great advantage of adopting this non-inertial frame of reference. We define thus new *absolute* variables that depend on the spatial coordinates $\mathbf{x} = (x, y)$

$$U(\mathbf{X}, t) = u(\mathbf{x}, t)\,, \tag{1.7}$$

where $u(\mathbf{x}, t)$ is the horizontal fluid velocity in the non-inertial frame of reference. This relationship highlights that the newly adopted variables are not relative but absolute and have the same value in both domains.

To rewrite the system of equations (Eqs. (1.2) - (1.3)) using the non-inertial frame of reference $\mathbf{x}$ and the newly introduced variables, we evaluate how adopting these modifies the time and spatial derivatives. By deriving in time Eq. (1.7) we obtain

$$\frac{\partial \mathbf{U}}{\partial t}(\mathbf{X}, t) = \frac{\partial \mathbf{u}}{\partial t}(\mathbf{x}, t) - \bar{\boldsymbol{\nabla}}\mathbf{u} \cdot \frac{\mathrm{d}\mathbf{x}_g}{\mathrm{d}t} = \frac{\partial \mathbf{u}}{\partial t}(\mathbf{x}, t) - \bar{\boldsymbol{\nabla}}\mathbf{u} \cdot \mathbf{u}_g\,, \tag{1.8}$$

where $\bar{\boldsymbol{\nabla}}$ is the gradient according to the inertial frame of reference $\mathbf{X}$. We can see that the time derivative of the inertial frame of reference when compared to the one in the non-inertial frame of reference has a correction associated to the convection by the solid movement. Since we work with a purely translating frame of reference and not a rotating one, as is the case for example of Jallas, Marquet, and Fabre (2017) or Tchoufag, Fabre, and Magnaudet (2014), the

spatial variation according to non-inertial or inertial frames of reference is equal and spatial operators remain unchanged

$$\bar{\boldsymbol{\nabla}}\mathbf{u} = \boldsymbol{\nabla}\mathbf{u}\,. \tag{1.9}$$

Introducing these modifications we rewrite the system of equations as a function of variables and differential operators in the non-inertial frame of reference

$$\begin{aligned} \frac{\partial \mathbf{u}}{\partial t} &= -\boldsymbol{\nabla}\mathbf{u}\cdot\left(\mathbf{u}-\mathbf{u}_g\right) - \boldsymbol{\nabla}p + \beta^{-1}\boldsymbol{\Delta}\mathbf{u} && \Omega_f\,, \\ \boldsymbol{\nabla}\cdot\mathbf{u} &= 0 && \Omega_f\,, \\ (u,v)(\mathbf{x}_w(t),t) &= (u_g, v_g) && \Gamma_w\,. \end{aligned} \tag{1.10}$$

The adoption of the frame of reference translating with the foil introduces a modification on the convective flow velocity, that becomes the relative $\mathbf{u}-\mathbf{u}_g$ instead of the absolute velocity $\mathbf{u}$ compared to the NS equations written in an inertial frame of reference. Spatial operators, however, are not modified. As velocities are absolute, the boundary condition over the foil surface Γ_w remains identical compared to the previous system. The same goes for solid equation

$$\frac{\mathrm{d}u_g}{\mathrm{d}t} = (\rho S)^{-1}F_x(\mathbf{u},p), \tag{1.11}$$

where we stress that the horizontal force is not modified since the newly adopted variables are absolute in value and spatial operators are identical between the two frames. The horizontal force when evaluated in inertial and non-inertial frame of references is the same. The greatest advantage of the equations written in this non-inertial frame is that the fluid domain Ω_f and the fluid-solid interface Γ_w are no longer time dependent as in the inertial frame. For the sake of simplicity, as well as adopting a compact notation, in the following the equations governing the coupled system, eqs. (1.10) and (1.11), are expressed using the system state variable $\mathbf{q} = (\mathbf{u}, p, u_g)^T$.

$$\mathcal{B}\frac{\partial \mathbf{q}}{\partial t} = \mathcal{R}(\mathbf{q}, v_g), \tag{1.12}$$

where the operators $\mathcal{B}$ and $\mathcal{R}$ are defined as

$$\mathcal{B} = \begin{bmatrix} \mathcal{I} & 0 & 0 \\ 0 & 0 & 0 \\ 0 & 0 & 1 \end{bmatrix},\ \mathcal{R}(\mathbf{q}, v_g) = \begin{bmatrix} -\nabla\mathbf{u}\cdot[\mathbf{u}-\mathbf{u}_g] - \nabla p + \beta^{-1}\Delta\mathbf{u} \\ -\nabla\cdot\mathbf{u} \\ (\rho S)^{-1}F_x(\mathbf{u},p) \end{bmatrix}. \tag{1.13}$$

1.2.2 Numerical method

The system of equations (1.10) and (1.11) is discretized in time using the following r-order semi-explicit scheme

$$\begin{aligned}
\frac{\alpha_0}{\Delta t}\mathbf{u}^{n+1} + \nabla p^{n+1} - \beta^{-1}\Delta\mathbf{u}^{n+1} &= \mathbf{f}^{n+1}, \\
\nabla\cdot\mathbf{u}^{n+1} &= 0, \\
(u^{n+1}, v^{n+1})(\Gamma_w) &= \left(u_g^{n+1}, 2\pi\, A\, sin(2\pi t^{n+1})\right), \\
(\rho S)\frac{\alpha_0}{\Delta t}u_g^{n+1} &= F_x(\mathbf{u}^{n+1}, p^{n+1}) - (\rho S)\sum_{k=1}^{r}\frac{\alpha_k}{\Delta t}u_g^{n+1-k}, \\
(u^{n+1}, v^{n+1})(\Gamma_e) &= (0,0).
\end{aligned} \tag{1.14}$$

The last boundary condition at Γ_e is applied at the external frontier of the computational domain to guarantee a quiescent fluid sufficiently far from the foil. The right-hand side forcing term $\mathbf{f}^{n+1}$ in the momentum equation is defined as

$$\mathbf{f}^{n+1} = -\sum_{k=1}^{r}\gamma_k(\mathbf{u}^{n+1-k} - \mathbf{u_g}^{n+1-k})\cdot\nabla\mathbf{u}^{n+1-k} - \sum_{k=1}^{r}\frac{\alpha_k}{\Delta t}\mathbf{u}^{n+1-k},$$

with Δt the time step and $(\mathbf{u}^{n+1}, p^{n+1})$ the velocity and pressure at time $t_{n+1} = (n+1)\Delta t$. The time derivatives are approximated by r-order backward differential formulae. The linear diffusion and pressure gradient terms are implicit, with the saddle-node problem for the pressure being solved through an Uzawa algorithm (Cahouet and Chabard 1988). The nonlinear convection terms are extrapolated with r-order formulae. A first-order scheme ($r = 1$, $\alpha_0 = 1$, $\alpha_1 = -1$ and $\gamma_1 = 1$) is used for the first two temporal iterations ($n \leq 1$), before switching in the subsequent iterations ($n > 1$) to a second-order scheme ($r = 2$, $\alpha_0 = 3/2$, $\alpha_1 = -2$, $\alpha_2 = 1/2$, $\gamma_1 = 2$ and $\gamma_2 = -1$). To avoid severe time-step restrictions for small values of density ratio induced by an explicit coupling (Causin, Gerbeau, and Nobile 2005), the equality of fluid and solid velocity is treated implicitly. To impose the velocity equality on the fluid-solid interface implicitly (and retain a strong fluid-solid coupling) while maintaining an existing fast implementation to solve the flow equations (Jallas, Marquet, and Fabre 2017) uncoupled from the solid ones, we use the segregated approach proposed by Jenny and Dušek (2004). This approach allow to identify two distinct problems with explicitly known boundary conditions on the solid surface. Manipulating the r-backward differential formula of the time derivative, we may split the unknown solid velocity u_g^{n+1} as,

$$u_g^{n+1} = (\Delta t/\alpha_0)\, a_g^{n+1} + \hat{u}_g\,, \tag{1.15}$$

where the first term is an unknown component, proportional to the unknown acceleration $a_g^{n+1} = \left(du_g/dt\right)^{n+1}$, and the second term is the known velocity component defined as

$$\hat{u}_g = -\sum_{k=1}^{r}(\alpha_k/\alpha_0)\, u_g^{n+1-k}\,.$$

The above decomposition of the horizontal solid velocity is then used to split the fluid variables as,

$$(\mathbf{u}^{n+1}, p^{n+1}) = \left(\frac{\Delta t}{\alpha_0}a_g^{n+1}\right)(\delta\mathbf{u}, \delta p) + (\hat{\mathbf{u}}^{n+1}, \hat{p}^{n+1}), \tag{1.16}$$

where we have introduced the flow component $(\delta\mathbf{u}, \delta p)$, proportional to the solid acceleration, and the flow component $(\hat{\mathbf{u}}^{n+1}, \hat{p}^{n+1})$ that will depend on the solid velocity $\hat{u}_g$. Using the linearity of the time-discrete coupled system of equations, this decomposition results in two uncoupled Stokes systems with known boundary conditions. Introducing the solid (1.15) and fluid (1.16) decomposition into the governing flow equations (1.14) , we obtain two independent linear system of equations. The first one governs the flow component $(\hat{\mathbf{u}}^{n+1}, \hat{p}^{n+1})$ as

$$\begin{aligned} \frac{\alpha_0}{\Delta t}\hat{\mathbf{u}}^{n+1} + \nabla\hat{p}^{n+1} - \beta^{-1}\Delta\hat{\mathbf{u}}^{n+1} &= \mathbf{f}^{n+1} \\ \nabla\cdot\hat{\mathbf{u}}^{n+1} &= 0 \\ (\hat{u}^{n+1}, \hat{v}^{n+1})(\Gamma_w) &= \left(\hat{u}_g, 2\pi A sin(2\pi t^{n+1})\right) \end{aligned} \tag{1.17}$$

The boundary conditions at the fluid-solid interface Γ_w are now explicitly known. As this problem depends on the flow history through the right-hand side forcing terms $\mathbf{f}^{n+1}$ and the boundary conditions, it is solved at each temporal iteration.

The second problem governs the flow component $(\delta\mathbf{u}, \delta p)$ that is proportional to the solid acceleration in the horizontal direction. It writes

$$\begin{aligned} \frac{\alpha_0}{\Delta t}\delta\mathbf{u} + \nabla\delta p^{n+1} - \beta^{-1}\Delta\boldsymbol{\delta u}^{n+1} &= 0 \\ \nabla\cdot\delta\mathbf{u} &= 0 \\ (\delta u, \delta v)(\Gamma_w) &= (1, 0) \end{aligned} \tag{1.18}$$

Again, the boundary conditions at the fluid-solid interface Γ_w are explicitly known. However, we remark now these conditions are independent from the flow history. The solution can thus be obtained prior to the temporal iteration. It can be viewed as the short time response of a Stokes flow, initially at rest, to a unitary horizontal velocity.
The solution of the (above) two independent flow problems does not give access to $(\mathbf{u}^{n+1}, p^{n+1})$ in (1.16) since the horizontal acceleration a_g^{n+1} is still unknown. The final step of the algorithm is obtained by introducing this decomposition into the last equation of the governing equation (1.14), yielding

$$(\rho S)\, a_g^{n+1} = \left(\frac{\Delta t}{\alpha_0} a_g^{n+1}\right) F_x(\delta\mathbf{u}, \delta p) + F_x(\hat{\mathbf{u}}, \hat{p}), \tag{1.19}$$

The horizontal acceleration is thus given by

$$a_g^{n+1} = \left(\rho S - \frac{\Delta t}{\alpha_0} F_x(\delta\mathbf{u}, \delta p)\right)^{-1} F_x(\hat{\mathbf{u}}, \hat{p}), \tag{1.20}$$

and the velocity and pressure can be obtained using (1.16).

The linear system of equations (1.17), and similarly (1.18), is then discretized in space using a classical finite-element method. Test functions $\psi_{u,p}$ are introduced from the same functional space W of the fluid velocity and pressure

$$W = \{\mathbf{u} \in (H^1)^2(\Omega_f), p \in L^2(\Omega_f), \mathbf{u} = 0 \in \Gamma_e, \mathbf{u} = \mathbf{u}_g \in \Gamma_w\}, \tag{1.21}$$

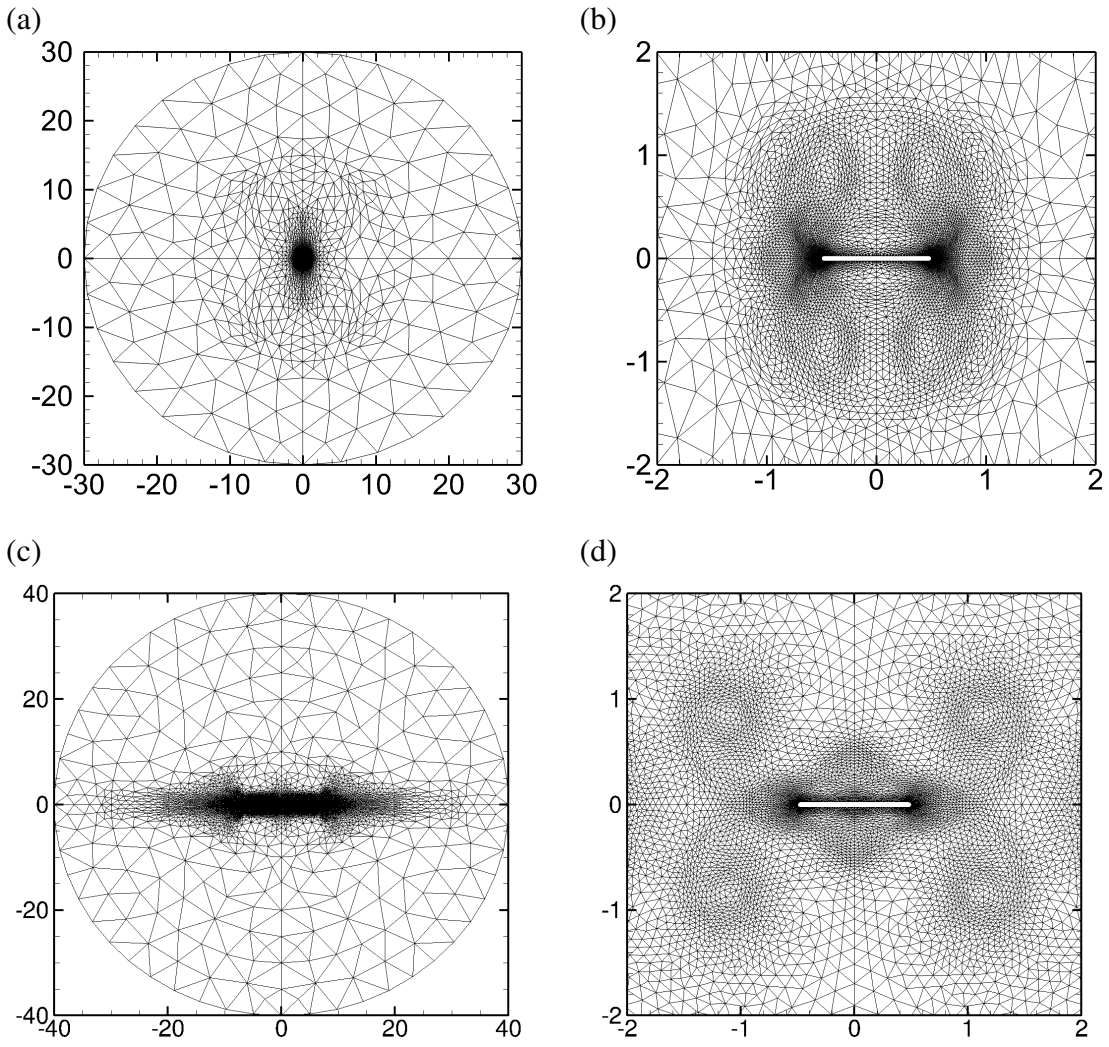

Figure 1.4: (a,c) Far and (b,d) close-up view of the computation domain and a typical adapted mesh used for the numerical simulations of a self-propelled rectangular foil of $A = 0.5$ and (a,b) $\beta \leq 20$ and (c,d) $\beta > 20$.

with Dirichlet boundary conditions being applied on the velocity in the external and solid frontier of the fluid domain. The continuous Galerkin weak formulation is then obtained multiplying the system of equations with appropriate test functions and integrating over the fluid domain.

$$\begin{aligned}\iint_{\Omega_f}\left[\frac{\alpha_0}{\Delta t}\hat{\mathbf{u}}^{n+1}\cdot\psi_u+(\hat{p}^{n+1}\mathcal{I}-\beta^{-1}(\nabla\hat{\mathbf{u}}^{n+1}+\nabla^T\hat{\mathbf{u}}^{n+1})):\nabla\psi_u\right]\mathrm{d}\Omega &= \iint_{\Omega_f}\left[\mathbf{f}^{n+1}\cdot\psi_u\right]\mathrm{d}\Omega,\\ \iint_{\Omega_f}\left[\nabla\cdot\hat{\mathbf{u}}^{n+1}\cdot\psi_p\right] &= 0,\\ (\hat{u}^{n+1},\hat{v}^{n+1})(\Gamma_w) &= \left(\hat{u}_g, 2\pi A sin(2\pi t^{n+1})\right).\end{aligned} \tag{1.22}$$

The weak formulation is discretized in an unstructured mesh that is generated using the software FreeFEM. The computational domain, figure 1.4, employed in our simulations is a circle of (non-dimensional) diameter 60 up to 80 centered at the foil center of mass. This external boundary of the circular domain is Γ_e. A Delaunay triangulation of the computational domain results in meshes with typically 1.2×10^4 ($\beta\leq 20$) up to 3.3×10^4 ($\beta>20$) triangles. As spatial symmetries are expected, a particular attention was kept to generate symmetric meshes and not artificially insert asymmetries in the system. To create a mesh that is symmetric with respect to the x and y-axis and refined in flow regions exhibiting large velocity gradients, figure 1.4(b,d), we have proceeded as follows. Once a first solution has been computed, we adapt a mesh of a quarter domain to several instants of the periodic flow, using the hessian-based mesh adaptation implemented in FreeFEM. We refer to Fabre et al. (2018) for a practical review. After duplicating and appropriately rotating this quarter-mesh, the full mesh can finally be assembled. The triangle size is typically of order $O(10^{-2})$ close to the foil, and 1 in the external part of the domain. Mesh refinement and domain size were chosen based on the convergence of the foil horizontal velocity and the vertical hydrodynamic force up to $O(10^{-4})$. The flow velocity and pressure are respectively discretized with quadratic Lagrange (P2) and linear (P1) Lagrange elements. The discrete unsteady Stokes problem assumes thus the form

$$\underbrace{\begin{bmatrix}\mathbf{A}_u & 0 & \mathbf{B}_x\\ 0 & \mathbf{A}_u & \mathbf{B}_y\\ \mathbf{B}_x^T & \mathbf{B}_y^T & 0\end{bmatrix}}_{\mathbf{A}}\cdot\begin{bmatrix}u^{n+1}\\ v^{n+1}\\ p^{n+1}\end{bmatrix}=\begin{bmatrix}\mathbf{r}_u\\ \mathbf{r}_v\\ 0\end{bmatrix}, \tag{1.23}$$

where the matrices are the spatially discrete equivalent of the weak formulation (1.22). The boundary conditions $\hat{u}_g$ and $\hat{v}_g$ of the fluid velocity are imposed through penalization. For elements belonging to Γ_e and Γ_w a user defined factor (of default value equal to 10^{30}) is included in the diagonal elements of $\mathbf{A}_u$ and the respective lines of $\mathbf{r}_u$ and $\mathbf{r}_v$.

The final algorithm consists then in one initial step (0) and three steps (1-3) during the time-marching loop that are detailed in the Algorithm 1. It is practically implemented using the FreeFEM software (Hecht 2012). For the resolution of the delta and hat fluid system of equations, the unsteady system matrix A is not explicitly constructed. Following Jallas, Marquet, and Fabre (2017), we have used an iterative preconditioned conjugate gradient algorithm (Cahouet and Chabard 1988) to solve the system while imposing the divergence-free condition. In this

Algorithm 1: IMEX time marching scheme with segregated approach for foil velocity boundary condition

(0) Obtain δF_x and $[\delta \mathbf{u}^{n+1}, \delta p^{n+1}]^T$ once and for all;
Time marching loop: for $i = 0; i <= imax; i++$ **do**
  (1) Use $[\mathbf{u}^n, p^n, u_g^n]^T$ to obtain $[\hat{\mathbf{u}}, \hat{p}, \hat{u}_g]^T$;
  (2) Obtain $\left(\frac{du_g}{dt}\right)^{n+1}$;
  (3) Use $\left(\frac{du_g}{dt}\right)^{n+1}$ to correct the system $[\hat{\mathbf{u}}, \hat{p}, \hat{u}_g]^T$ to $[\mathbf{u}^{n+1}, p^{n+1}, u_g^{n+1}]^T$.
end

way, only the matrix $\mathbf{A}_u$ needs to be factorized, what is done using the FreeFEM interface with MUMPS. This factorization is performed only at the beginning of the time-loop, with all matrices not being further reconstructed (except if the mesh is eventually adapted). The conjugate gradient method is then used at every time iteration to solve the system (1.23). This algorithm typically converges to an absolute residual of 10^{-10} in 1 or 2 iterations.

1.2.3 Validation of the unsteady nonlinear solver

The unsteady nonlinear solver was validated against three different moving rigid solid body problems (of increasing difficulty) found in the literature. The first problem, used for validation by Wang (2000), Spagnolie et al. (2010), and Bergmann and Iollo (2011), is the transitory regime of an impulsively started cylinder towed with a constant velocity. This problem is followed by a non-propelled oscillating cylinder, validation case of Jallas, Marquet, and Fabre (2017). Finally the self-propelled motion of elliptical foils studied by Alben and Shelley (2005) and Spagnolie et al. (2010) is analysed. When analysing self-propelled flapping foils, the mesh and time-step dependency of the rectangular foils studied in this part of the thesis are also addressed.

1.2.3.1 Impulsevily started cylinder

To test the vortex wake dynamics we have followed Wang (2000) and computed the streamwise velocity in the nearby wake of an impulsively started cylinder. The cylinder is impulsively started with a constant velocity $u_g = -1$, the Reynolds number based on this velocity and the cylinder diameter being $Re = 550$ (Re replacing β in the numerical solver). In the previous solver, the solid dynamics are decoupled from the fluid one and the solid velocities are permanently set to $(u_g, v_g) = (-1, 0)$.

A comparison between our numerical and the experimental results of Bouard and Coutanceau (1980), figure 1.5(a), reveals a very good agreement. Our simulations were performed with a mesh composed of 2×10^4 triangles, a time-step of $\Delta t = 10^{-4}$ and a circular domain of diameter 60. In all considered time instants, numerical and experimental values perfectly match the relative velocity between the fluid and the cylinder in its wake. Despite possible differences related to initial conditions and the exact and approximate two-dimensionality between numerical and experiments results, the wake velocity is well resolved by the numerical method. The numerical method allow, for instance, a good measure of the recirculation bubble behind the cylinder, its size being predicted by the horizontal position where velocities turn from negative to positive

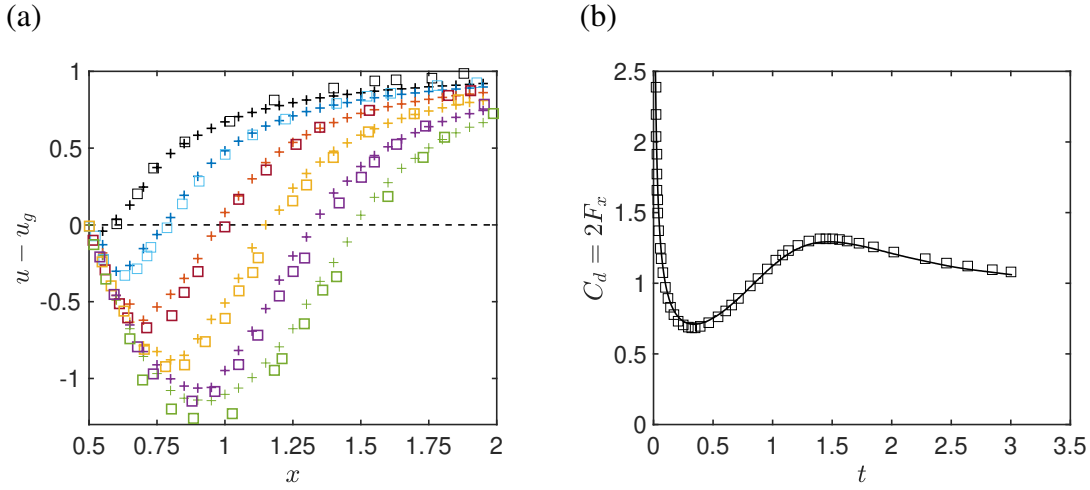

Figure 1.5: Nonlinear solver validation: impulsevily started cylinder with $u_g = -1$ and $Re = 550$. (a) Streamwise velocity u obtained with the present method (crosses) compared to experimental results of Bouard and Coutanceau (1980) (squares - figure 18 of the article) in the wake behind the cylinder for $x \in [0.5, 2]$ at the symmetry plan ($y = 0$). The different coloured markers correspond from top to bottom to time instants starting at $t = 0.5$ in steps of 0.5 up to 3. (b) Drag coefficient for $t \in [0, 3]$ obtained with the present method (line) compared to the one extracted from Bergmann and Iollo (2011) (squares - figure 8(a) of the article).

(1.5-a).

Another important validation concerns the hydrodynamic forces acting on the solid, as self-propelled regimes determined by these forces will be studied in this thesis. A comparison between the drag coefficient obtained with the unsteady nonlinear solver and that computed by Bergmann and Iollo (2011) with a different numerical method is made in figure 1.5(b). The authors perform numerical simulations with penalized Navier-Stokes equations (Angot, Bruneau, and Fabrie 1999). The time-evolution of the drag coefficient $C_d = 2F_x$ predicted by our numerical method presents a perfect agreement with their results.

1.2.3.2 Heaving non-propelled cylinder

Adding up on difficulty, a case where the imposed solid velocity is periodic and not steady is considered. In this case, the cylinder is animated with a sinusoidal horizontal motion of $x_g = -A\sin(2\pi t)$, the amplitude of motion being $A = 5/2\pi$ and the Stokes number $\beta = 20$. As the cylinder is non-propelled, the vertical velocity is permanently set to zero $v_g = 0$. The solid dynamics, as the previous validation case, are completely imposed and remain uncoupled from the fluid dynamics.

The selected flow regime correspond to a two-dimensional flow that does not break any symmetry (Dütsch et al. 1998). To compare the fluid dynamics with the experimentally measured one, we compare the stream-wise velocity at different vertical ($y \in [-1, 1]$) and a fixed horizontal position ($x = -0.6$), figure 1.6. Our simulations were performed with a mesh composed of 2×10^4 triangles, a time-step of $\Delta t = 5 \times 10^{-4}$ and a circular domain of diameter 60. The velocity vertical profile predicted by our simulations presents a very good agreement with the

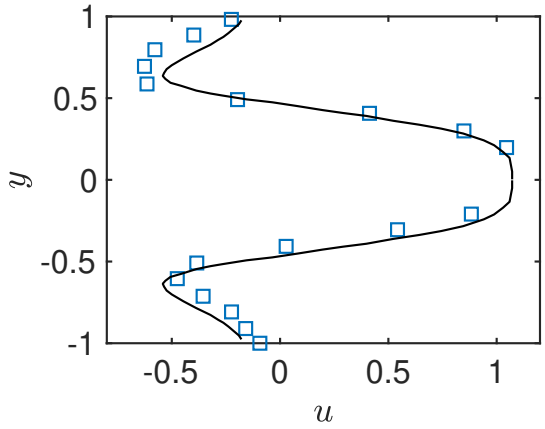

Figure 1.6: Nonlinear solver validation: Comparison of the values of the streamwise velocity in different vertical positions for $x = -0.6$ and $t = 0.5$ of the established regime of a non-propelled horizontally oscillating cylinder. Control parameters are $\beta = 20$ and $A = 5/2\pi$ with the horizontal position of the cylinder being given by the temporal law. $x_g = -A\sin(2\pi t)$. Experimental results of Dütsch et al. (1998) (squares - figure 8(a) of the article) and the present numerical method (solid line).

experimental measures at a given time instant $t = 0.5$ of the permanent regime. Although not displayed the present solver agrees very well with other numerical results (Jallas, Marquet, and Fabre 2017).

1.2.3.3 Self-propelled foils

Finally, we consider a case of coupled fluid-solid dynamics. The horizontal self-propelled locomotion of a vertically heaving two-dimensional elliptical foil of aspect ratio $h = 0.1$ was compared to the numerical results of Alben and Shelley (2005) and Spagnolie et al. (2010). Their numerical method, described by Spagnolie et al. (2010), consists in solving the coupled self-propelled foil and flow Navier-Stokes equations written in a vorticity/ stream function formulation in a non-inertial frame of reference attached to the body movement. Spatial discretization is achieved through a mixed Fourier/Finite differences method. A second-order, implicit Crank– Nicholson scheme is used for time stepping on the linear terms, and second-order Adams–Bashforth for the advection term.

We have simulated the self-propelled dynamics of the heaving ellipses for a fixed chord-based flapping amplitude $A = 0.25$, solid-fluid density ratio $\rho = 10$ and Stokes number $\beta \in [2, 15]$. We simulate this system using a circular computational domain of diameter equal to 60 times the ellipse major axis, composed of 10^4 triangles that vary in size from $O(10^{-2})$ close to the ellipse to unity order in the external boundary. For consistency, a time-step $\Delta t = 5 \times 10^{-3}$ was used for all simulated Stokes numbers.

The evolution with β of the time-averaged along a flapping period horizontal velocity of the reference (Spagnolie et al. 2010) (empty squares) is compared to our numerical results (filled circles) in figure 1.7. We first obtain a very good agreement for the onset of locomotion, symmetric non-propulsive solutions found up to $\beta \geq 8$ and propulsive solutions being retrieved after this critical threshold. After this value, a similar evolution with β for the time-averaged

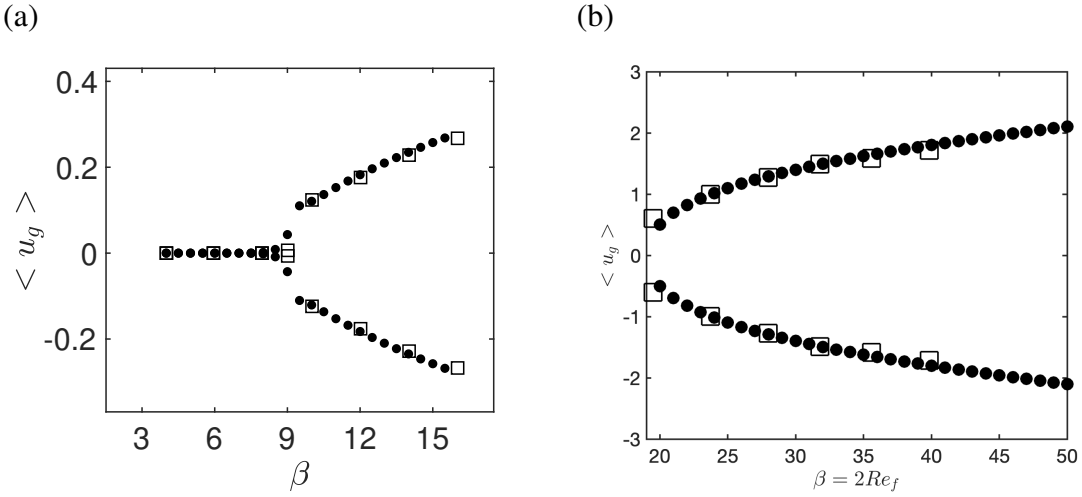

Figure 1.7: Nonlinear solver validation: time-averaged horizontal velocity of an ellipse of aspect ratio $h = 0.1$ for density ratio and flapping amplitudes of (a) $A = 0.25$ and $\rho = 10$, (b) $A = 0.5$ and $\rho = 32$. Values obtained for the implemented numerical code (Filled dots) compared to (Empty squares) the ones obtained by (a) (Spagnolie et al. 2010) – the data extracted is the *clamped* case in Fig. 13 (a) of the article – and (b) the values of (Alben and Shelley 2005) in the inset of figure 2 of the article.

Time step	max(F_y)	$< u_g >$	Mesh nb. of triangles	max(F_y)	$< u_g >$
$\Delta t = 0.01$	38.692	0.223	7836	38.641	0.226
$\Delta t = 0.005$	38.687	0.227	17116	38.687	0.227
$\Delta t = 0.001$	38.687	0.227	22580	38.687	0.227

Table 1.1: Influence of the time step and of the mesh number of triangles for the an unidirectional propulsive solution of Stokes numbers $\beta = 6$ evaluated through the convergence of the maximal vertical force max(F_y) and the time-averaged horizontal velocity $< u_g >$. In the case of time-step convergence a fixed mesh of 17116 triangles was used, whereas in the mesh convergence a fixed time step $\Delta t = 0.005$ was used.

horizontal velocity is observed for our results and those of the reference. We can see that in both cases for $\beta \geq 10$ the evolution of the time-averaged horizontal velocity with the Stokes number reaches a linear growth, what is in good agreement between our numerical method and the reference.

A similar validation was performed for higher Stokes numbers, a different density ratio $\rho = 32$ and flapping amplitude $A = 0.5$, a case dealt with by Alben and Shelley (2005). Again a very good agreement was obtained between our numerical and results and the ones presented in the reference.

Next, the influence of the spatial and time discretization over the time-averaged horizontal velocity and the maximal vertical force acting on the foil is studied through the mesh number of elements and time step size. In table 1.1 we analyse this influence for an unidirectional propulsive solution ($\beta = 6$) and we remark that a time step of $\Delta t = 0.005$ and a mesh of 17116 triangles are sufficient to guarantee the convergence of the the hydrodynamic force and

horizontal velocity up to order $O(10^{-3})$, a value that was also attained with for all other values of Stokes number presented in this article. Typically, the time step is set to $\Delta t = 10^{-2}$ for small value of the Stokes number ($\beta = 2$) and is decreased to $\Delta t = 5 \cdot 10^{-4}$ for larger values ($\beta = 19$). For $\beta \geq 20$ the mesh number of elements and the domain size are increased to attain this convergence. This discretization and domain increase is connected to the greater wakes displayed by propulsive solutions at higher Stokes numbers.

1.3 Methods for time-periodic solutions

In the problems studied throughout this work the coupled fluid-solid system is excited by a periodic heaving movement. The generated fluid flow and horizontal self-propelled velocity may sometimes retain this periodicity. As presented in the introduction of this chapter, existing theoretical methods take into account the periodicity of the problem, becoming a faster route towards equilibria of the system as those presented in the validation of the unsteady nonlinear solver (figure 1.7). The time spectral method, a time domain version of the harmonic balance method, will be introduced in §1.3.1. Alongside, the pseudo arc-length continuation method will be introduced §1.3.2, with its interest for the numerical continuation nearby turning points / saddle-nodes being presented. The validation of these two algorithms,§§1.3.1.3 and 1.3.2.1, is then detailed.

The last part of this section is dedicated to the study of the stability of periodic solutions. In this work, we introduce in §1.3.3 a fluid-solid Floquet stability analysis that considers a perturbation of both the self-propelled foil horizontal velocity and the surrounding flow. The numerical method and its validation will be equally introduced. It is interesting to note the possible overlapping application of the TSM and fluid-solid Floquet stability analyses. Although the system is periodically excited, not all self-propelled solutions obtained retain its imposed periodicity. In these cases, the Time Spectral Method will be particularly interesting to calculate unstable periodic solutions that will further be studied through Floquet stability analysis.

1.3.1 Time spectral methods

1.3.1.1 Mathematical formulation for the self-propelled configuration

The studied self-propelled dynamics of a flapping wing present the inherent periodicity of the imposed periodic heaving movement. Under the assumption that this periodicity is retained by the self-propelled nonlinear regimes of the system, an alternative way of obtaining periodic saturated solutions is to solve directly for the cruise regime periodic cycle without passing by transient regimes of temporal simulations. That is for instance the approach of Harmonic Balance Methods, or, their time-domain equivalent, Time Spectral Methods (TSM) which are hereafter introduced. In this section the time-periodicity of the system is explored to rewrite the unsteady nonlinear equation (1.10)-(1.11) in a spectral form. The resolution of the resulting system of equations determine then Fourier coefficients or the amplitude of selected time instants to determine them. This process is illustrated both for HBM and TSM in figure 1.8, where the amplitude of the 3 first harmonics of the time series of the horizontal velocity of a self-propelled foil, (1.8-a). Equivalently in (1.8-b) the time instants necessary to determine them are highlighted. HBM and TSM use then this information to reconstruct the temporal evolution of the periodic solution. In this work we adopt the time-domain version (TSM) of the harmonic

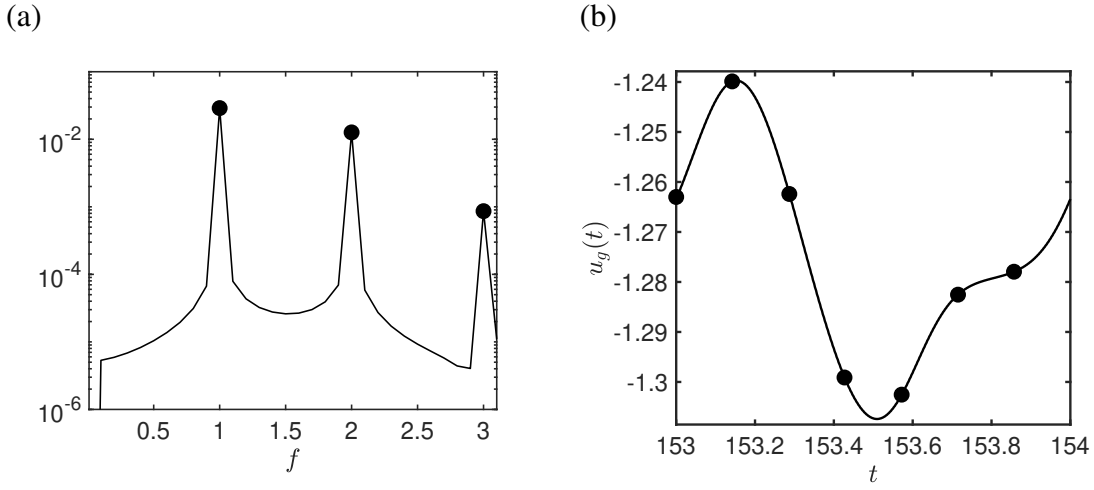

Figure 1.8: Harmonic balance and time spectral method (HBM and TSM) principle. Both methods aim at determining the spectral content of a limit cycle through (a) the amplitude of the harmonics (HBM) or (b) the time instants (TSM) as shown in the figures. (a) Fourier spectrum of the horizontal velocity showing the amplitude of the first 3 fundamental harmonics of non-dimensional frequency $f = 1$, 2 and 3. (b) Time-evolution of the horizontal velocity and the minimum 7 instants necessary to determine 3 harmonics.

balance methods. The derivation of both harmonic balance and time-spectral method is detailed in the following.

To obtain the spectral equations governing our nonlinear problem we expand the system variables in Fourier series

$$\mathbf{u}(\mathbf{x},t) = \sum_{k=-\infty}^{\infty} \hat{\mathbf{u}}_k(\mathbf{x}) e^{i2\pi kt},\ p(\mathbf{x},t) = \sum_{k=-\infty}^{\infty} \hat{p}_k(\mathbf{x}) e^{i2\pi kt},\ u_g(t) = \sum_{k=-\infty}^{\infty} \hat{u}_k e^{i2\pi kt}, \tag{1.24}$$

where as a reminder, the fundamental period and frequency are $f = 1$ and $T = 1$ and the angular frequency is $\omega = 2\pi$ due to our choice of characteristic time scale. Injecting the Fourier series decomposition in the system equation, Eq. (1.12), we obtain equations for determining each one of the Fourier coefficients of our series

$$\begin{aligned}
i2\pi k\hat{\mathbf{u}}_k &= -\textstyle\sum_{n=-\infty}^{\infty}\left[\boldsymbol{\nabla}\hat{\mathbf{u}}_{n-k}\cdot\left(\hat{\mathbf{u}}_{n+k}-\hat{\mathbf{u}}_{g,n+k}\right)\right] - \boldsymbol{\nabla}\hat{p}_k + \beta^{-1}\boldsymbol{\Delta}\hat{\mathbf{u}}_k \quad \Omega_f\,,\\
\boldsymbol{\nabla}\cdot\hat{\mathbf{u}}_k &= 0 \qquad\qquad \Omega_f\,,\\
(\hat{u}_k,\hat{v}_k)(\mathbf{x}_w(t),t) &= (\hat{u}_{g,k},\hat{v}_{g,k}) \qquad\qquad \Gamma_w\,,\\
i2\pi k\hat{u}_{g,k} &= (\rho S)^{-1}F_x(\hat{\mathbf{u}}_k,\hat{p}_k) \qquad\qquad .
\end{aligned} \tag{1.25}$$

$\forall k \in \mathbb{Z}$. Which cast in a compact form using the system state variable becomes

$$i2\pi k\mathcal{B}\hat{\mathbf{q}}_k = \hat{\mathcal{R}}(\hat{\mathbf{q}}_{n+k},\hat{\mathbf{q}}_{n-k}), \tag{1.26}$$

where we can see that the operator $\hat{\mathcal{R}}$, which is the harmonic version of the spatial operator in time-domain $\mathcal{R}$, couples the different harmonics due to the nonlinear term from the Navier-Stokes equations. Since in practice a finite number of harmonics N is computed, this equation can be expressed in a matrix form after truncating the Fourier series for $k \in [-N, N]$

$$\Lambda \cdot \hat{Q} = \hat{\mathbf{R}}(\hat{Q}), \tag{1.27}$$

where Λ is a diagonal matrix $\Lambda_{kk} = i2\pi(k - N)\mathcal{B}$ and the vectors $\hat{Q}$ and $\hat{\mathbf{R}}$ regroup the spectral system variables and spatial operators ordered from $[-N, N]$. To avoid dealing with complex variables, we can bring back this system of equations to the time domain, arriving finally at the equations of the Time Spectral Method. Using $2N + 1$ time instants to compute the $[-N, N]$ harmonics as to respect the Nyquist-Shannon criterion, we define the direct and inverse Fourier transforms

$$\mathcal{F}_{n,k} = \frac{1}{2N+1} \exp\left(\frac{-2\pi ik(n-N)}{2N+1}\right), \; \mathcal{F}^{-1}_{n,k} = \exp\left(\frac{2\pi ik(n-N)}{2N+1}\right). \tag{1.28}$$

The vector Q that regroups $2N + 1$ time instants along a period

$$Q = [\mathbf{q}(\mathbf{x}, t_0), \mathbf{q}(\mathbf{x}, t_0 + 1/(2N+1)), \ldots \mathbf{q}(\mathbf{x}, t_0 + 2N/(2N+1))]^T, \tag{1.29}$$

is related to the vector of harmonics of the system as $\hat{Q} = \mathcal{F} \cdot Q$, a relation that associated to the discrete inverse Fourier transform can be used to bring back eq. (1.27) to the time domain

$$\underbrace{\mathcal{F}^{-1} \cdot \Lambda \cdot \mathcal{F}}_{\mathcal{D}_\omega} \cdot Q = \mathcal{F}^{-1} \cdot \hat{\mathbf{R}}(\hat{Q}). \tag{1.30}$$

Under the hypothesis that a sufficient number of harmonics is used, there is no aliasing error and the application of the inverse Fourier transform over $\hat{\mathbf{R}}$ is a bijective operation, what results in the final TSM system of equations

$$\mathcal{N}_{TSM}(Q) = \mathcal{D}_\omega Q - \mathbf{R}(Q) = 0, \tag{1.31}$$

where $\mathcal{D}_\omega$ is the time-spectral version of the time-derivative with coefficients

$$(\mathcal{D}_\omega)_{n,k} = \begin{cases} \pi(-1)^{(n-k)} \csc\left(\dfrac{\pi(n-k)}{2N+1}\right)\mathcal{B}, & \text{if } (n-k) \neq 0 \\ 0, & \text{if } (n-k) = 0 \end{cases}, \tag{1.32}$$

and the vector $\mathbf{R}$ regroups the related spatial operator of each of these time instants.

$$\mathbf{R} = [\mathcal{R}(\mathbf{q}(\mathbf{x}, t_0)), \ldots, \mathcal{R}(\mathbf{q}(\mathbf{x}, t_0 + 2N/2N+1))]^T. \tag{1.33}$$

The Time Spectral Method transforms thus the continuous unsteady system of nonlinear equations, eqs. (1.10)-(1.11), into a stationary system eq. (1.31) that regroups $2N + 1$ time instants along a period. These instants are coupled through the time-spectral derivative $\mathcal{D}_\omega$ while the vector $\mathbf{R}$ depends solely on the considered time instant of each line. This last fact is the great difference between HBM and TSM methods. In the former the harmonics are coupled due to the spatial operator vector $\hat{\mathbf{R}}$ and not the temporal derivation coefficients Λ.

1.3.1.2 Numerical resolution

The weak formulation of the TSM system of equations is obtained by multiplying each time instant with the appropriate test functions. The spatial discretization of equations (1.31) is again based in a continuous Galerkin finite element formulation. In its discrete version of this system, the system variable (of an instant) $\mathbf{q} = (\mathbf{u}, p, u_g, l)$ is composed of the fluid velocity, pressure, solid horizontal velocity (as usual) and of an additional element. Lagrange multipliers l are introduced as additional degrees of freedom of the system, as done for instance by Tchoufag, Fabre, and Magnaudet (2014) and Pfister, Marquet, and Carini (2019), to enforce (implicitly and in an unified resolution) the no-slip boundary condition in the foil interface Γ_w and the outer domain Γ_e. The system weak formulation thus reads $\forall i \in [0, 2N]$

$$
\begin{aligned}
\iint_{\Omega_f} \left[\left(\sum_{j=0}^{2N} (\mathcal{D}_\omega)_{i,j} \mathbf{u}_j + \nabla \mathbf{u}_i \cdot (\mathbf{u}_i - \mathbf{u}_{g,i}) \right) \cdot \psi_u + (p_i \mathcal{I} - \beta^{-1} (\nabla \mathbf{u}_i + \nabla^T \mathbf{u}_i)) : \nabla \psi_u \right] \mathrm{d}\Omega + \int_{\Gamma_w \cup \Gamma_e} l_i \cdot \psi_u \mathrm{d}\Gamma &= 0, \\
\iint_{\Omega_f} \left[\nabla \cdot \mathbf{u}_i \cdot \psi_p \right] &= 0, \\
\int_{\Gamma_e} \left[\mathbf{u}_i \cdot \psi_l \right] \mathrm{d}\Gamma_e + \int_{\Gamma_w} \left[(\mathbf{u}_i - \mathbf{u}_{g,i}) \cdot \psi_l \right] \mathrm{d}\Gamma_w &= 0, \\
\sum_{j=0}^{2N} (\mathcal{D}_\omega)_{i,j} u_{g,j} - \int_{\Gamma_w} l_i \mathbf{e}_x \mathrm{d}\Gamma_w &= 0 .
\end{aligned}
$$

As explained by Pfister, Marquet, and Carini (2019), the inclusion of the Lagrange multiplier arises naturally in the derivation of the system weak formulation as to replace the non-defined fluid stress acting on the domain boundaries

$$
\iint_{\Omega_f} \left[(\nabla p - \beta^{-1} \Delta \mathbf{u}) \cdot \psi_u \right] \mathrm{d}\Omega = \iint_{\Omega_f} \left[(-p\mathcal{I} + \beta^{-1} (\nabla \mathbf{u} + \nabla^T \mathbf{u})) : \nabla \psi_u \right] \mathrm{d}\Omega - \int_{\Gamma_w \cup \Gamma_e} [\underbrace{(-p\mathcal{I} + \beta^{-1} (\nabla \mathbf{u} + \nabla^T \mathbf{u})) \cdot \mathbf{n}}_{l} \cdot \psi_u] \mathrm{d}\Omega , \tag{1.34}
$$

where $\mathbf{n}$ is the outward normal. Quadratic (P2) Lagrange elements are used for the fluid velocity whereas linear ones (P1) are used for the pressure and the Lagrange multiplier. The resultant discrete system of equations assume thus the form

$$
\mathbf{N}_{TSM}(\mathbf{Q}) = 0 . \tag{1.35}
$$

The root of this discrete stationary system can be sought through Newton's method, here illustrated for a single harmonic $N = 1$ (what results in three time instants):

$$
(\mathbf{J}_{stat} + \mathbf{D}_\omega) \cdot \mathbf{Q}' = \underbrace{\begin{bmatrix} \mathbf{J}^1_{stat} & (\mathcal{D}_\omega)_{1,2}\mathbf{B} & (\mathcal{D}_\omega)_{1,3}\mathbf{B} \\ (\mathcal{D}_\omega)_{1,3}\mathbf{B} & \mathbf{J}^2_{stat} & (\mathcal{D}_\omega)_{1,2}\mathbf{B} \\ (\mathcal{D}_\omega)_{1,2}\mathbf{B} & (\mathcal{D}_\omega)_{1,3}\mathbf{B} & \mathbf{J}^3_{stat} \end{bmatrix}}_{\mathbf{J}_{TSM}} \cdot \begin{bmatrix} \mathbf{q}'_1 \\ \mathbf{q}'_2 \\ \mathbf{q}'_3 \end{bmatrix} = -\mathbf{N}_{TSM}(\mathbf{Q}_0), \tag{1.36}
$$

where $\mathbf{B}$ is the discrete mass-matrix (associated to the continuous operator $\mathcal{B}$), $\mathbf{D}_\omega$ is the discrete version of the spectral time-differential operator (an off-diagonal matrix) and $\mathbf{J}^i_{stat}$ is the stationary Jacobian calculated at the time instant i

$$\mathbf{J}^i_{stat}((\mathbf{u}^0_i, u^0_{g,i})) = \begin{bmatrix} \mathbf{A}_f & \mathbf{A}_{sf} & \mathbf{I}_l \\ 0 & 0 & \mathbf{I}_s \\ \mathbf{I}_l^T & \mathbf{I}_s^T & 0 \end{bmatrix}. \tag{1.37}$$

The first line of $\mathbf{J}^i_{stat}$ corresponds to the (stationary/ instant) linearized Navier-Stokes equations, the second line to the linearized Newton's law governing the horizontal velocity, and the third line to the weakly imposed Dirichlet boundary conditions over the foil interface Γ_w and the outer domain Γ_e. The different operators of this matrix are defined as

$$\mathbf{A}_f = \iint_{\Omega_f} \left[(\nabla \mathbf{u}^0_i \cdot \mathbf{u}'_i + \nabla \mathbf{u}'_i \cdot (\mathbf{u}^0_i - \mathbf{u}^0_{g,i})) \cdot \psi_u + (-p'\mathcal{I} + \beta^{-1}(\nabla \mathbf{u}'_i + \nabla^T \mathbf{u}'_i)) : \nabla \psi_u + \nabla \cdot \mathbf{u}'_i \cdot \psi_p \right] \mathrm{d}\Omega,$$

$$\mathbf{A}_{sf} = \iint_{\Omega_f} \left[-\nabla \mathbf{u}^0_i \cdot \mathbf{u}'_{g,i} \cdot \psi_u \right] \mathrm{d}\Omega, \; \mathbf{I}_l = \int_{\Gamma_w \cup \Gamma_e} [l_i \cdot \psi_u] \, \mathrm{d}\Gamma, \mathbf{I}_s = \int_{\Gamma_w} [-l_i \cdot \mathbf{e}_x] \, \mathrm{d}\Gamma .$$

where the index i is referent to the time instant, and superscripts ^{0} and $'$ are the actual state and its perturbation at the Newton step.

Parallel implementation, iterative method and preconditionning strategy: The great drawback from the Time Spectral Method is that its Jacobian $\mathbf{J}_{TSM}$ is a dense matrix $(2N+1)^2$ times larger than the one inversed for unsteady nonlinear simulations. The increase of harmonics used leads to a very large scale system whose direct factorization would be impractical. In an optimistic perspective, this process would be very slow. In a more pessimist (realist) view the memory requirement for this factorization would be impossible. To overcome these harmonic discretization memory issues, a parallel implementation of the TSM algorithm and an iterative resolution of the linear system have been implemented. As each line of the TSM Jacobian is composed of a single isolated time instant (and Fourier coefficients of low memory requirement) the $2N+1$ time instant are separated in an equivalent number of CPUs. To avoid the factorization of the large scale TSM Jacobian then, the linear system solved in each iteration is handled through an iterative method (GMRES in the present work) with a preconditionning strategy that involves the diagonalization of the block-circulant part of the TSM Jacobian. Practically, this means that during the resolution of the linear system each processor handles the inversion of its isolated preconditionner diagonal block. The multiplication by the TSM Jacobian $\mathbf{J}_{TSM}$ involves, nevertheless, off-diagonal terms that require the knowledge of other time instants to compute the time-spectral time derivative. This multiplication, that intervenes in residual and iterative calculations, is then handled by the ensemble of the processors through MPI using a round-robin strategy as proposed by Mundis and Mavriplis (2017). This implementation is again done using the software FreeFEM, its interface with PETSc (Balay et al. 2015) been exploited in the iterative method.

The efficiency of an iterative method is severely increased when a suitable approximation of the inverse Jacobian is used to precondition its resolution. In this work, to approximate the inverse of the TSM Jacobian, we decompose this operator as the sum of a circulant $\mathbf{C}$ and a diagonal $\mathbf{D}$ matrix:

$$\mathbf{J}_{TSM} = \underbrace{\mathbf{D}_{\omega} - \mathbf{J}_{stat}(\langle \mathbf{Q} \rangle)}_{\mathbf{C}} \underbrace{- \mathbf{J}_{stat}(\tilde{\mathbf{Q}})}_{\mathbf{D}}, \tag{1.38}$$

where we have decomposed the system state variable in $\langle \mathbf{Q} \rangle$ its time-averaged over a flapping period and $\tilde{\mathbf{Q}}$ fluctuations along this time-average. The circulant matrix contain the time-averaged part of the spatial operators and the time-spectral time derivative coefficients. The diagonal matrix contain the fluctuation of the spatial operator along the latter time average. The preconditionning strategy consists finally in approximating the inversion of the Jacobian as the inverse of solely the circulant matrix:

$$\mathbf{J}_{TSM}^{-1} \approx \mathbf{C}^{-1} \,. \tag{1.39}$$

This choice was based on the ease of transforming the circulant matrix in a diagonal one, as proposed by Schmid, De Pando, and Peake (2017). As it contains the action of the time-spectral time derivative, the great advantage of this preconditionning strategy is that its performance is sustained with the increase of the number of harmonics N. In figure 1.9(a) the averaged number of GMRES iterations along all Newton iterations needed for the iterative method to converge is represented. This is evaluated for a required Newton and GMRES residual of resp. 10^{-6} and 10^{-4}, values that are kept constant in this work. This residual is usually reached after 7 iterations of the Newton algorithm. We remark in this figure that the performance of the preconditionner appears to be relatively constant (actually getting slightly better) with the increase of the number of harmonics, the number of iterations falling from 301 for $N = 3$ to 288 for $N = 28$. We imagine this performance enhancement is due to a better resolution of the mean solution with the increase of the number of harmonics. However, this preconditionner is not immune to performance deterioration. When the unsteady flow starts to become bad represented by the mean flow, as it is the case for higher Stokes numbers, figure 1.9(b), or flapping amplitudes, the performance of the preconditionner deteriorates. For instance, while the average iterative method solve takes 291 iterations for $\beta = 24$ where the velocity is $< u_g >= 0.22$ and the flow fluctuation is small, this number increases to 983 for $\beta = 36$ and $< u_g >= 1.63$. This increase of the GMRES number of iterations can be associated to the worse approximation of the actual unsteady flow, figure 1.9(c,d), by the mean solution, figure 1.9(e,f), as illustrated for the fluid flow between $\beta = 24$ and $\beta = 34$. Robust preconditionning strategies against physical frequency increase related issues are still an ongoing field of research.

1.3.1.3 Validation

The validation of the time-spectral method was performed by cross-comparison between an unsteady nonlinear simulation and the TSM with increasing number of harmonics. The results of this study are presented in table 1.2 and figure 1.10. As we can see from table 1.2, as the number of harmonics used in the TSM is progressively increased, the L_1 norm of the difference along a flapping period

$$||Q_{DNS} - Q_{TSM}|| = \underbrace{\int_0^1 \int_{\Omega_f} |\mathbf{u}_{DNS} - \mathbf{u}_{TSM}| \mathrm{d}\Omega_f \mathrm{d}t}_{||Q_{DNS} - Q_{TSM}||_f} + \underbrace{\int_0^1 |u_{g,DNS} - u_{g,TSM}| \mathrm{d}t}_{||Q_{DNS} - Q_{TSM}||_s}, \tag{1.40}$$

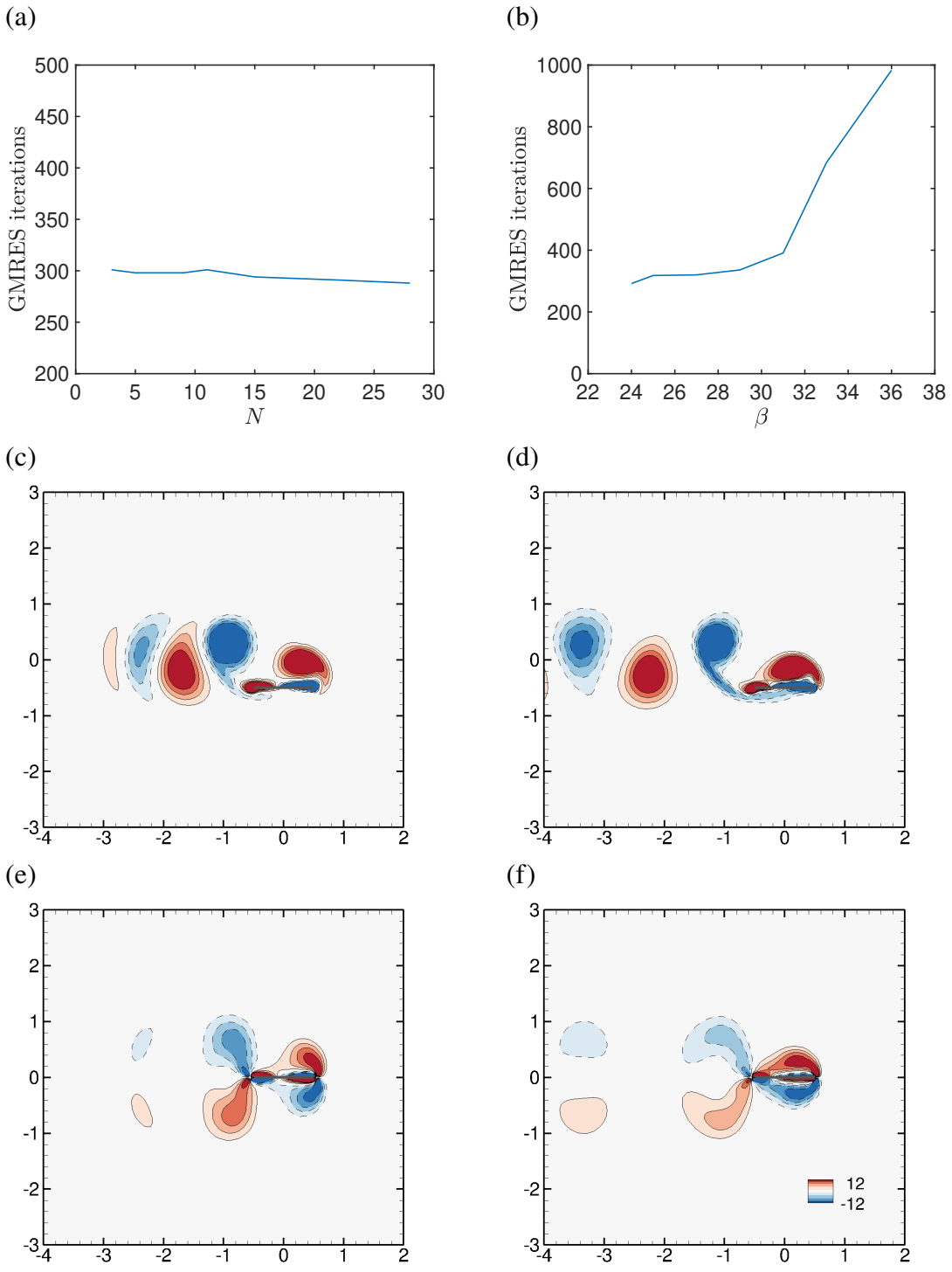

Figure 1.9: Average number of GMRES iterations to solve the linear system (1.36) using the circular preconditionner $\mathbf{C}^{-1}$, with the GMRES residual set to 10^{-4}. Case treated is the self-propulsion of a flapping rectangular foil with $h = 0.05$, $\rho = 100$ and $A = 0.5$. (a) Influence of the number of harmonics N for the case $\beta = 24$. (b) Influence of the Stokes number β for $N = 22$. Snapshot for $t = 0$ and mean-flow for (c,e) $\beta = 24$ and (d,f) $\beta = 34$.

N	$\|\|Q_{DNS} - Q_{TSM}\|\|$	$\|\|Q_{DNS} - Q_{TSM}\|\|_f$	$\|\|Q_{DNS} - Q_{TSM}\|\|_s$
5	2.7×10^{-3}	0.1×10^{-3}	2.6×10^{-3}
9	2.9×10^{-4}	0.14×10^{-4}	2.76×10^{-4}
15	1.6×10^{-6}	0.07×10^{-6}	1.53×10^{-6}
22	5.28×10^{-8}	0.02×10^{-8}	5.26×10^{-8}

Table 1.2: Convergence of the TSM with the increase of the number of harmonics N: Comparison of the difference norm between an unsteady nonlinear and a TSM system state Q and its fluid and solid parts for the control parameters $\beta = 24$, $A = 0.5$, $\rho = 100$ and $h = 0.05$.

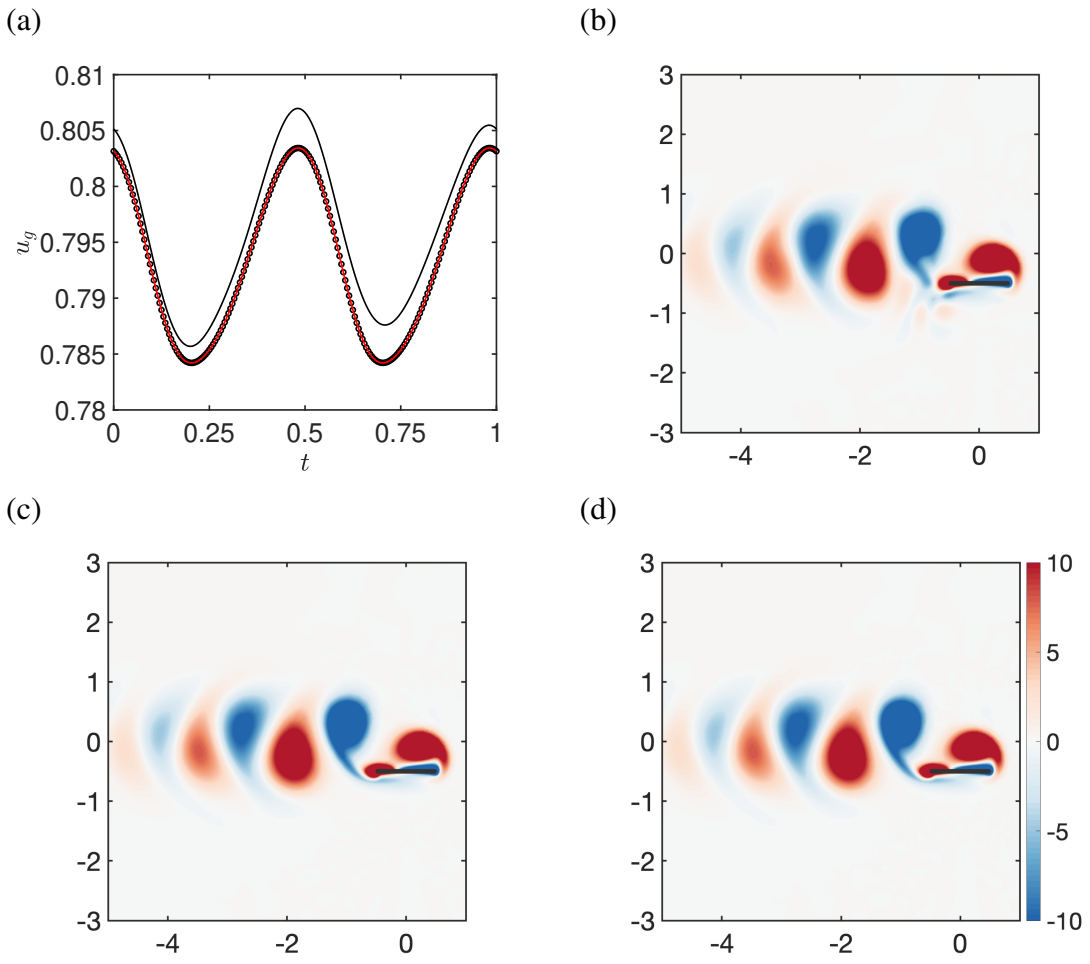

Figure 1.10: Study of the convergence of the TSM solution for $\beta = 24$, $A = 0.5$, $\rho = 100$ and $h = 0.05$: (a) time evolution of the horizontal speed u_g for $N = 5$ (black solid line), $N = 15$ (empty black circles) and the reference solution (red line). (b) Vorticity contours for $t = 0$ for the solution with $N = 5$, (c) $N = 15$ and (d) reference unsteady nonlinear solution. Small wavelength oscillations (aliasing error) are visible in (b) when harmonic convergence was not yet attained.

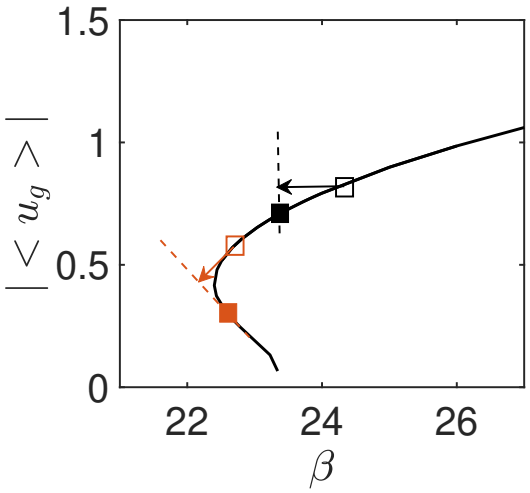

Figure 1.11: Sketch of different branch continuation strategies. Black arrow and squares indicate a typical continuation strategy where, provided an initial solution (empty square) the user projects this solution as an initial guess for the Newton method in a new chosen value of β (continuation indicated by the black arrow) to obtain a new solution (filled black square). Orange arrow and squares indicate the pseudo arc-length continuation. Provided an initial solution and its tangent (orange empty square and arrow) the next solution is sought in the line perpendicular (dashed orange line) to the tangent. The step size of the tangent (size of the orange arrow) is chosen by the user.

of the unsteady simulation and TSM solutions decreases, as expected. This norm is dominated by the solid horizontal velocity difference rather than the fluid velocities. As seen in figure 1.10(a), the horizontal velocity time-signal is far from the reference solution and it is only only above a higher number of harmonics, $N = 15$, that both signals approach an optimal convergence. However, the spatial distribution of the surrounding flow (1.10-b) reveals that, despite its smaller residual, the flow remains visibly disturbed for a small number of harmonics. Clear small wavelength oscillations of the fluid vorticity are visible nearby the foil trailing edge, where vortex contours are equally distorted. These oscillations are a typical signal that the harmonic convergence of the flow is not attained, aliasing errors being still present. Apart from this, the other flow structures are fairly represented by a small number of harmonics. The flow convergence, with a perfect representation of the trailing edge vortex, is only attainable for $||Q_{DNS} - Q_{TSM}|| \approx 10^{-6}$, as is the case for $N = 15$ (1.10-c). We have thus decided to adopt a threshold of 10^{-6} as to guarantee that flow structures and velocity time evolution are fairly represented for stability calculations. In our TSM works 22 harmonics were used to place ourselves well below this convergence level for all the Stokes numbers and flapping amplitudes investigated.

1.3.2 Pseudo arc-length continuation

In most of our TSM studies, the evolution of the coupled fluid-solid dynamics was followed through the variation of a single control parameter, for example the Stokes number β. To study

this evolution, the past described Newton method can normally be marched throughout small variations of β using a previously obtained solution as an initial guess. The procedure described above can be seen as one of the most basic continuation methods, which is illustrated in figure 1.11 by black squares and an arrow that indicates the direction of advancement. Although practical, this method lacks robustness when dealing with limit points of branches. Examples are saddle-nodes as the orange empty square is about to pass through in figure 1.11 and the case that will be studied in chapter 3. As we can see from the figure, if an arbitrary decrease of β is chosen at the initial orange square, the branch would no longer be found, as no solution exists beyond a certain Stokes number. The algorithm would then not converge and the branch information would be lost. Another problem in turning points is the existence of multiple solutions for a same value of Stokes number. A robust method is needed to guarantee that the Newton algorithm will continue the branch and not converge to a previously obtained solution. To overcome this issue, the strategy employed in our work was a pseudo arc-length continuation (Govaerts 2000). This method consists of following a branch of solutions parametrized by a control parameter $[Q, \beta]^T$ that respects a governing equations as the TSM system

$$\mathcal{N}_{TSM}(Q, \beta) = 0\,. \tag{1.41}$$

To continue a branch of solutions, we search the next one in the direction tangent to a curve defined by the already obtained solutions. The pre-existing solutions can be used to obtain a first tangent to the system. A tangent to the leading point that is to be continuated, in the case of figure 1.11 the empty orange square, can then be obtained by exploiting two facts. The new tangent should be perpendicular to the system Jacobian and also preserve the previous tangent orientation. For calculating the new tangent we enforce thus:

$$\begin{bmatrix} \dfrac{\partial \mathcal{N}_{TSM}}{\partial Q} & \dfrac{\partial \mathcal{N}_{TSM}}{\partial \beta} \\ (\mathbf{t}_Q^0)^T & t_\beta^0 \end{bmatrix} \cdot \begin{bmatrix} \mathbf{t}_Q^1 \\ t_\beta^1 \end{bmatrix} = \begin{bmatrix} 0 \\ 1 \end{bmatrix}\,. \tag{1.42}$$

The initial tangent vector $\mathbf{t}^0$, at a point previous to the orange empty square of figure 1.11, can be calculated through finite different between two previously existing solutions. After the tangent is obtained, a prediction along this vector is performed $[\hat{Q}, \hat{\beta}]^T$

$$\begin{cases} \hat{Q} = Q_1 + \Delta s \dfrac{\mathbf{t}_Q^1}{||t||} \\ \hat{\beta} = \beta_1 + \Delta s \dfrac{t_\beta^1}{||t||} \end{cases}\,, \tag{1.43}$$

with the step length Δs being defined by the user (steps of order $O(10^2)$ and $O(10)$ have been typically employed in this work). This initial prediction is used to start a loop where $[\hat{Q}, \hat{\beta}]^T$ will be corrected up to a solution $[Q, \beta]^T$ of the full TSM eqs. (1.41) alongside an equation that guarantees the new solution is sought in a plane perpendicular to the tangent vector (dashed orange line in figure 1.11)

$$\mathbf{R}_{AL} = (\mathbf{t}_Q^1)^T \cdot (Q - \hat{Q}) + t_\beta^1 \cdot (\beta - \hat{\beta}) = 0\,. \tag{1.44}$$

The coupled TSM and pseudo arc-length continuation system to be solved is thus

$$\begin{cases} \mathcal{N}_{TSM}(Q,\beta) = 0 \\ \mathbf{R}_{AL}(Q,\beta) = 0 \end{cases} . \tag{1.45}$$

Identically to the previous TSM algorithm without the imposed arc-length constraint, we employ a Newton method to find the root of this system

$$\begin{bmatrix} \dfrac{\partial \mathcal{N}_{TSM}}{\partial Q} & \dfrac{\partial \mathcal{N}_{TSM}}{\partial \beta} \\ (\mathbf{t}_Q^1)^T & t_\beta^1 \end{bmatrix} \cdot \begin{bmatrix} Q' \\ \beta' \end{bmatrix} = - \begin{bmatrix} \mathcal{N}_{TSM}(Q^0,\beta^0) \\ \mathbf{R}_{AL}(Q^0,\beta^0) \end{bmatrix} . \tag{1.46}$$

To tackle this large-scale linear system, a parallel implementation similar to the uncoupled TSM algorithm is used, the arc-length constraint being added to single processor (the processor 0 in our case). Throughout the Newton iterations this full matrix is again never explicitly constructed, the system being solved by an iterative method (GMRES). To enforce the arc-length constraint, the previous preconditionning strategy is adapted. A lower upper (LU) factorization that identifies an outer and inner problem

$$\begin{bmatrix} \dfrac{\partial \mathcal{N}_{TSM}}{\partial Q} & 0 \\ (\mathbf{t}_Q^1)^T & t_\beta^1 - (\mathbf{t}_Q^1)^T \cdot \dfrac{\partial \mathcal{N}_{TSM}}{\partial Q}^{-1} \cdot \dfrac{\partial \mathcal{N}_{TSM}}{\partial \beta} \end{bmatrix} \cdot \underbrace{\begin{bmatrix} \mathbb{I} & \dfrac{\partial \mathcal{N}_{TSM}}{\partial Q}^{-1} \cdot \dfrac{\partial \mathcal{N}_{TSM}}{\partial \beta} \\ 0 & \mathbb{I} \end{bmatrix} \cdot \begin{bmatrix} Q' \\ \beta' \end{bmatrix}}_{\text{upper problem}} = - \begin{bmatrix} \mathcal{N}_{TSM}(Q^0,\beta^0) \\ \mathbf{R}_{AL}(Q^0,\beta^0) \end{bmatrix} , \tag{1.47}$$

is used, lower and upper problems being sequentially solved to obtain $[Q', \beta']^T$. The preconditionner approximate the inversion of these two problems, applying (three times) the inverse of the circulant matrix $\mathbf{C}$ when the inversion of the TSM Jacobian is required.

1.3.2.1 Validation

The validation of the arclength method was done by a cross-comparison with the previously validated unsteady nonlinear simulations. Periodic propulsive solutions with $< u_g > \neq 0$ obtained in the range of Stokes number $23 \leq \beta \leq 26$ are compared to results of the TSM continuation with arc-length. As depicted in figure 1.12, the arc-length algorithm is initiated by a previously computed solution and a tangent vector that is obtained by finite differences between the initial and the precedent solutions. We see thus in figure 1.12 that the arc-length continuation with the TSM matches perfectly the unsteady nonlinear solutions, for $\beta \leq 24.5$ and $\beta \geq 24.5$, the continuation passing through all the unsteady solutions.

1.3.3 Floquet analysis of time-periodic self-propelled solutions

1.3.3.1 Governing equations

We investigate the growth of infinitesimal ($\epsilon \ll 1$) perturbations of a periodic base solution $(\mathbf{u_b}, p_b, u_g^b)$ of the coupled fluid - self-propelled foil system. The flow variables and the foil horizontal velocity are decomposed as

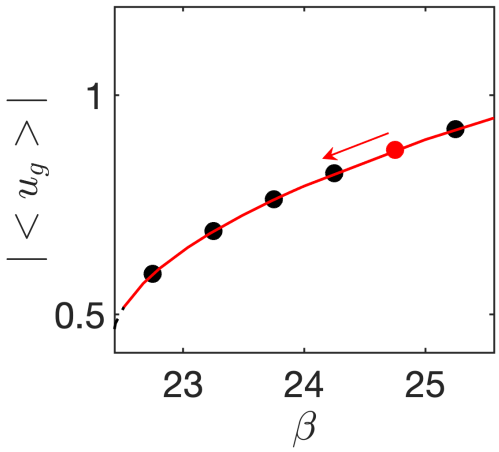

Figure 1.12: Validation of the pseudo arc-length continuation method (solid red line) with respect to results of unsteady nonlinear simulations (black filled circles) for $23 \leq \beta \leq 26$. The initial solution and tangent given to the algorithm are represented by a red filled circle and arrow.

$$(\mathbf{u}, p, u_g) = (\mathbf{u}_b, p_b, u_g^b) + \epsilon(\mathbf{u}', p', u_g'), \tag{1.48}$$

where perturbations $(\mathbf{u}', p', u_g')$ are superimposed to the periodic base solution, which includes both the base-flow field $(\mathbf{u}', p')$ and the foil horizontal velocity u_g' . In the case of non-propulsive base-flows, that satisfy the spatial symmetry (3) at every instant of the flapping period, the foil horizontal velocity of the periodic base solution is equal to zero. No perturbation of the vertical velocity is considered since the flapping velocity $\mathbf{v}_g$ is imposed in the present analysis. By injecting the above decomposition into (1.10)-(1.11) and retaining the first-order term in ϵ, we obtain the following system of equations governing the linear dynamic around the periodic base-solution

$$\mathcal{B}\,\frac{\partial}{\partial t}\underbrace{\begin{bmatrix}\mathbf{u}'\\ p'\\ u_g'\end{bmatrix}}_{\mathbf{q}'} = \underbrace{\begin{bmatrix} -\left[(\mathbf{u}_b(t)-\mathbf{u}_g^b(t))\cdot\boldsymbol{\nabla}\right] - \boldsymbol{\nabla}\mathbf{u}_b(t) + \beta^{-1}\boldsymbol{\Delta} & -\boldsymbol{\nabla} & (\boldsymbol{\nabla}\mathbf{u}_b)\cdot\mathbf{e}_x \\ -\boldsymbol{\nabla} & 0 & 0 \\ (\rho S)^{-1}\mathcal{F}_v & (\rho S)^{-1}\mathcal{F}_p & 0 \end{bmatrix}}_{\mathcal{L}(\mathbf{u}_b,p_b,\mathbf{u}_g^b)} \begin{bmatrix}\mathbf{u}'\\ p'\\ u_g'\end{bmatrix} \tag{1.49}$$

The first two rows are the linearized momentum and mass equations governing the fluid velocity and pressure perturbations. They are coupled to the foil velocity perturbation u_g' via two terms: firstly, the bulk term $(\boldsymbol{\nabla}\mathbf{u}_b)\cdot\mathbf{e}_x$ (block $(1,3)$ in the right-hand side matrix) that modifies the production of fluid perturbation in the momentum equation, and secondly, the boundary conditions at the foil surface Γ_w, where the equality of fluid and solid perturbations holds

$$(u', v')(\mathbf{x}_w, t) = (u_g', 0)\,. \tag{1.50}$$

The third row indicates that the horizontal acceleration of the foil is equal to the horizontal force exerted by the flow perturbation, which is the added contribution of viscous $\mathcal{F}_v$ and pressure $\mathcal{F}_p$ forces, respectively

$$\mathcal{F}_v(\mathbf{u}') = \beta^{-1} \int_{\Gamma_w} (\boldsymbol{\nabla}\mathbf{u}' + \boldsymbol{\nabla}\mathbf{u}'^T) \cdot \mathbf{n}) \cdot \mathbf{e}_\mathbf{x} \, \mathrm{d}\Gamma_w \quad , \quad \mathcal{F}_p(p') = \int_{\Gamma_w} (-p'\mathbf{n}) \cdot \mathbf{e}_\mathbf{x} \, \mathrm{d}\Gamma_w \, . \tag{1.51}$$

Following (Elston, Sheridan, and Blackburn 2004) or (Jallas, Marquet, and Fabre 2017), the perturbations are decomposed in the form

$$\mathbf{q}'(\mathbf{x}, t) = \sum \left(\hat{\mathbf{q}}_j(\mathbf{x}, t) e^{\lambda_j t} + \text{c.c.} \right) , \tag{1.52}$$

where $\hat{\mathbf{q}}_j$ are T-periodic functions, called the Floquet modes, associated to the complex numbers λ_j, called the Floquet exponents. The Floquet multiplier, defined as $\mu_j = e^{\lambda_j T}$, is rather used in the following. It represents the complex amplitude gain of the periodic Floquet mode over one period, i.e. $\hat{\mathbf{q}}_j(\mathbf{x}, T) = \mu_j \hat{\mathbf{q}}_j(\mathbf{x}, 0)$. The polar decomposition of the Floquet multiplier is $\mu_j = |\mu_j| e^{\mathrm{i}\phi_\mathrm{j}}$, where the modulus $|\mu_j|$ quantifies the growth (or decay) of the corresponding Floquet mode over the period, and ϕ_j represents its phase shift over the same period. The stability of the periodic base solution is then addressed by considering the Floquet multiplier with largest modulus. If its absolute value, denoted $|\mu_0|$, is greater than one, the corresponding Floquet mode will grow over one period and the periodic base solution is thus unstable. When the leading Floquet multiplier is real ($\phi_0 = 0$), the Floquet mode is *synchronous* as the perturbation evolves in time with the period of the base flow. When the leading Floquet multiplier is complex ($\phi_0 \neq 0$), the Floquet mode is *asynchronous* and a frequency, denoted f' in the following, related to the phase of the Floquet mode as $f' = \phi_0/(2\pi)$ is introduced.

1.3.3.2 Numerical Method

The strategy to compute Floquet modes is the one proposed by (Barkley and Henderson 1996). As the linearized operator l is time-dependent, the stability of an initial perturbation is assessed regarding the action of the propagator over one period $\boldsymbol{\Phi}$, also known as Monodromy matrix, over the perturbation at an arbitrary initial time t_0, formally denoted

$$\mathbf{q}'(\mathbf{x}, t_0 + T) = \boldsymbol{\Phi} \, \mathbf{q}'(\mathbf{x}, t_0) \, . \tag{1.53}$$

The action of this Monodromy matrix is obtained by time-integration along a period of the linearized equations (1.49) with boundary conditions (1.50), using the temporal and numerical discretization schemes previously described for the unsteady nonlinear method. The eigenvalues and eigenvectors of $\boldsymbol{\Phi}$ are precisely the Floquet multipliers and the mode at an arbitrary initial time. To calculate the modes and Floquet spectrum we have opted for an Arnoldi method with a modified Gram-Schmidt algorithm for the orthogonalization step (Saad 2011). This method has two major advantages: it is capable of converging to secondary dominant eigenvalues and the operator $\boldsymbol{\Phi}$ does not need to be explicitly known. That is not the case for power iteration or *shift-invert* methods, where resp. only the dominant eigenvalue can be calculated and the inverse of the Monodromy matrix needs to be determined. When complex conjugate multipliers are present in the Floquet spectra, a case where $|\mu_1| = |\mu_2|$, the power iteration method is, for example, incapable of converging.

The Arnoldi method is practically implemented in the FreeFEM software (Hecht 2012). This method consists in approximating the Monodromy matrix in a low-dimensional space. The

low dimensional approximation of the Monodromy matrix is progressively built by individual Arnoldi iterations j composed of time-advancing in one flapping period a initial perturbation $\mathbf{q}_{0,j}$

$$\mathbf{q}_{1,j} = \mathbf{\Phi} \cdot \mathbf{q}_{0,j}. \tag{1.54}$$

The Gram-Schmidt algorithm is then employed to extract and normalise the component $\mathbf{q}_{0,j+1}$ of $\mathbf{q}_{1,j}$, the preceding initial vectors being indexed as $k < j$

$$h_{j,k} = \left\langle \mathbf{q}_{1,j}, \mathbf{q}_{0,k} \right\rangle \ , \ \mathbf{q}_{1,j} = \mathbf{q}_{1,j} - h_{j,k}\, \mathbf{q}_{0,k}, \tag{1.55}$$

and $\langle q, q \rangle = \left(\int_{\Omega_f} [\mathbf{u}' \cdot \mathbf{u}] \mathrm{d}\Omega + u_g \cdot u_g \right)$ being the scalar product based on the mass-matrix $\mathcal{B}$. The orthogonal basis $\mathbf{Q}_0$ is then augmented by one at the end of the iteration $\mathbf{q}_{0,j+1} = \mathbf{q}_{1,j}/||\mathbf{q}_{1,j}||$.[1] As pointed out by (Saad 2011) this orthogonalization step is essential for recovering non-dominant eigenmodes.

For j iterations, a $j \times j$ Hessenberg matrix $\mathbf{H}$ approximating $\mathbf{\Phi}$ is built

$$\mathbf{\Phi} \cdot \mathbf{Q}_0 = \mathbf{Q}_0 \cdot \mathbf{H} + \mathbf{Q}_1 \cdot \mathbf{e}, \tag{1.56}$$

where $\mathbf{Q}_1$ is composed of the vectors $\mathbf{q}_1$ and $\mathbf{e}$ is the error committed in the approximation of $\mathbf{\Phi}$ by $\mathbf{H}$. The eigenvalues and vectors of this reduced matrix are calculated. These are then used to reconstruct and approximate the Floquet multiplier and modes at the initial time, i.e. $\hat{\mathbf{q}}(\mathbf{x}, t_0)$. In the present work, a minimal number of 30 Arnoldi iterations was used, this number being further increased in steps of 10 when necessary, in order for the error commited in the approximation of the dominant eigenvalue to converge to five significant digits. All computed modes are normalised by the kinetic energy of the coupled fluid-solid system.

The Arnoldi method allow us to access the Floquet mode only at an arbitrary initial time instant $\hat{\mathbf{q}}(\mathbf{x}, t_0)$. To obtain the complete temporal evolution of a periodic Floquet mode, we integrate in time the following equation over one flapping period,

$$\mathcal{B}\, \frac{\partial \hat{\mathbf{q}}}{\partial t} - \mathcal{L}(\mathbf{u}_b, v_g)\, \hat{\mathbf{q}} = -\lambda\, \mathcal{B}\, \hat{\mathbf{q}}, \tag{1.57}$$

using as initial condition the Floquet mode obtained with the Arnoldi algorithm. The Floquet exponent λ being known, the right-hand side term appropriately counteracts the temporal growth (resp. decay) of the unstable (resp. stable) Floquet mode.

The Floquet exponent and mode are complex variables. To avoid working with complex vectors, the implemented numerical method for the mode evolution makes a distinction between the real $\hat{\mathbf{q}}_r$ and imaginary $\hat{\mathbf{q}}_i$ part of the Floquet mode. Similar to the unsteady nonlinear solver, we use and IMEX scheme for the temporal evolution of the Floquet mode where its temporal growth and the nonlinear terms are treated explicitly. The previous unsteady nonlinear method (1.14) is accordingly modified to include the Floquet exponent in its right-hand side.

[1] It is rare the eventuality where the norm $||\mathbf{q}_{1,j}||$ becomes zero. That would mean that the Krylov subspace is complete and $\mathbf{q}_{1,j}$ is completely defined by this basis. This case is rarely attained in practice, since it means the number of iterations reached the rank of $\mathbf{\Phi}$.

	$\beta = 40, KC = 4.75$	$\beta = 100, KC = 3.65$
(Elston, Blackburn, and Sheridan 2006)	1.1282	1.1429
Present method	1.1273	1.1411

Table 1.3: Linear solver validation: Comparison of the leading Floquet multiplier $|\mu|$ with the values presented on Table 3 of (Elston, Blackburn, and Sheridan 2006)

1.3.3.3 Validation and numerical examples

Since there are no cases of self-propelle fluid-solid Floquet stability at the literature, the validation of our numerical method is done in two parts. In the first, we use our numerical method to perform the Floquet stability analysis of non-propelled heaving cylinders in two-dimensional quiescent flows. Second, we compare the growth rate predicted by fluid-solid Floquet stability analysis to the growth rate of unsteady nonlinear simulations.

Floquet multipliers are compared to the ones obtained in a purely hydrodynamic analysis of the symmetry breaking of the flow around a non-propelled heaving cylinder in Elston, Blackburn, and Sheridan (2006). Authors spatial discretization was carried out with two-dimensional quadrilateral spectral elements employing tensor-product Lagrange interpolant shape functions based on Gauss–Lobatto–Legendre quadrature points. A rectangular domain of size $40D$ with one-dimensional Lagrange interpolant of order 8 was retained by the authors. For each mesh, the radial thickness of the inner layer of elements was 0.1 D, with 16 elements around the circumference of the cylinder. With an interpolant order 8, 128 independent mesh points are obtained in the cylinder azimuthal direction.

We have performed the same stability analysis in a circular domain of size $40D$ with a mesh composed of 4×10^4 triangles that range in size from 10^{-2} nearby the cylinder to order unity in the external part of the domain. A time-step of $\Delta t = 5 \times 10^{-4}$ was used as to insure convergence of the IMEX solver at values of large flapping amplitude and Stokes number. Two distinct cases of flapping amplitude (using the Keulegan-Carpenter number $KC = 4\pi A$) and Stokes number, $(\beta, KC) = (40, 4.75)$ and $(\beta, KC) = (100, 3.65)$. We can see in the table 1.3 that the absolute value of the leading Floquet multiplier obtained in the two test cases is in a good agreement with values of Elston, Blackburn, and Sheridan (2006).

The second validation case is a cross-comparison between the unsteady growth of Floquet modes of amplitude $O(10^{-3})$ over symmetric non-propulsive solutions and the one predicted by the fluid-solid Floquet stability analysis. Two cases are here considered, Stokes numbers $\beta = 6$ and $\beta = 13$, for a self-propelled heaving rectangular foil of fixed flapping amplitude $A = 0.5$, density ratio $\rho = 100$ and a thickness-chord aspect ratio of $h = 0.05$. The fluid-solid stability analysis predicts an unstable synchronous and asynchronous leading Floquet multiplier for these Stokes numbers,as identified by the filled black squares in figure 1.13.

In the case of $\beta = 6$ we depict the obtained synchronous mode in figure 1.14. The fluid-solid Floquet mode is composed of a flow perturbation – 1.14(a-d) which is depicted through vorticity contours for four equally spaced time instants along a flapping period – and a perturbation of the foil horizontal velocity (1.14-f). The Floquet mode equally allow us to investigate the effect of the flow perturbation over the foil dynamics, by analysing the hydrodynamic force acting on the foil (1.14-e). In this specific case, for instance, as the time-averaged horizontal velocity and force of the foil have the same sign, we can see that the flow perturbation tends to accelerate the

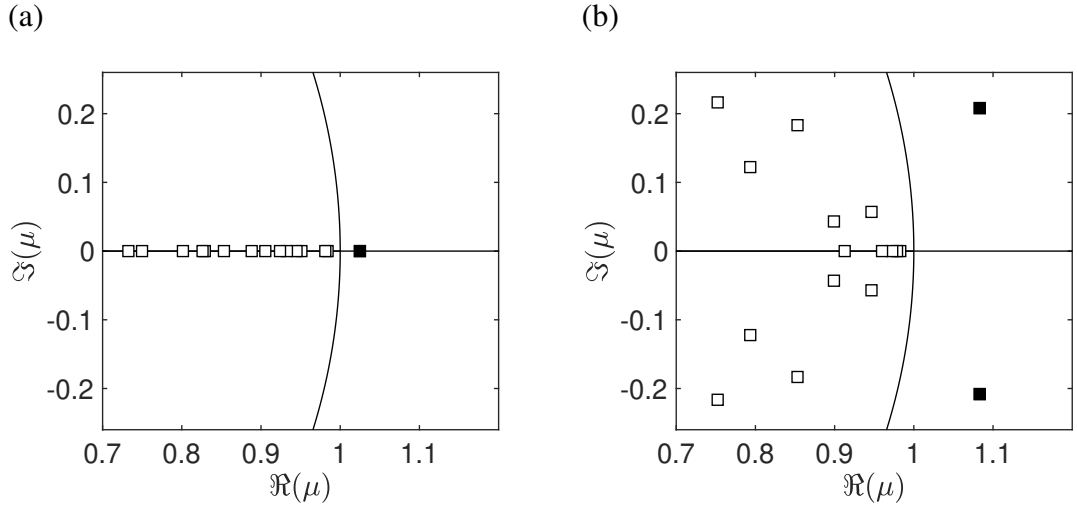

Figure 1.13: Spectra of the Floquet multipliers for two Stokes numbers obtained through fluid-solid Floquet stability analysis. Spectra for (a) $\beta = 6$ presenting one unstable synchronous multiplier (filled square) and (b) $\beta = 13$ presenting a pair of complex conjugate unstable asynchronous multipliers. Other control parameters are $A = 0.5$, $\rho = 100$ and $h = 0.05$.

foil along the flapping period.

The obtained perturbation is thus introduced in the unsteady solver. The growth rate observed in the unsteady nonlinear simulations is shown in figure 1.15. We observe in both figures that there is an excellent agreement between the growth rate predicted by fluid-solid Floquet stability analysis and the one of unsteady nonlinear simulations, concluding our linear solver validation.

1.4 Summary of theoretical and numerical tools

In this chapter we have introduced the theoretical and numerical tools which are employed along the first part of this thesis.

The governing nonlinear equations written in a non-inertial frame of reference were first introduced. While the adoption of this frame of reference generates a very small modification of the coupled fluid-solid equations, it has the great benefit of maintaining a conforming and time-independent fluid-solid interface and fluid domain for the numerical simulations. These aspects are essential for the simulation of self-propelled foils. Domains used to study the free dynamics of the foil no longer need to be a priori conceived to allow the full horizontal displacement of the wing until a permanent regime is achieved. In addition, no impurities due to non-conformity are present in our formulation. The governing equations were followed by the unsteady nonlinear solver employed across all the chapters of this part of the thesis.

Methods for time-periodic solutions, the time-spectral method (TSM) and the fluid-solid Floquet stability analysis, were then introduced for self-propelled foils. The TSM is not only very efficient to directly compute periodic solutions of the coupled fluid-solid system, but also capable of computing unstable periodic solutions. Coupled to the pseudo arc-length continuation, this method will be of great importance in chapter 3 for studying saddle-node bifurcations of the self-propelled foil at higher flapping frequencies. The fluid-solid Floquet

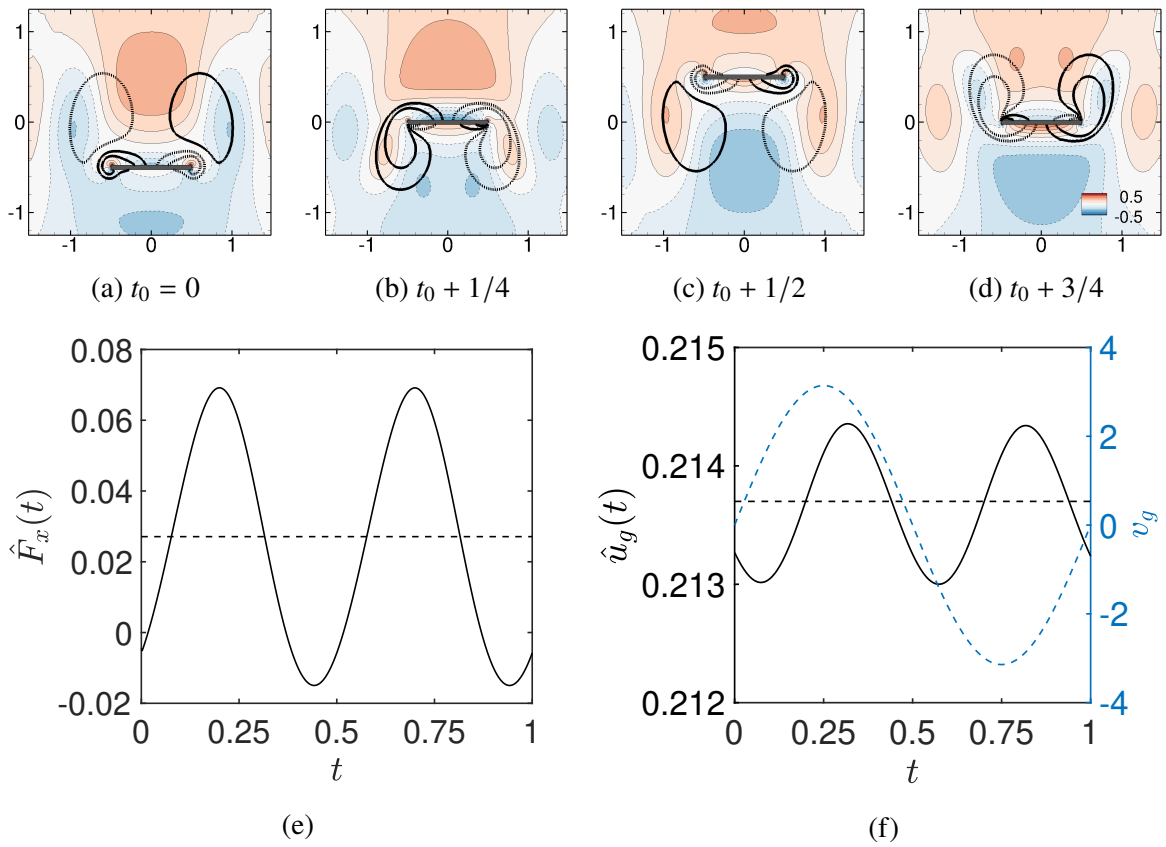

(a) $t_0 = 0$ (b) $t_0 + 1/4$ (c) $t_0 + 1/2$ (d) $t_0 + 3/4$

(e) (f)

Figure 1.14: Floquet mode obtained with the linear solver a self-propelled wing (fixed parameters $A = 0.5$, $\rho = 100$ and $h = 0.05$) for $\beta = 6$: (a-d) Vorticity contours for a flapping period (base flow represented by thick lines). (e) Horizontal force (black) acting on the solid, with pressure and viscous components in blue and red respectively, and (f) horizontal velocity. Mean force and velocity in both figures with dashed line.

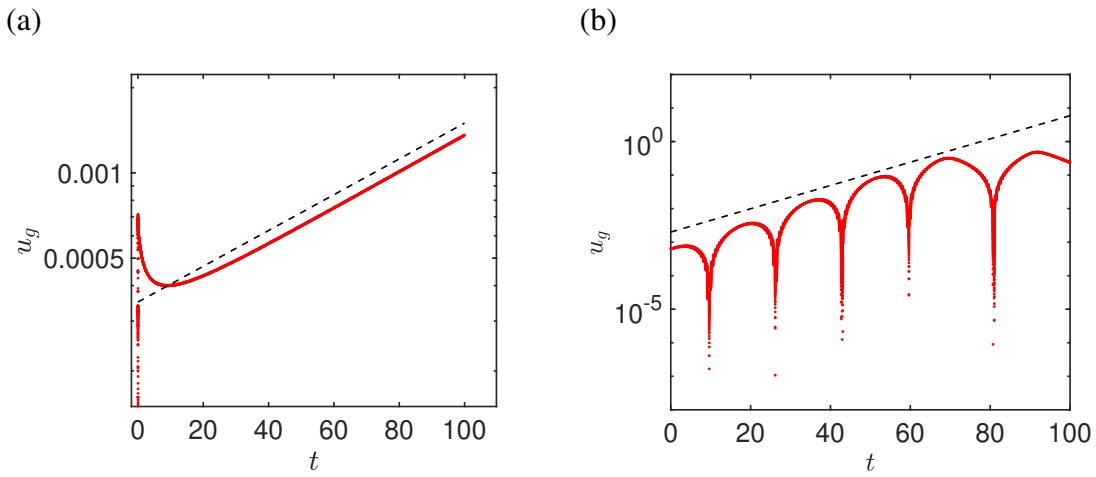

Figure 1.15: Comparison of the growth rate of the horizontal velocity u_g in unsteady nonlinear simulations with the growth (figure 1.13) predicted by the Floquet multipliers (dashed line) for two Stokes (a) $\beta = 6$ and (b) $\beta = 13$. Other control parameters are $A = 0.5$, $\rho = 100$ and $h = 0.05$.

stability analysis, used in chapters 2 and 3 is a very powerful tool that allows highlighting linear mechanisms leading to the coupled fluid-solid system instability. It not only encompasses the purely-hydrodynamic Floquet stability usually employed in the literature, as it will be shown in chapter 2, but its fluid-solid coupling is essential for the prediction of the onset of propulsive regimes. Further, this analysis allow us to establish physical instability criteria that link the hydrodynamic force and solid dynamics to the Floquet growth rate, as we will discuss in chapter 2.

Chapter 2

Self-propelled dynamics at low Stokes numbers: linear analysis

The content of this chapter is the same of the article: Benetti Ramos et al. (2020), Fluid-solid Floquet stability analysis of self-propelled heaving foils, accepted for publication in *Journal of Fluid Mechanics*.

In this chapter we investigate the dynamics of self-propelled wings at low Stokes numbers. This nondimensional number $\beta = fc^2/\nu$ is defined using the flapping frequency and the chord length as characteristic time and length scales, as well as the fluid viscosity. In low Stokes ($1 \leq \beta \leq 20$) the fluid-solid system, composed of the self-propelled foil and the surrounding quiescent fluid, breaks the flow initial left-right symmetry and attains its first regimes of locomotion. We show that the onset of its two first stages of locomotion can be predicted by a linear fluid-solid Floquet stability analysis, an analysis that considers not only the flow but also the foil velocity at the perturbation level.

We investigate the role of linear mechanisms in the emergence of nonlinear horizontal self-propelled states of a heaving foil in a quiescent fluid. Two states are analyzed: a periodic state of unidirectional motion and a quasi-periodic state of slow back & forth motion around a mean horizontal position. The states emergence is explained through a fluid-solid Floquet stability analysis of the non-propulsive symmetric base solution. Unlike a purely-hydrodynamic analysis, our analysis accurately determine the locomotion states onset. An unstable synchronous mode is found when the unidirectional propulsive solution is observed. The obtained mode has a propulsive character, featuring a mean horizontal velocity and an asymmetric flow that generates a horizontal force accelerating the foil. An unstable asynchronous mode, also featuring flow asymmetry and a non-zero velocity, is found when the back & forth state is observed. Its associated complex multiplier introduces a slow modulation of the flapping period, agreeing with the quasi-periodic nature of the back & forth regime. The temporal evolution of this perturbation shows how the horizontal force exerted by the flow is alternatively propulsive or resistive over a slow period. For both modes, an analysis of the velocity and force perturbation time-averaged over the flapping period is used to establish a physical instability criteria. The behaviour for large solid-to-fluid density ratio of the modes is thus analyzed. The asynchronous fluid-solid mode converges towards the purely-hydrodynamic one, whereas the synchronous mode becomes marginally unstable in our analysis not converging to the purely-hydrodynamic

analysis where it is never destabilised.

Contents

2.1 Introduction

A common locomotion strategy adopted by aquatic or flying animals (Gray 1933; Wu 2010; Shyy et al. 2010), and more recently employed in the conception of large and small-scale artificial swimmers (Barrett 1996; Ramananarivo, Godoy-Diana, and Thiria 2013; Williams et al. 2014), is the flapping motion of appendages such as wings, tails and fins. A fundamental question that impacts the design of micro-swimmers and aerial-vehicles (Williams et al. 2014; Faux et al. 2018) is the critical size above which flapping-based propulsion remains efficient and applicable. Indeed, micro-organisms of very small scales, as cells or sperm, are known to exploit other locomotion strategies (Lauga 2011), ciliar or flagelar propulsion, respectively. As first stated by Purcell (1977) in the so-called scallop theorem, a reciprocal motion of appendages, for which the paths during the two half-strokes are identical but time-reversal, does not allow to generate a net thrust at those very small scales. This is due to the linearity and timeless nature of the surrounding flows which are entirely dominated by the viscous effects. An emblematic observation of the transition from ciliar to flapping propulsion has been achieved for the mollusc *Clione Antartica* (Childress and Dudley 2004) that disposes both of cilia and wings attached to its body. Whereas its cilia are always employed, the wings remain retracted to his body, being flapped exclusively after a critical velocity is reached. This switch of locomotion strategy was related to the evolution of the dynamical response of the surrounding flow as the Reynolds number, based on the swimming velocity, increases. The present paper aims at better understanding the emergence of flapping locomotion based on reciprocal motion.

To that aim, Vandenberghe, Zhang, and Childress (2004) and Vandenberghe, Childress, and Zhang (2006) designed an experiment where flapping propulsion emerges exclusively from the flow and not from the motion asymmetry, which is generally explored in the animal world as to achieve a more efficient propulsion (Weis-Fogh 1973; Spagnolie et al. 2010). The experiment consists of a horizontal flat rectangular foil immersed in still water filling a cylindrical tank and attached in its mid-span to a shaft. This shaft is vertically flapped with a sinusoidal motion and the foil is allowed to rotate, together with the shaft, around the vertical axis in the horizontal direction. Note that the foil is only heaving, not simultaneously heaving and pitching like in the experiments of Spagnolie et al. (2010) where the foil besides the imposed heaving was allowed to passively pitch around its leading edge. For a small enough frequency, the flow induced by a heaving motion of fixed amplitude is left-right symmetric. Thus, no hydrodynamic force is generated over the foil in the horizontal direction for every instants, and the foil does not rotate. However, once a critical Stokes number $\beta = f^*(c^*)^2/\nu$ is attained (a non-dimensional number similar to the Reynolds number that uses the dimensional flapping frequency f^* and the foil chord c^* as characteristic time and length scales, as well as the fluid kinematic viscosity ν), the surrounding flow breaks its initial symmetry and generates horizontal forces. The foil then achieves locomotion and eventually reaches a permanent forward regime in equilibrium with the fluid. Subsequent numerical studies were dedicated to understand how the transient dynamics and the self-propelled regimes of this model problem evolve with respect to its control parameters. These studies simplified Vandenberghe, Zhang, and Childress (2004) configuration, working with a two-dimensional cross-section of the experiment (imposed heaving and horizontally self-propelled foils), thus neglecting its rotational flow effects. Investigating the self-propulsion of elliptical foils in a two-dimensional incompressible flow under a fixed nondimensional chord-based flapping amplitude $A = 0.5$, Alben and Shelley (2005) revealed that as the flapping frequency (equivalently the Stokes number) is increased, the foil motion

transition between different self-propelled regimes that are a unidirectional propulsion (as in the experiments of Vandenberghe, Zhang, and Childress (2004)), a quasi-periodic back & forth motion around a fixed point in space (with a frequency remarkably lower than the flapping one) and even a chaotic motion. These authors have also shown that these self-propelled regimes are greatly impacted by the thickness-to-chord aspect ratio h and the solid-to-fluid density ratio ρ. In one hand, thinner ellipses of aspect ratio $h = 0.1$ are able to break symmetry at lower flapping frequencies and present thus a greater exponential growth of their horizontal velocity than thicker foils. On the other hand, for foils of greater density ratio ($\rho > 10$) the existence of non-coherent and chaotic regimes is greatly reduced or even suppressed when compared to their lighter equivalents. Lu and Liao (2006) for instance have shown for a fixed flapping amplitude and frequency that a non-coherent state of motion can be suppressed thanks to the increase of the density ratio. A similar observation was made by Zhang et al. (2009) while decreasing the aspect ratio of elliptical and rectangular foils, where in both cases smaller aspect ratios were found to be more prone to unidirectional locomotion than thicker ones. Lu and Liao (2006) have equally mapped in the plan flapping amplitude/ frequency the transition between symmetric and non-symmetric flows (thus propelled ones) revealing that the transition occurs for smaller frequencies at higher flapping amplitudes. Later on, Deng and Caulfield (2016) established the same frontier for different aspect ratios, revealing that thinner foils break symmetry earlier in flapping amplitude and frequency. The authors also compared the frontier between symmetric and non symmetric flows for propelled and non-propelled foils for two-dimensional ellipses (Deng and Caulfield 2016) or three-dimensional oblate spheroids (Deng et al. 2016; Deng et al. 2017; Deng and Caulfield 2018b), indicating that the frontier of flow symmetry breaking is obtained in both two and three-dimensional cases for smaller frequency and amplitude for self-propelled foils. Using two-dimensional numerical simulations, we revisit in this work the nonlinear regimes of locomotion for a thin rectangular foil ($h^* = 0.05c^*$), of density $\rho_s = 100\rho_f$ and flapping with a fixed maximal amplitude $A^* = 0.5c^*$. By varying the Stokes numbers in the range $1 \leq \beta \leq 20$, we first aim at carefully characterizing and identifying the transition between various self-propelled regimes of the foil motion: the non-propulsive, the unidirectional propulsive and the back & forth motion. This parametric investigation is useful to accurately determine critical values of the Stokes numbers for which transition between these nonlinear regimes are observed. They will be used as basis of comparison for the second objective of this work, i.e. predicting the emergence of these regimes using linear stability analysis of the periodic flows generated by the flapping foil.

Floquet analysis allows to investigate the linear stability of periodic solutions (Floquet 1883). In hydrodynamics, Barkley and Henderson (1996) first performed this analysis on a two-dimensional time-periodic wake flow to explain the onset of three-dimensional structures in the wake of a *fixed* circular cylinder. The Floquet analysis of time-periodic flows generated by flapping bodies has then been considered by Elston, Sheridan, and Blackburn (2004) and Elston, Blackburn, and Sheridan (2006) for two-dimensional oscillating cylinder flows. They successfully explained the emergence of two and three dimensional flow asymmetries observed in experiments and simulations. More recently, Jallas, Marquet, and Fabre (2017) performed a Floquet analysis of time-periodic propulsive wake generated by a pitching wing. They identify an unstable synchronous mode that successfully explains the lateral deviation of the propulsive vortex street observed when increasing the flapping frequency. To investigate the emergence of the self-propelled regimes described above, Deng and Caulfield (2016), Deng et al. (2016),

Deng et al. (2017), and Deng and Caulfield (2018b) first proposed to consider a Floquet analysis for various flapping foil configurations. Based on the observation that flow symmetry breaking occurs prior to the self-propulsion of the foil in temporal simulations, Deng and Caulfield (2016) and Deng and Caulfield (2018b) applied a purely-hydrodynamic analysis, that does not consider a perturbation of the foil speed in the propulsion direction. For a certain range of control parameters, results of this purely hydrodynamics analysis are in good agreement with nonlinear results. In particular, they identify unstable asynchronous modes at flapping frequencies where the foil exhibit a slow quasi-periodic back & forth motion. However, some disagreements between results of the purely-hydrodynamic analysis and the nonlinear results of self-propelled simulations were also reported, as in the case of low aspect ratio $h = 0.1$ ellipses, where linear analysis fails to predict the onset of unidirectional forward locomotion (Deng and Caulfield 2016). In the present work, we introduce the so-called fluid-solid Floquet analysis that considers the foil speed as a perturbation variable and takes into account the inherent coupling between the flow perturbation and the rigid motion of the foil at the perturbation level. We will demonstrate, by comparison with nonlinear results, that this fluid-solid coupling is essential to correctly represent and predict the emergence of self-propelled regimes.

The importance of the fluid-solid coupling in linear stability analysis has a long history in aeroelasticity (see the review by Dowell et al. (1989)) that investigates the infinitesimal motion of structures immersed in high Reynolds number flows. Fluid-solid stability analyses for lower Reynolds number flows are more recent. To our knowledge, Cossu and Morino (2000) first performed the fluid-stability analysis of the steady wake cylinder flow to explain the sub-critical vortex-induced vibration of the cylinder when mounted on a spring. The path of bodies freely rising or falling in fluids under the effect of gravity (see Ern et al. (2012) for a review) is another example where fluid-solid linear stability analyses successfully explained the emergence of various trajectories. Tchoufag, Fabre, and Magnaudet (2014) first elucidate the path instability of buoyancy-driven disks/thin cylinders and then of freely rising spheroidal bubble (Tchoufag, Magnaudet, and Fabre 2014). Recently, Negi, Hanifi, and Henningson (2019) proposed a simplified formulation to handle the linearized fluid-structure interaction for rigid bodies. Fluid-solid stability analysis has also been extended to deformable (elastic) structures, to explain the dynamics of inverted flags in uniform flows (Goza, Colonius, and Sader 2018) and of flexible splitter plates clamped to the rear of a cylinder (Pfister and Marquet 2020). Note also that Tammisola, Lundell, and Söderberg (2012) investigated the global instability of planar jets and wakes in two immiscible fluids, focusing on the effect of surface tension. In all of these studies, the temporal evolution of perturbations over a steady base flow solutions was considered. To our knowledge, the fluid-solid stability analysis of time-periodic flow solutions has never been addressed in the context of fluid-solid interaction. In the present study, we introduce the mathematical formalism of such analysis and apply it to explain the emergence of self-propelled flapping states. Additionally, a time-averaged analysis is proposed to highlight the role of the fluid-solid coupling in the destabilization of the Floquet modes. Such connections between linear modes and thrust efficiency have been for instance highlighted in the literature as key factors for an optimal frequency selection in flapping wings (Triantafyllou, Triantafyllou, and Grosenbaugh 1993; Moored et al. 2012).

This article is organized in two parts. In §2.2, we investigate numerically the nonlinear regimes of locomotion for a self-propelled heaving foil. The configuration and non-dimensional

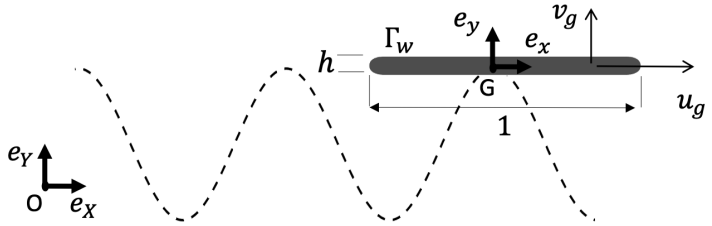

Figure 2.1: Sketch of the foil configuration under sinusoidal vertical motion and horizontal translation with velocity $\mathbf{u}_g$. The foil chord (trailing to leading edge) and its thickness, the frames of reference and the solid/fluid interface Γ_w are indicated.

parameters are introduced before describing the governing nonlinear equations and numerical methods. The self-propelled solutions obtained for a fixed flapping amplitude and density ratio are then carefully described for three values of the Stokes number. The transition between regimes of non-propulsive, unidirectional propulsive and back & forth motions are finally identified by varying the Stokes number in the range $2 \leq \beta \leq 20$. In §2.3, we introduce first the fluid-solid Floquet stability analysis of self-propelled foils and then the time-averaged analysis that allows to establish instability criteria based on the velocity and force of the Floquet mode. Results of this fluid-solid analysis, performed at $\rho = 100$ for symmetric non-propulsive solutions, are first described by analysing the synchronous and asynchronous modes found unstable at different Stokes numbers. Those results are then compared to those obtained with the purely-hydrodynamic Floquet analysis and with the nonlinear temporal simulations. The effect of the density ratio on the two unstable Floquet modes is finally described.

2.2 Problem formulation and self-propelled nonlinear solutions

We investigate the horizontally constrained locomotion of a vertically heaving foil of density ρ_s immersed in an initially quiescent fluid of density ρ_f and viscosity ν. The foil, shown in figure 2.1, is similar to the one used in the experimental studies by Vandenberghe, Zhang, and Childress (2004) and Vandenberghe, Childress, and Zhang (2006). Its rectangular shape is characterized by the thickness h^* and chord c^* with rounded corners of diameter equal to the foil thickness. The periodic displacement imposed along the vertical axis e_y is

$$y_g^*(t) = -A^* \cos(2\pi f^* t^*), \tag{2.1}$$

where the superscript * is used to indicate dimensional variables. A^* is the maximal vertical amplitude and f^* is the flapping frequency, and $T^* = 1/f^*$ is the flapping period. The foil is free to move along the horizontal axis e_x as a result of hydrodynamic forces acting on the solid-fluid interface Γ_w. This rigid-body fluid-structure interaction is characterized by four non-dimensional parameters, namely the frequency-based Stokes number β, the non-dimensional amplitude A, the solid-fluid density ratio ρ and the non-dimensional thickness h, defined

respectively as

$$\beta = \frac{f^*(c^*)^2}{\nu},\ A = \frac{A^*}{c^*},\ \rho = \frac{\rho_s}{\rho_f} \text{ and } h = \frac{h^*}{c^*}\,. \tag{2.2}$$

These parameters are obtained by choosing the chord c as characteristic length scale, the fluid density ρ_f as characteristic mass scale and the flapping period $1/f^*$ as characteristic time. In the following, all variables are thus made non-dimensional using these scales. Note that the non-dimensional flapping period T is thus equal to 1 whatever the values of the Stokes number β, which is the only parameter or variable containing the dependency to the dimensional frequency f^*. Other choices of characteristic scale are also possible and made in the literature. For instance, Alben and Shelley (2005) used the flapping velocity A^*f^* as characteristic velocity, thus introducing the flapping amplitude based Stokes number $\beta_A = A^*f^*c^*/\nu = A\beta$.

In the present study, the foil geometry and the flapping amplitude are fixed to $h = 1/20$ and $A = 0.5$, respectively. This aspect ratio is close to the experimental devices of Vandenberghe, Zhang, and Childress (2004), and this flapping amplitude equals the one adopted by Alben and Shelley (2005). A discussion of the influence of these two parameters can be found in Zhang et al. (2009) and Deng and Caulfield (2016). In this section, we will investigate numerically the nonlinear dynamics of the foil for the fixed density ratio $\rho = 100$ in the range of Stokes number $1 \leq \beta \leq 20$.

2.2.1 Governing non-linear equations

The dynamics of the foil interacting with the surrounding fluid is described by the non-dimensional variable $\mathbf{q} = (\mathbf{u}, p, u_g)^T$ where $\mathbf{u} = (u, v)$ is the two-dimensional fluid velocity field, p is the pressure field and u_g is the foil horizontal velocity. The fluid-solid variable is governed by the evolution equation

$$\mathcal{B}\frac{\partial \mathbf{q}}{\partial t} = \mathcal{R}(\mathbf{q}, v_g)\,, \tag{2.3}$$

where $v_g(t) = 2\pi A \sin(2\pi t)$ is the non-dimensional foil vertical velocity and the operators $\mathcal{B}$ and $\mathcal{R}$ are defined as

$$\mathcal{B} = \begin{bmatrix} \mathcal{I} & 0 & 0 \\ 0 & 0 & 0 \\ 0 & 0 & 1 \end{bmatrix},\ \mathcal{R}(\mathbf{q}, v_g) = \begin{bmatrix} -\left([\mathbf{u} - \mathbf{u}_g]\cdot\boldsymbol{\nabla}\right)\mathbf{u} - \nabla p + \beta^{-1}\Delta\mathbf{u} \\ -\nabla\cdot\mathbf{u} \\ (\rho S)^{-1}F_x(\mathbf{u}, p) \end{bmatrix}. \tag{2.4}$$

The first and second lines are the incompressible Navier-Stokes equations written in a non-inertial frame of reference, denoted $(G, \mathbf{e}_x, \mathbf{e}_y)$ in figure 2.1, that translates at the foil speed $\mathbf{u}_g = (u_g, v_g)$ in the laboratory frame of reference $(O, \mathbf{e}_X, \mathbf{e}_Y)$. Note that both solid and fluid velocities are absolute velocities (Mougin and Magnaudet 2003; Jenny and Dušek 2004), the relative flow velocity $(\mathbf{u} - \mathbf{u}_g)$ appearing in the non-linear term of the momentum equations. While the solid vertical velocity v_g is imposed, the temporal evolution of the foil horizontal velocity u_g is governed by the Newton's second law, as stated by the third line in (2.3,2.4). The horizontal acceleration is equal to the horizontal hydrodynamic force $F_x(\mathbf{u}, p)$ weighted by the non-dimensional mass of the foil ρS ($S = h(1-h) + \pi h^2/4$ being its non-dimensional surface). This hydrodynamic force depends on the fluid velocity and pressure as

$$F_x = \int_{\Gamma_w} ([-p\mathcal{I} + \beta^{-1}(\nabla\mathbf{u} + \nabla\mathbf{u}^T)]\cdot\mathbf{n})\cdot\mathbf{e_x}\,\mathrm{d}\Gamma_w\,. \tag{2.5}$$

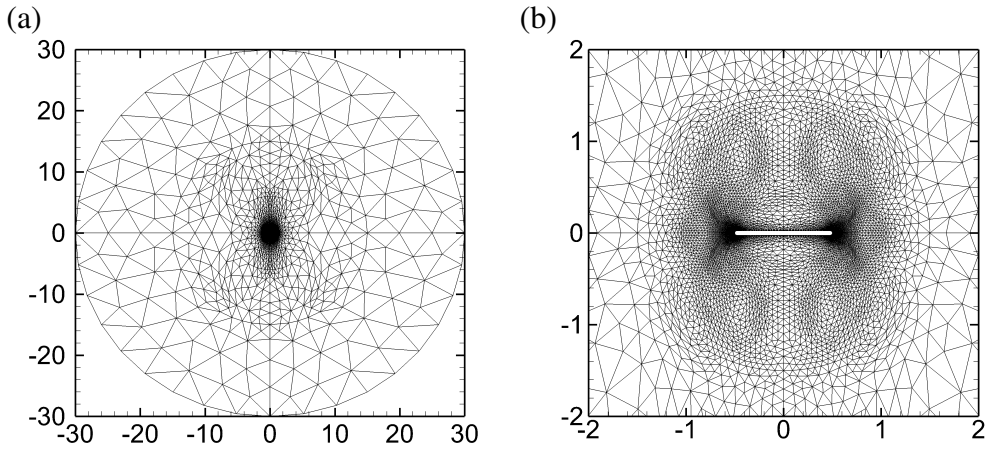

Figure 2.2: Computational domain and mesh. (a) Full and (b) close-up views of a typical mesh adapted to the flow solution

where Γ_w denotes the fluid-solid boundary. An additional coupling between the fluid and solid variables is due to the equality of velocities at the fluid-solid interface, i.e.

$$\mathbf{u}(\Gamma_w, t) = \mathbf{u}_g(t) = [u_g(t), 2\pi A \sin(2\pi t)]^T . \tag{2.6}$$

The fluid is at rest sufficiently far away from the foil.

2.2.2 Numerical methods

The system of equations (2.3), (2.4), (2.5) and (2.6) is discretized in time using the following r-order semi-explicit scheme

$$\begin{aligned}
\frac{\alpha_0}{\Delta t}\mathbf{u}^{n+1} + \nabla p^{n+1} - \beta^{-1}\Delta\mathbf{u}^{n+1} &= \mathbf{f}^{n+1} \\
\nabla\cdot\mathbf{u}^{n+1} &= 0 \\
(u^{n+1}, v^{n+1})(\Gamma_w) &= \left(u_g^{n+1}, 2\pi\, A\, \sin(2\pi t^{n+1})\right) \\
\frac{\alpha_0}{\Delta t}u_g^{n+1} &= (\rho S)^{-1}F_x(\mathbf{u}^{n+1}, p^{n+1}) - \sum_{k=1}^{r}\frac{\alpha_k}{\Delta t}u_g^{n+1-k} \\
(u^{n+1}, v^{n+1})(\Gamma_e) &= (0,0),
\end{aligned} \tag{2.7}$$

where the right-hand side forcing term $\mathbf{f}^{n+1}$ in the momentum equation is defined as

$$\mathbf{f}^{n+1} = -\sum_{k=1}^{r}\gamma_k(\mathbf{u}^{n+1-k} - \mathbf{u_g}^{n+1-k})\cdot\nabla\mathbf{u}^{n+1-k} - \sum_{k=1}^{r}\frac{\alpha_k}{\Delta t}\mathbf{u}^{n+1-k} .$$

with Δt the time step and $(\mathbf{u}^{n+1}, p^{n+1})$ the velocity and pressure at time $t_{n+1} = (n+1)\Delta t$. A quiescent fluid condition is applied in the external boundary Γ_e of the computational domain, typically far away from the foil. The time derivatives are approximated by r-order backward differential formulae. The linear diffusion and pressure gradient terms are implicit, while the

nonlinear convection terms are extrapolated with r-order formulae. A first-order scheme ($r = 1$, $\alpha_0 = 1$, $\alpha_1 = -1$ and $\gamma_1 = 1$) is used for the first two temporal iterations ($n \leq 1$), before switching in the subsequent iterations ($n > 1$) to a second-order scheme ($r = 2$, $\alpha_0 = 3/2$, $\alpha_1 = -2$, $\alpha_2 = 1/2$, $\gamma_1 = 2$ and $\gamma_2 = -1$). To avoid severe time-step restrictions for small values of density ratio induced by an explicit coupling (Causin, Gerbeau, and Nobile 2005), the equality of fluid and solid velocity is treated implicitly. To allow the use of an existing fast implementation to solve the flow equations Jallas, Marquet, and Fabre (2017), we use a segregated approach, proposed by Jenny and Dušek (2004) and detailed in Appendix 2.5, to solve the coupled fluid-solid problem. Typically, the time step is set to $\Delta t = 10^{-2}$ for small values of the Stokes number ($\beta = 2$) and is decreased to $\Delta t = 5 \cdot 10^{-4}$ for larger values ($\beta = 19$), so as to ensure the numerical stability of this semi-explicit temporal scheme (Kress and Lötstedt 2006).

The linear equations (2.7) are discretized in space using a classical finite-element method. The flow velocity is discretized with quadratic elements (P2) while the pressure is discretized with linear element (P1). The implementation is based on the FreeFEM software (Hecht 2012). The computational domain, displayed in figure 2.2(a), is a circle of (non-dimensional) diameter 60 centered at the foil center of mass, the external boundary of this circular domain being Γ_e. A Delaunay triangulation of the computational domain results in mesh with typically 1.2×10^4 triangles. As spatially symmetric solutions are expected, a particular attention was given to create a symmetric mesh and not artificially insert asymmetries in the flow. To create a mesh that is symmetric with respect to the x and y-axis and refined in flow regions exhibiting large velocity gradients (see figure 2.2-b), we have proceed as follows. Once a first solution has been computed, we adapt a mesh of a quarter domain to several instants of the periodic flow, using the hessian-based mesh adaptation implemented in FreeFEM. We refer to Fabre et al. (2018) for a practical review. After duplicating and appropriately rotating this quarter-mesh, the full mesh can finally be assembled. The triangle size is typically of order $O(10^{-2})$ close to the foil, and 1 in the external part of the domain. Mesh refinement and domain size were chosen based on the convergence of the foil horizontal velocity and the vertical hydrodynamic force. Greater domains or mesh refinement have exhibited little influence over these values. The validation of this numerical method is detailed in Appendix 2.6 by comparison with results of Spagnolie et al. (2010).

2.2.3 Results

Unsteady nonlinear simulations are performed for values of the Stokes numbers in the range $1 \leq \beta \leq 20$. The amplitude $A = 0.5$ and the foil aspect ratio $h = 1/20$ are kept fixed throughout this study. When increasing the Stokes number, three different types of solution are successively observed, called hereinafter the (1) symmetric non-propulsive, (2) unidirectional propulsive and (3) back & forth solutions. In §2.2.3.1 we first describe these solutions for three representative values of Stokes number and for a fixed density ratio $\rho = 100$, concluding the section by a summary of the Stokes numbers range for which these solutions are obtained. In §2.2.3.2 these results are compared to the ones of a smaller density ratio closer to aquatic swimming ($\rho = 1$). These different type of solutions have already been experimentally or numerically observed in previous studies. The transition from non-propulsive to unidirectional propulsive solutions was investigated in the works of Vandenberghe, Zhang, and Childress (2004) and Vandenberghe,

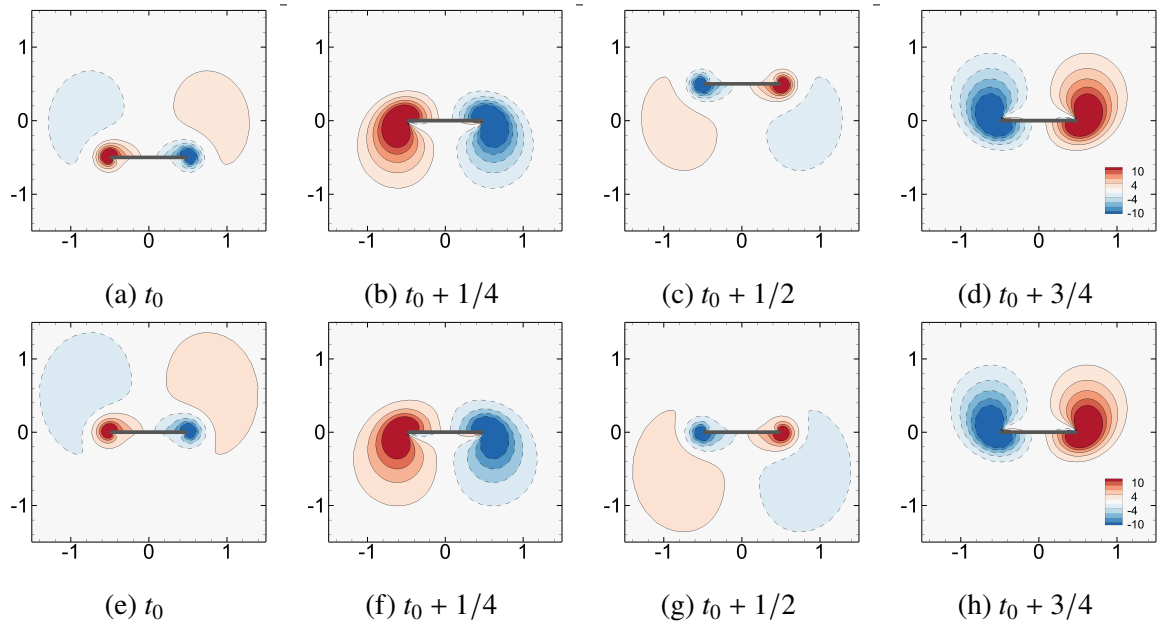

(a) t_0 (b) $t_0 + 1/4$ (c) $t_0 + 1/2$ (d) $t_0 + 3/4$

(e) t_0 (f) $t_0 + 1/4$ (g) $t_0 + 1/2$ (h) $t_0 + 3/4$

Figure 2.3: Symmetric solution for $\beta = 2$. The vorticity field is depicted in the laboratory frame of reference (X, Y) (a-d) and in the non-inertial frame of reference (x, y) (e-h) for four equally-spaced instant of the unitary period. The initial time t_0 corresponds to the lowest vertical position of the foil.

Childress, and Zhang (2006), while back & forth solutions have been computed numerically in (Lu and Liao 2006; Alben and Shelley 2005; Deng and Caulfield 2018b). Self-propelled regimes presented in this section are thus not new but aim to establish the transition route for comparison with the linear Floquet stability analysis performed in the next section.

2.2.3.1 Self-propelled regimes for $\rho = 100$

A typical solution obtained for small values of the Stokes number is displayed for $\beta = 2$ in figure 2.3. The flow induced by the flapping foil inherits the spatial symmetry of the foil and the temporal symmetry of the imposed vertical motion (Elston, Sheridan, and Blackburn 2004). It satisfies the x-reflection spatial symmetry in the non-inertial frame of reference, i.e.

$$(u, v, p, \omega_z)(x, y, t) = (-u, v, p, -\omega_z)(-x, y, t), \tag{2.8}$$

and the spatio-temporal symmetry

$$(u, v, p, \omega_z)(x, y, t) = (u, -v, p, -\omega_z)(x, -y, t + T/2), \tag{2.9}$$

which is the combination of the y-reflection symmetry and the $T/2$ time-reciprocal translation. The vorticity ω_z, used to display the solution, in figure 2.3(a-d) and (e-h) respectively at the inertial and non-inertial frames of reference for four equally-spaced instants of the period T, is clearly an odd function of the x variable for every time instants. Physically, the spatial symmetry is seen by the vortices of equal shape but different sign shed one each side of the foil during its vertical motion. The spatio-temporal flow symmetry is observed by the inversion of the vorticity sign in opposite foil strokes. A direct consequence of the spatial flow symmetry

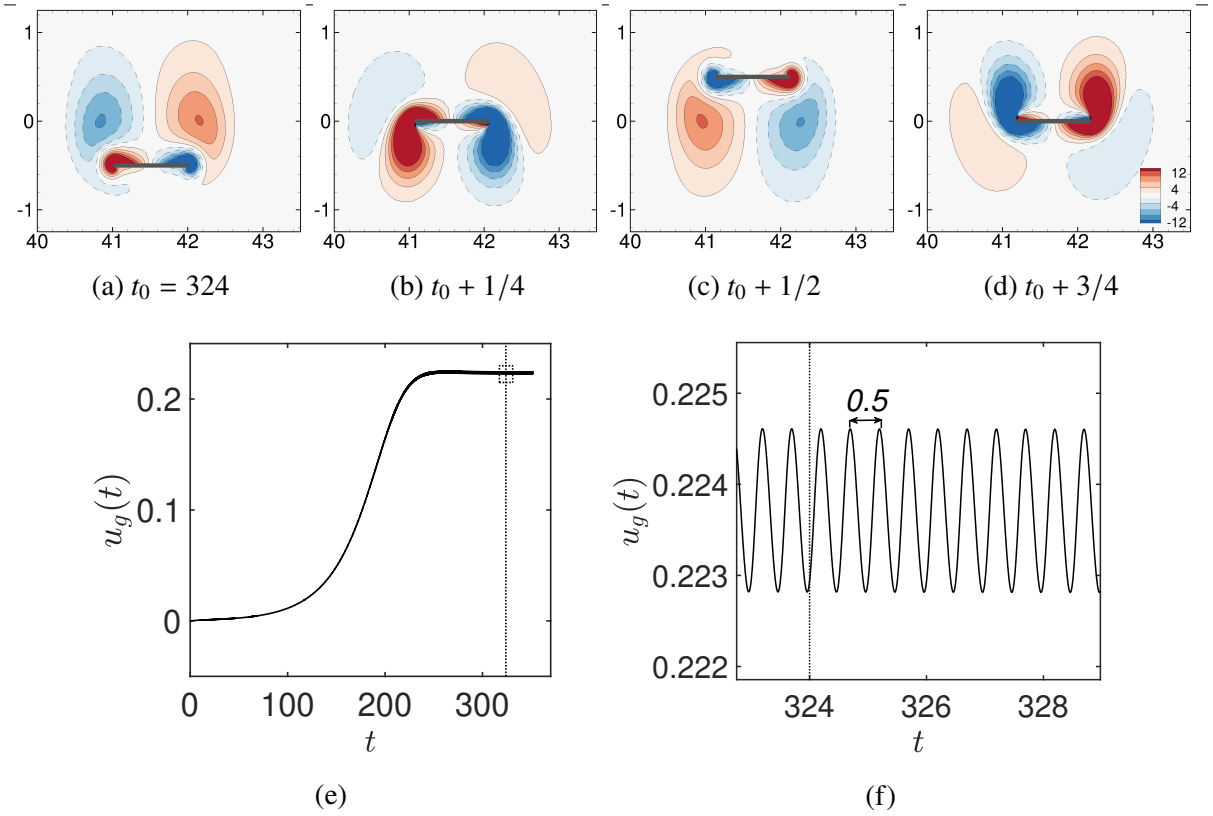

Figure 2.4: Unidirectional propulsive solution for $\beta = 6$: (a-d) Vorticity flow field along a flapping period. Time evolution of the horizontal velocity u_g (initially equal to zero) (e) over the whole simulated time and (f) restricted to time window indicated by the rectangle in (e). The instant t_0 is depicted with a vertical line in (e) and (f). The period of the horizontal velocity is 0.5, half the vertical flapping period 1.

is the absence of instantaneous hydrodynamic forces acting in the horizontal direction, i.e. $F_x(t) = 0$. Consequently, the foil is not accelerated in that direction and its velocity remains equal zero, hence the name of symmetric non-propulsive solution.

As the Stokes number (dimensional frequency) is increased, the flow breaks the spatial symmetry (2.8), as seen in figure 2.4(a-d) for $\beta = 6$. Vortices shed on each side of the foil are of slightly different shape and intensity for all time instants. This asymmetric flow then induces an instantaneous horizontal force accelerating the foil. Figure 2.4(e) shows that an initial small perturbation of the horizontal velocity u_g grows exponentially in time, before saturating for $t > 200$ towards a periodic state, as shown in the close-up view displayed in figure 2.4(f). The amplitude of oscillation of the horizontal velocity is very weak compared to its time-averaged value, denoted hereinafter $< u_g >$. Being positive, the flapping foil self-propels in the positive x-direction. Solutions self-propelling in the negative x-direction can also be found by modifying the initial horizontal velocity. The effect of the initial condition on the symmetry breaking direction was investigated in Jallas, Marquet, and Fabre (2017). The Fourier spectrum of the foil horizontal velocity, displayed in figure 2.5(a), shows that it oscillates at the (non-dimensional) frequency $f = 2$, i.e. twice the (non-dimensional) flapping frequency equal to $f = 1$ independently from the Stokes number. This doubling-frequency of the horizontal velocity is related to the spatio-temporal flow symmetry (Eq. 2.9). Over one flapping period,

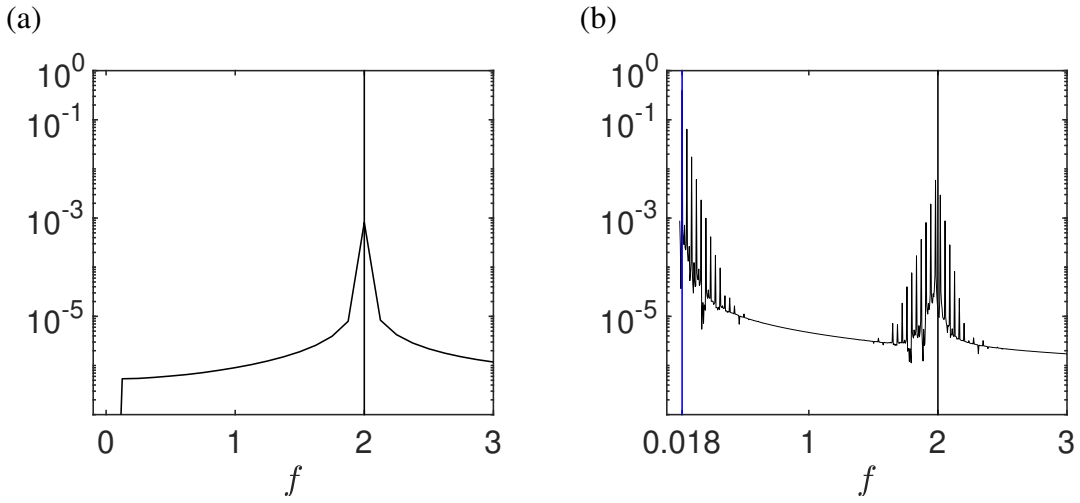

Figure 2.5: Frequency spectra of the horizontal foil speed for (a) the periodic unidirectional propulsive solution ($\beta = 6$) and (b) the quasi-periodic back & forth propulsive solution ($\beta = 13$). The fundamental frequency of the horizontal speed (vertical black lines) is twice the vertical flapping frequency. The low frequency of the quasi-periodic solution (figure 2.6-e) is identified by the blue line.

the horizontal force acting on the foil is identical during upward and downward strokes.

For higher values of the Stokes number, the spatial flow symmetry is still broken but the propulsion is no longer unidirectional. The foil periodically reverses its propulsive direction, as if a restoring force was at play. A typical solution obtained for $\beta = 13$ is displayed in figure 2.6. The time evolution of the horizontal velocity shown in 2.6(e) clearly indicates that, after an initial exponential growth in time, the foil velocity slowly oscillates between positive and negative values, over a period about 50 times larger than the flapping period. This solution is no longer periodic, but quasi-periodic, as clearly shown by the Fourier spectrum of the foil horizontal velocity displayed in figure 2.5(b). Two fundamental frequencies are obtained, one at $f = 2$ corresponding to twice the flapping frequency, and one around $f = 0.018$ corresponding to the slow period. The multiple peaks observed around each fundamental frequency are induced by non-linear interactions. Coming back to the horizontal velocity of the foil, its time-average over the long period is zero. Thus, this solution is not a coherent (unidirectional) propulsive state (Alben and Shelley 2005). The foil oscillates back & forth around a fixed point in space. Nevertheless, the horizontal velocity, time-averaged along the (short) flapping period, is either positive or negative, as seen in figure 2.6(f). A propulsive effect is thus obtained at this time-scale. The instantaneous vorticity fields displayed in figures 2.6 (a-d) correspond to a flapping period (marked with the green dot in figure 2.6-e) where the velocity of the foil is positive, while those shown in figure 2.6(g-j) correspond to a negative foil velocity (blue dot). In both cases, the leading-edge vortex is of smaller size and closer to the foil than the trailing-edge vortex. Interestingly, such vortex pattern is not observed for all phases of the long period, and in particular in the acceleration phases, marked with red dots in figure 2.6(e). The corresponding instantaneous vorticity fields are depicted in figure 2.7. In between the instants corresponding to figure 2.7(a) and (b), the foil accelerates and self-propels in the right direction

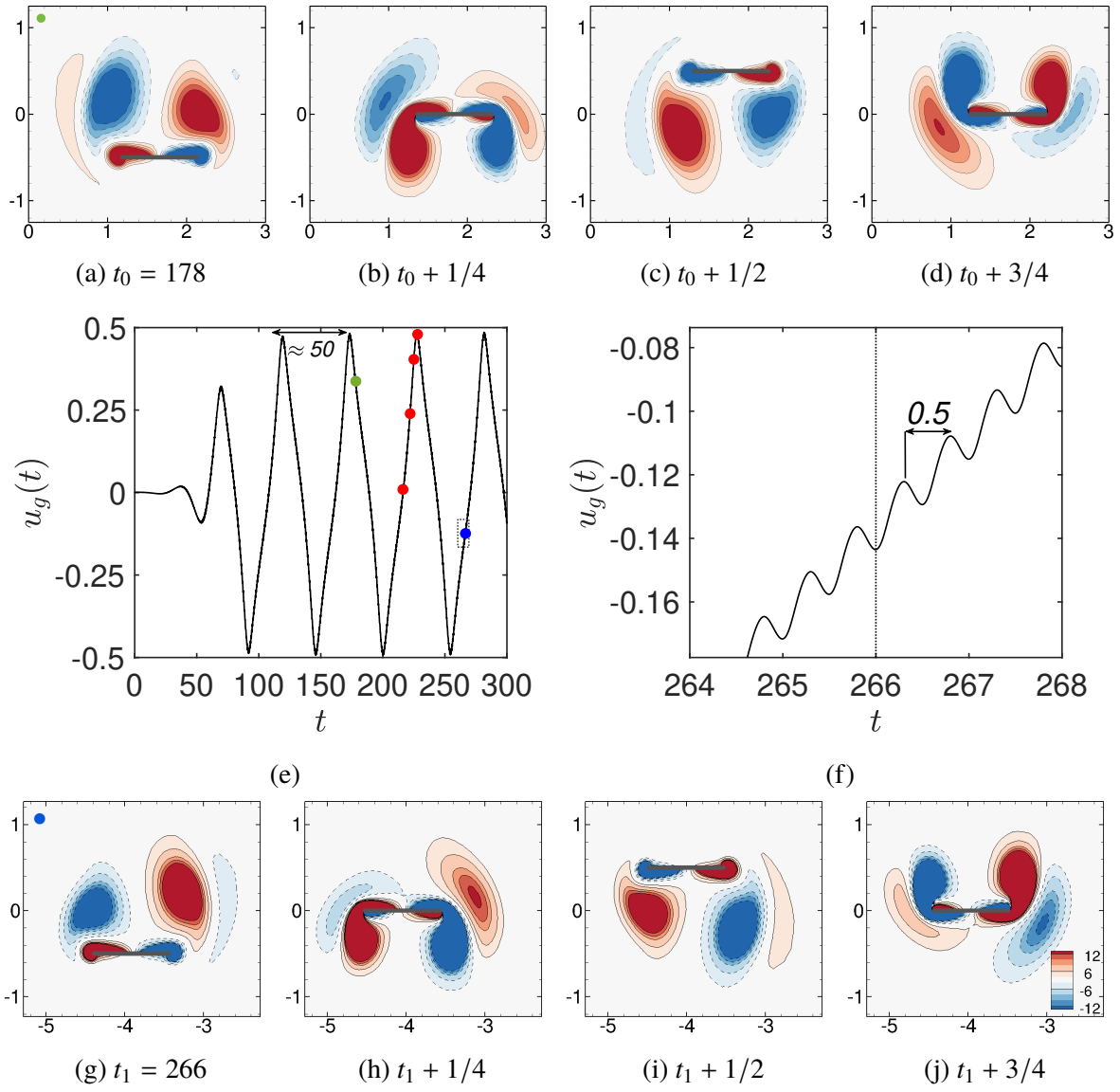

Figure 2.6: Back & Forth solution for $\beta = 13$: (a-d) and (g-j) Vorticity contours for a flapping period – starting from different time instants in (a) and (g). (e-f) Horizontal speed u_g time evolution with dotted rectangle close-up in (f). Instants (a) and (g) are indicated by filled green and blue dots in (e). Long and small periods of $u_g(t)$ are respectively indicated in (e) and (f).

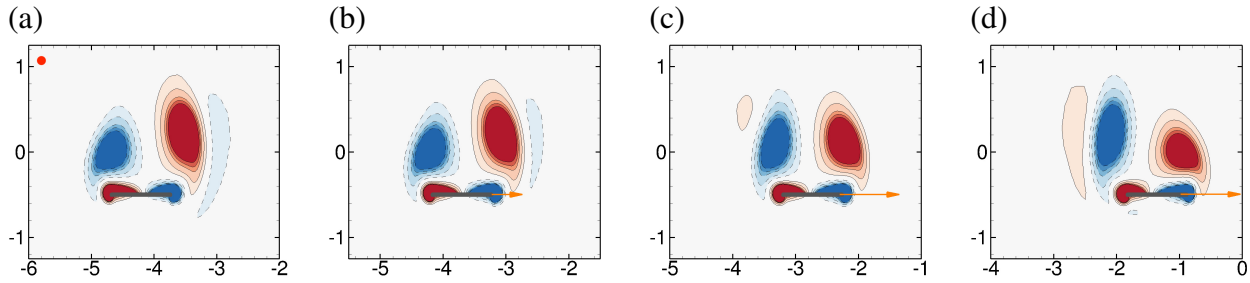

Figure 2.7: Back & Forth solution for $\beta = 13$: (a-d) Vorticity contours of the time instants represented in figure 2.6(e) by filled red dots. An orange arrow indicates the horizontal velocity of these time instants. These time instants are equally spaced of 3 flapping periods.

but the leading-edge vortex (right) is now of larger size and further away from the foil, compared to the trailing-edge vortex (left). This suggests that the foil motion is induced by a suction of the leading-edge vortex. As the foil further accelerates, the leading and trailing-edge vortices are progressively convected downstream until the more classical propulsive pattern is recovered when the foil reaches its maximal velocity (see figure 2.7-d).

The existence and characterization of the three propulsive solutions is displayed in figure 2.8 as a function of the Stokes number in the range $2 \leq \beta \leq 20$. The regimes of non-propulsive, propulsive and back & forth solutions are identified with white, red and grey background colors, respectively. The horizontal velocity is depicted in figure 2.8(a) and (c), with black dots for the time-averaged value $< u_g >$ and vertical bars for the fluctuation amplitude. For the back & forth solution, the long period is used for time-averaging. The frequencies f of the foil velocities are shown in figure 2.8(b) and (d), the open circles denoting the vertical flapping frequency, while the filled circles correspond to the frequency of the horizontal velocity. Symmetric non-propulsive solutions exist for small Stokes numbers $\beta < 4$ (region I) and for intermediate values in the range $9.53 \leq \beta \leq 11.25$ (region III). For these Stokes numbers, no locomotion is achieved and the foil remain in its position, producing a spatially symmetric periodic flow. Propulsive solutions appear for $\beta = 4$. They are characterized by non-zero time-averaged horizontal velocities — both negative and positive depending on initial conditions — with very small amplitudes of fluctuations ad a frequency of oscillation equal to $f = 2$. As the Stokes number is increased, this frequency remains constant while the (absolute value of) time-averaged propulsive velocity continuously increases until $\beta \sim 8.5$. The mean velocity then decreases and abruptly (discontinuously) falls to zero for $\beta = 9.58$. By decreasing again the Stokes number, we have identified a small range of Stokes number ($9.53 \leq \beta \leq 9.58$), visible in Figure 2.8(c), where non-propulsive and propulsive solutions co-exist. Therefore, the bifurcation from propulsive to non-propulsive solution is sub-critical around $\beta = 9.5$, unlike the transition from non-propulsive to propulsive solution at $\beta = 4$, which is super-critical. Finally, back & forth solutions are observed when increasing the Stokes number $\beta \geq 11.25$ (region IV). They are characterized by zero time-averaged horizontal speed with large amplitude of fluctuations. These quasi-periodic solutions are characterized by two fundamental frequencies, the high frequency (black dots) and the low-frequency (blue dots). As seen in figure 2.8(d), the low-frequency decreases towards zero when increasing the Stokes number.

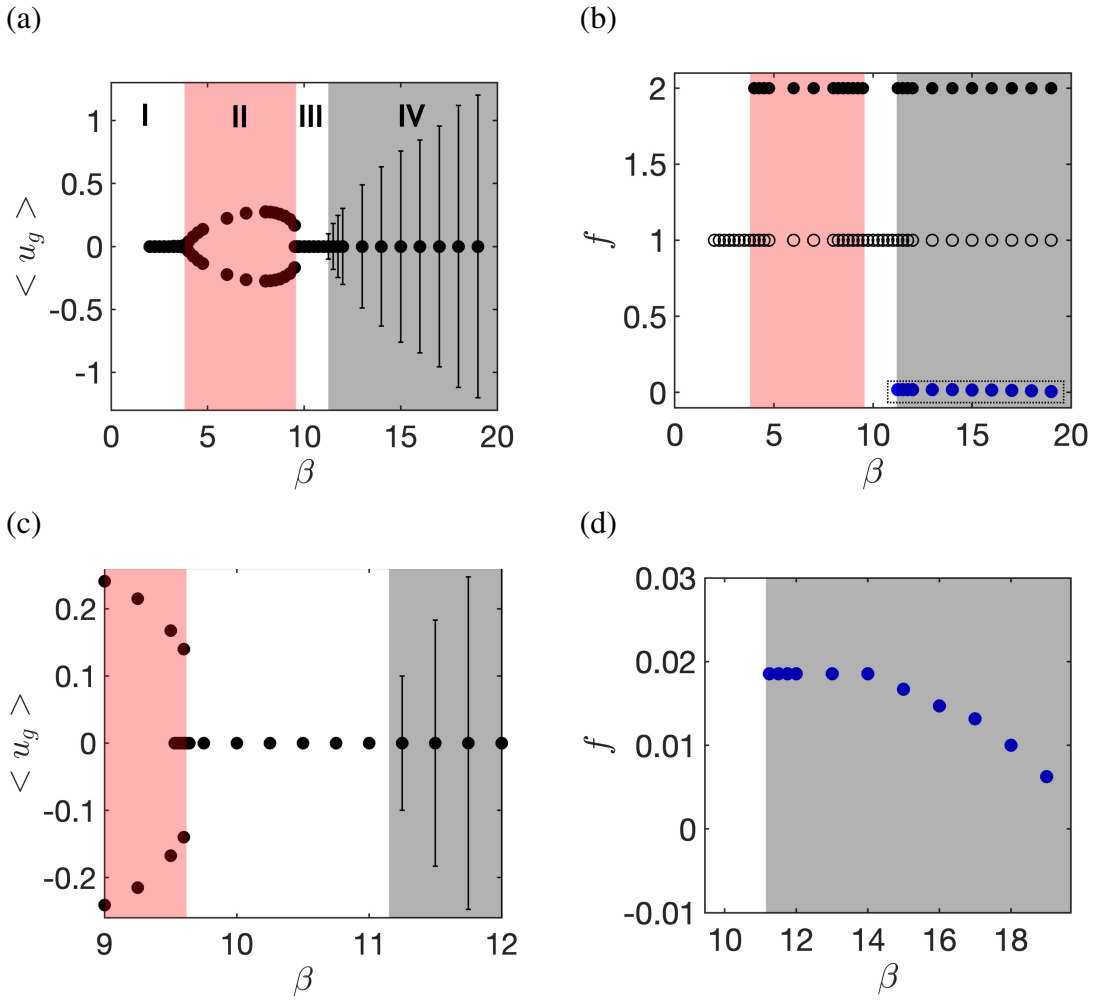

Figure 2.8: Non-propulsive (white), unidirectional propulsive (red) and back & forth (grey) regimes as a function of the Stokes number β. (a,c) Time-averaged (circles) and oscillation amplitude (error bars) of the foil horizontal velocity. (b,d) Forcing frequency of the foil vertical velocity (open circles) and frequency of the horizontal foil velocity (filled circles). (c) is a close-up view of (a) highlighting the transition between unidirectional propulsive, non-propulsive and back & forth solutions. (d) is a close-up view of (b) showing the evolution of the low-frequency in the back & forth solution as a function of the Stokes number. Parameters: $A = 0.5$ and $\rho = 100$.

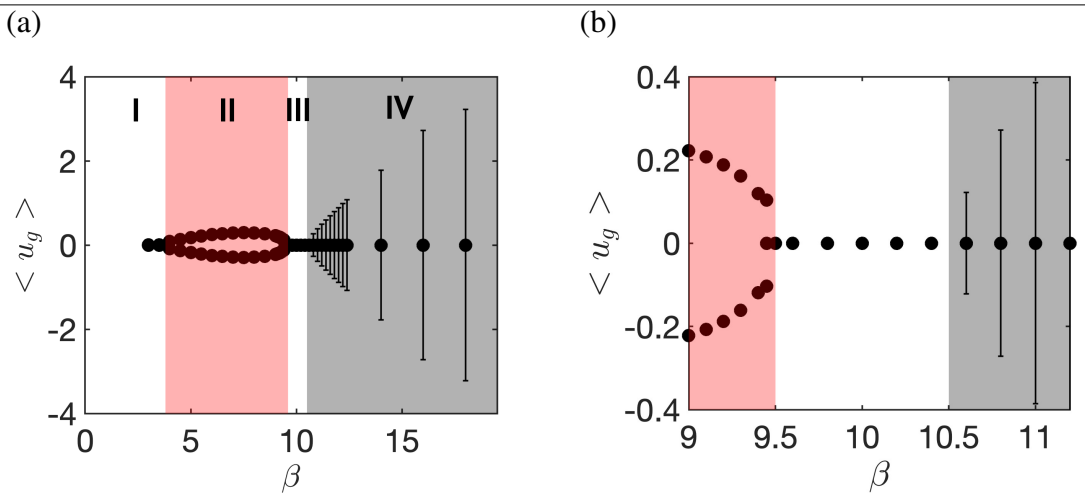

Figure 2.9: Self-propelled regimes for a density ratio $\rho = 1$. Background colors are the same as the previous figure. (a) Evolution of the time-averaged (circles) and amplitude (error bars) of the foil horizontal velocity with the Stokes number. (b) Close-up view highlighting the transition between the self-propelled regimes. Other control parameters: $A = 0.5$ and $h = 0.05$.

2.2.3.2 Self-propelled regimes for $\rho = 1$

Considering a density ratio closer to swimming organisms ($\rho = 1$), figure 2.9, the same self-propelled regimes and transitions are identified. In figure 2.9(a), as the previously presented case of $\rho = 100$, symmetric non-propulsive solutions become unidirectional propulsive ones for the critical Stokes number $\beta = 4$. The time-averaged velocity thus increase with an average value slightly slower than $\rho = 100$ up to $\beta \sim 8.5$, decreasing beyond this point and abruptly falling to zero for $\beta = 9.5$, a small change in the re-stabilization β of the previous density ratio. By decreasing the Stokes number, co-existing unidirectional propulsive and non-propulsive solutions were again obtained, this time for $9.42 \leq \beta \leq 9.5$, visible in figure 2.9(b). Back & forth solutions are finally observed for $\beta \geq 10.6$. These solutions are significantly encouraged for smaller density ratios. Beside the smaller critical Stokes number, they present now a velocity four times greater in amplitude than for $\rho = 100$. As presented by the two considered values of $\rho = 1$ and $\rho = 100$, the self-propelled regimes transition route appears to be robust to variations of the density ratio.

Self-propelled regimes and the transition route, for this Stokes number range, are also invariant with respect to the foil geometry. Simulations conducted for an elliptical foil of aspect ratio $h = 0.1$, reported in §2.7, have presented similar results and transition route as the ones described for the rectangular foil with rounded edges.

2.3 Fluid-solid stability analysis of non-propulsive periodic solutions

The emergence of the propulsive solutions identified in the previous section with nonlinear unsteady simulations is now investigated by analyzing the stability of non-propulsive periodic solutions. The Floquet stability analysis is introduced in §2.3.1 by considering a perturbation of the horizontal foil velocity, in addition to the flow perturbation. The numerical method is then explained in §2.3.3. Results of such stability analysis, that couples the fluid and solid perturbations, are presented in §2.3.4 for the density ratio $\rho = 100$. First the two synchronous and asynchronous modes found unstable are carefully described. Then these modes are discussed in light of the non-linear results previously described. Finally, the influence of the density ratio on the linear results is discussed in §2.3.5.

2.3.1 Fluid-solid Floquet stability analysis

The flow variables and the foil horizontal velocity are decomposed as

$$(\mathbf{u}, p, u_g) = (\mathbf{u}_b, p_b, 0) + \epsilon(\mathbf{u}', p', u_g'), \tag{2.10}$$

where $(\mathbf{u_b}, p_b)$ denote the periodic base flow fields. Since it satisfies the spatial symmetry (2.8) at every instant of the flapping period, the foil horizontal velocity of the periodic base solution is equal to zero. Infinitesimal perturbations ($\epsilon \ll 1$) are superimposed to the periodic base solution meaning that in addition to perturbing the base-flow field $(\mathbf{u}', p')$ as in Deng and Caulfield (2016), the foil horizontal velocity u_g' is perturbed. Note that no perturbation of the vertical velocity is considered since the flapping velocity $\mathbf{v}_g$ is imposed in the present analysis. By injecting the above decomposition into (2.3)-(2.6) and retaining the first-order term in ϵ, we obtain the following system of equations governing the linear dynamic around the non-propulsive periodic solution

$$\mathcal{B}\frac{\partial}{\partial t}\underbrace{\begin{bmatrix}\mathbf{u}'\\ p'\\ u_g'\end{bmatrix}}_{\mathbf{q}'} = \underbrace{\begin{bmatrix} -\left[(\mathbf{u}_b(t) - v_g(t)\mathbf{e}_y)\cdot\boldsymbol{\nabla}\right] - \boldsymbol{\nabla}\mathbf{u}_b(t) + \beta^{-1}\boldsymbol{\Delta} & -\boldsymbol{\nabla} & (\boldsymbol{\nabla}\mathbf{u}_b)\cdot\mathbf{e}_x \\ -\boldsymbol{\nabla} & 0 & 0 \\ (\rho S)^{-1}\mathcal{F}_v & (\rho S)^{-1}\mathcal{F}_p & 0 \end{bmatrix}}_{\mathcal{L}(\mathbf{u}_b, p_b)}\begin{bmatrix}\mathbf{u}'\\ p'\\ u_g'\end{bmatrix} \tag{2.11}$$

The first two rows are the linearized momentum and mass equations governing the fluid velocity and pressure perturbations. They are coupled to the foil velocity perturbation u_g' via two terms: firstly, the bulk term $(\boldsymbol{\nabla}\mathbf{u}_b)\cdot\mathbf{e}_x$ (block $(1,3)$ in the right-hand side matrix) that modifies the production of fluid perturbation in the momentum equation, and secondly, the boundary conditions at the foil surface Γ_w, where the equality of fluid and solid perturbations holds

$$(u', v')(\mathbf{x}_w, t) = (u_g', 0)\,. \tag{2.12}$$

The third row indicates that the horizontal acceleration of the foil is equal to the horizontal force exerted by the flow perturbation, which is here separated into viscous $\mathcal{F}_v$ and pressure $\mathcal{F}_p$ contributions, respectively defined as

$$\mathcal{F}_v(\mathbf{u}') = \beta^{-1}\int_{\Gamma_w}(\nabla\mathbf{u}' + \nabla\mathbf{u}'^T)\cdot\mathbf{n})\cdot\mathbf{e_x}\,\mathrm{d}\Gamma_w \quad , \quad \mathcal{F}_p(p') = \int_{\Gamma_w}(-p'\mathbf{n})\cdot\mathbf{e_x}\,\mathrm{d}\Gamma_w\,. \tag{2.13}$$

We note that, in (2.11), the viscous and pressure forces are weighted by the invert of the foil mass ρS . Consequently, when the ratio of solid to fluid density increases, the effect of the flow on foil perturbations decreases. In the limit of infinite density ratio, i.e. $\rho \to \infty$, it even vanishes leading to the following one-way coupled fluid-solid system

$$\mathcal{B}\,\frac{\partial}{\partial t}\begin{bmatrix}\mathbf{u}'\\ p'\\ u'_g\end{bmatrix} = \begin{bmatrix} -\left[(\mathbf{u}_b - v_g\mathbf{e}_y)\cdot\boldsymbol{\nabla}\right] - \boldsymbol{\nabla}\mathbf{u}_b + \beta^{-1}\boldsymbol{\Delta} & -\boldsymbol{\nabla} & (\boldsymbol{\nabla}\mathbf{u}_b)\cdot\mathbf{e}_x \\ -\boldsymbol{\nabla} & 0 & 0 \\ 0 & 0 & 0 \end{bmatrix}\begin{bmatrix}\mathbf{u}'\\ p'\\ u'_g\end{bmatrix} \tag{2.14}$$

In that limit case, the horizontal acceleration of the foil is zero, but not its horizontal velocity. This velocity might still affect the flow perturbation via the coupling terms described above. This one-way coupling analysis is thus different from the hydrodynamic Floquet analysis, performed for instance by Elston, Sheridan, and Blackburn (2004), Elston, Blackburn, and Sheridan (2006) on a forced oscillating cylinder and more recently applied by Deng et al. (2016) and Deng and Caulfield (2016) respectively on the forced oscillation of an ellipsoid and on the self-propulsion of different aspect ratio oscillating ellipses.

In the hydrodynamic Floquet analysis, the horizontal perturbation velocity is assumed to be zero ($u'_g = 0$). The perturbation equations (2.11) then simplify to

$$\mathcal{B}_f\,\frac{\partial}{\partial t}\begin{bmatrix}\mathbf{u}'_f\\ p'_f\end{bmatrix} = \begin{bmatrix} -\left[(\mathbf{u}_b - v_g\mathbf{e}_y)\cdot\boldsymbol{\nabla}\right] - \boldsymbol{\nabla}\mathbf{u}_b + \beta^{-1}\boldsymbol{\Delta} & -\boldsymbol{\nabla} \\ -\boldsymbol{\nabla} & 0 \end{bmatrix}\begin{bmatrix}\mathbf{u}'_f\\ p'_f\end{bmatrix} \tag{2.15}$$

where $\mathcal{B}_f$ is the portion of the operator $\mathcal{B}$ related to the fluid variable, and the subscript f is introduced to indicate that the perturbation is purely hydrodynamic. At the foil boundary, they satisfy the no-slip boundary condition

$$(u'_f, v'_f)(\mathbf{x}_w, t) = (0, 0)\,. \tag{2.16}$$

All the above equations are closed by considering that the fluid perturbations vanish $\mathbf{u}' = 0$ far away from the foil.

We would like to stress that the fluid-solid perturbation analysis encompasses the purely hydrodynamic perturbation analysis, since hydrodynamic perturbations should be retrieved in the fluid-solid analysis if the foil velocity perturbation is zero. This will be further discussed when presenting results in §2.3.5 in the limit case $\rho \to \infty$.

Following Elston, Sheridan, and Blackburn (2004) or Jallas, Marquet, and Fabre (2017), the perturbations are further decomposed in the form

$$\mathbf{q}'(\mathbf{x}, t) = \sum \left(\hat{\mathbf{q}}_j(\mathbf{x}, t)e^{\lambda_j t} + \text{c.c.}\right), \tag{2.17}$$

where $\hat{\mathbf{q}}_j$ are T-periodic functions, called the Floquet modes, associated to the complex numbers λ_j, called the Floquet exponents. The Floquet multiplier, defined as $\mu_j = e^{\lambda_j T}$, is rather used in the following. It represents the complex amplitude gain of the periodic Floquet mode over one period, i.e. $\hat{\mathbf{q}}_j(\mathbf{x}, T) = \mu_j\hat{\mathbf{q}}_j(\mathbf{x}, 0)$. The polar decomposition of the Floquet multiplier is $\mu_j = |\mu_j|e^{\mathrm{i}\phi_j}$, where the modulus $|\mu_j|$ quantifies the growth (or decay) of the corresponding

Floquet mode over the period, and ϕ_j represents its phase shift over the same period. The stability of the periodic base solution is then addressed by considering the Floquet multiplier with largest modulus. If its absolute value, denoted $|\mu_0|$, is greater than one, the corresponding Floquet mode will grow over one period and the periodic base solution is thus unstable. When the leading Floquet multiplier is real ($\phi_0 = 0$), the Floquet mode is *synchronous* as the perturbation evolves in time with the period of the base flow. When the leading Floquet multiplier is complex ($\phi_0 \neq 0$), the Floquet mode is *asynchronous* and a frequency, denoted f' in the following, related to the phase of the Floquet mode as $f' = \phi_0/(2\pi)$ is introduced.

2.3.2 Time-averaged analysis of fluid-solid Floquet modes

To better understand how the periodic flow perturbation is related to the destabilisation of a fluid-solid Floquet mode, we examine the equation

$$\lambda \hat{u}_g + \frac{d\hat{u}_g}{dt} = \frac{1}{\rho S} F_x(\hat{\mathbf{u}}, \hat{p}) \tag{2.18}$$

that expresses the instantaneous equilibrium between the horizontal force exerted by the flow component of the Floquet mode and the horizontal acceleration of the foil. The latter is composed of two terms, one related to the growth/decay of the mode, and one related to its instantaneous acceleration. Due to the periodicity of the Floquet mode, the latter disappears when time-averaging over a flapping period, yielding

$$\lambda \left\langle \hat{u}_g \right\rangle = \frac{1}{\rho S} \left\langle \hat{F}_x \right\rangle \tag{2.19}$$

where $\langle \cdot \rangle$ denotes the time-average over a flapping period.
For synchronous modes, the Floquet exponent and mode are real variables and the above expression gets

$$\lambda_r = \frac{1}{\rho S} \frac{\left\langle \hat{F}_x \right\rangle}{\left\langle \hat{u}_g \right\rangle} \,. \tag{2.20}$$

The growth rate of the Floquet mode is thus proportional to the ratio between the mean component of the force and the mean velocity of the Floquet mode. The Floquet mode is thus unstable (res. stable) when the force and velocity are of same (different) sign. In the case of asynchronous modes, we introduce the polar decomposition of the time-averaged horizontal force and velocity in (2.19) to obtain the simple relation

$$\lambda = \frac{1}{\rho S} \frac{\left| \left\langle \hat{F}_x \right\rangle \right|}{\left| \left\langle \hat{u}_g \right\rangle \right|} e^{\mathrm{i}\psi} \tag{2.21}$$

showing that the growth rate (real part) is now also related to the phase difference ψ between the time-averaged force and velocity, and not only to their ratio. The relations (2.20) and (2.21) will be used in §2.3.4 for a physical discussion of the Floquet mode

2.3.3 Numerical method

The periodic non-propulsive solutions ($\mathbf{u_b}$, p_b) are computed by integrating in time the governing equations (2.3),(2.4) using the same temporal and spatial discretization scheme as described in

the previous section, but with the following boundary conditions

$$(u_b, v_b)(x_w, y_w, t) = (0, 2\pi A sin(2\pi t)) \quad (2.22)$$

$$(u_b, \partial_x v_b)(0, y, t) = (0, 0) \quad (2.23)$$

The first set of boundary condition, applied at any point (x_w, y_w) of the foil surface, allows imposing the flapping motion of the foil in the vertical direction without any motion in the horizontal direction. The second set of boundary condition, applied on the $y-$ axis, is used to enforce the spatial reflection symmetry of the flow characteristic of the non-propulsive solution. Typically, 50 flapping periods are simulated to reach a periodic solution. Note that, for computational efficiency, the computational domain can be reduced to the left or right part of the full domain shown in figure 2.2, but this is not mandatory. In that case, the periodic base solution on the full domain is retrieved by using the spatial symmetry relation (2.8).

The strategy to compute Floquet modes is the one proposed by Barkley and Henderson (1996). The stability of an initial perturbation is assessed regarding the action of the propagator over one period $\mathbf{\Phi}$, also known as Monodromy matrix. The action of this Monodromy matrix over the perturbation at an arbitrary initial time t_0 is formally denoted $\mathbf{q}'(\mathbf{x}, t_0 + T) = \mathbf{\Phi}\,\mathbf{q}'(\mathbf{x}, t_0)$. It is actually obtained by time-integration along a period of the linearized equations (2.11) with boundary conditions (2.12), using the temporal and numerical discretization schemes previously described. An Arnoldi method with a modified Gram-Schmidt algorithm for the orthogonalization step (Saad 2011) is implemented in the FreeFEM software (Hecht 2012) to approximate the Monodromy matrix in a low-dimensional space. The eigenvalues of this reduced matrix approximate the Floquet multiplier and its eigenvectors allow reconstructing the Floquet modes at the initial time, i.e. $\hat{\mathbf{q}}(\mathbf{x}, t_0)$. A minimal number of 30 Arnoldi vectors is used in the following, this number being further increased in steps of 10 when necessary in order for the dominant eigenvalue to converge to five significant digits. All computed modes are normalised by the kinetic energy of the coupled fluid-solid system. A validation of this method is detailed in Appendix 2.6.

Finally, as the Arnoldi method gives access to the Floquet mode at an initial time, the mode complete temporal evolution is obtained through time-integration of the following equation over one flapping period,

$$\mathcal{B}\,\frac{\partial \hat{\mathbf{q}}}{\partial t} - \mathcal{L}(\mathbf{u}_b, v_g)\,\hat{\mathbf{q}} = -\lambda\,\mathcal{B}\,\hat{\mathbf{q}}, \quad (2.24)$$

using as initial condition the Floquet mode obtained with the Arnoldi algorithm. The Floquet exponent λ being known, the right-hand side term appropriately counteracts the temporal growth (resp. decay) of the unstable (resp. stable) Floquet mode.

2.3.4 Results of Floquet analyses for $\rho = 100$

The stability analysis of non-propulsive periodic solutions has been performed for the flapping amplitude $A = 0.5$ and Stokes numbers in the range $1 \leq \beta \leq 20$. The instantaneous vorticity fields of a typical base non-propulsive solution, obtained for $\beta = 13$, are depicted in figure 2.10 at four instants in the flapping period. The spatial left-right symmetry (2.8) along the y-axis is clearly satisfied at every instant of the flapping period. By comparing the dipolar structure at time $t_0 + 1/2$ and t_0, this solution also satisfies the spatio-temporal symmetry (2.9).

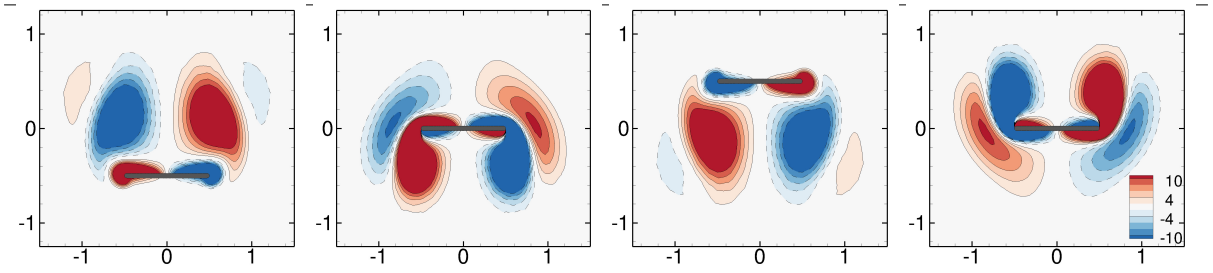

(a) t_0 (b) $t_0 + 1/4$ (c) $t_0 + 1/2$ (d) $t_0 + 3/4$

Figure 2.10: Non-propulsive solution obtained for $A = 0.5$ and $\beta = 13$. The instantaneous vorticity field is depicted at four instants of the (unitary) flapping period.

2.3.4.1 Floquet multipliers: fluid-solid versus hydrodynamic analysis

Results of the fluid-solid Floquet analysis performed for the density ratio $\rho = 100$ are first depicted in figure 2.11, with the modulus and frequency of the leading Floquet multipliers as a function of β in figures 2.11(a) and 2.11(b), respectively. We can clearly identify two ranges of Stokes number where the leading Floquet modes get unstable ($|\mu_0| > 1$) and they compare very well with regions II and IV, where unidirectional and back & forth self-propelled solutions were obtained in the nonlinear unsteady simulations.

In the range $4.00 \leq \beta \leq 9.53$, the unstable Floquet modes are synchronous ($f' = 0$). Thus, the perturbation does not break the periodicity of the base solution, in agreement with the unidirectional propulsive solution observed in region II. The frequency $f = 2$ characterizing the horizontal speed of this propulsive solution (see figure 2.8-b) is rather related to the spatio-temporal symmetry of the Floquet mode, as will be seen in §2.3.4.2. A quantitative comparison of the thresholds is provided in table 2.1. The destabilisation of the synchronous mode at $\beta = 4$ is in perfect agreement with the emergence of the unidirectional propulsive solution, i.e. the transition between region I and II. On the other hand, the threshold value $\beta = 9.53$ corresponding to the stabilization of this mode is slightly different from the threshold $\beta = 9.58$ above which the unidirectional propulsive solution disappears (transition from II to III). This is due to the sub-critical nature of the bifurcation at this threshold, clearly seen in figure 2.8(c). But the threshold value $\beta = 9.53$ found with the linear stability corresponds perfectly to the disappearance of the symmetric solution when decreasing the Stokes number (transition from III to II).

When further increasing the Stokes number $\beta \geq 11.25$, an asynchronous Floquet mode gets unstable, with a very low frequency ($f' \sim 0.01$) compared to the flapping frequency ($f = 1$). The destabilization of this asynchronous mode occurs at the same value of the Stokes number for which the back & forth solution appears. The frequency of the asynchronous mode is compared to the frequency of this solution in figure 2.11(b). They compare very well at the threshold $\beta = 11.25$, but when the Stokes number is increased, the agreement gets worse. Opposite trends are observed, with an increase of the Floquet mode frequency and a decrease of the back & forth frequency. The flow nonlinearities, i.e. which can be mean-flow distortion or higher-harmonics generation/interaction, clearly play a role in the frequency selection of this back & forth solutions. Note that such discrepancy between the linear and nonlinear frequency has been observed for the unsteady wake of a fixed cylinder flow, and is predominantly due to

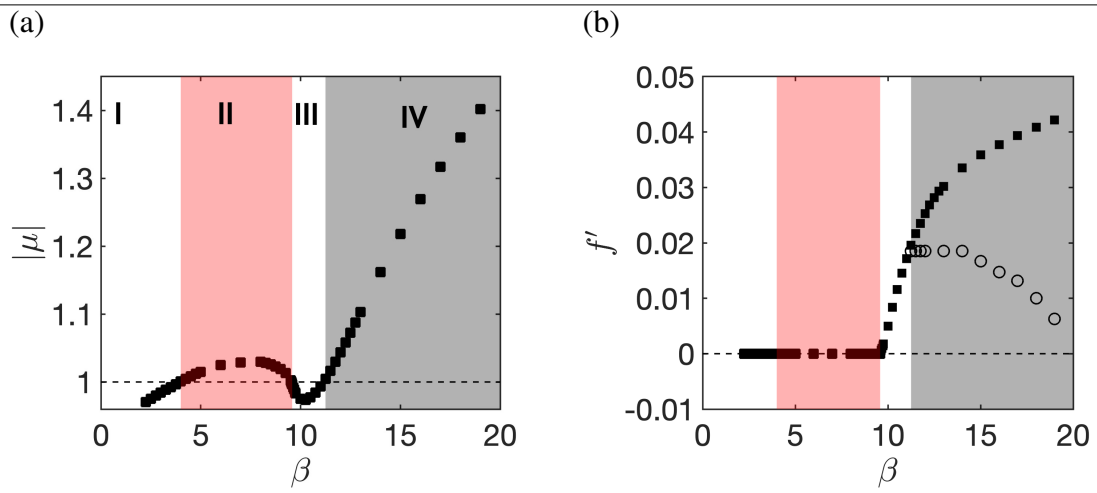

Figure 2.11: Fluid-solid Floquet analysis for $\rho = 100$. (a) Absolute value and (b) frequency of the dominant Floquet multiplier (black circles) as a function of the Stokes number β. The latin numbers indicate regimes of non-linear solution identified in §2.2, the red region corresponding to unidirectional self-propelled solutions, while the grey regions correspond to back & forth self-propelled solutions. In (b), the open circles indicate the low-frequencies characteristic of the Back & Forth solutions.

mean-flow distortion in that case (Barkley 2006; Sipp and Lebedev 2007).

Before examining the unstable synchronous and asynchronous Floquet modes, we describe results of the purely-hydrodynamic Floquet analysis, performed in the same range of Stokes number and displayed in figure 2.12 with black squares. First, we note that no unstable mode is found in the range of Stokes number corresponding to the region II. So, the purely-hydrodynamic Floquet analysis cannot explain the emergence of the unidirectional propulsive solution. One unstable Floquet mode is found only for larger Stokes number $\beta \geq 12.20$. Just above the threshold, this mode is asynchronous, but when the Stokes number is increased to $\beta = 13.3$, the pair of complex asynchronous modes collapses on the real axis becoming two real synchronous modes. One of these modes is further destabilized when increasing β, while the other one is stabilized for $\beta > 15$. The spatial structure of the unstable asynchronous modes found with the hydrodynamic stability analysis are very similar to the asynchronous mode obtained with the fluid-solid analysis, that are described in §2.3.4.3, and thus will not be further described. Their frequency is much smaller, as displayed in figure 2.12(b), failing to predict the frequency of the back & forth solution even at the threshold. As indicated in table 2.1, this threshold is under-predicted by the purely-hydrodynamic analysis. Unlike the fluid-solid Floquet analysis, the purely-hydrodynamic Floquet analysis in one hand cannot explain the emergence of the unidirectional propulsive solutions, and on the other hand does not accurately predict the occurrence of the back & forth solutions. These two observations offer a possible explanation to observations made by Deng and Caulfield (2016) when comparing the results of unsteady nonlinear simulations and a purely-hydrodynamic stability analysis. In their study, the purely-hydrodynamic analysis did not estimate the enhancement (earlier transition) of the quasi-periodic nonlinear solutions for ellipses of aspect-ratio $h = 0.5$ and did not predict the

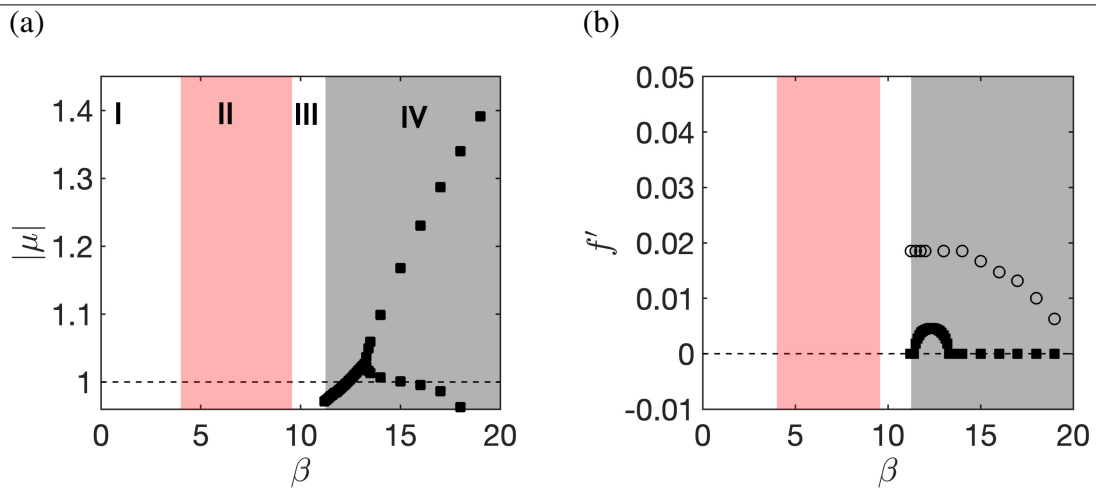

Figure 2.12: Hydrodynamic Floquet analysis. Same legend as in previous figure.

Transition between regimes	I – II	II – III	III – IV
Fluid-solid stability analysis ($\rho = 100$)	4.00	9.53	11.25
Purely-hydrodynamic stability analysis	×	×	12.20
Nonlinear simulations	4.00	9.53 and 9.58	11.25

Table 2.1: Critical thresholds obtained with the unsteady nonlinear simulations and the stability analyses. × indicates that no unstable modes were obtained.

unidirectional propulsion threshold for ellipses of aspect-ratio $h = 0.1$. Visibly, the onset of self-propulsion cannot be explained by the flow symmetry breaking instability alone and the self-propelled fluid-solid coupling is vital for its prediction.

2.3.4.2 Synchronous Floquet modes: emergence of unidirectional propulsion

Turning back to results of the fluid-solid Floquet analysis, the synchronous Floquet mode is depicted in figure 2.13 for $\beta = 6$. The vorticity field of this periodic mode is displayed with colored map at four instants of the flapping period in figure 2.13(a-d), and the vorticity of the periodic base flow is superimposed using black (dashed) isolines for positive (negative) values. First we note that the synchronous Floquet mode breaks the left-right symmetry (2.8) of the base flow, since the perturbative vorticity is an even function of x while the base vorticity is an odd function of x. But, as the base flow, it still satisfies the spatio-temporal symmetry (2.9), so that we can restrict our description of the mode to the up-stroke phase $0 \leq t \leq 1/2$. During the acceleration phase of this up-stroke motion ($t < 1/4$), a patch of positive vorticity exists above the foil, in a region where the vorticity of the base flow is weak, since the latter is rather generated under the foil during the upstroke. This patch of vorticity corresponds to a shear region in the flow perturbation, that induces an increase in the horizontal forces exerted on the foil, as seen in figure 2.13(f). During the second-half of the up-stroke ($1/4 < t < 1/2$) where the vertical velocity of the foil decreases, the patch of positive vorticity also decreases in size and amplitude. Meanwhile, a patch of negative vorticity appears under the foil, leading

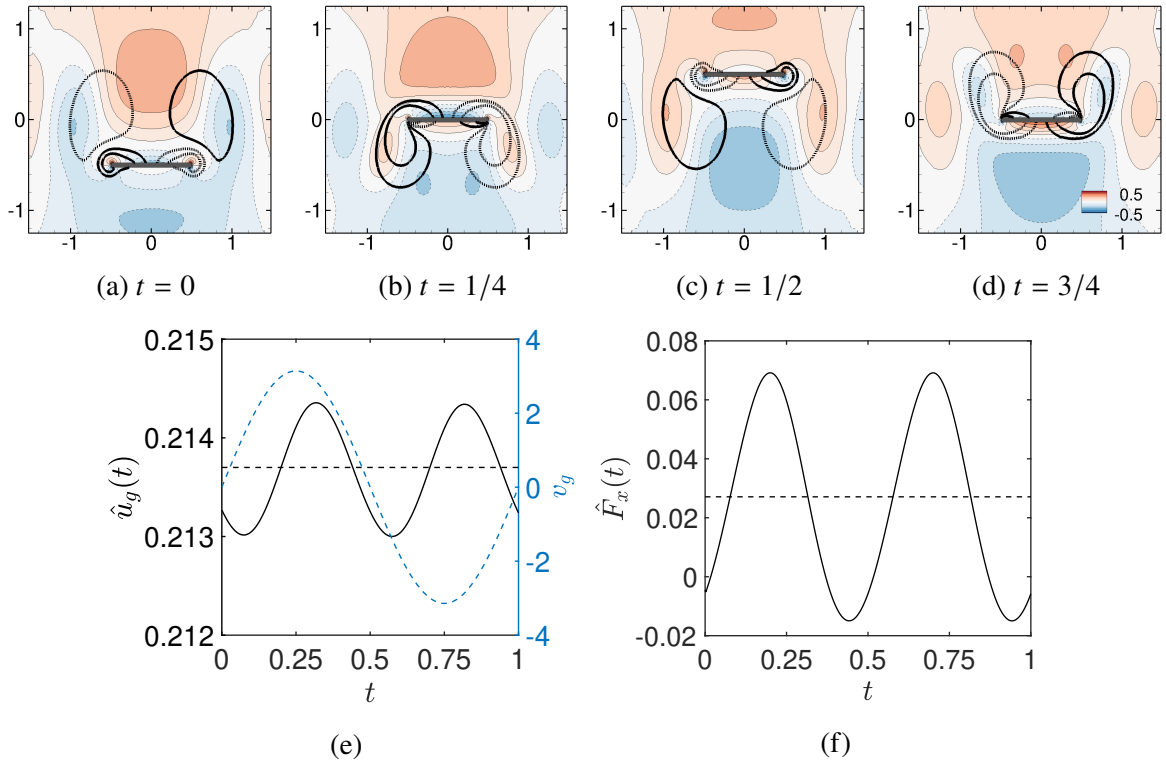

(a) $t = 0$ (b) $t = 1/4$ (c) $t = 1/2$ (d) $t = 3/4$

(e) (f)

Figure 2.13: Unstable synchronous Floquet mode for $\beta = 6$: (a-d) Vorticity contours for a flapping period (base flow positive (resp. negative) values represented by solid (resp. dashed) lines). (e) Foil horizontal speed and (f) force. Time-averaged value along a flapping period of both values is represented by a dashed line in (e,f). In (e) the vertical speed v_g of the base-flow (light blue dashed line) is represented in the right axis.

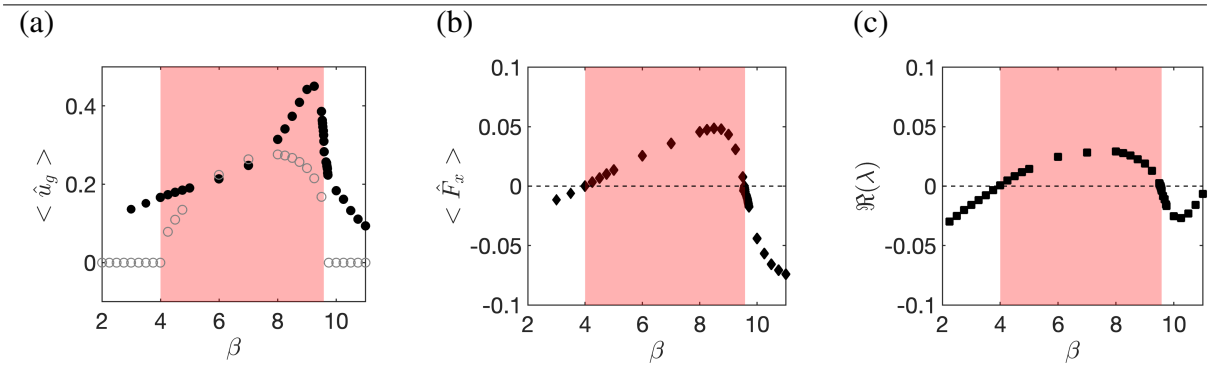

Figure 2.14: Time-averaged horizontal (a) velocity and (b) force for the synchronous Floquet mode as a function of β. (c) Real part of the Floquet exponent. In (a) the mean horizontal speed obtained with nonlinear simulations is represented with empty grey circles for comparison.

to a decrease of the horizontal force. This oscillation of the horizontal force results in an out-of-phase oscillation of the horizontal velocity, shown in figure 2.13(e). Interestingly, the average of the horizontal force and velocity over a flapping period (indicated with dashed line in figures) are non-zero and positive here. Therefore, this synchronous Floquet mode is clearly at the origin of the propulsion of the foil in the horizontal direction. Note that the direction of propulsion is not determined by the Floquet mode, since its amplitude is arbitrarily positive (here) or negative, leading to a right (here) or left displacement of the foil.

To stress again the role of the fluid-solid coupling in the destabilization of the mode, we consider the time-averaged analysis of the Floquet mode exposed in §2.3.2. For synchronous modes, it was shown that their growth rate is given by

$$\lambda_r = \frac{1}{\rho S} \frac{\langle \hat{F}_x \rangle}{\langle \hat{u}_g \rangle},$$

i.e. the ratio between the time-averaged horizontal force and velocity, weighted by the foil mass. These quantities are plotted in figure 2.14 as a function of β. The time-averaged horizontal velocity, shown with black circles in (a), is positive for all values of the Stokes number. We note that its evolution is different from the time-averaged velocity of the foil computed with temporal simulation (open circles), indicating the importance of flow nonlinearities in the terminal foil velocity. Examining now the horizontal force in figure 2.14(b), its changes of sign correspond clearly to the destabilization and stabilization of the Floquet mode (c). When this force is positive (resp. negative), the growth rate is also positive (resp. negative), in agreement with the above relation (recalling that the horizontal velocity is always positive). Finally, we conclude that this synchronous Floquet mode is responsible for the emergence of the unidirectional propulsion solution obtained in the region II, delimited in red in the figure. Retaining the fluid-solid coupling at the perturbation level is fundamental to explain the destabilization of this mode.

2.3.4.3 Asynchronous Floquet modes: emergence of back & forth solution

We now examine the asynchronous Floquet modes that gets unstable for larger Stokes number. The complex mode, obtained at $\beta = 13$ and displayed in figure 2.15, also breaks the left-right

symmetry and satisfies the spatio-temporal symmetry (2.9). The instantaneous real (resp. imaginary) part of the vorticity is shown in figures (a-d) (resp. e-h) at four instants of the flapping period. The amplitude of the real part is noticeably larger than that of the imaginary part, and their spatial structures are quite different. The real part of the mode bears similarities with the synchronous Floquet mode found by Jallas, Marquet, and Fabre (2017) to explain the deviation of propulsive wakes in flapping wings and the displacement modes of vortices (Fabre, Sipp, and Jacquin 2006; Brion, Sipp, and Jacquin 2014). Let us consider the right solid dark line representing the base flow vortex of positive vorticity in figure 2.15(a). The perturbation has positive vorticity on the lower left and negative vorticity on the upper right part of the monopole. This superposition strengthens the lower left part of the monopole while weakening the upper right one, resulting in a net displacement of its center to the lower left. The displacement of the dipolar vortex structure results in an horizontal force exerted on the foil whose temporal evolution is shown in figure 2.15 (k). Due to the spatio-temporal flow symmetry, the frequency is twice the flapping frequency. Interestingly, the horizontal force strongly oscillates around a negative time-averaged value. Compared to the oscillation of the foil horizontal velocity displayed in figure 2.15(i), we first note that they are not in phase. As explained later, this phase difference is crucial to understand the destabilization of the asynchronous mode. Then, we also remark that the fluctuation of the horizontal velocity is much smaller and around a time-averaged value that is positive. Therefore, the real part of the asynchronous mode produces a mean resistive force over the flapping period, that decreases the foil horizontal velocity.

Turning now to the imaginary part of the asynchronous mode depicted in figure 2.15(e-h), its spatial structure is of much smaller amplitude than for the real part. It looks like a combination between the synchronous mode (see figure 2.13), responsible for the unidirectional self-propulsion of the foil, and the real part of the asynchronous mode, which creates a mean resistive force during a flapping period. The temporal evolution of the foil velocity and horizontal force are displayed in figure 2.15(j) and (l), respectively. The fluctuation of the force (l) is now much smaller than for the real part (k). The real and imaginary horizontal forces are out-of-phase by $1/4$. During the upstroke of the foil ($t < 0.5$), the minimal and maximal values of the imaginary horizontal force are obtained at $t = 1/2$ and $t = 1/4$, respectively, while they are obtained at $t = 1/8$ and $t = 3/8$ for the real part. Interestingly, the time-averaged value of the imaginary part is now positive, as for the horizontal velocity (j). Therefore, the imaginary part of this asynchronous mode produces a mean propulsive force that increases the foil velocity.

To further understand the contrasting actions of the real and imaginary parts of the Floquet mode, we introduce the real *quasi-periodic* perturbation defined as $\tilde{\mathbf{q}} = \mathbf{q}' e^{-\lambda_r t}$. Compared to the real perturbation $\mathbf{q}'$, the exponential growth/decay given by the real part of the Floquet exponent is counteracted. The perturbation $\tilde{\mathbf{q}}$ is quasi-periodic as it retains the low-frequency oscillation given by the imaginary part of the Floquet exponent, in addition to the high-frequency flapping period. Using the Floquet decomposition (3.19), the temporal evolution of this quasi-periodic perturbation is simply given by

$$\tilde{\mathbf{q}}(\mathbf{x}, t, t_\epsilon) = \Re(\hat{\mathbf{q}})(\mathbf{x}, t)\cos(2\pi t_\epsilon) - \Im(\hat{\mathbf{q}})(\mathbf{x}, t)\sin(2\pi t_\epsilon), \tag{2.25}$$

where $t_\epsilon = f' t$ is a slow time-scale, as the frequency of the Floquet mode is very small compared to the flapping frequency, i.e. $f' \ll 1$. For $t_\epsilon \sim 0$, the above expression shows that the quasi-periodic perturbation is dominated by the real part of the periodic Floquet mode $\Re(\hat{\mathbf{q}})(\mathbf{x}, t)$, while

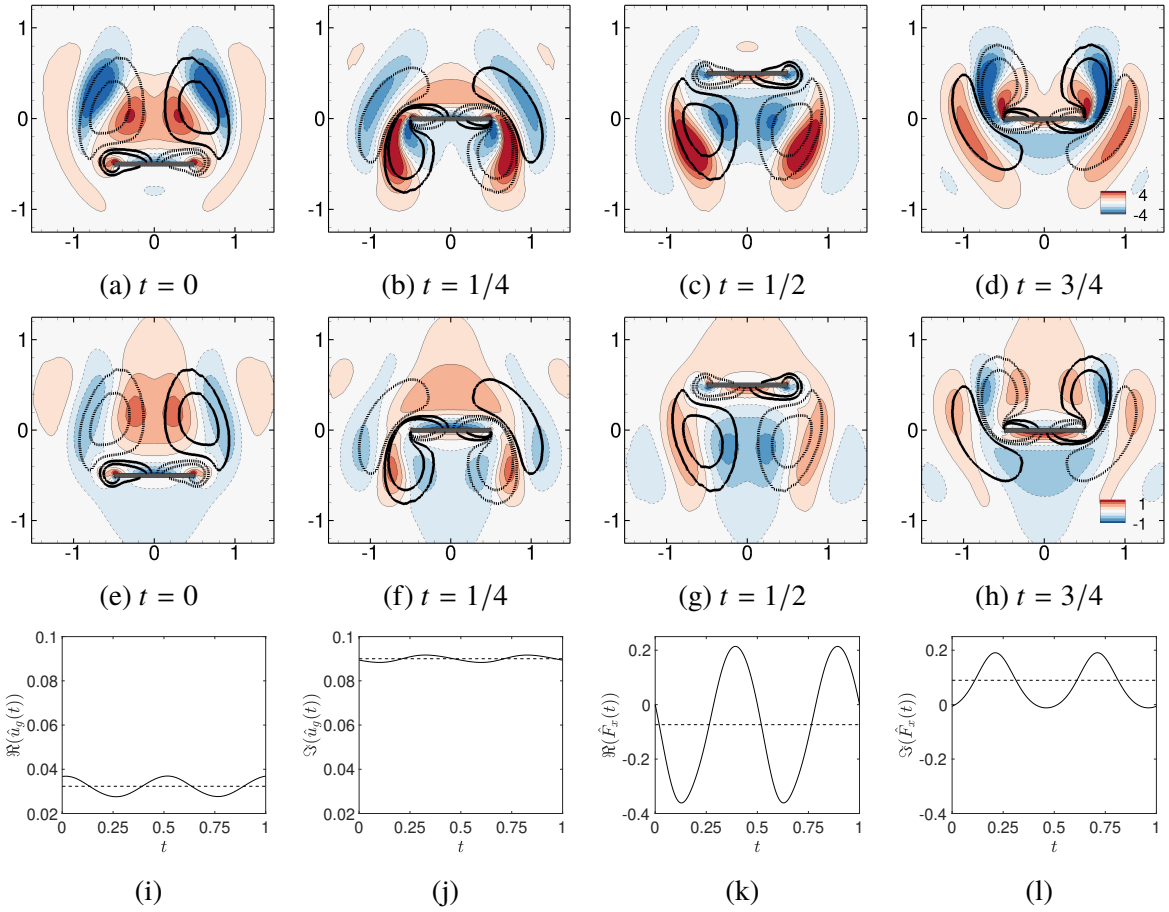

Figure 2.15: Unstable asynchronous Floquet mode for $\beta = 13$. Vorticity contours of the (a-d) real and (e-h) imaginary parts of the mode at four instants of the flapping period. Positive and negative values of the base-flow vorticity are depicted with solid and dashed contours. (i-j) Real and imaginary parts of the horizontal velocity $\hat{u}_g$. (k-l) Real and imaginary part of the horizontal force $\hat{F}_x$. In (i-l), dashed lines represents the time-averaged value of the plotted quantity.

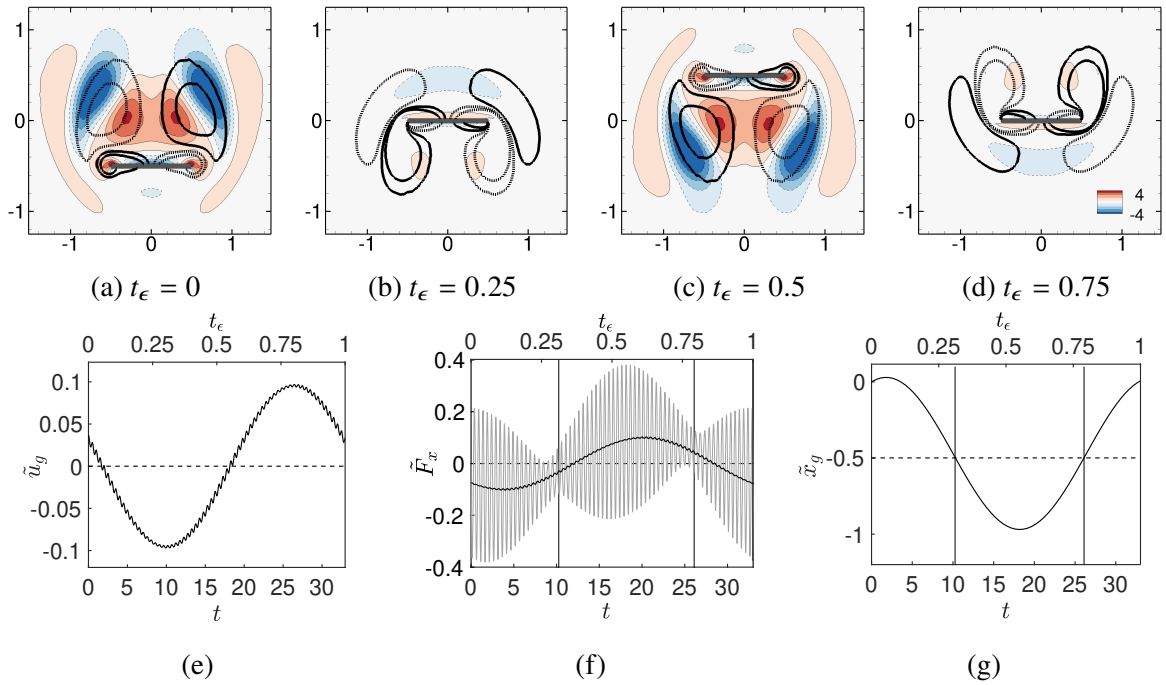

(a) $t_\epsilon = 0$ (b) $t_\epsilon = 0.25$ (c) $t_\epsilon = 0.5$ (d) $t_\epsilon = 0.75$

(e) (f) (g)

Figure 2.16: Temporal evolution of the quasi-periodic perturbation $\tilde{\mathbf{q}}$ for $\beta = 13$. (a-d) Vorticity of the perturbation (colors) and base flow (black lines) at four instants t_ϵ of the slow period $T_\epsilon = 1/f' = 33$. (e-g) Time evolution of the horizontal (e) velocity , (f) force and (g) position of the foil over the slow period, shown as a function of both time t and t_ϵ. The horizontal dashed lines are for the time-averaged value of the plotted quantity over the slow time period. In (f), the thick curve depicts the time-averaged value of the horizontal force over the flapping period. The vertical solid lines in (f-g) indicate the instants where the foil pass by its mean horizontal position.

for $t_\epsilon \sim 1/4$, it is dominated by its imaginary part $\Im(\hat{\mathbf{q}})(\mathbf{x}, t)$. The quasi-periodic perturbation thus slowly evolves between the real and imaginary parts of the Floquet mode, on a time scale given by the low frequency of this asynchronous Floquet mode. This slow evolution is depicted in figure 2.16 for the unstable asynchronous mode at $\beta = 13$. The contrasting actions of the real and imaginary parts of the Floquet mode are clearly visible in figures 2.16(a-d), that show the vorticity fields at four instants of the slow period. As expected from (2.25), the quasi-periodic perturbation is similar to the real part of the Floquet mode at time $t_\epsilon = 0$ (compare figures 2.15-a and 2.16-a) or to its opposite at time $t_\epsilon = 0.5$, while it is of much smaller amplitude and similar to the imaginary part of the Floquet mode at time $t_\epsilon = 0.25$ and $t_\epsilon = 0.75$. Let us now examine the quasi-periodic evolution of the horizontal force exerted on the foil displayed in figure 2.16(f), as well as the resulting foil speed and displacement shown in figures 2.16(e) and and (g), respectively. Around the slow time $t_\epsilon = 0$, the horizontal force time-averaged over the fast flapping period (thick line in f) is negative and opposite to the positive horizontal velocity (e). So the quasi-perturbation, shown in (a) and dominated by the real part of the Floquet mode, creates a resistive force. When it slowly evolves towards $t_\epsilon = 0.25$, the horizontal force remains negative but it is then a propulsive force since the foil velocity is negative. For $t_\epsilon > 0.32$, the horizontal force gets positive and is a resistive force to its horizontal motion until the sign of the foil velocity changes around $t_\epsilon = 0.6$. This slow oscillation of the time-averaged force and velocity creates a back and forth displacement of the foil depicted in 2.16(g) around a mean position value around $\tilde{x}_g = 0.5$. Although this displacement is infinitesimally small, it is in agreement with the direction switching observed in the unsteady nonlinear solutions of regime IV. Note also the horizontal forces and speed time-averaged along the slow period $T_\epsilon = 1/f'$ is zero, so that there is no unidirectional propulsion of the foil at that slow time scale.

Finally, to understand the destabilisation of this asynchronous mode in light of the fluid-solid interaction, we consider again the time-averaged analysis. The asynchronous mode being complex, the polar decomposition of the time-averaged force and velocity is $\left\langle \hat{F}_x \right\rangle = |\left\langle \hat{F}_x \right\rangle| e^{i\phi_F}$ and $\left\langle \hat{u}_g \right\rangle = |\left\langle \hat{u}_g \right\rangle| e^{i\phi_U}$. As shown in §2.3.2, the Floquet exponent then satisfies

$$\lambda = \frac{1}{\rho S} \frac{|\left\langle \hat{F}_x \right\rangle|}{|\left\langle \hat{u}_g \right\rangle|} e^{i\psi}$$

where $\psi = \phi_F - \phi_U$ is the phase difference between the force and velocity phases. The asynchronous mode is unstable ($\Re(\lambda) > 0$) when this phase difference lies in the interval $-\pi/2 < \psi < \pi/2$. The crucial role of the phase difference (rather than the force-to-velocity ratio) in the asynchronous mode destabilization is confirmed by examining figures 2.17(a) and (b) where both quantities are depicted as a function of the Stokes number. The mode gets unstable (gray area) precisely when the phase difference $\phi < \pi/2$. To better understand the physical meaning of this phase difference, the temporal evolution of the *quasi-periodic* perturbation of the time-averaged velocity $< \tilde{u}_g >$ (solid) and force $< \tilde{F}_x >$ (dashed) are plotted as a function of time in figure 2.17(c) for a stable and in 2.17(d) for an unstable mode. Note that the velocity and force are time-averaged over the (short) flapping period and their evolution is depicted over the long period (slow time scale t_ϵ). In both figures, the green areas identify phases of motion where the hydrodynamic force is propulsive (since the force and velocity are of same sign), while the white areas correspond to resistive phases of motion (force and velocity of opposite signs). In the case of a stable mode (see figure 2.17-c), the phase difference slightly above $\pi/2$ results in a mode with propulsive phases of motion that are shorter than

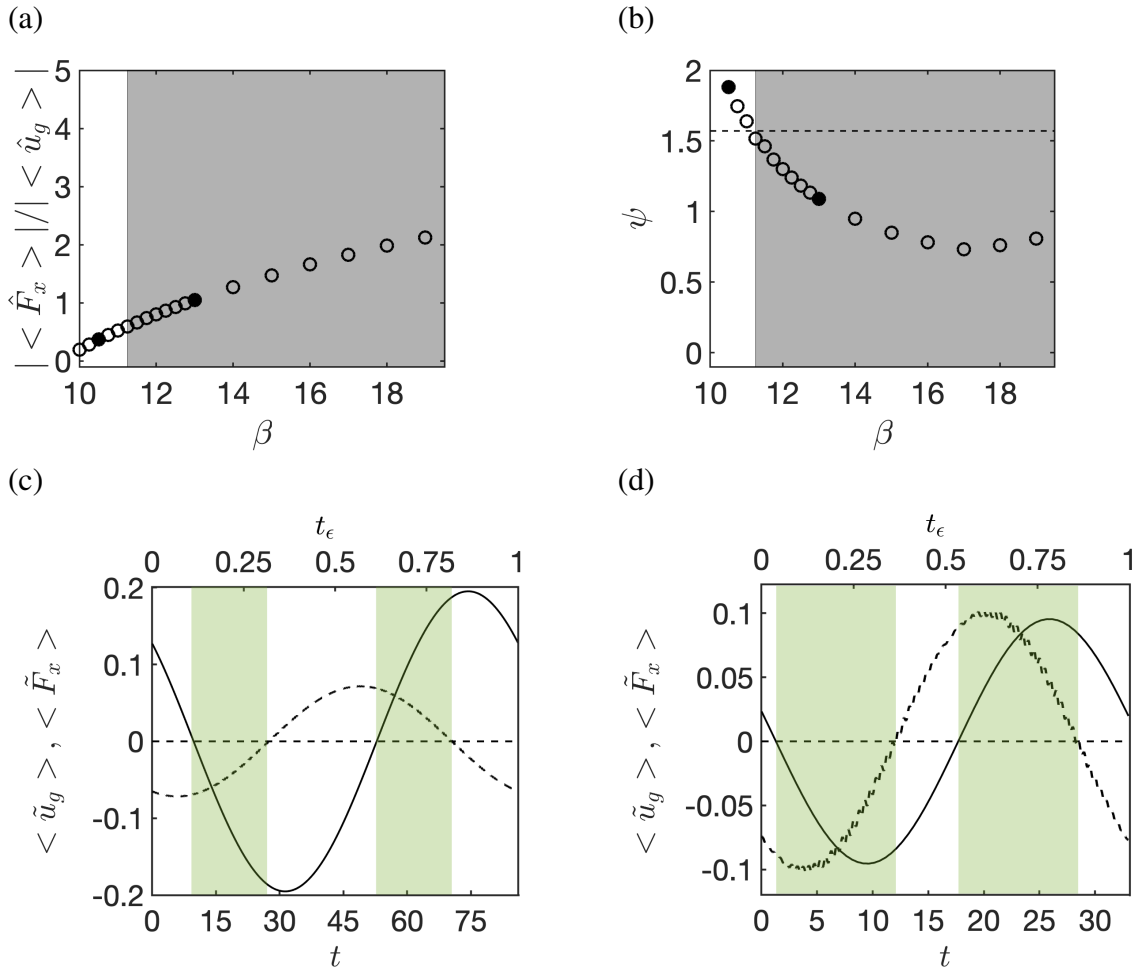

Figure 2.17: (a) Amplitude ratio and (b) phase difference of the (time-averaged) horizontal force and foil velocity of the asynchronous modes as a function of the Stokes number. The instability region is marked in grey. The dashed line corresponds to $\psi = \pi/2$. (c,d) Temporal evolution of the quasi-periodic foil velocity $< \tilde{u}_g >$ (solid curve) and force $< \tilde{F}_x >$ (dashed curve) time-averaged along a flapping period for (c) a stable ($\beta = 10.5$) and (d) an unstable ($\beta = 13$) asynchronous mode, shown in (a,b) with black dots. The green area corresponds to propulsive phases (velocity and force have the same sign) while white area correspond to resistive phases (velocity and force are of opposite sign).

resistive ones. On the other hand, in the case of an unstable mode (see figure 2.17-d), the phase difference slightly under $\pi/2$ results in a mode with longer propulsive phases of motion that resistive ones. The phase difference between the horizontal force and velocity is thus related to the cumulative time of propulsive phase over resistive phase. When $-\pi/2 < \psi < \pi/2$, the propulsive phases last longer than resistive ones, and the asynchronous mode is unstable. A similar criterion was established by Navrose and Mittal (2016) for the instability threshold of a spring-mounted cylinder flow, based on the global stability analysis of the steady base flow solution. They showed that the phase difference between the vertical hydrodynamic force and displacement of the cylinder perturbation is related to the transfer of energy from the flow to the cylinder and drives the destabilization of the mode. The present criterion can be viewed as an extension to the instability of periodic fluid-solid interaction problems.

2.3.5 Effect of the fluid-solid density ratio

Before concluding, we investigate the effect of the fluid-solid density ratio ρ on the results of the Floquet analysis. Two limit cases are considered in this section: high density ratios $\rho >> 100$, that lead to a loosely coupled fluid-solid due to the vanishing action of the fluid over the solid problem (as presented in §2.3.1), and the range of lower density ratios $\rho < 100$ that tend to the one of swimming organisms.

Let us first consider the high density ratio limit. The evolution of the Floquet exponent is shown in figure 2.18(a) and (b) for the synchronous and asynchronous modes, respectively. Starting from the value $\rho = 100$ considered until now, and increasing the density ratio, the absolute value of the Floquet multipliers (black solid curve) decreases for both modes. However, their asymptotic behaviour in the limit $\rho \to \infty$, displayed with the dashed red curves in the two figures, is different. The synchronous mode evolves as $1/\rho$ and thus only gets marginally stable. The asynchronous mode is stabilized for $\rho > 10^3$ and its growth rate tends towards that of the purely-hydrodynamic analysis.

To further understand why the Floquet exponents of the synchronous and asynchronous mode exhibit different behaviour in that limit case, we propose to reconsider the time-averaged analysis. In the infinite density ratio limit, the relation (2.19), that links the growth rate to the mean value of the horizontal solid velocity and force, gets:

$$\lambda < \hat{u}_g >= 0 \,.$$

Thus, either the Floquet exponent or the mean horizontal velocity is zero. The synchronous mode corresponds clearly to the case $\lambda = 0$ (figure 2.18-a). The foil mean velocity does not necessarily vanish for high density ratios, as observed in figure 2.18(c) that displays the evolution of the time-averaged horizontal speed with the density ratio. The asynchronous modes corresponds to the second case $< \hat{u}_g >= 0$, as seen in 2.18(d). As a matter of fact, not only the mean horizontal velocity converges to zero, but so does the entire temporal evolution due to the negligible acceleration generated by high density ratios. In this case, the Floquet exponent does not tend to zero (see figure 2.18-b), but rather to the value predicted by the purely-hydrodynamic stability analysis (red dashed line). Indeed, in the limit $\rho \to \infty$, the fluid-solid linearized operator is block triangular as seen in (2.14) and the purely-hydrodynamic Floquet multipliers are included in the fluid-solid Floquet spectrum. A similar asymptotic behaviour was observed by Fabre, Assemat, and Magnaudet (2011) when investigating the dynamics of free falling bodies in fluids using a fluid-solid stability analysis of the steady base solution (not periodic as in the

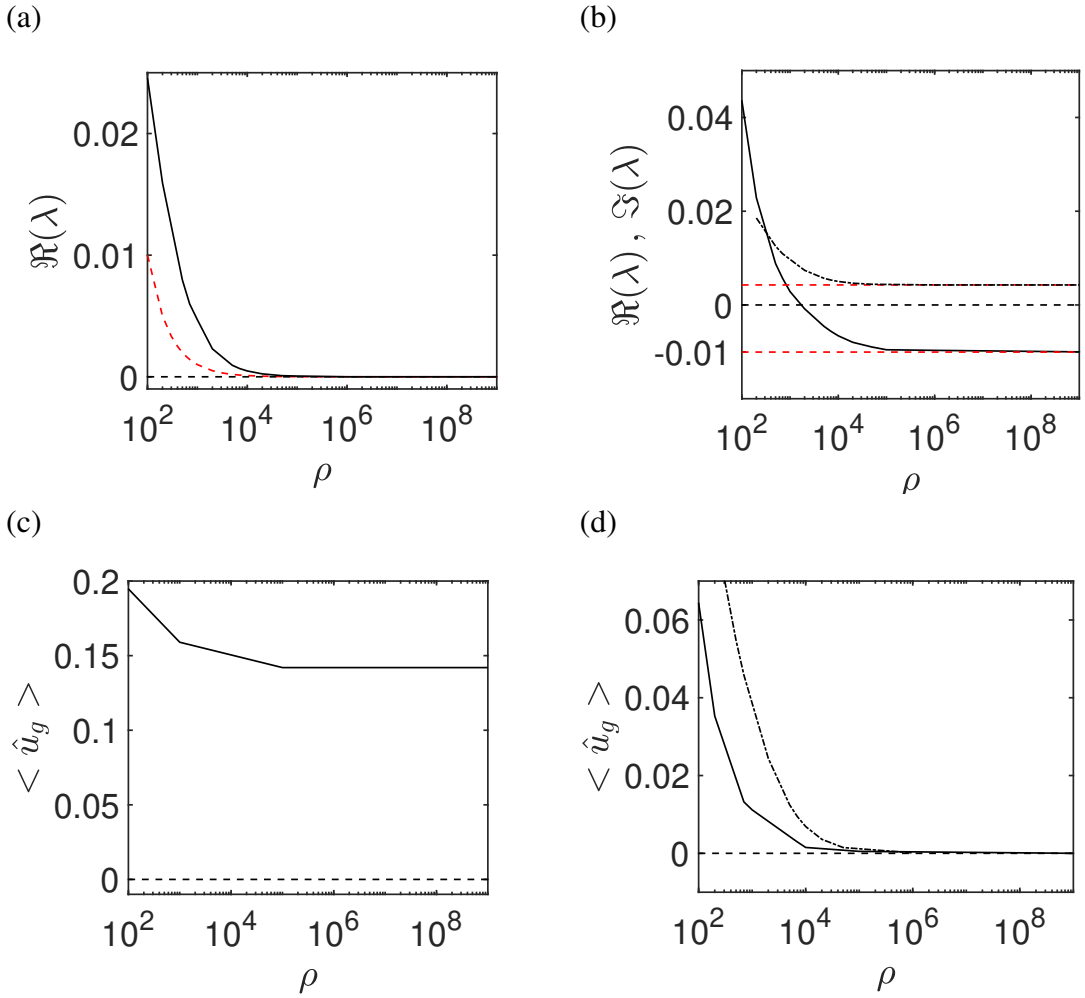

Figure 2.18: Effect of the fluid-solid density ratio ρ on (a,b) the Floquet exponent and (c,d) the perturbation of the foil horizontal speed for (a,c) the synchronous mode ($\beta = 6$) and (b,d) the asynchronous mode ($\beta = 12$). In (b) and (d) the real and imaginary part of respectively the Floquet exponent and the horizontal speed are represented by solid and dash-and-dot lines. The solid curves correspond to results of the fluid-solid analysis. The red dashed curve correspond to the asymptotic limits of the exponent: (a) $1/\rho$ curve and (b) the values of the purely-hydrodynamic analysis $\Re(\lambda) = -0.01$ and $\Im(\lambda) = 0.0043$. The dashed horizontal lines delimit in (a,b) $\Re(\lambda) = 0$ and in (b) $< u_g >= 0$.

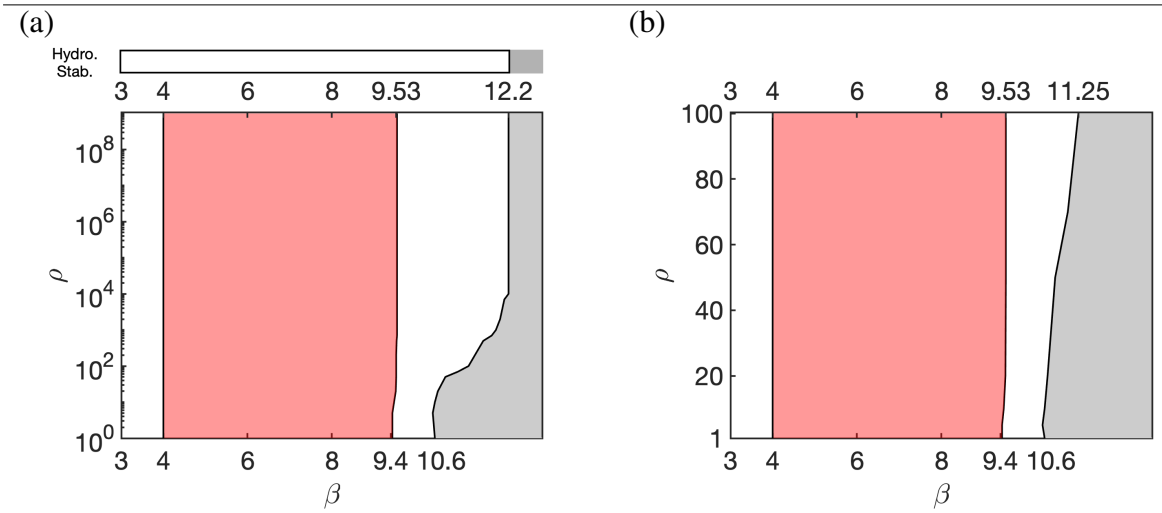

Figure 2.19: (a) Asymptotic limit ($1 \leq \rho \leq 10^9$) and (b) close-up on low density ratios ($1 \leq \rho \leq 100$) of the instability regimes of the symmetric non-propulsive periodic solution identified with the fluid-solid Floquet analysis in the parameters plane (β,ρ). White regions correspond to stable solutions, while red and grey regions indicate unstable solutions to synchronous and asynchronous Floquet modes, respectively. Results of the purely-hydrodynamics stability analysis are displayed in the top of (a) for comparison.

present case). In the limit case, results of the purely-hydrodynamic and fluid-solid stability analyses converged to the well know Von-Kármán vortex wake instability without effect on the path of the falling body. The present result is somehow an extension to the fluid-solid stability analysis of periodic solution.

Finally, figure 2.19 presents results of the fluid-solid stability analysis in the parameter space (β, ρ). The white area correspond to stable regions, while the red and grey areas corresponds to regions of unstable synchronous and asynchronous modes, respectively. We first consider the asymptotic limit of very large density ratios $\rho >> 100$. As one can see in figure 2.19(a), the synchronous unstable modes (red region) thresholds are barely modified for high density ratios, always taking place for $\beta = 4$ and $\beta = 9.53$ for $\rho > 100$. The instability threshold of asynchronous modes (grey region), on the other hand, is strongly modified with the increase of ρ going from $\beta = 11.25$ for $\rho = 100$ to $\beta = 12.2$ for $\rho = 10^4$. For Stokes numbers between these two thresholds, the density ratio presents thus a stabilizing effect. Accordingly to our previous analysis, as $\rho \to \infty$ the asynchronous modes threshold tends to the purely hydrodynamic analysis one (displayed at the top of the figure). Synchronous modes, on the other hand, become marginally unstable and do not converge to the purely hydrodynamic analysis, their marginal instability explaining the minimal threshold changes for high density ratios.

For small density ratios $1 \leq \rho \leq 100$, figure 2.19(b) the synchronous mode thresholds are again not strongly modified with the ρ decrease. While the transition from stable to unstable synchronous modes remains constant at $\beta = 4$, the stabilization threshold presents a significant variation going from $\beta = 9.42$ for $\rho = 1$ to $\beta = 9.53$ for $\rho = 100$. The instability threshold of the asynchronous mode is strongly modified, as for high density ratios. Its onset is now encouraged rather than delayed, varying from $\beta = 11.25$ for $\rho = 100$ to $\beta = 10.6$ for $\rho = 1$.

Transition between regimes	I – II	II – III	III – IV
Fluid-solid stability analysis	4.00	9.42	10.60
Nonlinear simulations	4.00	9.42 and 9.50	10.60

Table 2.2: Critical thresholds obtained with the unsteady nonlinear simulations and the fluid-solid stability analysis for $\rho = 1$.

These results indicate that swimming organisms (nearby an unity density ratio) are significantly more prone to non-coherent motions than flying organisms.

All instability thresholds and their trends are coherent with the unsteady nonlinear results previously reported. As shown for $\rho = 1$ in table 2.2, the destabilisation of the synchronous mode and the onset of unidirectional propulsion take both place for $\beta = 4$. The threshold value $\beta = 9.42$ of the synchronous mode stabilization is again slightly different from the threshold $\beta = 9.50$ of the transition between propulsive and non-propulsive solutions due to the bifurcation sub-critical nature (see figure 2.9-b). The threshold value $\beta = 9.42$ found with the linear stability corresponds, as in the case $\rho = 100$, to the disappearance of the symmetric solution when decreasing the Stokes number (transition from III to II). The onset of back & forth solutions matches again the destabilization of the asynchronous Floquet mode for $\beta = 10.6$.

2.4 Conclusions

The role of linear mechanisms in the transition to horizontal locomotion of a vertically flapping foil has been investigated. First, the occurrence of non-propulsive, unidirectional propulsive and back & forth solutions was established in the range of Stokes numbers $\beta \in [1, 20]$ for a rectangular shaped foil with an aspect ratio $h = 1/20$ with a flapping amplitude $A = 0.5$ and a solid-fluid density ratio $\rho = 100$. Floquet stability analysis of the coupled fluid-solid system was thus performed over symmetry preserved non-propulsive solutions. Our study was finally concluded by analysing the effect of the solid-fluid density ratio on the stability analysis, this last study being compared to predictions of non-propelled foil stability analysis usually employed in the literature.

First, symmetric non-propulsive, unidirectional propulsive and back & forth solutions were obtained while raising β, as in Alben and Shelley (2005) and Lu and Liao (2006). As expected for a low aspect ratio foil (Deng and Caulfield 2016), non-propulsive solutions first transition to unidirectional propulsion. The results presented in this paper highlight the existence of a sub-critical transition between propulsive and again non-propulsive solutions (regimes II-III), with back & forth oscillations finally reached (regime IV) for higher β. The emergence of these nonlinear solutions was then investigated through a self-propelled stability analysis of non-propulsive solutions. This analysis revealed the existence of unstable synchronous and asynchronous Floquet modes in the region of unidirectional and back & forth solutions, respectively. We therefore studied the characteristics of these unstable modes, investigating their associated fluid flow, horizontal force and speed to finally relate these mechanisms to the locomotion regimes obtained in nonlinear simulations. The evolution of the modes mean horizontal force and speed with β allowed us to establish a criterion of instability that link these quantities to the Floquet exponent.

In the case of synchronous modes, spatial symmetry breaking modes with non zero force and

speed are obtained, similar to unidirectional propulsion. Hydrodynamic forces that accelerates the horizontal speed lead to unstable Floquet exponents, and the transition to unstable modes is driven by the increase of the hydrodynamic force. The decay of this horizontal force leads subsequently to the mode stabilization and the re-emergence of symmetric non-propulsive solutions. Concerning asynchronous modes, the direction switching phenomenon observed in nonlinear solutions is explained by the competing action of the complex and real parts of these modes associated to the complex phase of their multiplier. This complex multiplier accurately predicts the low frequency of back & forth solutions at their onset. The temporal evolution of the quasi-periodic perturbation, resulting from the superposition of the real and imaginary part of the Floquet mode, clearly shows how the horizontal force exerted by the flow perturbation is alternatively propulsive or resistive, i.e of the same or opposite sign to the foil velocity, acting as a restoring spring-like force on the foil position over the slow period. The destabilization of the asynchronous modes depends on the phase difference between the time-averaged force and velocity perturbation, as it measures how long this force is propulsive or resistive over the slow period. A generalization to three-dimensional foils and different flapping movements of this mode might offer an additional path to understand, for example, the *snaking* trajectory presented by Deng and Caulfield (2018b) in the horizontal locomotion of oblate spheroids, first supposed to be connected to nonlinear effects, or the non-coherent motion of living organisms as the planktonic sea butterfly (Murphy et al. 2016).

The influence of the solid-fluid density ratio was finally investigated. For $\rho \in [1, 10^9]$ we observed that the β range of synchronous modes is not largely affected by the density ratio, whereas the transition to asynchronous modes is greatly impacted. To understand this behaviour, we have studied the coupled stability equations in the limit of high density ratios. We have shown that synchronous modes are asymptotically marginally unstable, whereas asynchronous modes converge to the uncoupled fluid system, since their horizontal speed converge to zero. These results explain the observed sensibility to the density ratio of the asynchronous modes threshold and the small variation of the transition to synchronous modes. Comparing these results to the non-propelled stability analysis, we have highlighted that the later converges to the self-propelled analysis only for asynchronous modes in the limit of very large density ratios, since in this limit the fluid-solid coupling terms disappear.

We conclude thus that the studied fluid-solid Floquet stability analysis, that takes into account the inherently fluid-solid coupling of the studied self-propelled foil interacting with a viscous fluid, is best adapted to predict the onset of unidirectional and back & forth propulsion. Possible future applications of this coupled stability analysis are the return from back & forth to coherent unidirectional propulsion observed for higher stokes numbers (Alben and Shelley 2005), as well as bifurcations of self-propelled heaving foils passively pitching around their leading edge (Spagnolie et al. 2010) and of a self-propelled infinite array of flapping wings (Becker et al. 2015).

2.5 Segregated approach for solving the implicitly coupled fluid-solid problem

We describe here the segregated approach used to solve efficiently the temporally discretized equations (2.7). Manipulating the r-backward differential formula of the time derivative, we

may split the unknown solid velocity u_g^{n+1} as,

$$u_g^{n+1} = (\Delta t/\alpha_0)\, a_g^{n+1} + \hat{u}_g\,, \tag{2.26}$$

where the first term is an unknown component, proportional to the unknown acceleration $a_g^{n+1} = \left(du_g/dt\right)^{n+1}$, and the second term is the known velocity component defined as

$$\hat{u}_g = -\sum_{k=1}^{r} (\alpha_k/\alpha_0)\, u_g^{n+1-k}\,.$$

The above decomposition of the horizontal solid velocity is then used to split the fluid variables as,

$$(\mathbf{u}^{n+1}, p^{n+1}) = \left(\frac{\Delta t}{\alpha_0} a_g^{n+1}\right)(\delta\mathbf{u}, \delta p) + (\hat{\mathbf{u}}^{n+1}, \hat{p}^{n+1}), \tag{2.27}$$

where we have introduced the flow component $(\delta\mathbf{u}, \delta p)$, proportional to the solid acceleration, and the flow component $(\hat{\mathbf{u}}^{n+1}, \hat{p}^{n+1})$ that will depend on the solid velocity $\hat{u}_g$. Introducing the solid (2.26) and fluid (2.27) decomposition into the governing flow equations (2.7) , we obtain two independent linear system of equations. The first one governs the flow component $(\hat{\mathbf{u}}^{n+1}, \hat{p}^{n+1})$ as

$$\begin{aligned} \frac{\alpha_0}{\Delta t}\hat{\mathbf{u}}^{n+1} + \nabla\hat{p}^{n+1} - \beta^{-1}\Delta\hat{\mathbf{u}}^{n+1} &= \mathbf{f}^{n+1} \\ \nabla\cdot\hat{\mathbf{u}}^{n+1} &= 0 \\ (\hat{u}^{n+1}, \hat{v}^{n+1})(\Gamma_w) &= \left(\hat{u}_g, 2\pi A sin(2\pi t^{n+1})\right) \end{aligned} \tag{2.28}$$

The boundary conditions at the fluid-solid interface Γ_w is explicitly known. Therefore, any classical algorithm such as the Uzawa method or the projection splitting method can be used to obtain the solution of this discretized forced unsteady Stokes equations. Following Jallas, Marquet, and Fabre (2017), we have used an a preconditioned conjugate gradient algorithm (Cahouet and Chabard 1988) to impose the divergence-free condition. As it depends on the flow history through the right-hand side forcing terms $\mathbf{f}^{n+1}$ and the boundary conditions, it is solved at each temporal iteration.

The second problem governs the flow component $(\delta\mathbf{u}, \delta p)$ that is proportional to the solid acceleration in the horizontal direction. It writes

$$\begin{aligned} \frac{\alpha_0}{\Delta t}\delta\mathbf{u} + \nabla\delta p^{n+1} - \beta^{-1}\Delta\boldsymbol{\delta u}^{n+1} &= 0 \\ \nabla\cdot\delta\mathbf{u} &= 0 \\ (\delta u, \delta v)(\Gamma_w) &= (1, 0) \end{aligned} \tag{2.29}$$

Again, the boundary conditions at the fluid-solid interface Γ_w is explicitly known, but it is now independent from the temporal iteration. The solution can thus be obtained prior to the temporal iteration. It can be viewed as the short time response of a Stokes flow, initially at rest, to a unitary horizontal velocity.

The solution of the (above) two independent flow problems does not give access to $(\mathbf{u}^{n+1}, p^{n+1})$ in (2.27) since the horizontal acceleration a_g^{n+1} is still unknown. The final step

Time step	$\max(F_y)$	$< u_g >$	Mesh nb. of triangles	$\max(F_y)$	$< u_g >$
$\Delta t = 0.01$	38.692	0.223	7836	38.641	0.226
$\Delta t = 0.005$	38.687	0.227	17116	38.687	0.227
$\Delta t = 0.001$	38.687	0.227	22580	38.687	0.227

Table 2.3: Convergence of the maximal vertical force $\max(F_y)$ and the time-averaged horizontal velocity $< u_g >$ with time step and mesh number of triangles for an unidirectional propulsive solution ($\beta = 6$). For the time-step convergence a fixed mesh of 17116 triangles was adopted, whereas for the mesh convergence a fixed time step $\Delta t = 0.005$ was used.

of the algorithm is obtained by introducing this decomposition into the last equation of the governing equation (2.7), yielding

$$(\rho S)\, a_g^{n+1} = \left(\frac{\Delta t}{\alpha_0} a_g^{n+1}\right) F_x(\delta\mathbf{u}, \delta p) + F_x(\hat{\mathbf{u}}, \hat{p}), \tag{2.30}$$

The horizontal acceleration is thus given by

$$a_g^{n+1} = \left(\rho S - \frac{\Delta t}{\alpha_0} F_x(\delta\mathbf{u}, \delta p)\right)^{-1} F_x(\hat{\mathbf{u}}, \hat{p}), \tag{2.31}$$

and the velocity and pressure are obtained using (2.27).

2.6 Validation of the nonlinear and linear fluid-solid solvers

The numerical method is primarily validated through the convergence of the time-averaged horizontal velocity and the maximal vertical force acting on the foil with the mesh number of elements and time step. In table 2.3 the influence of the time and spatial discretization is evaluated for an unidirectional propulsive solution ($\beta = 6$). A time step of $\Delta t = 0.005$ and a mesh of 17116 triangles are sufficient to guarantee the convergence of the the hydrodynamic force and horizontal velocity up to order $O(10^{-3})$. This convergence was attained for all other Stokes number explored in this article. The mesh of 17116 was used in all cases and the time step evolved from $\Delta t = 10^{-2}$ for small values of the Stokes number ($\beta = 2$) being decreased to $\Delta t = 5 \cdot 10^{-4}$ for larger values ($\beta = 19$).

The nonlinear solver employed in this study has then been validated by simulating the horizontal locomotion of a two-dimensional ellipsoid of aspect ratio $h = 0.1$, flapping amplitude $A = 0.25$, density ratio $\rho = 10$ and Stokes number $\beta \in [2, 15]$ as in the numerical study of (Spagnolie et al. 2010). In this work the onset of locomotion is around $\beta > 8$, and as seen in figure 2.20 both the emergence of propulsive solutions and their time-averaged horizontal velocities compare very well between the present numerical method and the values found on the reference.

The linear solver is validated through the purely hydrodynamic Floquet stability analysis of the flow symmetry breaking around a heaving cylinder. Two distinct flapping amplitudes and Stokes numbers are considered (using the Keulegan-Carpenter number $KC = 4\pi A$): $(\beta, KC) = (40, 4.75)$ and $(\beta, KC) = (100, 3.65)$. We can see in the table 2.4 that the absolute

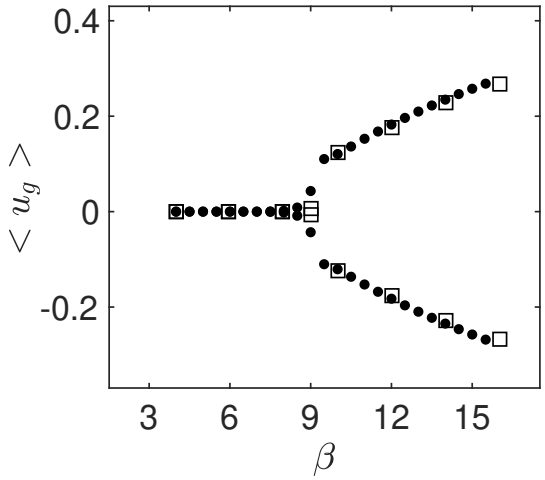

Figure 2.20: Validation of the nonlinear solver. Time-averaged horizontal velocity of the foil as a function of the Stokes number β. Results of the numerical algorithm described in 2.5 (filled dots) are compared to results (empty squares) extracted from figure 13 (*clamped* case) in Spagnolie et al. (2010).

	$\beta = 40$, $KC = 4.75$	$\beta = 100$, $KC = 3.65$
Elston, Blackburn, and Sheridan (2006)	1.1282	1.1429
Present method	1.1273	1.1411

Table 2.4: Linear solver validation: Comparison of the leading Floquet multiplier $|\mu|$ with the values presented on Table 3 of Elston, Blackburn, and Sheridan (2006)

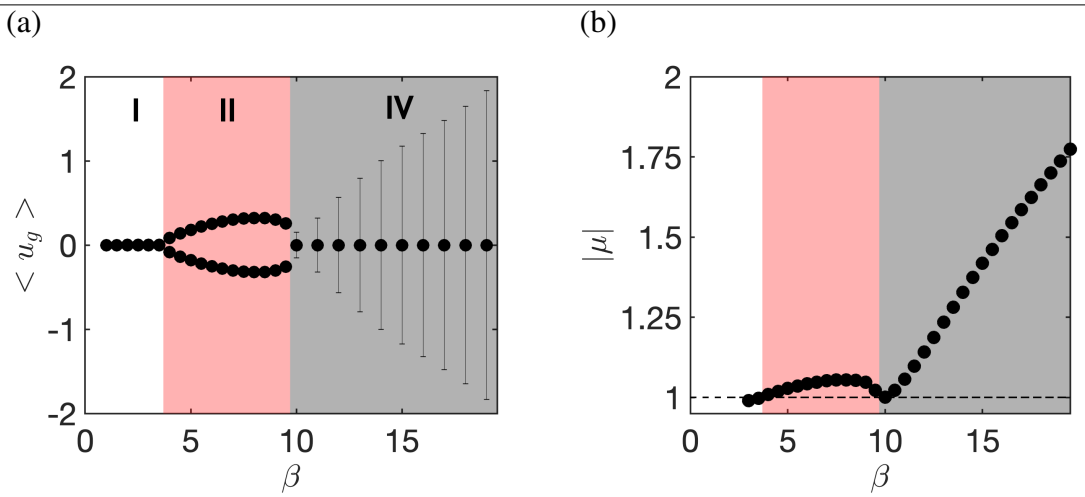

Figure 2.21: Evolution of the (a) time-averaged horizontal velocity and (b) leading Floquet multiplier absolute value of an elliptical foil of minor/major axis aspect ratio $h = 0.1$ with control parameters $A = 0.5$ and $\rho = 32$. In (a) - resp. (b) - white, red and grey background colors identify symmetric non-propulsive, unidirectional propulsive and back & forth regimes - resp. stable, synchronous unstable and asynchronous unstable multipliers.

value of the leading Floquet multiplier obtained in the two test cases is in a good agreement with values of Elston, Blackburn, and Sheridan (2006).

2.7 Effect of the foil shape on self-propelled regimes and stability

To evaluate the influence of the foil shape and aspect ratio, the evolution with the Stokes number β of the unsteady nonlinear dynamics and fluid-solid Floquet stability of an elliptical foil of aspect ratio $h = 0.01$ is shown in figure 2.21. The flapping amplitude $A = 0.5$ (identical to this work) and the density ratio $\rho = 32$ have been fixed as to approach one of the configurations explored by Alben and Shelley (2005).

The self-propelled regimes and their transition are similar to the rectangular foil with rounded edges. A remarkable difference is, nevertheless, the suppression of the intermediary non-propulsive regime III, between the unidirectional propulsive and the back & forth regimes. Apparently the increase of the aspect ratio favours, as the decrease of the density ratio (§2.2.3.2), the onset of non-coherent propulsion. The obtained onset of back & forth solutions ($\beta > 9.5$) closely matches the one of Alben and Shelley (2005). The existence of an unidirectional propulsive regime prior to the back & forth one is, however, to our knowledge newly reported in the literature (apart from being briefly mentioned in the works of Deng and Caulfield (2016)). We suspect this regime has not yet been characterized due to two factors. In one hand, as illustrated in figure 2.4, this propulsive regime features a very long transitory regime of ~ 200 flapping periods. In addition, owing to the low Stokes number and its viscous nature, velocity perturbations added to the quiescent system initially decay. Following this initial decay, more than 100 flapping periods are commonly needed for the horizontal velocity to grow above an

initial perturbation $u_g = 0.05$. This threshold is indeed beyond the one employed, for example, by Alben and Shelley (2005) who differentiated non-propulsive and propulsive solutions by the growth of initial velocity perturbations after 80 flapping periods.

Unstable synchronous and asynchronous modes, figure 2.21(b), are again obtained in the same β range as the unidirectional propulsive and back & forth solutions. Despite the different geometry and the suppression of the intermediary non-propulsive regime, the fluid-solid Floquet stability analysis correctly predicts the onset of unidirectional propulsive and back & forth solutions.

Chapter 3

Self-propelled dynamics at large Stokes numbers: non-linear analysis

The content of this chapter is based on the article: Benetti Ramos, L. *et al*, Local and global bifurcations of a self-propelled heaving foil at high flapping frequencies, in preparation for *Journal of Fluid Mechanics*.

In this chapter we extend the study made in Chapter 2 to higher Stokes numbers ($20 \leq \beta \leq 40$*) where three new propulsive solutions are found. We remark, however, they are not explained by the previous chapter fluid-solid stability analysis of non-propulsive solutions. Non-linear methods, the Time Spectral Method (TSM) associated to pseudo arc-length continuation, are thus employed to study their emergence. We then study the fluid-solid Floquet stability of self-propelled rather than non-propulsive base-solutions, considering as problem variables not only the surrounding flow but also the foil velocity both at perturbation (as the last chapter) and at the base-solution level.*

Complex dynamics may emerge from the interaction of a horizontally self-propelled heaving foil and its induced flow, as for instance slow non-coherent back & forth motions of the foil at intermediate flapping frequencies. We focus here on self-propelled states appearing for higher frequencies. Using time marching simulations, we report the existence of a new quasi-periodic self-propelled state of unidirectional locomotion where its propulsive wake slowly deviates upward and downward. When further increasing the frequency, this quasi-periodic deviation disappears and a periodic unidirectional propulsive state of symmetric wake is first obtained, followed by a deviated wake periodic propulsive state. To understand these transitions, a time spectral method coupled to a pseudo arc-length continuation method is used to follow the branch of periodic propulsive solutions of symmetric wake. It shows that, at high flapping frequency where the deviated propulsive solution is observed, the symmetric solution still exists. In addition, a saddle-node bifurcation of periodic cycles occurs at lower frequencies. The linear stability of symmetric periodic wake propulsive solutions is then investigated through a fluid-solid Floquet analysis. Unstable synchronous and asynchronous Floquet modes, both related to displacement of the wake vortices, are obtained in the frequencies where periodic and quasi-periodic wake deviations are observed, respectively. If the transition from the symmetric propulsive solution to these two regimes is local in the sense of bifurcation analysis, the transition between the back & forth and quasi-periodic propulsive turns out to be global. By analyzing

the evolution of this dynamic system through its phase space representation, we finally show that a collision between the two regimes occurs as it approaches the saddle-node bifurcation of the periodic symmetric branch.

Contents

3.1 Introduction

The flapping wing propulsion adopted by aquatic and flying animals in nature (Lighthill 1969; Wu 2010) offers nowadays a great source of inspiration for the conception of artificial swimmers (Barrett 1996; Ramananarivo, Godoy-Diana, and Thiria 2013) and micro-aerial vehicles (Ristroph and Childress 2014; Faux et al. 2018). A key problematic regarding the exploitation of this locomotion strategy concerns the capability of predicting trajectories for the exploited flapping amplitudes and frequencies. For certain imposed flapping movements non-coherent self-propelled regimes such as oscillatory motions around fixed points are observed in nature for living organisms (Murphy et al. 2016). Due to their efficiency decrease and loss of trajectory control, these regimes are clear limitations from an exploitation point of view. To avoid them, flapping wings self-propelled regimes and their transition are actively investigated problems (Alben and Shelley 2005; Deng and Caulfield 2016; Deng and Caulfield 2018a). As artificial flying devices tend to smaller scales (Chen et al. 2017), the present work aims at developing tools and a physical understanding of the transition between non-coherent and coherent self-propelled regimes of locomotion near the flapping propulsion onset.

In a previous work (Benetti Ramos et al. 2020) we have studied the emergence of flapping locomotion based on reciprocal motion. Our study revealed that the first two self-propelled regimes to emerge from symmetric non-propulsive solutions are a periodic state of unidirectional motion and a quasi-periodic state of slow back & forth motion around a fixed position. A natural question that arises from this study is how this non-coherent back & forth solution can evolve while modifying control parameters. In literature, different parametric studies were conducted to investigate the evolution of this non-coherent locomotion. The decrease of the thickness-to-chord aspect ratio h of ellipses and rectangular foils (Zhang et al. 2009) and the increase of the solid-to-fluid density ratio of elliptical foils (Lu and Liao 2006) were found to bring back non-coherent dynamics to unidirectional propulsive ones. A strategy best adapted to suppress non-coherent regimes during engineering devices exploitation might be to control the imposed flapping movement. In the case of elliptical foils, Alben and Shelley (2005) has shown that the increase of the flapping frequency can be explored to bring non-coherent dynamics back to a coherent propulsion. In this work, we decided to follow a similar approach investigating through unsteady nonlinear simulations this possible return to coherent propulsion for our previously studied problem (Benetti Ramos et al. 2020). The problem setup is a thin rectangular foil of nondimensional thickness-to-chord aspect ratio $h = 0.05$, solid-to-fluid density ratio $\rho = 100$, flapping at a constant chord-based amplitude $A = 0.5$. By varying the Stokes number $\beta = f^*(c^*)^2/\nu$, a nondimensional number that uses the flapping frequency f^*, the foil chord c^* and the fluid kinematic viscosity ν as characteristic scales, in the range $10 \leq \beta \leq 40$ we will show that three new regimes of unidirectional propulsion emerge from back & forth motion around a fixed point: a deviated quasi-periodic wake (DQPW), a symmetric periodic wake (SPW) and a deviated periodic wake (DPW) propulsive regime. This parametric investigation accurately determines the Stokes number thresholds of these nonlinear regimes. This basis is then explored in the second objective of this work: predict these thresholds using nonlinear and linear stability analyses.

Floquet stability analysis (Floquet 1883) is a promising path to predict the transitions of these periodic solutions. A purely-hydrodynamic analysis, first introduced for oscillating objects by Elston, Sheridan, and Blackburn (2004) in the symmetry breaking of heaving cylinders, has been recently employed by Deng et al. (2016) and Deng and Caulfield (2018a) to study the emergence

of different non-coherent (snaking and stair-step trajectories) and unidirectional propulsive self-propelled regimes of a three-dimensional ellipsoid in a quiescent fluid. Studying the stability of the initially axisymmetric base-flow around the non-propelled flapping ellipsoid, Deng et al. (2016) found that unstable Floquet modes of high azimuthal wave number are present at the onset of flow asymmetry. As the flapping frequency is increased, the least unstable modes become purely left-right asymmetric. These *non-propelled* foil stability results have been thus compared to self-propelled regimes of locomotion (Deng and Caulfield 2018a) trying to establish, for certain flapping frequencies and amplitudes, links between (possibly nonlinearly interacting) high azimuthal numbers unstable modes with non-coherent regimes and left-right asymmetry with coherent propulsive regimes. The different regimes onsets have however not been predicted by this *purely*-hydrodynamic Floquet analysis of non-propulsive base-solutions. In the present work, instead of analysing the purely-hydrodynamic stability of non-propulsive base flows, we will employ again the fluid-solid Floquet stability analysis introduced in our previous work (Benetti Ramos et al. 2020), which considers not only the flow but also the foil velocity as a perturbation variable. In addition, the stability of self-propelled base solutions, instead of non-propulsive base-flows, will be studied. As transitions beyond the onset of self-propulsion generally involve solutions whose foil velocity is non-zero, we will add to the fluid dynamics at the base-solution level the solid ones. In this way, the inherently fluid-solid coupling of the problem intervenes in the perturbation level through two different mechanisms: the base solution and the perturbation of the foil velocity.

To calculate self-propelled periodic base-solutions when these are unstable numerical bifurcation tools (Dijkstra et al. 2014) can be employed. In this work the bifurcations at higher flapping frequencies will be studied through the phase space representation of the transition between back & forth and deviated wake quasi-periodic propulsive solutions and the stability of symmetric periodic wake propulsive solutions, found between deviated quasi-periodic wake and deviated periodic wake propulsive regimes in our nonlinear study. To follow periodic propulsive solutions beyond their range found in unstable nonlinear simulations a coupled strategy composed of pseudo arc-length continuation (Govaerts 2000) and a spectral method to directly compute cruise regime solutions will be employed. The alternative here explored to directly obtain (stable and unstable) cruise regime solutions is to use their intrinsic flapping periodicity. This approach is essential when unstable limit cycles are sought, since in unsteady nonlinear simulations small perturbations introduced by the numerical method are temporally amplified drifting the solution away from the unstable cycle. Harmonic Balance Methods (HBM) and, more particularly, their time domain variation Time-Spectral Method (TSM) (Gopinath and Jameson 2005) used in this work, seek the periodic solution of a self-propelled foil under the form of a Fourier series. The TSM transforms then an unsteady equation into a (coupled) system of equations that determine the amplitude of the Fourier coefficients of the unknown periodic solution. This approach has been successfully adopted in recent studies of flapping airfoils (Gopinath and Jameson 2005), turbomachines (Hall, Thomas, and Clark 2002; Weide, Gopinath, and Jameson 2005; Gopinath et al. 2007) and in the transition mechanisms of boundary layers (Rigas, Sipp, and Colonius 2020). The stability of the symmetric periodic wake propulsion solutions determined with this coupled TSM/ pseudo arc-lenth approach will be finally studied using fluid-solid Floquet stability analysis.

This work is organized in four distinct parts. At first, unsteady nonlinear simulations are performed, §3.2.2, and self-propelled regimes for higher flapping frequencies are described. The transitions between back & forth motion, deviated quasi-periodic wake, symmetric periodic

wake and deviated periodic wake propulsion are identified for $10 \leq \beta \leq 40$. In §3.3 nonlinear bifurcation methods, time spectral method coupled to pseudo arc-length continuation, are used to follow symmetric periodic wake propulsive solutions. Their fluid-solid Floquet stability is thus analysed. This section is concluded by the analysis of the unstable regions and the obtained quasi-periodic and periodic wake deviation modes. We finally regard the transition between two quasi-periodic regimes, the back & forth and deviated quasi-periodic wake propulsive solutions in §3.4. Conclusions about the local and global nature of self-propelled heaving foil bifurcations of at higher flapping frequencies are finally drawn in §3.5.

3.2 Problem formulation and self-propelled nonlinear solutions

We investigate in this work the horizontal self-propulsion of a heaving symmetric rectangular foil. The rigid body has a rectangular shape with rounded edges and is characterized by its chord $c = 1$ and its non-dimensional thickness $h = h^*/c$ (where * is adopted to differentiate dimensional and nondimensional parameters) with the round edges being of diameter equivalent to the foil thickness. The nondimensional foil surface is $S = (1-h)h + \pi h^2/4$ and the (uniform) density ρ_s. This body translates in an initially quiescent two-dimensional fluid of density ρ_f and kinematic viscosity ν with a velocity $\mathbf{u}_g = (u_g, v_g)$. While the vertical velocity is imposed through a heaving motion $y_g^*(t) = -A^* \cos(2\pi f^* t^*)$, the horizontal velocity is free as a result of hydrodynamic forces acting on the solid-fluid interface Γ_w. This rigid-body fluid-structure interaction is characterized by four non-dimensional parameters: the frequency-based Stokes number β, the non-dimensional amplitude A, the solid-fluid density ratio ρ and the non-dimensional thickness h, defined respectively as

$$\beta = \frac{f^* c^2}{\nu},\ A = \frac{A^*}{c},\ \rho = \frac{\rho_s}{\rho_f} \text{ and } h = \frac{h^*}{c}\,. \tag{3.1}$$

The non-dimensional flapping period T is equal to 1 whatever the values of the Stokes number β due to the choice of characteristic time-length. The surrounding fluid, absolute fluid velocity $\mathbf{u} = (u, v)$ and pressure p, is governed by the two-dimensional incompressible Navier-Stokes equations

$$\frac{\partial \mathbf{u}}{\partial t} = -\boldsymbol{\nabla}\mathbf{u} \cdot (\mathbf{u} - \mathbf{u}_g) - \boldsymbol{\nabla} p + \beta^{-1} \boldsymbol{\Delta}\mathbf{u},\ \boldsymbol{\nabla} \cdot \mathbf{u} = 0\,, \tag{3.2}$$

written in the non-inertial frame of reference that follows the foil center of mass G as done in other fluid-structure interactions studies, such as falling and rising bodies in fluids (Jenny, Bouchet, and Dušek 2003; Tchoufag, Fabre, and Magnaudet 2014) or pitching foils (Jallas, Marquet, and Fabre 2017). The body is self-propelled and the evolution of its horizontal motion is governed by Newton's second law

$$\frac{\mathrm{d}u_g}{\mathrm{d}t} = (\rho S)^{-1} F_x(\mathbf{u}, p)\ ,\ F_x(\mathbf{u}, p) = \int_{\Gamma_w} ([-p\mathbf{I} + \beta^{-1}(\boldsymbol{\nabla}\mathbf{u} + \boldsymbol{\nabla}^T\mathbf{u})] \cdot \mathbf{n}) \cdot \mathbf{e}_x \mathrm{d}\Gamma_w\,, \tag{3.3}$$

where $\mathbf{n}$ is the outward normal. Equations (3.2) and (3.3) are closed by a no-slip boundary condition on the foil surface $\mathbf{u}(\Gamma_w, t) = \mathbf{u}_g(t)$. This equations can be cast in a compact for using the system state variable $\mathbf{q} = [\mathbf{u}, p, u_g]^T$

$$\mathcal{B}\frac{\partial \mathbf{q}}{\partial t} = \mathcal{R}(\mathbf{q}, v_g), \tag{3.4}$$

where the operators $\mathcal{B}$ and $\mathcal{R}$ are respectively the system mass-matrix (that select the appropriate time-derivatives) and the spatial operator that contains the Navier-Stokes equations and the Newton's second law.

3.2.1 Numerical method

The system of equations (3.4) is discretized in time using the following r-order semi-implicit scheme

$$\begin{aligned}
\frac{\alpha_0}{\Delta t}\mathbf{u}^{n+1} + \nabla p^{n+1} - \beta^{-1}\Delta \mathbf{u}^{n+1} &= \mathbf{f}^{n+1} \\
\nabla \cdot \mathbf{u}^{n+1} &= 0 \\
(u^{n+1}, v^{n+1})(\Gamma_w) &= \left(u_g^{n+1}, 2\pi\, A\, sin(2\pi t^{n+1})\right) \\
\frac{\alpha_0}{\Delta t}u_g^{n+1} &= (\rho S)^{-1} F_x(\mathbf{u}^{n+1}, p^{n+1}) - \sum_{k=1}^{r}\frac{\alpha_k}{\Delta t}u_g^{n+1-k} \\
(u^{n+1}, v^{n+1})(\Gamma_e) &= (0,0),
\end{aligned} \tag{3.5}$$

where the linear diffusion terms are implicit and the nonlinear convective terms are explicit, with the right-hand side forcing term $\mathbf{f}^{n+1}$ in the momentum equation defined as

$$\mathbf{f}^{n+1} = -\sum_{k=1}^{r}\gamma_k(\mathbf{u}^{n+1-k} - \mathbf{u_g}^{n+1-k})\cdot\nabla\mathbf{u}^{n+1-k} - \sum_{k=1}^{r}\frac{\alpha_k}{\Delta t}\mathbf{u}^{n+1-k},$$

with Δt the time step and $(\mathbf{u}^{n+1}, p^{n+1})$ the velocity and pressure at time $t_{n+1} = (n+1)\Delta t$. The time derivatives (nonlinear convection terms) are approximated (extrapolated) by r-order backward differential formulae. A first-order scheme ($r = 1$, $\alpha_0 = 1$, $\alpha_1 = -1$ and $\gamma_1 = 1$) is used for the first two temporal iterations ($n \leq 1$), followed by a second-order scheme ($r = 2$, $\alpha_0 = 3/2$, $\alpha_1 = -2$, $\alpha_2 = 1/2$, $\gamma_1 = 2$ and $\gamma_2 = -1$). The equality of fluid and solid velocity is treated implicitly, to avoid time-step restrictions induced by an explicit coupling (Causin, Gerbeau, and Nobile 2005). To allow the use of an existing fast implementation to solve the flow equations (Jallas, Marquet, and Fabre 2017), we use the segregated approach proposed by Jenny and Dušek (2004). Typically, the time step is set to $\Delta t = 5\cdot 10^{-4}$ for small values of the Stokes number ($\beta = 19$) and is decreased to $\Delta t = 2.5\cdot 10^{-4}$ for larger values ($\beta = 32$), so as to ensure the numerical stability of this semi-explicit temporal scheme (Kress and Lötstedt 2006).

A continuous Galerkin finite-element method is employed to discretize the equations (3.5) in space. Quadratic elements (P2) and linear elements (P1) are respectively used for the flow velocity and the pressure. The implementation is based on the FreeFEM software (Hecht 2012). A circle of (non-dimensional) diameter 80 centered at the foil center of mass is used as computational domain, with its external boundary denoted Γ_e. A Delaunay triangulation of the computational domain results in a mesh with typically 3.3×10^4 triangles. As spatio-temporal symmetries are expected for the solutions and spatial symmetries are not, a particular attention is made to generate vertically symmetric meshes. To create a mesh that is symmetric with respect

to the y-axis and refined in flow regions exhibiting large velocity gradients we have proceed as follows. Once a first solution has been computed, we adapt a mesh of a half domain to several instants of the periodic flow, using the hessian-based mesh adaptation implemented in FreeFEM (see Fabre et al. (2018) for a practical review). This mesh is thus duplicated to assemble the full mesh. The triangle size is typically of order $O(10^{-2})$ close to the foil and over the wake behind the foil, and 1 in the external part of the domain. Mesh refinement and domain size were chosen based on the convergence of the foil horizontal velocity and the vertical hydrodynamic force. Greater domains or mesh refinement have exhibited little influence over these values. The validation of this numerical method is detailed in Benetti Ramos et al. (2020).

3.2.2 Three propulsive self-propelled solutions at higher Stokes numbers

Unsteady nonlinear simulations are performed for values of Stokes numbers in the range $15 \leq \beta \leq 35$. Other control parameters (flapping amplitude $A = 0.5$, the density ratio $\rho = 100$ and the foil aspect ratio $h = 0.05$) are kept fixed. When increasing the Stokes number four distinct self-propelled solutions are obtained: back & forth solutions (discussed in a previous work (Benetti Ramos et al. 2020) and briefly described in §3.4), (1) deviated quasi-periodic wake (DQPW), (2) symmetric periodic wake (SPW) and (3) deviated periodic wake (DPW) propulsive solutions. These three additional propulsive regimes are characterized hereafter. In figure 3.1 we characterize the unsteady flow of these regimes through the out-of-plane vorticity ω_z for three representative values of Stokes number, $\beta = 21$ for the DQPW, $\beta = 23$ for the SPW and $\beta = 30$ for the DPW solution. Although all solutions here presented have positive velocities, negative velocities are equally attainable depending on the initial condition, with the choice for positive velocities being a mere convention induced by a positive initial velocity perturbation imposed to the system.

Due to their propulsive character all these solutions present a non spatially symmetric flow. In the three regimes, we observe the formation of a vortex wake behind the foil trailing edge, with this vortex wake having different dynamics in each case. For DQPW solutions (3.1-a) only a small wake consisting of a vortex dipole is seen. The distance separating successive vortex is very small, and the dipole is periodically deviated upward (downward) as it can be seen in the two first (last) figures. The quasi-periodic nature of this regime is precisely linked to the cyclic alternation between upward and downward wake deviation. An increase of the Stokes number leads to a greater distance separating successive vortex. When SPW solutions (3.1-b) are obtained the wake is no longer constituted solely of a vortex dipole or presents a quasi-periodic deviation. The propulsive solution retrieves the spatio-temporal symmetry (Elston, Sheridan, and Blackburn 2004)

$$(u, v, p, \omega_z)(x, y, t) = (u, -v, p, -\omega_z)(x, -y, t + 1/2), \tag{3.6}$$

which is the combination of the y-reflection symmetry and the $1/2$ time-reciprocal translation. These solutions feature a reversed Von-Kármán vortex street (Triantafyllou, Triantafyllou, and Gopalkrishnan 1991), a clear sign of a propulsive solution. As the Stokes numbers is further risen, this vortex street start to form dipoles. The wake is again spatio-temporally asymmetric and DPW propulsive solutions are obtained (figure 3.1-c). Although the foil is self-propelled in our case, the deviation process is very similar to that observed for non-propelled flapping foils (Godoy-Diana et al. 2009; Jallas, Marquet, and Fabre 2017).

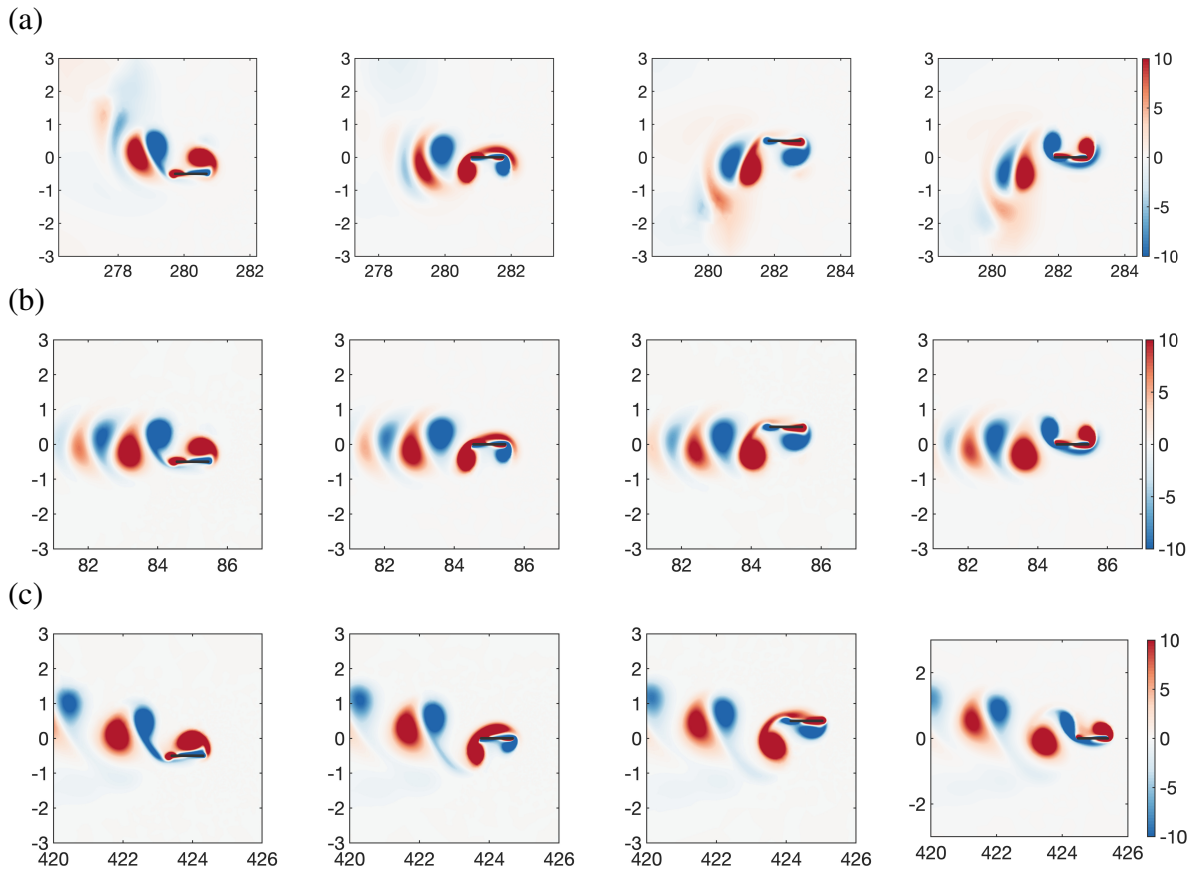

Figure 3.1: Vorticity snapshots for (a) Deviated Quasi- Periodic Wake (DQPW, $\beta = 21$), (b) Symmetric Periodic Wake (SPW, $\beta = 23$) and (c) Deviated Periodic Wake (DPW, $\beta = 30$) propulsive solutions. The time instants are separated by 4.25 in (a) and by 0.25 in (b,c). The initial instants (shown in the next figure) correspond to the position $y_g = -0.5$.

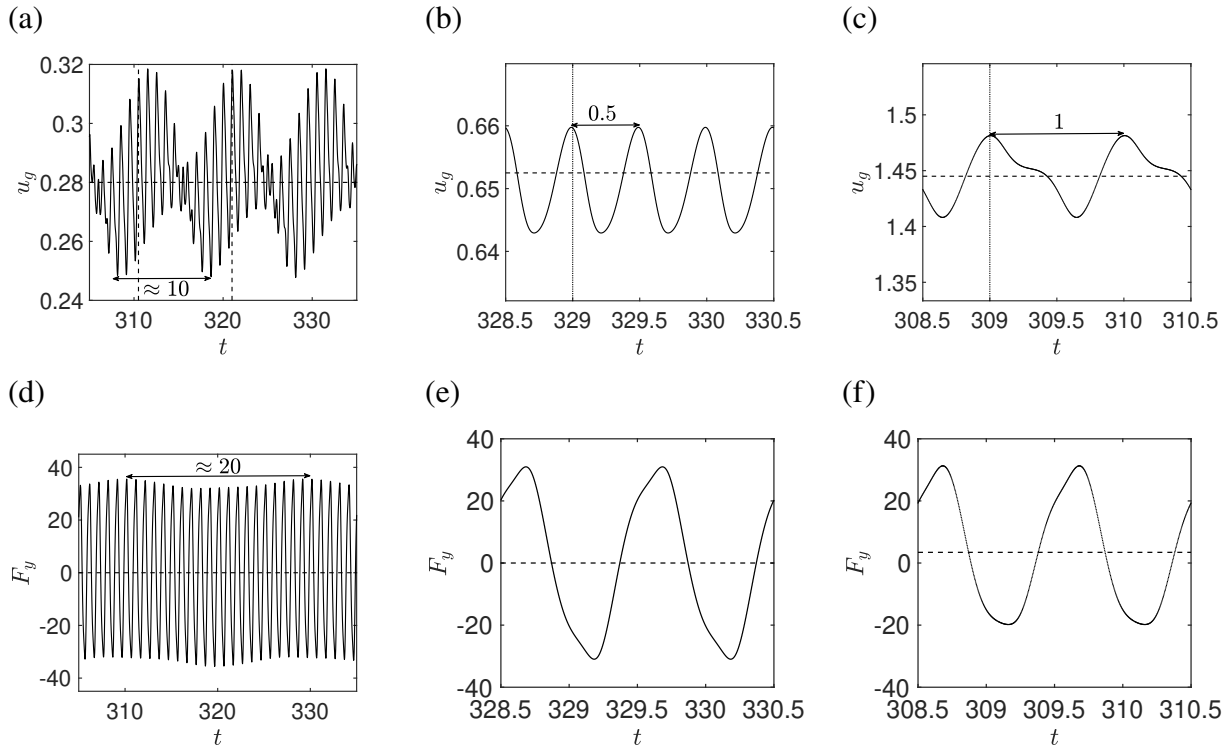

Figure 3.2: Temporal evolution of the (a-c) horizontal velocity u_g and (d-f) vertical force F_y for the (a,d) DQPW ($\beta = 21$), (b,e) SPW ($\beta = 23$) and (c,f) DPW ($\beta = 30$) propulsive solutions. The temporal evolution is displayed during a flapping period in (b,c,e,f) and for a slow period in (a,d). Horizontal dashed lines indicate the time-averaged value of the plotted quantity. Vertical lines in (a-c) indicate the initial times, and final in the case of (a), of figure 3.1.

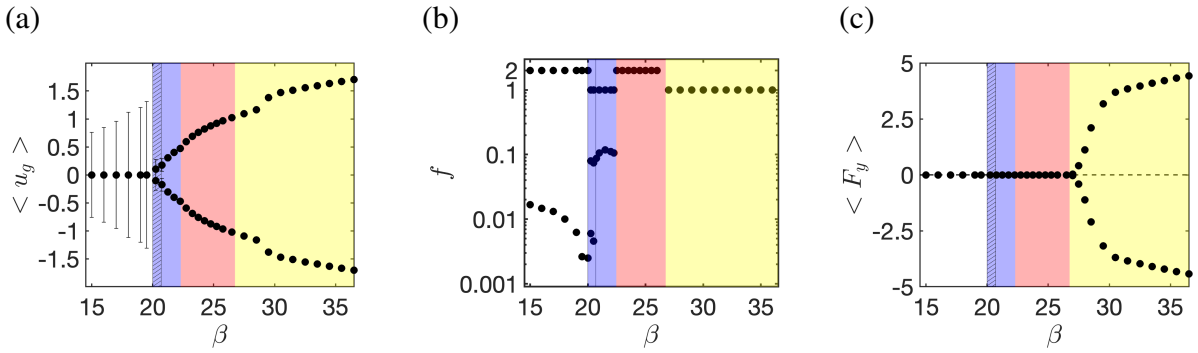

Figure 3.3: Evolution with β for $A = 0.5$ and $\rho = 100$ of the foil (a) mean horizontal speed (filled circles) and its amplitude (error bars) as well as (b) dominant frequency of this time signal, and (c) time-averaged vertical force. Violet, red and yellow areas are highlighted for the occurrence of respectively deviated quasi-periodic wake (DQPW), symmetric periodic wake (SPW) and deviated periodic wake (DPW) propulsive solutions. The hatched area indicates the transition between back & forth motion and DQPW solutions where two small frequencies remain (three frequencies in total).

These solutions can be further characterized by their horizontal velocity and vertical force temporal evolution, shown in figure 3.2. The horizontal velocity of the DQPW solutions (3.2-a) oscillate around a non-zero time-averaged value with two distinct periods. The first is identical to the imposed heaving movement. The second is a slow period of order $O(10^{-1})$, half the one of the vertical force (3.2-d). This slow period is associated to the cyclic upward and downward wake deviation. Due to the wake deviation symmetry along a flapping period, upward and downward deviation are spatio-temporally symmetric, the vertical force averaged along the slow period is zero. The horizontal velocities are similar for deviation in both senses, resulting in their half slow period compared to the vertical force. This same spatio-temporal symmetry, in upward and downward strokes in this case, results in a half vertical force period (or flapping period) for the SPW propulsive solution horizontal velocity (see figure 3.2-b,e). Besides the frequency of twice the flapping one, the SPW propulsive solution horizontal velocity time signal present a small amplitude oscillation around a non-zero time-averaged value. The time-averaged value reached by the horizontal velocity is much greater than the propulsive solutions existing for $4 \leq \beta \leq 9.58$ in our previous study (Benetti Ramos et al. 2020). The Reynolds number based on these $Re =< u_g > \beta$ reaches an order $10 - 100$, an increase of one order of magnitude when compared to the previous low Stokes number regime. Since this solution respects the spatio-temporal symmetry, the vertical force acting on the foil goes through positive and negative values within a flapping period (3.2-e) around a zero time average. For DPW solution this symmetry is lost due to the wake deviation. A frequency equal to the flapping one in both horizontal velocity and vertical force is then observed (figure 3.2-c,f). Deviated wake periodic solution present a non-zero positive (negative) time-averaged vertical force associated to upward (downward) wake deviation. This wake deviation, as the propulsion direction, can occur both in upward and downward directions depending solely on the initial conditions applied to the system.

(1) Deviated quasi-periodic wake (DQPW), (2) symmetric periodic wake (SPW) and (3)

deviated periodic wake (DPW) propulsive solutions are summarized in figure 3.3 respectively identified by violet, red and yellow background colors. The horizontal velocity is shown in (a) by its time-average value $< u_g >$ (represented by dots) and its amplitude (error bars). This time-average is executed along many periods and, in the case of quasi-periodic solutions, enclose an entire slow period. The frequencies f of the horizontal velocity time signal are shown in (b) whereas the time-averaged vertical forces $< F_y >$ in (c). This summary is a detailed description of the return to coherent propulsion for a rectangular symmetric foil. A similar scenario of the frontiers between non-propulsive, coherent and non-coherent propulsion has been drawn by Alben and Shelley (2005) for an ellipse of aspect ratio $h = 0.1$, flapping at a constant amplitude $A = 0.5$ for several density ratios in the range $1 \leq \rho \leq 100$. DQPW solutions have not been described in this scenario and are the great novelty of the present results.

As we can see from Figure 3.3, a coherent state of locomotion is retrieved for $\beta = 20$. Unidirectional propulsive solutions are obtained after non-coherent back & forth motion around a fixed point, as is the case in Alben and Shelley (2005). Back & forth solutions, studied in detail in a previous work (Benetti Ramos et al. 2020) present a large oscillation amplitude but zero time-averaged velocities. This velocity behaviour is linked to the slow oscillation of the foil around a mean position, whose very small frequencies tend to zero as β tends to 20. For $20 \leq \beta < 22.5$ deviated quasi-periodic wake propulsive solutions are obtained, with the quasi-periodic nature of the back & forth solutions being retained. The quasi-periodicity is, now, associated to the periodic wake deviation and not to a direction switching. The characteristic frequencies of the DQPW solution are the flapping one 1, since wake deviation breaks the spatio-temporal symmetry, and the cyclic wake deviation frequency of $O(10^{-1})$. During a transition range ($20 \leq \beta \leq 20.5$) identified by a hatched path, the small frequency of order $O(10^{-2})$ of back & forth solutions is retained. This range will be further discussed in §3.4. For $22.5 \leq \beta < 27$ propulsive solutions with a symmetric periodic wake (SPW) are obtained. SPW solutions are characterized by a non-zero time-averaged velocity and a frequency of twice the flapping one. Finally, this frequency becomes one when the wake spatio-temporal symmetry is broken for $\beta \geq 27$. Propulsive solutions with deviated periodic wakes (DPW) are obtained. This transition to wake deviation is captured due to the solutions non-zero time-averaged vertical force, visible in figure 3.3(c). At the onset of DPW solutions we do not observe a particular increase of the time-averaged horizontal velocity. Nevertheless, a significant increase is obtained for $\beta \geq 29$. This velocity increase is not associated to any major transition in the self-propelled dynamics. The only visible feature acquired by the flow is the wake deviation taking place immediately behind the foil trailing edge.

3.3 Local bifurcation of symmetric periodic wake propulsive solutions

The emergence of DQPW and DPW propulsive solutions is investigated by the nonlinear bifurcation and fluid-solid Floquet stability of SPW propulsive solutions. The nonlinear bifurcation method, that couples time-spectral method (TSM) to pseudo arc-length continuation, is introduced in §3.3.1. Fluid-solid Floquet stability analysis is then presented in §3.3.2. The results of SPW continuation and their stability are presented (§3.3.3) by carefully describing the branch obtained through numerical continuation and its stability. This analysis is followed by the study of the unstable modes, which are discussed in light of the previously described nonlinear

self-propelled solutions.

3.3.1 Time Spectral Method and Pseudo Arc-Length continuation

The studied problem possess the inherent periodicity of the imposed flapping movement. This is retained by some of the nonlinear regimes seen in the previous section, i.e. SPW propulsive solutions. Harmonic balance methods, such as the Time Spectral Method (TSM) (Gopinath and Jameson 2005), can take advantage of this time-periodicity to solve directly for the limit cycle rather than following the temporal evolution in unsteady nonlinear simulations up to saturation. This strategy consists in rewriting in a spectral form the originally unsteady problem eq. (3.4). An identical expression can be written for several time instants along a period

$$\mathbf{B}\frac{\partial Q}{\partial t} = \mathbf{R}(Q, v_g), \tag{3.7}$$

where $\mathbf{B}$ is a matrix of diagonal entries equal to $\mathcal{B}$ and Q regroups $2N+1$ time instants

$$Q = \left[\mathbf{q}(\mathbf{x}, t_0), \mathbf{q}\left(\mathbf{x}, t_0 + \frac{1}{2N+1}\right), ..., \mathbf{q}\left(\mathbf{x}, t_0 + \frac{2N}{2N+1}\right)\right]^T, \tag{3.8}$$

and the vector $\mathbf{R}$ the related spatial operators

$$\mathbf{R} = \left[\mathcal{R}(\mathbf{q}(\mathbf{x}, t_0)), ..., \mathcal{R}\left(\mathbf{q}\left(\mathbf{x}, t_0 + \frac{2N}{2N+1}\right)\right)\right]^T. \tag{3.9}$$

These $2N+1$ instants are used to determine, following the Nyquist-Shannon criterion (Gopinath and Jameson 2005), the spectral content of N harmonics, contained in the vector $\hat{Q}$

$$\hat{Q} = [\hat{\mathbf{q}}_{-N}(\mathbf{x}), ..., \hat{\mathbf{q}}_0(\mathbf{x}), ..., \hat{\mathbf{q}}_N(\mathbf{x})]^T, \tag{3.10}$$

through application of discrete $\hat{Q} = \mathcal{F}Q$ and inverse discrete Fourier transforms $Q = \mathcal{F}^{-1}\hat{Q}$, resp. defined as

$$\mathcal{F}_{n,k} = \frac{1}{2N+1}\exp\left(\frac{-i2k\pi(n-N)}{2N+1}\right),\ \mathcal{F}^{-1}_{n,k} = \exp\left(\frac{i2k\pi(n-N)}{2N+1}\right), \tag{3.11}$$

the continuous time-differential operator can be approximated by a discrete spectral time-domain equivalent as

$$\frac{\partial Q}{\partial t} \approx \frac{\partial}{\partial t}(\mathcal{F}^{-1}\hat{Q}) = \frac{\partial \mathcal{F}^{-1}}{\partial t}\hat{Q} = \underbrace{\mathcal{F}^{-1}\Lambda\mathcal{F}}_{\mathcal{D}_\omega} Q\,. \tag{3.12}$$

Here $\Lambda_{n,n} = (i2\pi(n-N)/2N+1)$ is a diagonal matrix that contains the time-derivative of the inverse Fourier transform coefficients for the n-th harmonic. $\mathcal{D}_\omega$ is finally the spectral version (in time) of the time-differential operator composed of off-diagonal coefficients

$$(\mathcal{D}_\omega)_{i,j} = \begin{cases} \pi(-1)^{(i-j)}\csc\left(\dfrac{\pi(i-j)}{2N+1}\right), & \text{if } (i-j) \neq 0 \\ 0, & \text{if } (i-j) = 0 \end{cases}. \tag{3.13}$$

This time-differential operator couples all the time instants together. The TSM system of equations is finally written in a synthetic form

$$\mathcal{N}_{TSM}(Q) = \mathbf{B}\mathcal{D}_\omega Q - \mathbf{R}(Q, v_g) = 0\,. \tag{3.14}$$

The Time Spectral Method transforms thus the unsteady eqs. (3.4), into a stationary system eq. (3.14). Its root can be sought through a proper method for the resolution of nonlinear steady problems such as Newton's method. The great advantage of this kind of resolution is that unstable roots of the system of equations can be obtained, the convergence to these only depending on the initial guess fed to the algorithm. This is the case for example when the steady Navier-Stokes equation is solved for determining unstable base-flows (i.e. Sipp and Lebedev (2007) and Tchoufag, Fabre, and Magnaudet (2014) and many others).

The great computational challenge from the TSM is the resultant large scale linear system. To efficiently solve this problem we use an iterative resolution (GMRES) with a preconditionning strategy based on the approximation of the TSM Jacobian $\dfrac{\partial \mathcal{R}}{\partial Q}$ by the block-circulant matrix $\mathbf{C} = \mathcal{D}_\omega - \dfrac{\partial \mathcal{R}}{\partial Q}(\langle Q \rangle)$. This circulant matrix, which is easily diagonalizable (Schmid, De Pando, and Peake 2017), includes the time-derivative operator and the stationary Jacobian with respect to the time-averaged over a flapping period solution $\langle Q \rangle$. This strategy is thus robust with respect to the number of harmonics, but not with the fluctuation around this mean-solution. The continuation of the solution through the variation of the Stokes number was based on a pseudo arc-lenght continuation (Govaerts 2000), rather than a constant evolution of the Stokes number. This continuation strategy allows to follow the branch even when turning points and fold bifurcations are present. This numerical method is implemented in FreeFEM exploiting its interface with PETSc (Balay et al. 2015). The method has been cross-validated against the unsteady nonlinear solver employed in this work. Twenty-two harmonics have been necessary to reduce the L_1-norm of the difference of the periodic-cycle obtained by the two-methods under 10^{-6} for a Stokes number of $\beta = 32$ and this value was thus employed throughout our entire study.

3.3.2 Fluid-solid Floquet stability analysis of self-propelled foils

Infinitesimal perturbations ($\epsilon \ll 1$) are superimposed to the periodic base solution $(\mathbf{u_b}, p_b, u_{g,b})$

$$(\mathbf{u}, p, u_g) = (\mathbf{u}_b, p_b, u_{g,b}) + \epsilon(\mathbf{u}', p', u_g'), \tag{3.15}$$

where both base-flow $(\mathbf{u}', p')$ and the foil horizontal velocity u_g' are perturbed. No perturbation of the vertical velocity $\mathbf{v}_g$ is considered since this movement is imposed. The dynamics of the perturbations are governed at leading order by the following system of equations

$$\mathcal{B}\frac{\partial}{\partial t}\underbrace{\begin{bmatrix}\mathbf{u}'\\ p'\\ u_g'\end{bmatrix}}_{\mathbf{q}'} = \underbrace{\begin{bmatrix} -\left[(\mathbf{u}_b(t) - \mathbf{u}_{g,b}(t))\cdot\boldsymbol{\nabla}\right] - \boldsymbol{\nabla}\mathbf{u}_b(t) + \beta^{-1}\boldsymbol{\Delta} & -\boldsymbol{\nabla} & (\boldsymbol{\nabla}\mathbf{u}_b)\cdot\mathbf{e}_x \\ -\boldsymbol{\nabla} & 0 & 0 \\ (\rho S)^{-1}\mathcal{F}_v & (\rho S)^{-1}\mathcal{F}_p & 0 \end{bmatrix}}_{\mathcal{L}(\mathbf{u}_b, p_b, \mathbf{u}_{g,b})} \begin{bmatrix}\mathbf{u}'\\ p'\\ u_g'\end{bmatrix} \tag{3.16}$$

The first two rows are the linearized momentum and mass equations governing the fluid velocity and pressure perturbations. They are coupled to the foil velocity perturbation u_g' via two

terms: firstly, the bulk term $(\boldsymbol{\nabla}\mathbf{u}_b)\cdot\mathbf{e}_x$ (block $(1,3)$ in the right-hand side matrix) that modifies the production of fluid perturbation in the momentum equation, and secondly, the boundary conditions at the foil surface Γ_w, where the equality of fluid and solid perturbations holds

$$(u',v')(\mathbf{x}_w,t) = (u'_g,0)\,. \tag{3.17}$$

The third row indicates that the horizontal acceleration of the foil is equal to the horizontal force exerted by the flow perturbation, which is here separated into viscous $\mathcal{F}_v$ and pressure $\mathcal{F}_p$ contributions, respectively defined as

$$\mathcal{F}_v(\mathbf{u}') = \beta^{-1}\int_{\Gamma_w}(\nabla\mathbf{u}' + \nabla\mathbf{u}'^T)\cdot\mathbf{n})\cdot\mathbf{e}_\mathbf{x}\,\mathrm{d}\Gamma_w \quad , \quad \mathcal{F}_p(p') = \int_{\Gamma_w}(-p'\mathbf{n})\cdot\mathbf{e}_\mathbf{x}\,\mathrm{d}\Gamma_w\,. \tag{3.18}$$

Following Elston, Sheridan, and Blackburn (2004) or Jallas, Marquet, and Fabre (2017), the perturbations are further decomposed in the form

$$\mathbf{q}'(\mathbf{x},t) = \sum\left(\hat{\mathbf{q}}_j(\mathbf{x},t)e^{\lambda_j t} + \text{c.c.}\right), \tag{3.19}$$

where $\hat{\mathbf{q}}_j$ are T-periodic functions, called the Floquet modes, associated to the complex numbers λ_j, called the Floquet exponents. The Floquet multiplier $\mu_j = e^{\lambda_j T}$, rather used in the following, represents the complex amplitude gain of the periodic Floquet mode over one period, i.e. $\hat{\mathbf{q}}_j(\mathbf{x},T) = \mu_j\hat{\mathbf{q}}_j(\mathbf{x},0)$. The Floquet multiplier can be decomposed as $\mu_j = |\mu_j|e^{\mathrm{i}\phi_j}$, with its modulus $|\mu_j|$ quantifying the growth (or decay) of the corresponding Floquet mode and ϕ_j representing its phase shift over a period. The stability of the periodic base solution is then addressed by considering the Floquet multiplier with largest modulus where if $|\mu_0|$ is greater than one the corresponding Floquet mode will grow over one period and the periodic base solution is unstable. When the leading Floquet multiplier is real ($\phi_0 = 0$), the Floquet mode is *synchronous* and the perturbation evolves in time with the period of the base flow. When the leading Floquet multiplier is complex ($\phi_0 \neq 0$) the mode is *asynchronous* and a frequency, denoted f' and related to the phase of the Floquet mode as $f' = \phi_0/(2\pi)$ is introduced.

To compute Floquet modes we employed the strategy proposed by Barkley and Henderson (1996). We assess the stability of an initial perturbation through the action of the propagator over one period $\boldsymbol{\Phi}$ – Monodromy matrix – whose action over the perturbation at an arbitrary initial time t_0, formally denoted $\mathbf{q}'(\mathbf{x},t_0+T) = \boldsymbol{\Phi}\,\mathbf{q}'(\mathbf{x},t_0)$, is obtained by time-integration along a period of the linearized equations (3.16). The temporal and numerical discretization schemes previously described for the nonlinear method are again employed. An Arnoldi method with a modified Gram-Schmidt algorithm for the orthogonalization step (Saad 2011) is implemented in the FreeFEM software (Hecht 2012) to approximate the Monodromy matrix in a low-dimensional space. The eigenvalues of this reduced matrix approximate the Floquet multiplier and its eigenvectors allow reconstructing the Floquet modes at the initial time, i.e. $\hat{\mathbf{q}}(\mathbf{x},t_0)$. A minimal number of 30 Arnoldi vectors is used in the following, this number being further increased in steps of 10 when necessary in order for the dominant eigenvalue to converge to five significant digits. All computed modes are normalised by the kinetic energy of the coupled fluid-solid system. This method has been equaly validated at Benetti Ramos et al. (2020).

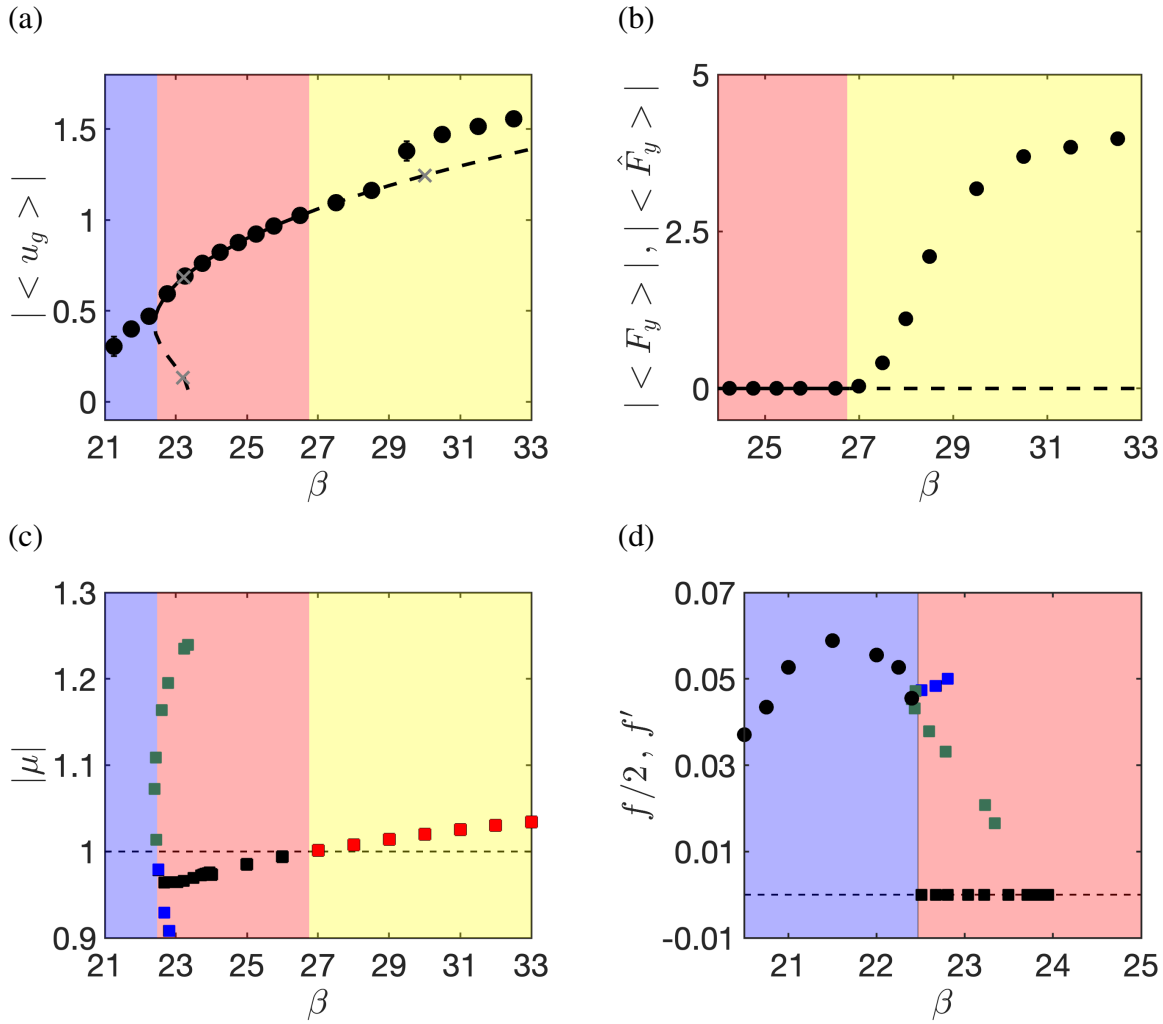

Figure 3.4: Time spectral method continuation (thick lines – solid/dashed lines indicating stable/unstable solutions) of SPW propulsive solutions and the branch fluid-solid Floquet stability (squares) compared to unsteady nonlinear results (circles). (a) Evolution of the absolute value of the time-averaged horizontal velocity and (b) vertical force as a function of the Stokes number β. The three grey $\times$ in (a) highlight solutions shown in Fig. 3.5. Leading Floquet multiplier (c) absolute value and (d) frequency evolution with the Stokes number – in (d) the frequency of the vertical force (half the one of the horizontal velocity $f/2$) is displayed for comparison. Stable (unstable) synchronous (asynchronous) modes are resp. identified by black (blue) and red (green) colors.

3.3.3 TSM continuation and stability analysis results

SPW propulsive solutions obtained with TSM pseudo arc-length continuation and the branch fluid-solid Floquet stability results are depicted in figure 3.4. TSM solutions were obtained for Stokes numbers $22.4 \leq \beta \leq 36$ by adopting an increasing and decreasing direction for the continuation starting from a SPW solution at $\beta = 24$. Although a positive velocity is shown, a branch of negative velocity can equally be obtained. While raising the Stokes number ($\beta \geq 24$), the time-averaged velocity (3.4-a) increases monotonically along the branch. When β reaches values above 29 the branch does not pass through the velocity increase undergone by DPW solutions. The time-averaged vertical force (3.4-b) of the TSM solutions is always zero, differing from nonlinear solutions for $\beta \geq 27$. This is due to the conserved symmetry of the reversed Von-Kármán wake behind the foil, that will be further discussed in figure 3.5. Decreasing the Stokes number, a fold bifurcation is obtained at $\beta = 22.4$. In this saddle-node of periodic solutions, multiple solutions exist for a single value of Stokes number in the interval $22.4 \leq \beta \leq 23.5$. For $\beta = 23.5$ in the lower part of the saddle branch, the solution approaches a zero time-averaged velocity. A further continuation of the branch however did not reach symmetric non-propulsive solutions. Although possible, this continuation of the SPW branch has not been pursued as the results here described are sufficient to explain the transition to DQPW and DPW nonlinear regimes.

The fluid-solid Floquet stability analysis of the TSM branch identified two regions, dashed lines in figures 3.4 (a) and (b), where the leading Floquet multiplier (3.4-c) becomes unstable ($|\mu| > 1$). The first region occurs for $\beta \geq 27$, a region where TSM and unsteady nonlinear solutions present a disagreement concerning the time-averaged vertical force and the wake deviation. Unstable synchronous modes that do not modify the base-solution periodicity are obtained in this region. The saddle-node branch that appears for $22.4 \leq \beta \leq 23.5$, on the other hand, presents unstable asynchronous modes. In this second region, the branch becomes unstable shortly before ($\beta = 22.45$) the turning point of the fold bifurcation. The unstable TSM solutions are mainly the coexisting limit cycles observed in figure 3.4 (a). We remark that, different than steady solutions fold bifurcations, the mode that becomes unstable is not necessarily a zero-frequency eigenvalue at the turning point (Iooss and Joseph 1997). In the intermediary region, for $22.45 \leq \beta \leq 27$, the branch is stable. The modes that become unstable in the saddle branch and for $\beta \geq 27$ belong to distinct branches (see 3.4-c). The asynchronous mode that is destabilized for $\beta = 22.45$ appears for $\beta \approx 23$, below the synchronous multiplier branch. This branch of asynchronous multipliers ($|\mu| > 1$, $f' \neq 0$), and more precisely the multiplier destabilized for $\beta = 22.45$, introduce in the base solution a small frequency. The value of the Floquet predicted frequency, represented in figure (3.4-d), matches very well that of the DQPW propulsive solutions vertical force (thus half the one of the velocity $f/2$) at the asynchronous multiplier threshold.

To illustrate the evolution of the flow along this branch, the vorticity field of three solutions is shown in figure 3.5. The position of these solutions along the branch is previously highlighted in figure 3.4(a). All solutions are very similar to the SPW one previously shown in figure 3.1. Starting from $\beta = 30$, we observe a SPW solution with a wake that does not deviate or break the spatio-temporal symmetry, as the DPW solution of same β value in figure 3.1. As the Stokes number is decreased so is the the time-averaged horizontal velocity of the foil. Diffusive effects become more important and the wake behind the flapping foil progressively decreases in length ($\beta = 23.2$ in b). The wake behind the foil is reduced until only a vortex dipole remains. This

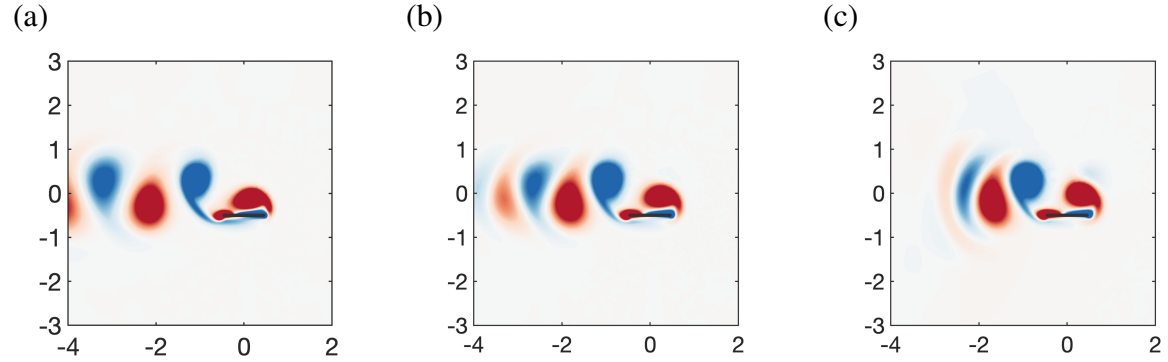

Figure 3.5: Symmetric periodic wake propulsive solutions obtained with the Time Spectral Methods. The three solutions represented are the grey × in figure 3.4 progressively decreasing the horizontal speed (a) $\beta = 30$, (b) $\beta = 23.2$ and (c) $\beta = 23.2$ (inside the saddle branch). The same scale as fig. 3.1 is used for the contours.

is the case for all solutions at the saddle-node branch, illustrated by the coexisting solution for $\beta = 23.2$ in (c). The two coexisting solutions for $22.4 \leq \beta \leq 23.5$ are generally one with a greater time-averaged horizontal velocity and a fully developed wake, as in (b), and another with a wake constituted of a vortex dipole with a smaller time-averaged velocity, as in (c). All these solutions feature the same time-periodicity, horizontal velocity and vertical force behaviour as the typical SPW propulsive solution discussed in figure 3.2.

A zoom of the saddle-node branch and phase portraits of horizontal force and velocity, figure 3.6, depicts the collision of limit cycles at the saddle-node bifurcation and the transition between SPW and DQPW propulsive solutions. The zoom in the TSM branch superposed with unsteady nonlinear solutions, (3.6-a), reveals that the instability of this branch occurs shortly before the limit cycles collision at the turning point $\beta = 22.4$. Figure (3.6-b) shows the the coexisting limit cycles of the branch near the onset. For a Stokes number $\beta = 22.6$ two limit cycles exist, one stable at a higher horizontal velocity and a second unstable of smaller horizontal velocity u_g and force F_x. As β is progressively decreased these coexisting orbits approach themselves at $\beta = 22.45$. At this point, however, the two limit cycles are unstable. Unsteady nonlinear solutions for this β departing from both unstable cycles converge towards the same DQPW propulsive solution. The phase portrait of the quasi-periodic solution is depicted in figure 3.6(c). It consists of a thicker orbit, composed of multiple ellipses instead of a single one as in the SPW case. Superposing to this portrait the SPW one of higher horizontal velocity indicates the DQPW solutions appear as an instability of the unstable SPW limit cycle. Interestingly the faith of the lower horizontal velocity SPW unstable orbit, 3.6(d), is the same previous DQPW solution existing at a higher horizontal velocity.

Unstable synchronous and asynchronous fluid-solid Floquet modes are present over the symmetry preserved wake solutions in the same region ($\beta \geq 27$) of DPW and in the transition threshold between DQPW and SPW solutions. The unstable modes also feature a similar time-periodicity as these nonlinear regimes. In the next subsections, the unstable Floquet modes are thus analysed to investigate either their internal mechanisms can shed further insights on the emergence of DQPW and DPW nonlinear solutions.

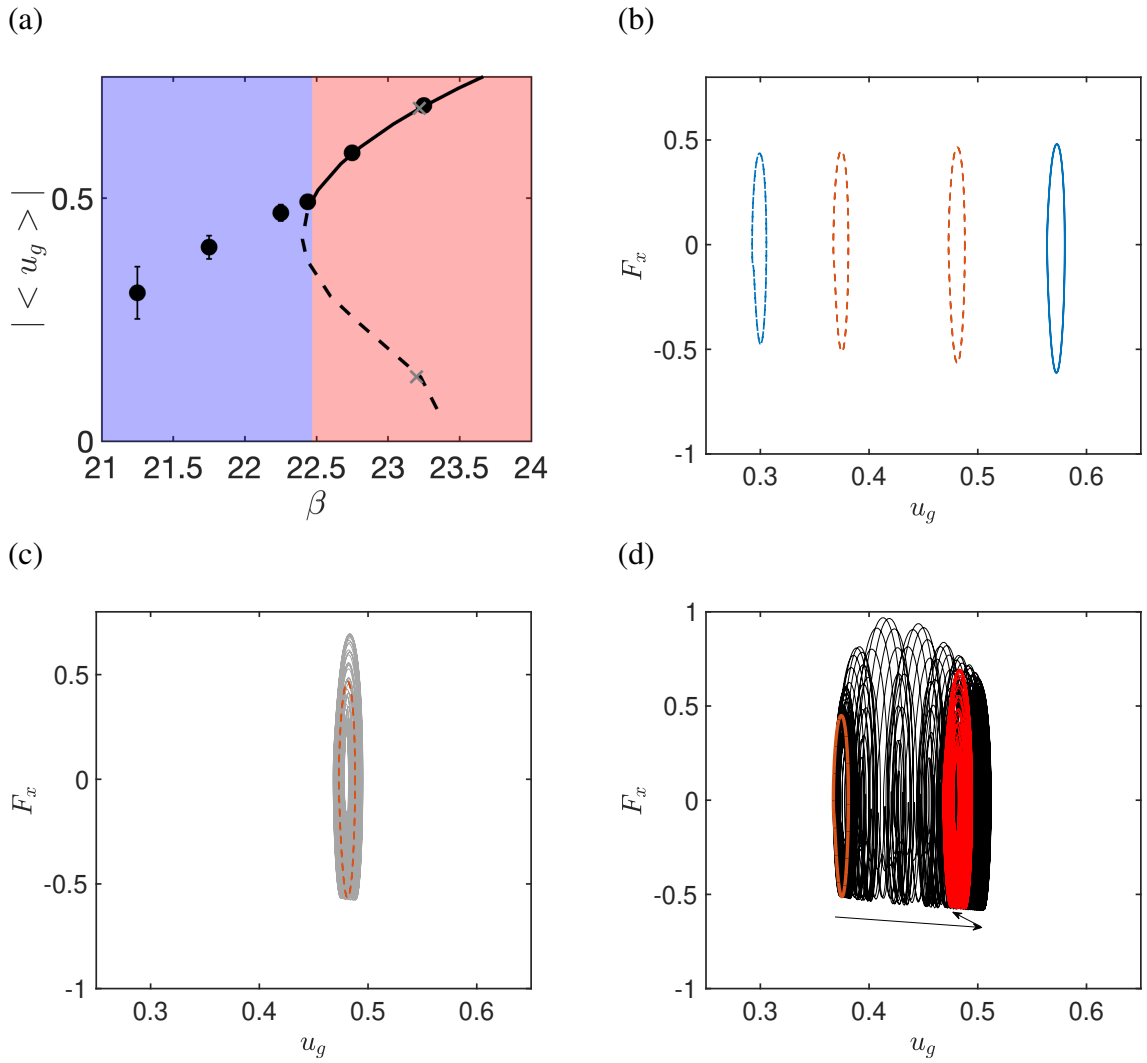

Figure 3.6: (a) Zoom in the horizontal velocity comparison between the TSM and unsteady nonlinear solutions. Phase portraits of horizontal force and velocity for (b) four TSM solutions – $\beta = 22.6$ (blue lines) and $\beta = 22.45$ (orange lines) – (c) A DQPW solution for $\beta = 22.45$ and (d) transient regime departing for the $\beta = 22.45$ lower unstable solution. An arrow indicates the temporal evolution of the solution. Its final state is the DQPW orbit shown in (c) here depicted in red. Solid lines represent stable solutions while dashed lines represent unstable solutions.

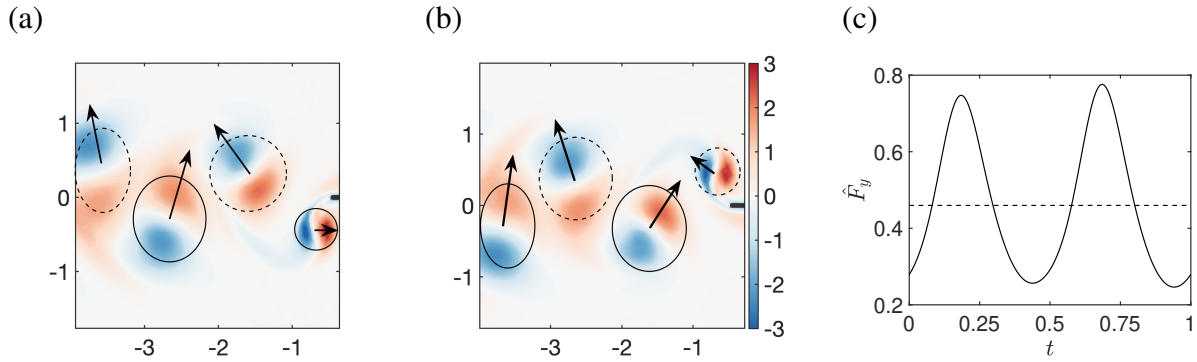

Figure 3.7: Unstable synchronous mode for $\beta = 30$: (a,b) perturbation vorticity contours for $t = 0.25$ and $t = 0.75$ and base flow positive (resp. negative) vortex contours represented by solid (resp. dashed) lines. Arrows indicate the core displacement of the base-flow vortex due to the perturbation. (c) Vertical force acting on the foil with its time-averaged value represented by a dashed line.

3.3.3.1 Synchronous wake deviation mode

The unstable synchronous Floquet mode existent for Stokes numbers $\beta \geq 27$ is characterized for a representative value $\beta = 30$ in figure 3.7. Its action mainly lies over the wake behind the flapping foil, as seen by the superposition of mode and base-flow vorticity for two equally spaced time instants along a flapping period 3.7(a,b). This superposition reveals that the perturbation consists of vortex dipoles acting on base-flow monopoles. The mode bears a great similarity to the one obtained by Jallas, Marquet, and Fabre (2017) for the wake deviation of a non-propelled foil. Its instantaneous superposition over the base-flow (represented by thick black lines) is similar to displacement modes (Fabre, Sipp, and Jacquin 2006; Brion, Sipp, and Jacquin 2014). The perturbation generates a net displacement of the vortex core due to simultaneous increase/decrease of the base-flow vorticity. As shown in figure 3.7(a,b), the effect of this perturbation over time instants (a) $t = 0.25$ and (b) $t = 0.75$ is to form vortex dipoles. The horizontal and vertical core displacement of nearby vortices approach them and displace the whole wake in the upward y direction, originating the deviation observed in nonlinear simulations. This upward deviation is sustained across the whole period. As the mode is invariant in amplitude, a negative perturbation could equally sustain a downward wake deviation along the flapping period. The vertical force acting on the foil, 3.7(c), oscillates around a non-zero time-average that is of the same sign of the wake deviation. An upward deviation (positive y) implies a positive time-averaged vertical force. This mode is capable of originating the wake deviation and the non-zero time-averaged vertical force exhibited by deviated periodic wake (DPW) solutions in this Stokes number range.

This periodic wake deviation mode generates perturbations of the foil horizontal velocity and forces. Those are, however, not displayed since they present a very low amplitude, $O(10^{-3})$, undergoing positive and negative values along a flapping period and oscillating around a zero time-average. This zero average allow us to understand why TSM-SPW and nonlinear DPW solutions present the same average velocity for $27 \leq \beta \leq 29$. However, it does not explain the increase of the average horizontal velocity observed for $\beta \geq 29$. Similar to the case of Jallas,

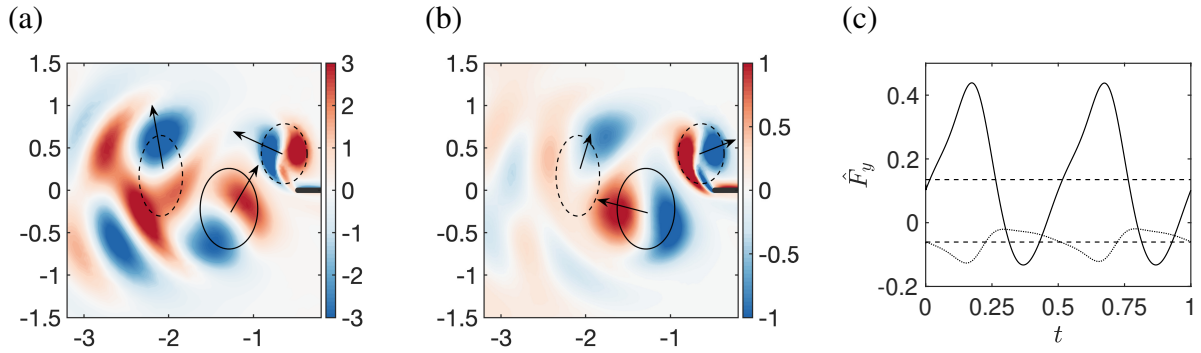

Figure 3.8: Unstable asynchronous mode for $\beta = 22.43$: perturbation vorticity contours of the (a) real part and (b) imaginary part for $t = 0.75$. Solid and dashed superposed thick lines represent positive and negative values of the base-flow vorticity. Arrows indicate the core displacement of the base-flow vortex due to the perturbation. (c) Real (solid line) and imaginary (dotted line) parts of the vertical force where a dashed line indicate its time-averaged value.

Marquet, and Fabre (2017), where the non-propelled foil wake deviation mode is incapable of explaining the increase of the foil thrust, the self-propelled periodic wake deviation mode is incapable of producing a time-averaged increase of the foil horizontal velocity. We imagine that nonlinear effects, observed by Jallas, Marquet, and Fabre (2017) to be the source of the sharp increase in the horizontal thrust of non-propelled foils beyond the threshold of the Floquet instability, might be the source of the horizontal velocity increase.

3.3.3.2 Quasi-periodic wake deviation mode

The asynchronous Floquet modes that gets unstable at the saddle-node branch is presented in figure 3.8 for $\beta = 22.4$. The instantaneous real and imaginary parts of the vorticity contours for $t = 0.25$ are displayed in 3.8(a,b). The amplitude of the real part is three times larger than the imaginary one. Both their spatial structures consist of two very clear vortex dipoles centered around base-flow monopoles (solid and dashed lines for positive and negative vorticity). Further away, the perturbation slowly vanishes as diffusive effects come to play. Similar to the synchronous case, these two complex parts are vortex-core displacement modes. The orientation of the perturbation dipoles and their generated displacement is, however, quite different for each complex part. The real part tends to assemble the base-flow vortex in dipoles and displace them upward, visible in 3.8(a). The perturbation superposed to the base-flow generates on the first (second) base-flow vortex starting at the trailing edge an increase of its negative (positive) vorticity on its upper left (right) corner, resulting on the approximation of these vortex as to form a dipole displaced upward. The imaginary part, on the other hand, tends to separate the vortex. In 3.8(b), the negative base-flow vortex is moved to the right by an increase of its vorticity on its right portion whereas the positive vortex is reinforced on its upper left portion. These contrasting complex parts flow effects are translated in their vertical force (figure 3.8-c), where real and imaginary parts are out-of-phase and have opposite effects. The first one presents a positive time-average along a flapping period whereas the second one presents a negative one. The imaginary part is smaller than the real part owing to its smaller flow amplitude. The vertical force frequency is twice rather than one. This fact comes from the spatio-temporal

asymmetry of the perturbation, which results in an equal vertical force during upward and downward strokes. The horizontal velocity and force, as for the synchronous mode, oscillate around a zero time-averaged value, and have a small amplitude in both cases. The mode thus, do not generate in neither case an increase of the self-propelled velocity.

To further study the interplay of the mode real and imaginary parts we study the real *quasi-periodic* perturbation $\tilde{\mathbf{q}} = \mathbf{q}' e^{-\lambda_r t}$. Its temporal evolution can be developed as

$$\tilde{\mathbf{q}}(\mathbf{x}, t, t_\epsilon) = \Re(\hat{\mathbf{q}})(\mathbf{x}, t)\cos(2\pi t_\epsilon) - \Im(\hat{\mathbf{q}})(\mathbf{x}, t)\sin(2\pi t_\epsilon), \tag{3.20}$$

where we have introduced the slow time scale $t_\epsilon = f' t$ since the frequency of the Floquet exponent $f' \ll 1$ is small compared to the frequency of the Floquet mode. For $t_\epsilon \sim 0$, the quasi-periodic perturbation should be dominated by the real part of the periodic Floquet mode $\Re(\hat{\mathbf{q}})(\mathbf{x}, t)$, while for $t_\epsilon \sim 0.25$, it should be dominated by its imaginary part $\Im(\hat{\mathbf{q}})(\mathbf{x}, t)$. The quasi-periodic perturbation thus slowly evolves between the real and imaginary parts of the Floquet mode, on a time scale given by the low frequency of this asynchronous Floquet mode.

The temporal evolution of the quasi-periodic perturbation is displayed in figure 3.9. This perturbation is similar to the real part of the Floquet mode at times $t_\epsilon = 0$ and $t_\epsilon = 0.5$, 3.9(a,b). It respectively deviates the wake upward and downward at these instants, as the Floquet multiplier imaginary part modulation induces a sign inversion at the second half of the slow period. The action of the real part of the Floquet mode are predominant when compared to the imaginary one. This is clear when analysing the forces acting on the foil and its horizontal velocity 3.9(c,d). For $t_\epsilon = 0.25$ and $t_\epsilon = 0.75$, all quantities are very small in amplitude. They appear to be a simple transition between the positive and negative amplitude switching of the real part asynchronous mode. The switching between upward and downward deviations, for $t_\epsilon = 0$ and $t_\epsilon = 0.5$, is remarkably clear when regarding the vertical force 3.9(c), which assumes a positive and negative average values in these two instants. The vertical force perturbation goes through positive and negative mean values following the wake upward and downward deviation, but oscillates along the slow period around a zero average. The quasi-periodic horizontal velocity perturbation (d) oscillates around a zero average, as expected due to the zero-time average of both real and imaginary parts of the mode. It presents a slow period of half the one of the vertical force (≈ 10 rather than ≈ 20). This fact is due to the similar effect in the horizontal dynamics of upward and downward wake deviation. The mode does not modify the base-solution time-averaged horizontal velocity and force, but introduces a slow period on the horizontal velocity that is equal to twice the one of the vertical force. These summed observations match completely the behaviour observed in the nonlinear simulations seen for DQPW propulsive solutions in figure 3.1. In addition, the fact that the perturbation does not alters the time-averaged horizontal velocity of the solution offers a possible explanation to the smooth transition between the mean horizontal speed of DQPW and SPW propulsive solutions obtained in unsteady nonlinear simulations (figure 3.3-a).

3.4 Global bifurcation from back & forth to deviated quasi-periodic wake propulsion

In the previous section Floquet stability analyses of the fluid-solid system were used to study the emergence of deviated quasi-periodic wake and deviated periodic wake propulsive solutions.

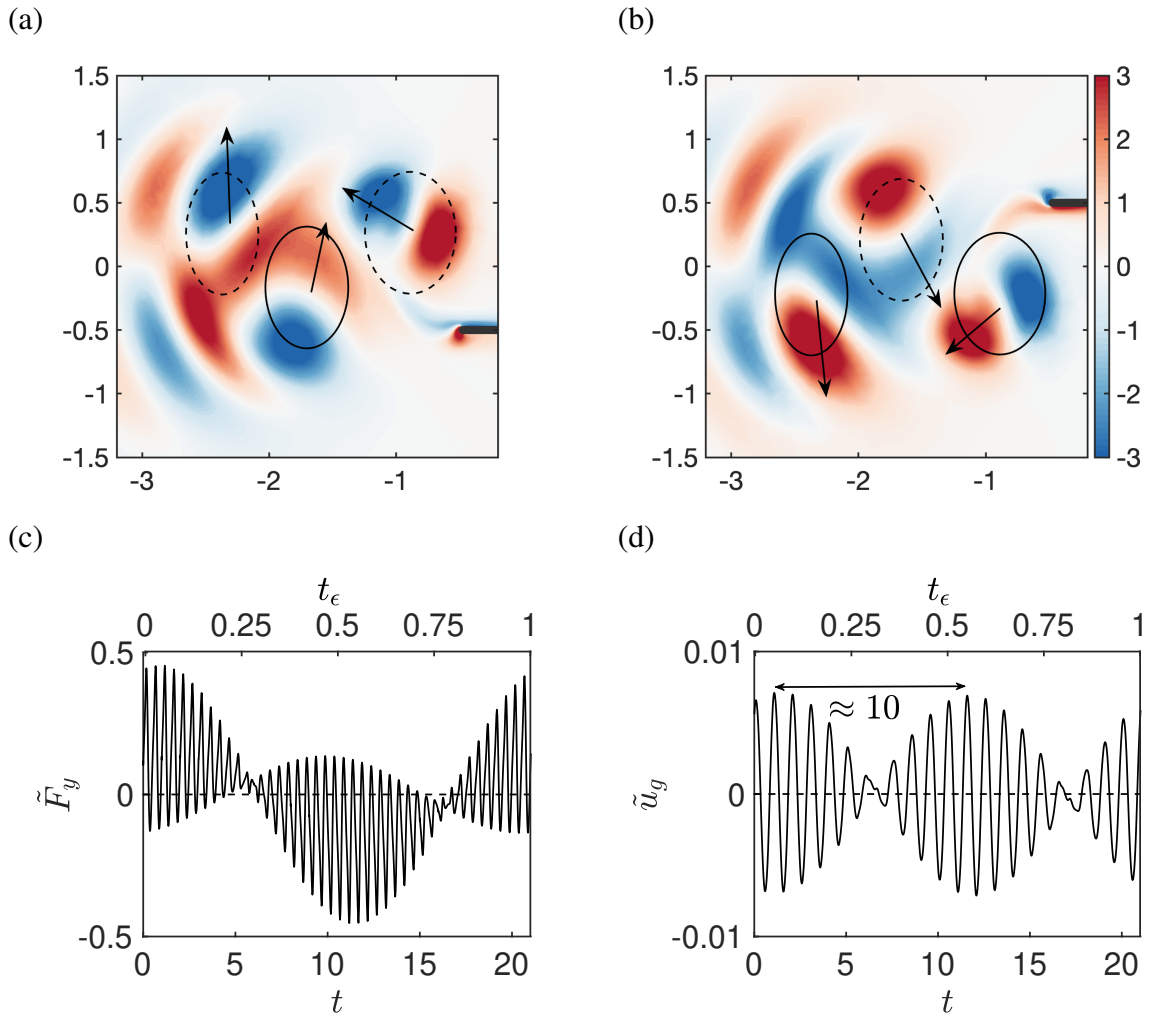

Figure 3.9: Temporal evolution of the quasi-periodic perturbation $\tilde{\mathbf{q}}$ for $\beta = 22.43$: (a,b) Perturbation (colors) and base-flow (with positive values in solid and negative in dashed lines) vorticity for $t_\epsilon = 0$ and $t_\epsilon = 0.5$ of the slow period $T_\epsilon = 1/f' = 23$. (c) Vertical force and (d) horizontal velocity. The time-averaged value of these quantities along the slow period is shown in (c,d) by a dashed line.

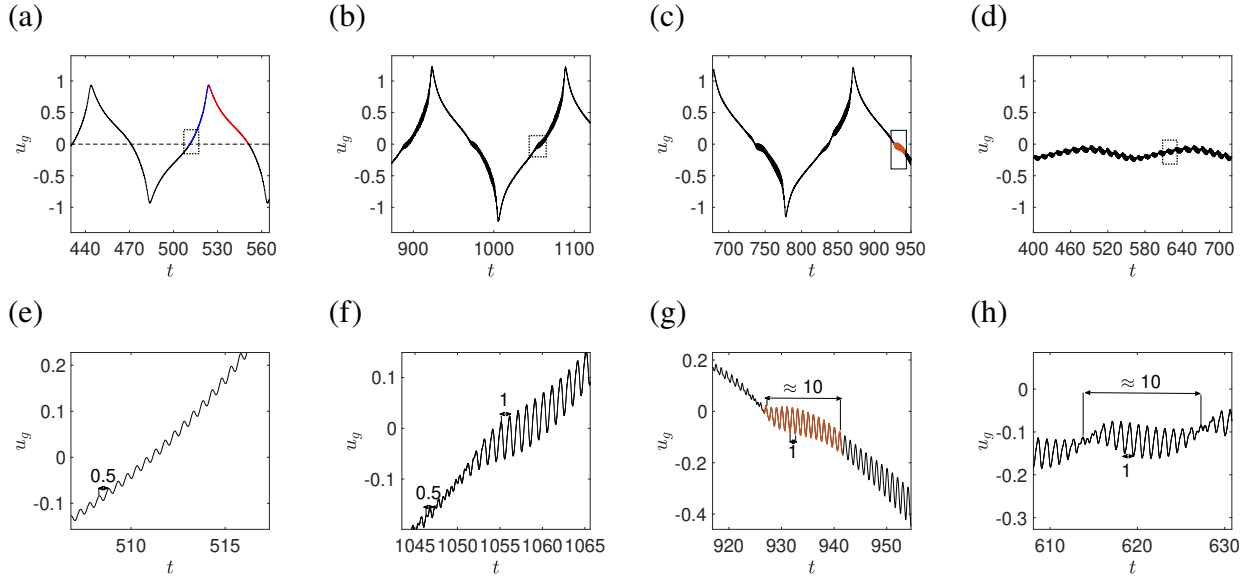

Figure 3.10: Transition from Back & Forth to deviated quasi-periodic wake propulsive solutions: horizontal velocity time signals with close-up views for (a,e) $\beta = 17$, (b,f) $\beta = 19$, (c,g) $\beta = 19.5$ and (d,h) $\beta = 20.25$. This last solution belongs to the DQPW propulsive solutions transition zone (hatched zone in figure 3.3) where two small frequencies are still found. In (a) the red and blue lines identify respectively time ranges where the velocity is accelerated and decelerated. In (c) the orange line identify a horizontal velocity spot.

This method was particularly adapted to these transitions, since they involved bifurcations of the SPW propulsive solution which is periodic. This is, however, not the case for the last transition between DQPW and back & forth propulsion, a transition that involves two quasi-periodic solutions. In this section outputs of unsteady nonlinear simulations will be used to draw a better picture of this transition. We first investigate the appearance of increased amplitude spots of the horizontal velocity time signal in back & forth solutions for $18 \leq \beta \leq 20$. The emergence of wake deviation and frequency modifications in these spots are equally studied. This analysis is followed by the evolution with the Stokes number of phase portraits of horizontal velocity and force of the dynamical system.

Nonlinear simulations revealed that the transition between back & forth solutions and DQPW propulsion presents horizontal velocity spots for $18 \leq \beta \leq 20$. Figure 3.10 shows horizontal velocity time signals for (a-c) three back & forth and (d) the first obtained DQPW propulsive solution. These spots are evident when comparing the time signals of $\beta = 17$ and $\beta = 19$ in figure 3.10(a) and (b). In the first, the horizontal speed evolves in the time scale of one flapping period with a constant amplitude (the line presents a constant thickness) and a mean value that fluctuates between -1 and 1. Due to the back & forth behaviour, velocity goes through acceleration and deceleration phases (that have been highlighted in blue and red for a positive velocity). In the second case, on the other hand, when the horizontal speed approaches 0, either from positive or negative values, its amplitude suddenly increases and we visualize a velocity amplitude thickening. Thickenings can be seen in the close-up views of figures 3.10(e) and (f). In these not only the increase of the oscillation amplitude is comparable, but also the horizontal velocity period switches from 0.5 to 1 when the spot is reached. Such period is

typical of deviated wake propulsive solutions due to the loss of spatio-temporal symmetry, that is generated by the wake deviation for these two solutions.

The emergence of wake deviation is precisely observed in the flow for $\beta = 19$, represented in figure 3.11 for time instants equally separated in 15 flapping periods, identified over a close-up of the horizontal velocity time signal in (3.11-a). As we see, starting at (3.11-c), the wake behind the flapping foil for velocities close to 0 consists merely of a vortex dipole at the foil trailing edge. This dipole is deviated upward as the velocity changes of sign, becoming negative. This deviated dipole (3.11-d,e) keeps the normal suction effect at back & forth solutions direction reversal as described in Benetti Ramos et al. (2020). The deviated periodic wake justifies the unitary frequency observed in (3.10-f), and we remark that the vortex dipole deviation is very similar to the one of DQPW solutions, figure 3.1. In (3.11-f), as the foil velocity increases, the vortex street looses its mean deviation becoming an usual reversed Von-Kármán vortex street. The subsequent deceleration of the foil will shorten this wake up to a vortex dipole, that will again be deviated, this time downward rather than upward.

When the Stokes number β is further increased, the horizontal velocity spot will feature an additional quasi-periodic behaviour. For $\beta \geq 19.5$, figure 3.10(c), we highlight in orange the appearance of this spot of frequency $O(10^{-1})$. Two characteristics differentiates this spot from the previous presented one at $\beta = 19$. In one hand, its time-averaged velocity becomes almost constant during the slow period ≈ 10. In the other hand, the amplitude of the horizontal velocity features a cycle of increase/decrease along the spot. Increasing the Stokes leads to the emergence of DQPW propulsive solutions, such as the one depicted in figure 3.10 (d) for $\beta = 20.25$. Comparing this solution with the back & forth quasi-periodic spot, we see that both spot and DQPW exist exactly at the same velocity range $-0.2 < u_g < 0$. The spot observed for $\beta = 19.5$ is very similar to the $O(10^{-1})$ horizontal velocity oscillation of the DQPW propulsive solution. The DQPW solution appears in fact to be trapped within this spot in this transition zone, retaining the frequency of $O(10^{-2})$ characteristic of back & forth solutions. Furthermore, figure 3.11 reveals that the flow exhibited at the instants marked in 3.11(b) is very similar to the one presented by the spot at $\beta = 19.5$. However, no direction reversal and suction effect of the vortex are observed. A vortex pair is observed at the foil trailing edge, figure 3.11(g-j). The length of the vortex street periodically decreases (g-h) and increases (h-j) as the foil velocity oscillates with the very low frequency of back & forth solutions.

These summed observations lead us to believe that reminiscences of DQPW propulsive solutions are trapped within back & forth solution spots. To visualize this entanglement we recur to phase portraits of horizontal speed and force (acceleration), shown in figure 3.12, of the previously discussed β. In these figures, the evolution of the horizontal velocity and force are depicted through the solutions slow period resulting in a closed curve drawn in the phase space. The first three figures 3.12(a-c) represent the phase portraits of back & forth solutions. The structures depicted by these portraits are centered around the origin $(0, 0)$, consistently with solutions zero time-averaged velocity and self-propelled character (zero acceleration). The shape of a back & forth phase portrait is initially unperturbed for Stokes numbers up to $\beta = 17$, as seen in figure 3.12(a). The obtained curve consists of similar structures for positive and negative velocities. Since the positive velocity side adopt the same color code of figure 3.10(a), we can see that the portrait is composed of an external/ right side structure (in blue) that corresponds to a time window where the velocity is being accelerated, and an internal/ left side structure (in red) when the velocity decays. When the velocity approaches zero it "switches" from the internal to the external structure of the negative velocities. This portrait

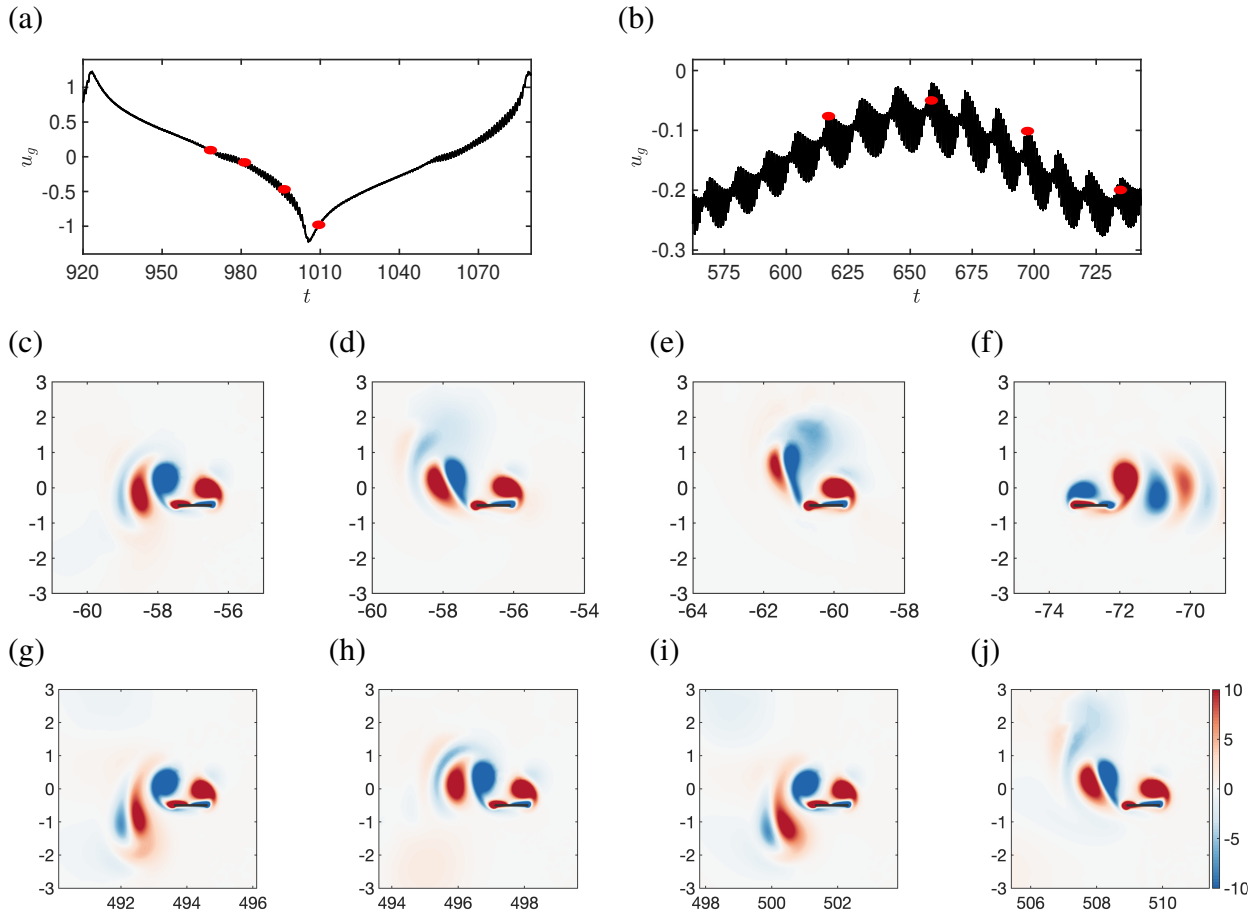

Figure 3.11: Back & Forth solution, $\beta = 19$ - (a) and (c-f), and transition DQPW solution, $\beta = 20.25$ - (b) and (g-j). (a,b) Horizontal speed time signals with red filled circles showing the equidistant time instants of (c-f) and (g-j) where the vorticity contours are presented. Images are presented in different horizontal positions.

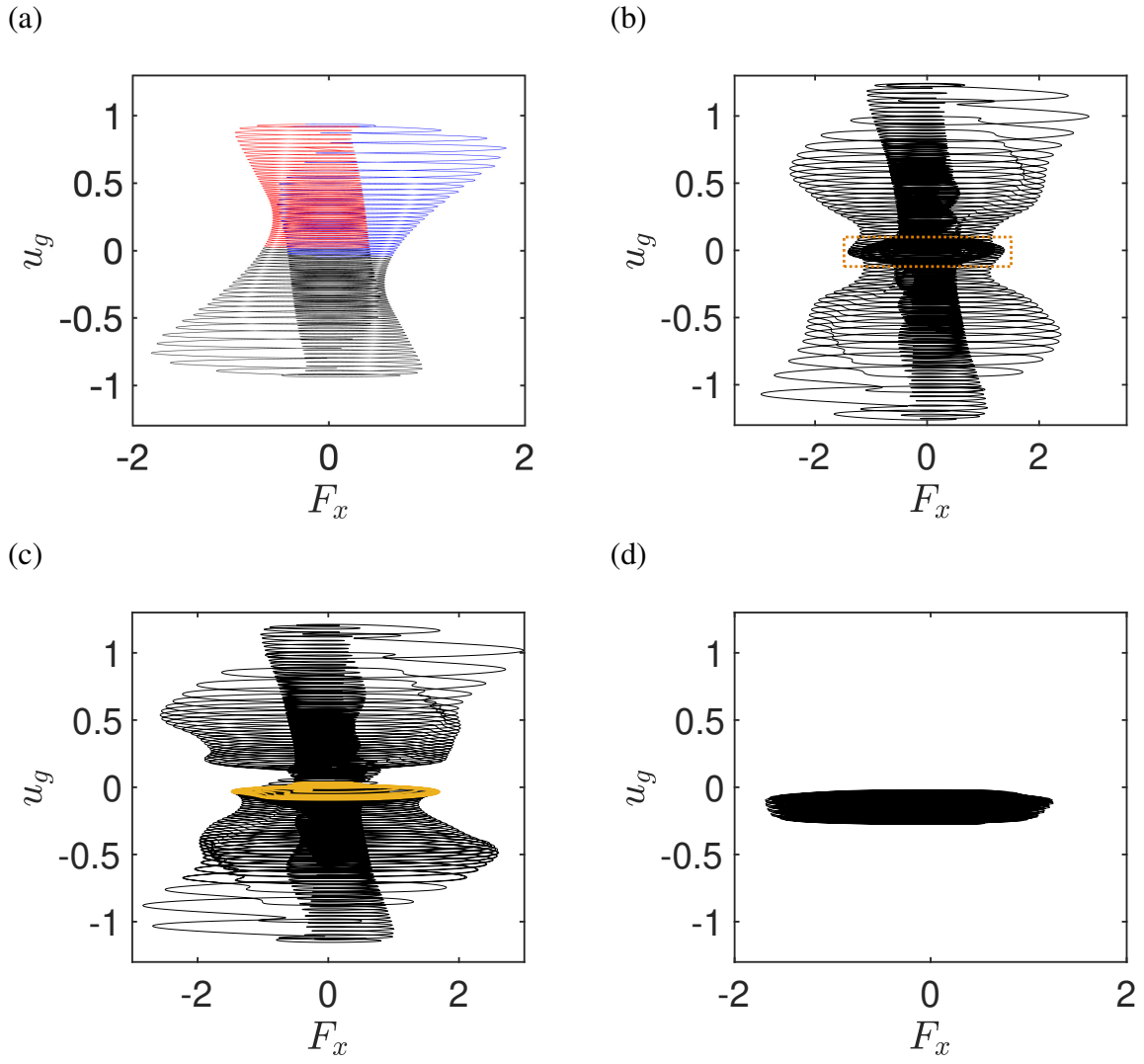

Figure 3.12: Transition from back & forth to deviated quasi-periodic wake propulsion: Phase portraits of the horizontal speed and force of (a-c) back & forth and (d) a deviated quasi-periodic wake propulsive solution for (a) $\beta = 17$, (b) $\beta = 19$, (c) $\beta = 19.5$ and (d) $\beta = 20.25$ previously presented in figure 3.10. In (a) and (c) we have adopted the same line color used in 3.10.

begins to be perturbed by the appearance of a secondary structure from $\beta = 19$. This structure, identified in (3.12-b) by a dotted orange rectangle, starts to grow precisely over the path followed by the decelerating red structure when the velocity changes of sign. This secondary structure becomes more complex for $\beta = 19.5$ (3.12-c), where a bottle neck starts to appear near zero velocities. Again following the time signal of figure 3.10, the orange trace used to identify the quasi-periodic spot help us visualize that the secondary structure is precisely the quasi-periodic spot of figure 3.10(c). The phase portrait of the DQPW solution for $\beta = 20.25$ is shown in figure 3.12 (d). It is remarkably similar to the orange structure highlighted in (3.12-c), with both DQPW propulsive solution and spot centered around a negative time-averaged speed. The slight displacement between the orange structure in (3.12-c) and the phase portrait in (3.12-d) suggests that, as the Stokes number is risen above the onset of DQPW propulsive solutions, the back & forth solution gets stuck at the quasi-periodic spot, which is in fact a DQPW propulsive orbit. As the frequency of back & forth solutions sharply decreases in Figure 3.3 (d) with the period of these solutions heading towards infinity and a saddle-node of limit cycles is observed in our system, the transition scenario seems to be a collision of a limit cycle with a saddle-node. These observations added to the similarity of the DQPW and quasi-periodic spots of back & forth solutions indicate the bifurcation between back & forth and deviated quasi-periodic wake propulsive solutions could be in fact a global bifurcation of *homoclinic* type (Wiggins 1988; Schaeffer and Cain 2016).

3.5 Conclusions

In this work, we have studied the transition between self-propelled regimes of a heaving rectangular foil immersed in a quiescent fluid for Stokes numbers $10 \leq \beta \leq 40$. The chosen foil had an aspect ratio $h = 0.05$, solid-fluid density ratio $\rho = 100$ and flapping amplitude $A = 0.5$. First, the occurrence of deviated quasi-periodic wake (DQPW), symmetric periodic wake (SPW) and deviated periodic wake (DPW) propulsive solutions was established using unsteady nonlinear simulations. The nonlinear bifurcation of SPW propulsive solutions for $22.4 \leq \beta \leq 36$ and their fluid-solid Floquet stability analysis were then investigate, followed by the phase space analysis of the transition between back & forth and DQPW propulsive solutions. Through the summed up contributions of these analyses, this work has identified that the transition route of self-propelled regimes beyond the onset of flapping propulsion presents global and local bifurcations that bring the self-propelled dynamics from non-coherent to coherent locomotion.

The transition route was first drawn using unsteady nonlinear simulations. The coupled dynamics evolve while increasing β from back & forth motion around a fixed point ($11.25 \leq \beta \leq 20$) to deviated quasi-periodic wake (DQPW) ($20.25 \leq \beta \leq 22.4$), symmetric periodic wake (SPW), $22.4 \leq \beta \leq 26.75$, finally reaching deviated periodic wake (DPW) propulsive solutions for $\beta \geq 27$. The results presented in this work highlight the existence of the intermediary state of deviated quasi-periodic wake propulsion between back & forth and SPW propulsive solutions. This regime has not yet been described, to our knowledge, in the literature.

Nonlinear bifurcation methods were then employed to follow SPW propulsive solutions. The time spectral (TSM) coupled to pseudo arc-length continuation revealed that SPW solutions exist beyond their unsteady nonlinear simulations β range. Particularly, the TSM revealed the existence of solutions that do not feature wake deviation in the range of DPW solutions, and a saddle-node bifurcation of limit cycles in the vicinity of the transition between DQPW and

SPW propulsive solutions. Fluid-solid Floquet stability analyses of the TSM solutions were performed. Asynchronous unstable Floquet modes were obtained on the saddle-node branch, and synchronous unstable Floquet modes were found for $\beta \geq 27$. Both synchronous and asynchronous unstable modes feature vortex displacement and generate wake deviation. In the case of the asynchronous mode, the quasi-periodic behaviour of the Floquet exponent generates a slow period modulation, responsible for the periodic upward and downward wake deviation. This slow period matches, at the onset, the ones of DQPW solutions. The asychronous and synchronous unstable multipliers correctly predict the onset of DQPW and DPW solutions. In addition, their associated modes explain the emergence of the quasi-periodic and periodic wake deviation. In the last case, the mode is not responsible for the increase of time-averaged horizontal velocity of the DPW solutions. We suppose this mechanism must be connected to nonlinearities as for Jallas, Marquet, and Fabre (2017). The study of the last transition between back and forth and deviated quasi-periodic wake propulsive solutions assembled elements of the unsteady nonlinear analysis and the TSM. The existence of the saddle-node bifurcation, the decrease of the frequency through the back & forth regime, the spots of horizontal speed present in back & forth solutions and the entanglement revealed by the phase portraits drawn for $18 \leq \beta \leq 21$ lead us to conclude this is a global bifurcation of homoclinic type.

This study has added to the transition route of symmetric foils heaving in quiescent fluids a comprehension of the bifurcations that lead from non-coherent to coherent locomotion. In our previous study we have shown that the first transitions to propulsion and the back & forth motion of a horizontally self-propelled flapping foil in a quiescent fluid are fluid-solid Floquet stabilities of non-propelled solutions (Benetti Ramos et al. 2020). Here we conclude that the further transitions taking place from back & forth to coherent propulsion are associated to a nonlinear bifurcation. The transition between back & forth and deviated quasi-periodic wake propulsive solutions is a global bifurcation. The further transitions are local bifurcations of a branch of symmetry periodic wake (SPW) propulsive solution that undergoes a fold bifurcation. Appropriate nonlinear tools, as time spectral and continuation methods, should be employed to study these transitions.

3.6 Fluid-solid Floquet stability analysis of non-propulsive solutions

We investigate either the emergence of the three regimes of DQPW, SPW and DPW propulsive solutions can be predicted by stability analyses of non-propulsive periodic solutions. The coupled fluid-solid Floquet stability analysis has been performed for $20 \leq \beta \leq 40$. Other fixed parameters are $\rho = 100$, $A = 0.5$ and $h = 0.05$. The evolution with the Stokes number $10 \leq \beta \leq 40$ of the (a) modulus and (b) the frequency of the leading Floquet multiplier is shown in figure 3.13. For almost all the studied interval $\beta \geq 11.25$ the leading Floquet multiplier is unstable. A pair of unstable complex multipliers (asynchronous nature) exists for $11.25 \leq \beta \leq 30$. This pair of multipliers collapses on the real axis becoming two unstable synchronous modes for $30 \leq \beta \leq 41$ when one of the synchronous modes is stabilized. Since asynchronous (synchronous) Floquet multipliers (do not) break the time-periodicity of the base solution, the unstable modes share the time-periodicity of DQPW and DPW propulsive solutions, for $\beta \geq 30$ in the former case. The asynchronous unstable mode is, nevertheless,

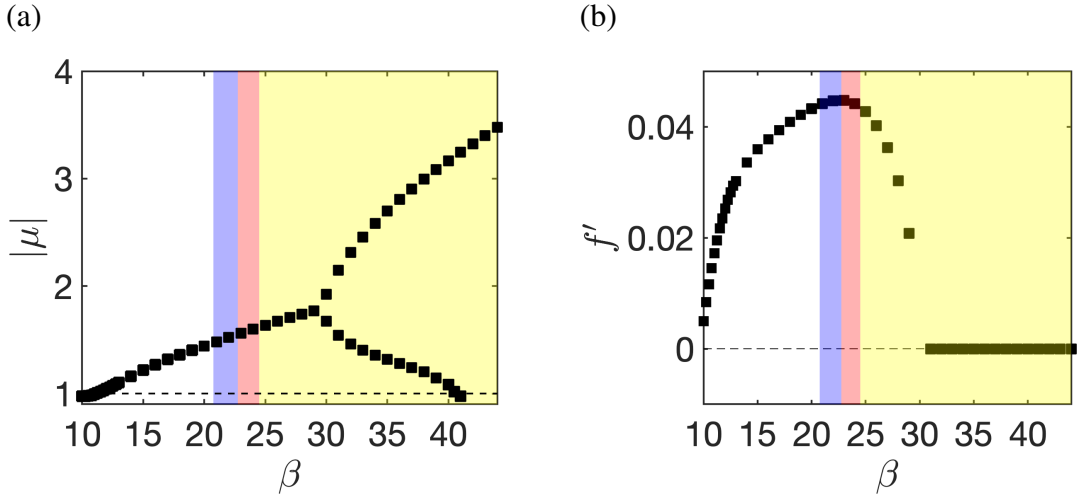

Figure 3.13: Fluid-solid stability analysis of non-propulsive solutions. (a) Absolute value and (b) frequency of the leading Floquet multiplier as a function of the Stokes number β. For comparison, the background colors violet, red and yellow indicate regions presenting quasi-periodic, symmetric periodic wake and deviated wake propulsive solutions, as identified in §3.2.2

the same as analysed in Benetti Ramos et al. (2020), originating back & forth dynamics. This mode does not match the DQPW behaviour. The unstable synchronous mode will be analysed in the following paragraphs. The onset of the solutions, highlighted by the background colors in the figures, is however not predicted by any major change in the non-propulsive base-flow stability. When SPW and DPW solutions are retrieved the leading unstable multiplier is still asynchronous in nature and the temporal dynamics predicted by stability and unsteady nonlinear analysis do not match.

Two unstable synchronous modes are obtained starting from $\beta = 30$. Since both modes are very similar, we choose to represent only the most unstable one in figure 3.14 to analyse its characteristics. This mode is very similar to the real part of the asynchronous back & forth mode of Benetti Ramos et al. (2020). It breaks the left-right spatial symmetry and is again similar to a displacement mode. The mode is a propulsive one, but it does not break the spatio-temporal symmetry. No combination of this mode with a similar unstable one could result in the wake deviation observed in nonlinear solutions at this Stokes number range. This leads to the conclusion that the results of the Floquet stability around non-propulsive solutions do not match the unsteady nonlinear behaviour for $\beta \geq 20$. The transition between these different regimes – back & forth, DQPW, SPW and DPW propulsive regimes – cannot be explained by these stability analyses. To understand them we have thus recurred to the nonlinear method employed in this work.

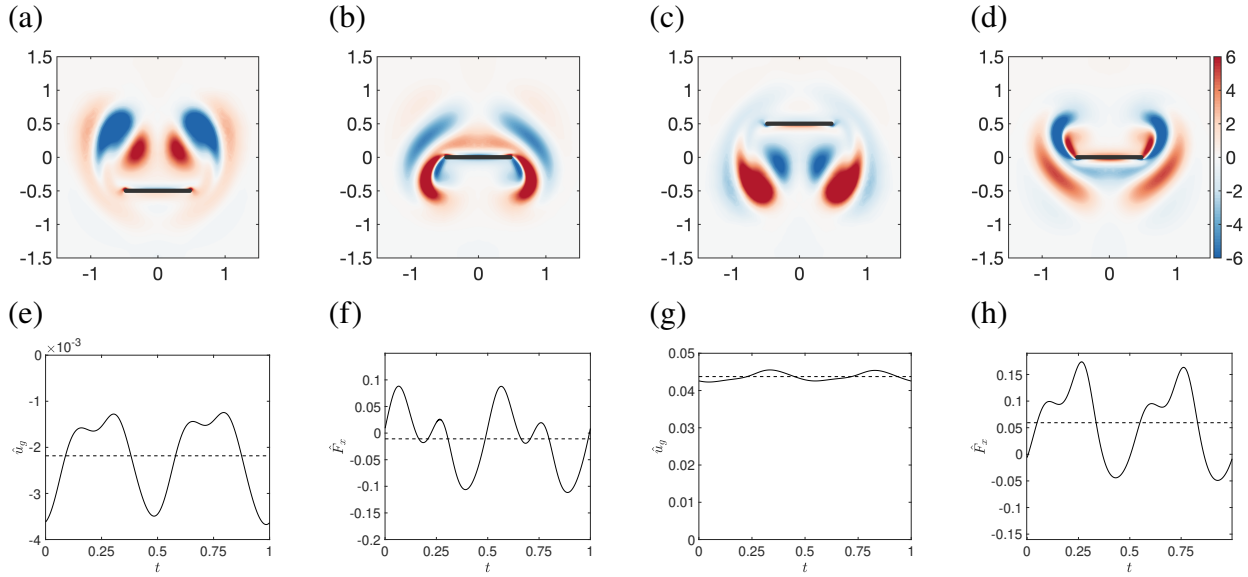

Figure 3.14: Leading and secondary unstable synchronous Floquet mode for $\beta = 35$: (a-d) Vorticity contours for four equally spaced time instants along a flapping period. Foil horizontal (e,g) velocity and (f,h) force respectively for the leading and secondary unstable multipliers. Mean force and speed in all figures represented by a dashed line.

Chapter 4

Transition between diffusion and pressure-driven thrust of self-propelled heaving foils

The content of this chapter is based on the article: Benetti Ramos, L. *et al*, Transition between diffusion and pressure-driven thrust of self-propelled heaving foils, in preparation for *Journal of Fluid Mechanics*.

In chapters 1 and 2 we have focused on describing stable self-propelled solutions and explaining their emergence through linear or nonlinear stability analyses. Now, we turn our attention to a physical analysis of how these solutions produce thrust thus achieving locomotion.

Flapping propulsion is a locomotion strategy adopted by living organisms whose thrust origin is normally associated to fluid inertia rather than viscous friction. Studies show, however, that the latter diffusive forces might still play an important role on its thrust generation. In this work, we address this issue studying diffusion and pressure time-averaged contributions to the thrust generated by a horizontally self-propelled heaving foil in a quiescent fluid. Using numerical simulations we show that increasing the flapping frequency or amplitude this system transition between two distinct thrust regimes. In the first one the time-averaged thrust is driven by viscous diffusion, with forces generated by the asymmetric shear on the foil lateral surface. In the second, thrust is driven by the trailing edge pressure increase, a consequence of the fluid acceleration behind the foil. We finally study the effect of flapping amplitude and thickness-to-chord aspect ratio over these regimes, highlighting that the diffusion-driven thrust regime is enhanced for smaller aspect ratios and that the transition between both takes place for a constant Stokes number $\beta_A = fAc/\nu \approx 10$ based on A and f the flapping amplitude and frequency, c the foil chord and ν the fluid viscosity.

Contents

4.1 Introduction

The propulsion of fish and birds in nature (Wu 2010; Smits 2019) is a great source of inspiration to conceive innovative artificial swimming and flying devices (Ramananarivo, Godoy-Diana, and Thiria 2013; Ristroph and Childress 2014; Lucas et al. 2014). One of the key points addressed by researches and engineers intending to reproduce these locomotion strategies is how animals generate thrust forces to propel themselves through fluids. These forces are generated, in the case of aerial and aquatic locomotion, as a response of the surrounding fluid to the imposed body movement. The thrust origin may thus greatly vary according to the kind of adopted structural motion and the physical nature of the surrounding flow.

Nature is rich in complexity and variety of swimming and flying styles. This variety is associated to styles adaptation to the balance of fluid inertia and viscosity of the surrounding flow. This ratio is generally expressed in bio-propulsion through the non-dimensional Reynolds and Stokes numbers which, being normally from a similar order of magnitude, can be used for a primary sorting of locomotion strategies. In very low Stokes numbers, viscous forces predominate and inertial effects do not exist. Propulsion strategies of small micro-organisms, as flagelar and ciliary (see Lauga (2011) for a review), adapt to this diffusive medium. Non-reciprocal motions mainly in the propulsion direction are required by the time-less and linear character of the flow governing equations (Purcell 1977), with thrust forces being generated by viscous friction on the fluid-solid interface. When finite Reynolds and Stokes numbers are reached, the flow presents both inertia and viscosity. Imposed movements are then adapted to exploit them. Two major styles of swimming and flying are then adopted, namely oscillatory (flapping), adopted by animals like tuna and birds, and undulatory propulsion, adopted for example by eels (Floryan et al. 2017; Smits 2019). Both styles are characterized by body movements in a direction perpendicular to that of propulsion, be it through an appendage oscillation or wave propagation along the body. In the limit of large Reynolds and Stokes numbers, these strategies generate thrust mainly through inertial forces (Lighthill 1971; Garrick 1936), the reaction of the body to the surrounding fluid acceleration. Viscous forces, different than low Reynolds numbers, generate then drag (i.e. through skin friction), rather than thrust, balancing the inertial forces in the swimming direction during cruise regimes (Lighthill 1975).

However, for not so high Reynolds ranges, transverse Reynolds numbers are relatively low and energy dissipation in this direction cannot be ignored. Recent studies have thus reconsidered the addition of drag forces that resist against the body motion perpendicular to the propulsion direction, called resistive forces, to dynamical models. These studies have shown that resistive forces can in fact contribute to thrust due to their projection from the flapping to swimming direction through the body curvature (Piñeirua, Godoy-Diana, and Thiria 2015). Through a very detailed model for studying optimal undulatory swimmers, whose ingredients were forces that resist against the body in the swimming direction (viscous and pressure drag), and two possibly thrust producing components: reactive forces (Lighthill 1971) and resistive forces (Taylor 1952), Eloy (2013) has shown that resistive forces can assume either a secondary (contributing even at 20 percent) thrust or a drag role depending on the swimmer shape and swimming style. In addition to this secondary contribution, resistive forces appear to assume a key thrust role in anguilliform swimmers. The energy dissipation generated by these forces seems to be essential essential for passively deforming bodies obtaining anguilliform kinematics (Ramananarivo, Godoy-Diana, and Thiria 2014) and the thrust forces generated by anguilliform swimmers of low thickness-to-chord aspect ratio (Piñeirua, Godoy-Diana, and Thiria 2015) is dominated (90

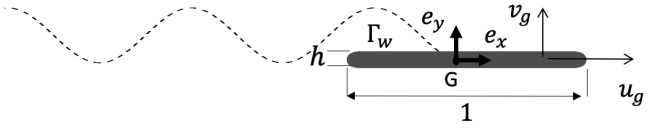

Figure 4.1: Sketch of the foil configuration under vertical and horizontal motion with velocity $\mathbf{u}_g$. The foil chord (trailing to leading edge), thickness, the frames of reference and the solid/fluid interface Γ_w are indicated.

percent) by resistive force contributions.

In the case of flapping propulsion, a route towards intermediary Reynolds and Stokes regimes are experimental and numerical studies (Vandenberghe, Zhang, and Childress 2004; Alben and Shelley 2005) that search the onset of flapping locomotion, and the emergence of fluid inertia and nonlinearities, through the critical scale where reciprocal motions of symmetric profiles result in locomotion. These studies found, as a secondary output, that viscous forces that resist against the body flapping movement might be essential to trigger locomotion. In the case of the horizontal locomotion of symmetrical heaving foils in quiescent fluids, studies of bodies as ellipses and ellipsoids in respectively two and three-dimensional flows (Alben and Shelley 2005; Deng and Caulfield 2018a) have noticed that viscous forces are at the origin of the thrust generation during transient regimes, particularly in the early phases where the foil velocity becomes non-zero. In this transient phase, the foil is accelerated along its flapping period with viscous and pressure forces actuating together as thrust sources. However, once a cruise regime is achieved (and thus the foil is no longer accelerated along a flapping period) the time-averaged viscous and pressure forces should mutually compensate each other, and viscous forces were observed to fall into an usual drag role with pressure driving the thrust forces in cruise regime. A question can be raised whether a cruise regime where thrust is driven by viscous forces exists. In this study, we will show that for self-propelled symmetric heaving foils in quiescent fluids it exists, in fact, a transition between a diffusion- and a pressure-driven thrust regime. As in cruise regimes pressure and viscous contributions along a flapping period should mutually compensate, we will distinguish these regimes through their time-averaged thrust physical nature. Through a detailed numerical investigation, further characterizations with the dependence on control parameters, such as the flapping frequency and amplitude or the foil shape, and their surrounding flow will be performed. As studies have long associated thrust production to wake patterns (Triantafyllou, Triantafyllou, and Grosenbaugh 1993; Zhang 2017; Andersen et al. 2017), we wish to extend this analysis to identify pressure and diffusion-driven thrust producing flows. After describing the studied configuration and the numerical method (§4.2), numerical results are addressed in §4.3. Finally, §4.4 concludes on the existence of a transition between diffusion and pressure-driven thrust regimes as well as their characteristics for self-propelled heaving symmetric foils.

4.2 Configuration and numerical method

In this work, the physical diffusive or pressure nature of the thrust generated by a self-propelled heaving symmetric rectangular foil is investigated. This rectangular body, figure 4.1, rigid with rounded edges is characterized by its non-dimensional chord $c = 1$ and thickness-to-chord aspect

ratio h, the diameter of the rounded edges being equal to the foil thickness. This body translates in an initially quiescent two-dimensional fluid with a velocity $\mathbf{u}_g = (u_g, v_g)$ that is imposed along the vertical axis through a (non-dimensional) heaving motion $y_g(t) = -A\cos(2\pi t)$, but free along the horizontal axis e_x as a result of hydrodynamic forces acting on the solid interface. This rigid-body fluid-structure interaction is characterized by four non-dimensional parameters, namely the frequency-based Stokes number β (or the flapping amplitude-based Stokes number β_A depending whether the velocity characteristic scale is based on the foil chord $c^* f^*$ or the flapping amplitude $A^* f^*$), the chord-based flapping amplitude A, the solid-fluid density ratio ρ and the thickness-to-chord aspect ratio h, defined respectively as

$$\beta = \frac{f^*(c^*)^2}{\nu}\left(\text{or } \beta_A = \frac{A^* f^* c^*}{\nu}\right),\ A = \frac{A^*}{c^*},\ \rho = \frac{\rho_s}{\rho_f} \text{ and } h = \frac{h^*}{c^*}, \tag{4.1}$$

where * differentiate dimensional and non-dimensional parameters, ν is the fluid kinematic viscosity and the solid and fluid densities are resp. ρ_s and ρ_f. The flapping period $1/f^*$, the foil chord c^* and the fluid density ρ_f are used as characteristic time, length and density scales. The surrounding fluid absolute velocity $\mathbf{u} = (u, v)$ and pressure p are governed by the two-dimensional incompressible Navier-Stokes equations

$$\frac{\partial \mathbf{u}}{\partial t} = -\boldsymbol{\nabla}\mathbf{u}\cdot(\mathbf{u}-\mathbf{u}_g) - \boldsymbol{\nabla}p + \beta^{-1}\boldsymbol{\Delta}\mathbf{u},\ \boldsymbol{\nabla}\cdot\mathbf{u} = 0, \tag{4.2}$$

written in the non-inertial frame of reference that follows the foil center of mass G as done in other rigid-body fluid-structure interactions studies (i.e. falling and rising bodies in fluids (Jenny, Bouchet, and Dušek 2003; Tchoufag, Fabre, and Magnaudet 2014) or pitching foils (Jallas, Marquet, and Fabre 2017)). The body is self-propelled and the evolution of its horizontal motion is governed by Newton's second law

$$\frac{\mathrm{d}u_g}{\mathrm{d}t} = (\rho S)^{-1}F_x(\mathbf{u},p)\ ,\ F_x(\mathbf{u},p) = F_x^p(p) + F_x^\nu(\mathbf{u}) = \int_{\Gamma_w}([-p\mathbf{I} + \beta^{-1}(\boldsymbol{\nabla}\mathbf{u} + \boldsymbol{\nabla}^T\mathbf{u})]\cdot\mathbf{n})\cdot\mathbf{e}_x \mathrm{d}\Gamma_w\,, \tag{4.3}$$

where S is the non dimensional surface of the foil and $\mathbf{n}$ is the outward normal. Equations (4.2) and (4.3) are closed by a no-slip boundary condition on the foil surface $\mathbf{u}(\Gamma_w, t) = \mathbf{u}_g(t)$. As seen in eq. (4.3), the horizontal force has two physically distinct contributions: one linked to pressure F_x^p and another that depends on viscous diffusion F_x^ν through velocity gradients and the Stokes number β. In this work, we will primarily evaluate the physical nature of the hydrodynamic thrust (drag) force that sustains (resist against) the motion at cruise conditions. $\langle\cdot\rangle$ denoting the time-average over a flapping period, three important physical quantities will be studied: the time-averaged horizontal velocity as well as the viscous and pressure forces contributions to the total horizontal force

$$< u_g >= \int_{t_0}^{t_0+1} u_g \mathrm{d}t,\ < F_x >=< F_x^p > + < F_x^\nu > \ . \tag{4.4}$$

In the cruise regime, the time-averaged horizontal velocity is constant and the averaged horizontal force is zero. Therefore pressure and viscous components of the mean force shall mutually compensate and we can clearly identify a thrust and a resistive role, which will be employed to identify diffusion and pressure-driven thrust regimes of locomotion.

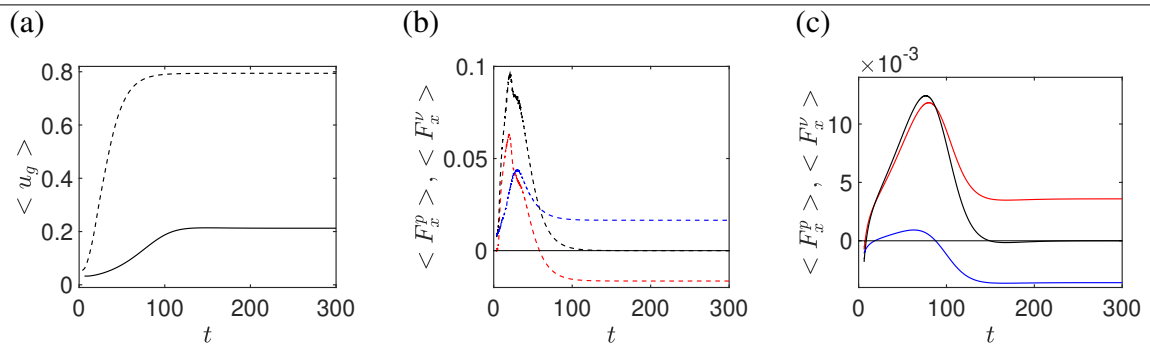

Figure 4.2: Temporal evolution of a diffusion-driven, Stokes number $\beta = 14$ (solid line), and a pressure-driven, $\beta = 62$ (dashed line), self-propelled solutions. (a) Horizontal velocity time-averaged over the non-dimensional flapping period $T = 1$. (b,c) Time-averaged pressure (blue) and viscous (red) components of the horizontal force (black). Parameters: $A = 0.25$, $\rho = 100$ and $h = 0.05$.

The coupled fluid-solid equations are solved numerically using the unsteady nonlinear solver described and validated in Benetti Ramos et al. 2020, written using the non-commercial finite-element software FreeFEM (Hecht 2012). To achieve a numerical convergence of $O(10^{-5})$ of the present results, a mesh consisting of 1.7×10^4 triangles and a time step $\Delta t = 5 \times 10^{-4}$ are used. The fluid-solid interface is discretized by 480 points, from which 96 are placed on the round edges. In this study, we will investigate the effect of the Stokes number $1 \leq \beta \leq 300$, the flapping amplitude $0.1 \leq A \leq 0.5$ and the foil thickness $0.025 \leq h \leq 0.1$. Two values of density ratio, $\rho = 1$ and $\rho = 100$, are considered. This choice of parameter is made to explore thicknesses, flapping frequencies and amplitudes usually employed in the literature (Alben and Shelley 2005; Lu and Liao 2006; Deng and Caulfield 2016). The density ratios lie in the range observed for real tails and wings of swimming and flying animals $O(1 - 1000)$ (Lu and Liao 2006).

4.3 Results and discussion

We initially consider the heaving foil for a fixed flapping amplitude $A = 0.25$, density $\rho = 100$ and aspect ratio $h = 0.05$ while varying the Stokes number $1 \leq \beta \leq 80$. As the Stokes number is increased, the temporal evolution of the average horizontal velocity $< u_g >$, horizontal force and its pressure and viscous components ($< F_x >$ $< F_x^p >$ and $< F_x^v >$) reveals two distinct behaviours, exemplified in figure 4.2 for $\beta = 14$ and $\beta = 62$. For both β, $< u_g >$ (4.2-a) increases until it reaches a constant value in the cruise regime, the cruise velocity being greater for the highest Stokes number. Since this velocity is positive in both cases, its increase is linked to the existence of a positive average horizontal force. Through the temporal evolution, this average force progressively tends towards zero, value reached when the cruise regime is attained, pressure and viscous components compensating each other. In both cases, the hydrodynamic thrust is initially dominated by viscous forces. The temporal evolution reserves, however, distinct faiths for this diffusive-driven thrust at different Stokes numbers. For $\beta = 62$ (4.2-b), it will be surpassed by pressure contributions ($t \leq 50$) during the transient regime with the viscous forces eventually turning into a classical viscous drag role ($t \geq 70$) that is kept

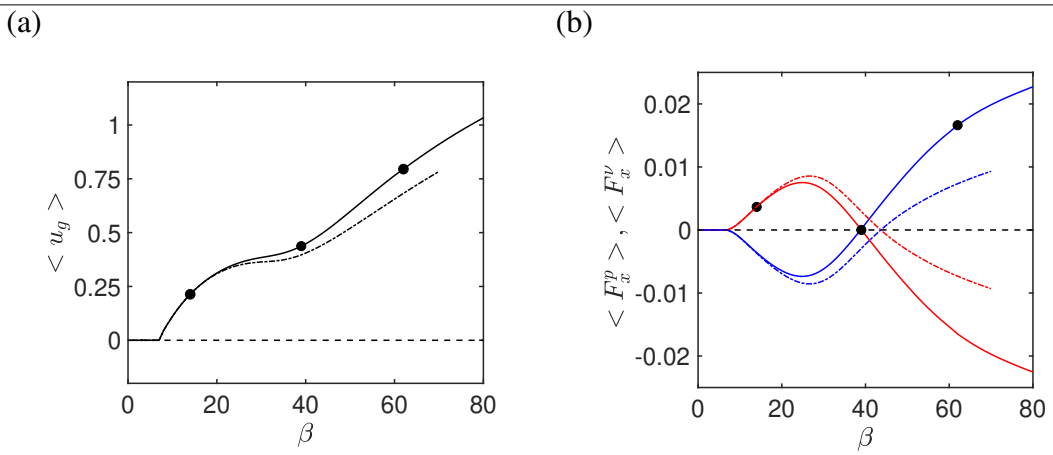

Figure 4.3: Time-averaged (a) horizontal velocity $< u_g >$ and (b) horizontal forces (viscous $< F_x^v >$ in red, pressure $< F_x^p >$ in blue) as a function of the Stokes number β for $\rho = 100$ (solid line) and $\rho = 1$ (dash-dot line). The black dashed lines indicate a zero value in both cases. Black dots indicate a diffusion-driven ($\beta = 14$), a transitional ($\beta = 39$) and a pressure-driven ($\beta = 62$) solution in presented in figure 4.4. Parameters: $A = 0.25$ and $h = 0.05$.

during the cruise regime. In this case, the thrust is driven by pressure forces. This thrust-drag transition, observed also for other foil shapes and density ratios (Alben and Shelley 2005; Deng and Caulfield 2018a), is however not reproduced for $\beta = 14$ (4.2-c). Here pressure contributions are those that fall into a resistive role (for $t \geq 100$) leading to a diffusive-driven thrust in the cruise regime – a behaviour never highlighted, to our best knowledge, in literature.

To understand how the foil undergoes a transition between these two regimes, the evolution with the Stokes number β of $< u_g >$, $< F_x^p >$ and $< F_x^v >$ at the foil permanent regime is depicted in figure 4.3 (a) and (b) for two density ratios. Let us consider first the case $\rho = 100$. We see in (4.3-a) that, for $\beta \geq 8$, $< u_g >$ starts to grow. This growth is, however, non-monotonous with the Stokes number, being reduced for $\beta \in [23, 39]$, and re-increasing for $\beta \geq 40$. This variation of the horizontal velocity growth tendency can be associated to the transition between diffusion and pressure-driven thrust regimes. In figure 4.3 (b) the thrust is dominated by diffusive forces for small Stokes number $8 \leq \beta \leq 39$, reaching a maximum value for $\beta = 25$, after which it decays until it becomes negative for $\beta \geq 40$. The range where the switch between both thrust regimes takes place is precisely the one where the horizontal velocity growth decreases. When the diffusive force finally becomes negative, it switches roles with the pressure force, transitioning to the pressure-driven thrust regime. Both pressure forces and velocity grow following this transition. Comparing the previous results for $\rho = 100$ with $\rho = 1$, we remark that, apart from a small difference on the transition threshold and absolute values of forces and velocity, the phenomenon is robust to a density ratio variation. Therefore, in the remainder of this article, only the case $\rho = 100$ will be considered. Results are, in fact, very similar inside the density ratio range $1 - 1000$.

Albeit the flow viscous nature of low Stokes numbers, the existence of the diffusion-driven thrust regime is surprising due to the time-reciprocal gait adopted in this case. The imposed movement is very different than non-reciprocal gaits adopted by swimmers relying on diffusive forces at very low Stokes numbers (Purcell 1977; Lauga 2011). Two central questions then

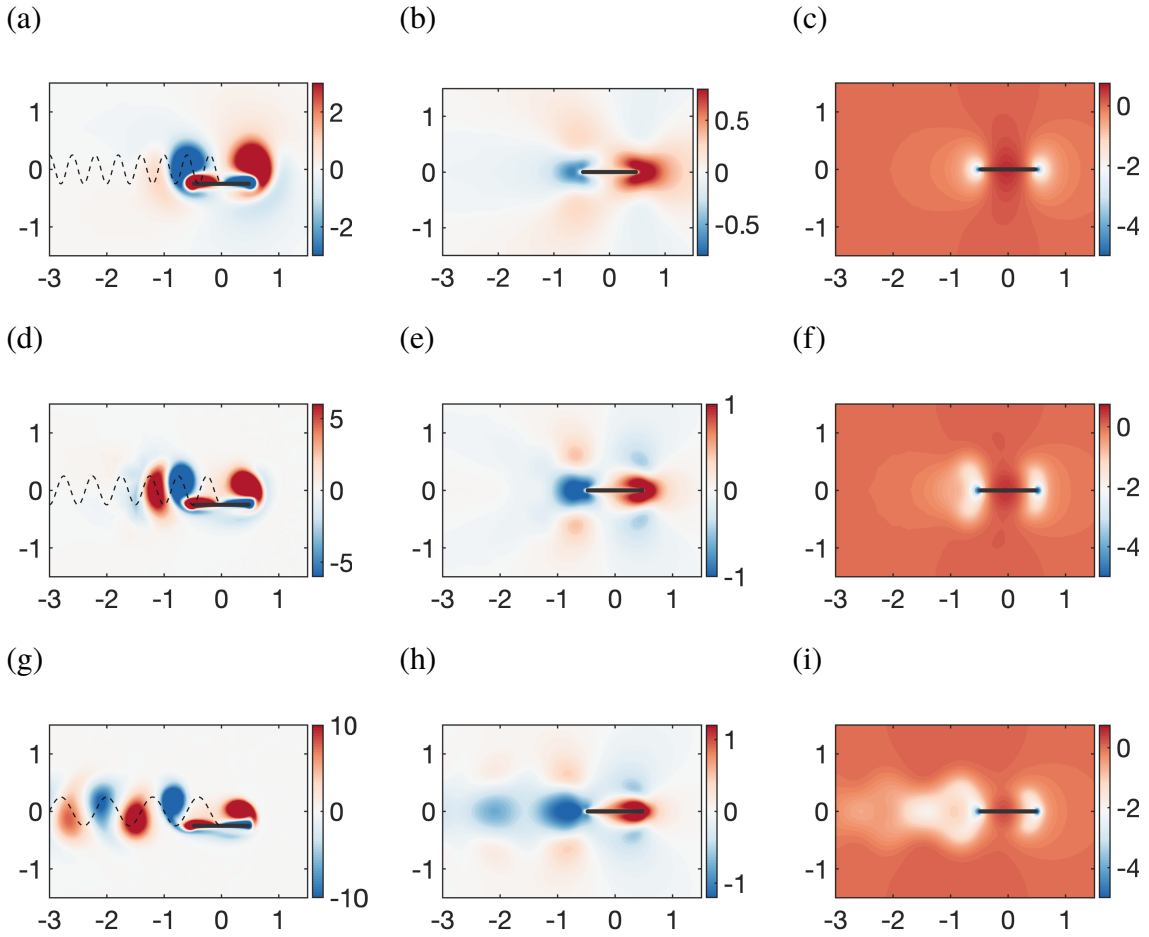

Figure 4.4: (a-c) Diffusion-driven ($\beta = 14$) (d-f) transitional ($\beta = 39$) and (g-i) pressure-driven ($\beta = 62$) self-propelled solutions. (a,d,g) Instantaneous vorticity field, (b,e,h) Time-averaged stream-wise velocity u field and (c,f,i) the time-averaged pressure p field. The dashed lines in (a,d,g) correspond to the foil center of mass trajectory.

appear: how is the diffusive-driven thrust regime originated and how does it transition to the pressure-driven regime? To answer these questions three typical solutions are selected to study their flow (figure 4.4): a diffusion-driven thrust $\beta = 14$, a transitional $\beta = 39$ and a pressure-driven thrust $\beta = 62$ solution. We observe for the diffusion-driven thrust solution, figure 4.4(a-c), that no vortices are shed away from the foil. The unsteady flow depicted by the out-of-plane vorticity ω_z (4.4-a) consists of a pair of opposite sign vortices attached to the foil leading and trailing edge, a structure remarkably similar to so-called *starting flows* (Lian and Huang 1989). In the present case, however, the pair of vortex breaks the left-right flow symmetry

$$(u, v, p, \omega_z)(x, y, t) = (-u, v, p, -\omega_z)(-x, y, t)\,, \tag{4.5}$$

which is at the origin of an instantaneous non-zero horizontal force (Jallas, Marquet, and Fabre 2017) produced by the flapping foil. This left-right asymmetry is also present in the flow time-averaged streamwise velocity, 4.4-b), which reveals a greater spatial portion of higher value

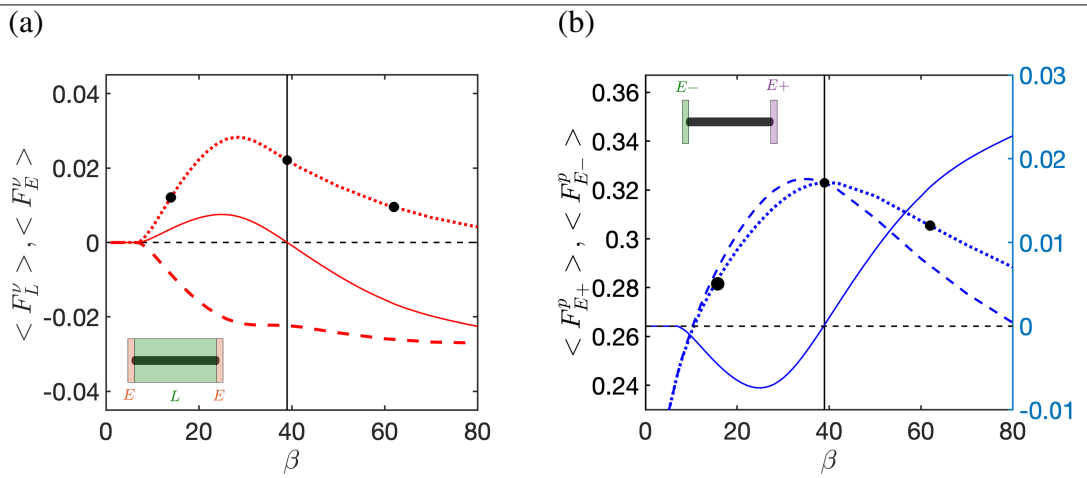

Figure 4.5: Evolution with the Stokes number β of (a) viscous forces lateral-wall $< F_L^\nu >$ (dotted) and leading/trailing edges $< F_E^\nu >$ (dashed) contributions and (b) pressure forces leading-edge $< F_{E+}^p >$ (dotted) and trailing-edge $< F_{E-}^p >$ (dashed) contributions. In all figures solid lines represent the total force and the vertical line delimits the transition between diffusion and pressure-driven regimes. In (b) the total force values are fixed on the right axis.

positive velocity, same orientation as the foil horizontal velocity u_g, surrounding the foil leading edge. The flow time-averaged pressure (4.4-c) has a slightly asymmetric spatial distribution, the minimum pressure being observed at the foil trailing edge. These flow structures lead to the forces exhibited by the diffusion-driven thrust regime. Thrust is generated by the asymmetric velocity and shear distribution, with the leading edge positive contribution (and its greater foil surface) overcoming negative shear contributions. Finally, the trailing edge pressure minimum results in a pressure drag.

At the transitional solution, figure 4.4(d-f), the flow similarity with a starting flow starts to disappear, the trailing edge featuring now a vortex dipole (4.4-d). This same dipolar structure was report to trigger the transition to horizontal motion (Alben and Shelley 2005) due to a reduction of the trailing edge suction force. This reduction comes from the increase of negative velocity at the foil trailing edge (4.4-e), indicating an increase of the fluid acceleration opposite to the foil travel direction (towards the right in the figure). The positive velocity around the foil leading edge is reduced compared to the diffusive solution. The pressure (4.4-f) becomes more left-right asymmetric and the value behind the trailing edge decreases. The decrease of the trailing edge suction and of the leading edge shear result in the decay of the diffusion-driven thrust and the pressure drag. Passing this transition point, vortices no longer remain attached to the trailing edge. A reversed Von-Kármán wake (Triantafyllou, Triantafyllou, and Gopalkrishnan 1991), found for all pressure driven solutions, is formed by the vortex shed by the wing (figure 4.4g-i). The time-averaged flow (4.4-h) consists of a negative horizontal velocity jet behind the foil. The fluid acceleration behind the foil creates a large zone of pressure decrease, which is visible behind the foil trailing edge (4.4-i). The pressure balance is shifted, with the trailing edge suction being significantly reduced when compared to the leading edge forces, finally resulting in a pressure-driven thrust force.

Since diffusion and pressure driven thrust solutions present very different flow spatial distributions around the foil surface, we decompose the viscous forces ($< F_x^\nu >=< F_L^\nu > + <$

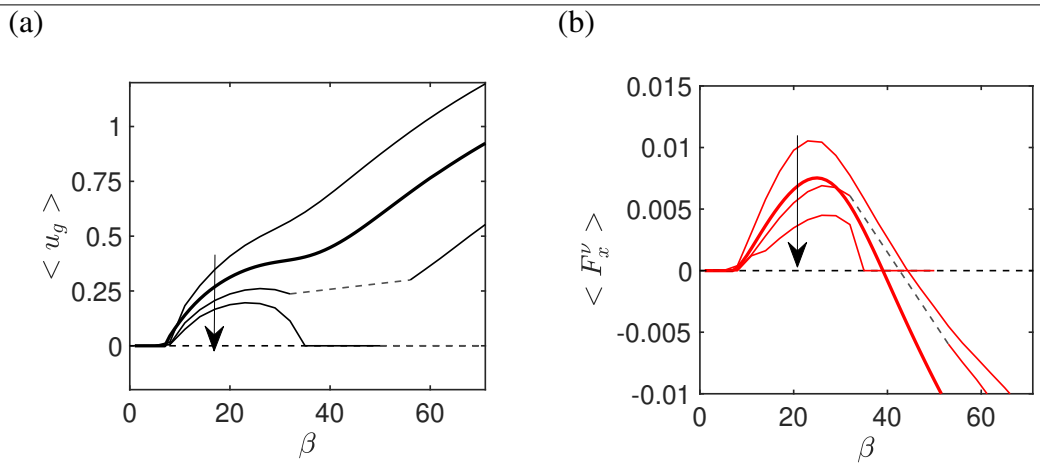

Figure 4.6: Evolution with the Stokes number for aspect ratios $h = 0.025$, $h = 0.05$ (previous treated case and thicker line), $h = 0.075$ and $h = 0.1$ (arrow indicating the direction of aspect ratio growth in both figures) of the time-averaged horizontal (a) velocity $< u_g >$ and (b) viscous force component $< F_x^\nu >$. The solid lines correspond to periodic solutions, whereas grey dotted lines to quasi-periodic solutions, the latter being found for $h = 0.075$ and $h = 0.1$. In both figures, a black dotted line indicate zero values.

$F_E^\nu >$) in components integrated over the flat lateral walls $< F_L^\nu >$ and round leading/trailing edges $< F_E^\nu >$ and the pressure forces ($< F_x^p =< F_+^p > - < F_-^p >$) over the leading $< F_+^p >$ and $< F_-^p >$ trailing edge. The evolution of these contributions with the Stokes numbers (figure 4.5) reveals that the diffusion driven thrust is generated by diffusive forces alongside the foil lateral wall $< F_L^\nu >$ (4.5-a). This component is thrust producer (positive) for all investigated β, growing for $\beta \leq 25$ and decaying afterwards. Diffusive forces on the foil edge $< F_E^\nu >$, on the other hand, are always negative. The enhancement of flapping bodies skin friction (Ehrenstein and Eloy 2013) appears thus to be associated to edge forces over this β range. The diffusion-driven thrust is generated by the shear asymmetry alongside the lateral wall. This mechanism is similar to the thrust source of low aspect ratio anguilliform swimmers Piñeirua, Godoy-Diana, and Thiria 2015. In this case, however, the thrust is originated by a "projection" through the flow left-right asymmetry and not the body curvature.

The transition from diffusive to pressure-driven thrust results from the decay of both the diffusive forces and trailing edge $< F_-^p >$ pressure suction force generated by the apparition of the time-averaged jet behind the foil for $\beta \geq 39$. The propulsion in the pressure-driven regime is driven by the fluid acceleration in the foil trailing edge. This late transition to a regime where the trailing fluid acceleration drives thrust forces might have important implications for passively elastic devices that aim at enhancing propulsion through greater trailing edge flapping amplitudes (Spagnolie et al. 2010). As observed in literature passive elasticity just enhances propulsion after reaching a higher Stokes numbers, probably after the transition to pressure-driven thrust.

As the diffusion-driven thrust is mainly generated by the foil lateral wall, we have studied its sensibility to the thickness-to-chord aspect ratio in the range $0.025 \leq h \leq 0.1$ (figure 4.6). An increase of the aspect ratio reduces the foil lateral surface, which may have a great

impact on the evolution of the time-averaged horizontal velocity and viscous force. In fact, $< u_g >$ and $< F_x^\nu >$ are enhanced for smaller aspect ratios (greater foil lateral surface). For the smallest aspect ratio ($h = 0.025$) the horizontal velocity permanently grows, its evolution with β becoming less monotonous and sharp as h is increased. At $h = 0.075$ the evolution becomes non-continuous and quasi-periodic propulsive solutions, identified by a dashed grey line, emerge. These solutions, already investigated in the literature (Alben and Shelley 2005; Lu and Liao 2006), are non-coherent states where the foil exhibits a back & forth motion around a fixed point in space. We suppose these solutions emerge due to the decrease of the foil velocity, the system becoming incapable of attaining the transition between viscosity thrust and drag role exhibited in figure 4.2. While the aspect ratio present a small influence on the locomotion onset, attained for $\beta \sim 8$, the transition between thrust regimes is greatly impacted. It first decreases between $h = 0.025$ and $h = 0.05$ from $\beta = 46$ to $\beta = 39$. Although non-coherent states of locomotion emerge, we can infer that the β threshold is greater beyond $h = 0.075$, using the non-continuous evolution of the viscous force in (4.2-b) as well as the fact that for $h = 0.1$ the emergence of a pressure-driven thrust is not observed for $\beta \leq 80$. For this aspect ratio the diffusion-driven thrust regime is suppressed for $\beta = 33$ and symmetric non-propulsive solutions are obtained beyond this value, non-coherent solutions being obtained for $\beta \geq 52$.

In order to further characterize the transition between diffusion and pressure-driven thrust regimes, the influence of the flapping amplitude is investigated in the plans (A, β) and (A, β_A). Figure 4.7 depicts the frontier in these plans between non-propulsive, diffusion-driven thrust and pressure-driven thrust regimes. Comparing the plans (A, β) and (A, β_A) we remark that the two transitions (from non-propulsive to the diffusion-driven thrust regime, as well as the transition from diffusion to pressure-driven thrust regime) are better characterized by the flapping amplitude based Stokes number β_A. The transitions must then be linked to a sufficient vertical velocity/amplitude that generates both flow symmetry breaking and vortex shedding, granting the onset of diffusion and pressure-driven thrust regimes.

The first transition obtained for all flapping amplitudes while increasing the Stokes numbers is the transition between a non-propulsive (white background) and diffusion-driven thrust (red background) regimes, which takes place for an almost constant $\beta_A \approx 3$. This predominance indicates the importance of this thrust regime to the flapping propulsion onset in cruise regime, adding up to its importance to the locomotion onset at transient regimes (figure 4.4). The transition between diffusion and pressure-driven thrust is then obtained for an almost constant $\beta_A \approx 10$. This fact is particularly true for small amplitudes $A \leq 0.3$, this frontier growing up to $\beta_A = 13.5$ for $A = 0.5$. The delay of this transition for higher flapping amplitudes is connected to the emergence of non-coherent states of locomotion.

4.4 Conclusions

In this work, the time-averaged contributions of diffusion and pressure forces to the horizontal forces generated by a horizontally self-propelled heaving foil in a quiescent fluid were investigated. The existence of a transition between diffusion and pressure-driven thrust regimes has been highlighted. Studying the time-averaged flow associated to each of these regimes, we have shown that the diffusion-driven thrust is based on the asymmetric shear on the foil lateral surface, whereas the pressure-driven thrust regime relies on the fluid acceleration behind the flapping body and its consequent reduction of the trailing edge suction force. We have finally studied

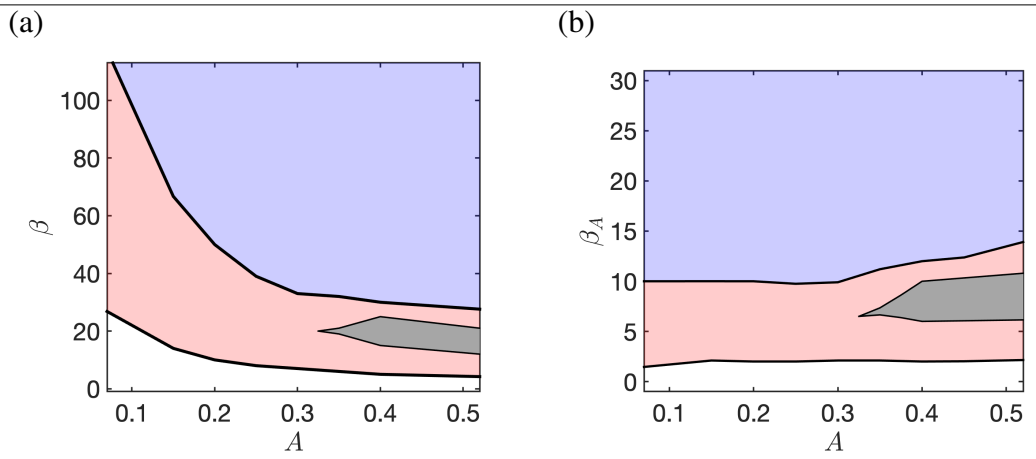

Figure 4.7: Diffusion-driven and pressure-driven self-propelled regimes in the parameter space (a) (A, β) and (b) (A, β_A) where $\beta_A = A\,\beta$. Diffusion- and pressure-driven thrust regimes are red and blue background colors. The white background correspond to non-propulsive solutions. The black curves delimit the transition between those regimes. Grey regions correspond to non-coherent quasi-periodic solutions. Fixed control parameters are $h = 0.05$ and $\rho = 100$.

the influence of the thickness-to-chord aspect ratio and the flapping amplitude, revealing that the diffusive-driven thrust is enhanced for smaller thickness-to-chord aspect ratios and might be mitigated for greater ones. In the flapping amplitude and frequency plan, the transition between these thrust regimes takes place for a flapping amplitude based Stokes number $\beta_A \approx 10$. The existence of a diffusive thrust regime appear to be of key importance both for the onset of a permanent and transient regime locomotion.

Part II

Collective dynamics of an infinite array of flapping wings in a viscous flow

Chapter 5

Theoretical and numerical methods

This chapter introduces the theoretical and numerical methods used in the Part II of this thesis. The unsteady dynamics of an infinite self-propelled array of flapping wings confined in a channel will be studied in chapter 6. Owing to this confinement, the non-inertial frame of reference introduced in chapter 1 is not capable of taking the array heaving motion into account. A fictitious domain with distributed Lagrange multipliers formulation is then adopted. After detailing its derivation, some numerical aspects are discussed and the implementation of the unsteady nonlinear solver is detailed. Three validation cases are finally presented.

Contents

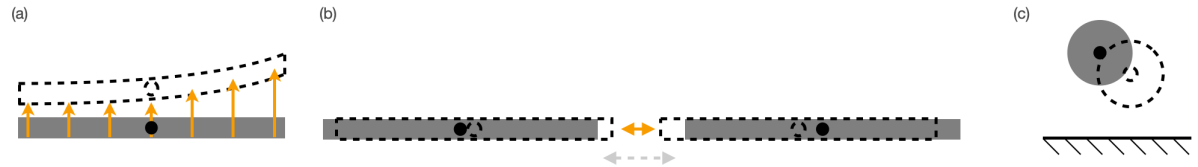

Figure 5.1: Examples of configurations where the adoption of a non-inertial frame of reference does not eliminate the time-dependency of solid boundaries. (a) Elastic deformation of a rectangular foil, (b) relative motion with decreasing gap between two rectangular foils and (c) circular cylinder moving next to a immobile solid wall. The initial (perturbed) configuration is represented by the solid (dashed) object. A solid and dashed circle represent the object center of gravity in these two instants. In (a), orange arrows indicate the foil movement, while in (b) the gap at the two instants is indicated by a dashed gray and a solid orange double-arrow.

5.1 Introduction

Judo is a martial art with an embedded (very beautiful) moral pedagogy. The term in Japanese is composed of two *kanjis* (logo-graphic characters adopted in the Japanese writing system). The first one means flexibility or gentle and the second one path or way, the martial art being informally known as the "gentle path". The legend behind judo philosophy (and also that of ju-jitsu) tells that the martial art has as inspiration the spectacle of plants covered by snow after a hard winter. While cheery tree branches, very rigid, were broken by the snow weight, the flexible/elastic willow branches just bent and would gently get rid of the weight, letting the accumulated snow fall on the ground. In the martial art, one should learn the lesson from the willow: be flexible and elastic, gently adapting to the enemy movement to use his weight and force against him [1]. For the purpose of flapping propulsion, elastic deformations are not only useful to get rid of forces. They can be used to decrease ones effort by projecting incoming forces in the swimming direction (Liao, Beal, and Lauder 2003). In addition, different than the snow/ willow or judo collective dynamics, flapping wing interactions are not as one sided, in a sense just one of the involved parts use the other energy to get rid of the other. Constructive collective interactions, where individuals mutually benefit from the forces/vortices shed in the fluid by another are also possible. Bird flocks and fish schools are example of how living organisms actively or passively use the unsteady flow of a flapping neighbour to ease their own flapping movement and achieve energetic advantages (Portugal et al. 2014; Hemelrijk et al. 2015). These interactions are not limited to other flapping organisms, and solid walls can also be exploited to improve a flapping wing energetic efficiency (Fernández-Prats et al. 2015). Understanding the physical principles of these mechanisms is of great importance to enhance the efficiency of human made flapping devices. However, to study elastic deforming, numerous free and confined bodies the tools developed in the first chapter of this thesis will need to be adapted.

The non-inertial frame of reference, introduced in the first chapter of this thesis, has limitations and is not capable of withdrawing solid boundaries time-dependency in certain cases.

[1] For those who appreciate the beauty of plants flexibility/elastic reconfiguration both the fable *Le chêne et le roseau* from Jean de la Fontaine and *Flow-induced deformations and stress reduction by flexibility* (Tristan Leclercq, 2018) are highly recommended.

Examples are illustrated in figure 5.1. For wings with deforming interface (5.1-a) following the wing center of gravity might reduce the interface deformation, but the foil surface will still deform and be time-dependent in the non-inertial frame of reference. That is equally the case for arrays with a free separation gap (5.1-b) or objects interacting with a steady solid wall (5.1-c). In the first case, adopting a non-inertial frame of reference in no matter which foil still leads to the time-dependency of the other foil solid wall. For the object interacting with a solid wall, although the time-dependency of the object boundary itself is removed by the non-inertial frame, the steady wall becomes time-dependent. A more general method capable of handling time-dependent frontiers needs to be considered to take into account the solid flapping movement. This chapter introduces one of these methods: a fictitious domain formulation with distributed Lagrange multipliers (Boffi, Hecht, and Pironneau 2018). This method will be used in the next chapter to study the self-propulsion of an infinite array of rigid flapping wings confined in a channel (Becker et al. 2015). In this case the confinement by solid walls in the vertical direction does not allow the non-inertial frame to take into account the wing heaving motion.

Many strategies are available in the literature to handle equations defined in moving domains. These strategies can be distinguished by their choice of requiring either conforming or non-conforming fluid and solid domains (examples of these two kinds are latter given in figure 5.4). In the case of conforming strategies, the separation between the media is precisely defined by the computational mesh. One of these strategies is the so-called Arbitrary Lagrangian Eulerian approach (Pfister, Marquet, and Carini 2019). This approach, widely employed in the case of fluid-structure interactions, adopt a Lagrangian description of the solid and an Eulerian description of the fluid domain. To achieve the conformity in the fluid-solid interface, this approach requires an additional ingredient to handle the deformation of the fluid domain near the interface. Either the domain deforms and re-meshing for every time iteration is needed along the simulation temporal evolution, or a extension domain where the equations smoothly switch between the Lagrangian and Eulerian description, the mesh deformation being analytically handled in the equations needs to be defined. However, these two alternative might become impractical for self-propelled foils. In the case of reference domain, the Lagrangian description of the solid and extension domain, well adapted for small displacements, might not handle the large amplitude flapping movement and non-physical negative volume or surface variations of the mesh appear in the equation. Re-meshing strategies on the other hand, might be computationally expensive and suffer from interpolation issues. Non-conforming methods, do not require conformity between solid and fluid domain, being an attractive option to handle large amplitude flapping movements. In these methods, the Eulerian description is normally kept for the whole fluid and solid domains. Generally, the fluid equations are solved both in the fluid and solid domains. The presence of the solid inside this combined domain is then embedded into the equations by the introduction of source terms. These correct the coupled equations to impose boundary conditions and take the solid into account. From those the largest employed are so-called *immersed boundary methods* (Peskin 1972), where the solid is included in the fluid equations through *Dirac* delta function source terms. A closely related approach is found in *Fictitious domain methods* (Glowinski et al. 1999) that enforce the solid boundary conditions in the problem variational formulation through Lagrange multipliers rather than discontinuous terms. *Penalization methods* (Angot, Bruneau, and Fabrie 1999) are also very similar. In this case, a penalization parameter is introduced in the equations, turning the volumes occupied by the solid into zones of very small permeability. The boundary condition is then imposed

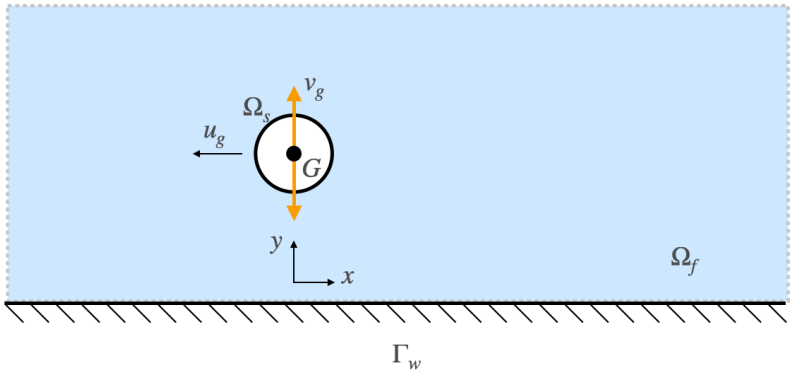

Figure 5.2: Arbitrary configuration of a rigid solid body Ω_s interacting with a surrouding fluid Ω_f nearby a solid wall Γ_w. The body horizontal u_g, vertical velocity v_g flapping movement (orange arrow), center of gravity G and the frame of reference are indicated in the figure.

at a separated order of magnitude generated by this penalization coefficient. In this work we will adopt a fictitious domain methods with distributed Lagrange multipliers (FD/DLM) formulation, based on its recent implementation (Boffi, Hecht, and Pironneau 2018) in the open-source software FreeFEM, employed along this thesis. This choice was also motivated by this method ease of directly computing local and global forces acting on the solid through the Lagrange multipliers, and its easy adaptability to thin and thick solids or elastic problems (Boffi and Gastaldi 2017). In the following sections the governing nonlinear equations and the theoretical derivation of this approach will be detailed in §§5.2 and 5.3. The validation of the numerical method,and some of its particularities are then presented in §5.3.2.

5.2 Unsteady nonlinear equations

In this initial derivation, we will consider an arbitrary rigid body surrounded by a quiescent fluid in a domain bounded by a solid wall Γ_w infinite in the horizontal direction, as the one show in figure 5.2. The solid body has a characteristic length (chord in the case of a foil $c = 1$), density ρ_s and flap with a characteristic frequency f^* and amplitude A^*. This solid is free to translate in a two-dimensional fluid of density ρ_f and kinematic viscosity ν with a velocity $\mathbf{u}_g = (u_g, v_g)$. This rigid-body fluid-structure interaction is characterized, as usual in this thesis, by the (non-dimensional) flapping amplitude, frequency-based Stokes number β and the solid-fluid density ratio ρ defined as

$$A = \frac{A^*}{c}, \; \beta = \frac{f^* c^2}{\nu}, \; \rho = \frac{\rho_s}{\rho_f}. \tag{5.1}$$

The characteristic scales for length, mass and time are respectively the body length (chord) c, the fluid density ρ_f and the flapping period $1/f^*$. The non-dimensional flapping period T is equal to 1 whatever the value of the Stokes number β due to the choice of characteristic time-length, and β encodes the effect of the flapping frequency movement.

The surrounding flow is governed by the Navier-Stokes equations

$$\begin{array}{rcll} \partial_t \mathbf{u} & = & -\nabla \mathbf{u} \cdot (\mathbf{u} - u_g \mathbf{e}_x) + \nabla \cdot \sigma(p, \mathbf{u}), & \text{in } \Omega_f(t), \\ 0 & = & \nabla \cdot \mathbf{u}, & \text{in } \Omega_f(t), \end{array} \tag{5.2}$$

that are here written in a non-inertial frame of reference that follows exclusively the foil center of mass g **horizontal** motion. This fluid problem is closed by two no-slip boundary conditions

$$\begin{array}{rcll} \mathbf{u}(\mathbf{x}, t) & = & [u_g, v_g]^T, & \text{on } \Gamma_s(t), \\ \mathbf{u}(\mathbf{x}, t) & = & 0, & \text{on } \Gamma_w, \end{array} \tag{5.3}$$

one at the solid boundary $\Gamma_s(t)$ and one at the bottom wall Γ_w. Finally, the temporal evolution of the foil horizontal velocity $\mathbf{u}_g$ is governed by Newton's second law

$$\frac{d\mathbf{u}_g}{dt} = (\rho S)^{-1} \int_{\Gamma_s(t)} (\sigma(p, \mathbf{u}) \cdot \mathbf{n}) \cdot \mathbf{e}_\mathbf{x} d\Gamma + F_d \cdot \mathbf{e}_y, \tag{5.4}$$

that balances the solid inertia (ρS), its acceleration and the hydrodynamic forces acting over the body. To impose the flapping vertical velocity $v_g = 2\pi A \sin(2\pi t)$, a driving vertical force F_d appears in the solid equation. The Cauchy stress tensor $\sigma(p, \mathbf{u})$ of an incompressible Newtonian fluid is

$$\sigma(p, \mathbf{u}) = -p\mathcal{I} + \beta^{-1}(\nabla \mathbf{u} + \nabla \mathbf{u}^T). \tag{5.5}$$

Inside the definition of the former system of equations lies the challenge of numerically addressing self-propelled flapping foils or deforming bodies: the fluid and time domain are both time-dependent due to the interface motion. To take into account the coupling between the fluid and the solid, two theoretical steps are necessary. As already introduced, a non-inertial frame of reference that follows the wing horizontal motion has been adopted[2]. The horizontal position of the solid domain Ω_s is known for every time instant and the size of the fluid domain is no longer dependent of the wing trajectory. However, different than the problem studied in the first part of the thesis, our domain is bounded by a solid wall Γ_w. This solid wall, infinite in the horizontal direction, do not become time-dependent in a frame of reference that follows the solid horizontal motion. It would, however, become if the solid vertical motion would be followed. While a non-inertial frame of reference would withdraw the Γ_s time-dependency, Γ_w would become time-dependent. The time-dependency would then be just transferred to another boundary. To overcome this issue, a fictitious domain formulation with distributed Lagrange multipliers (FD-DLM) (Glowinski et al. 2001; Boffi and Gastaldi 2017; Boffi, Hecht, and Pironneau 2018) is introduced in the weak formulation of the problem. To derive it, we first define the combined variation space

$$W = \{(\psi_u, \psi_p, \mathbf{V}) | \psi_u \in (H^1)^2(\Omega_f(t)), \psi_p \in L^2(\Omega_f(t)), \mathbf{V} \in \mathcal{R}^2, \psi_u = \mathbf{V} \, on \, \Gamma_s(t), \, \psi_u = 0 \, on \, \Gamma_w\}, \tag{5.6}$$

[2]This treatment will not be discussed in this chapter since it has been detailed in chapter 1.

for the fluid velocity, pressure and two scalars for the solid domain vertical and horizontal velocity. The first step of the fictitious domain approach is to introduce a combined weak formulation of the fluid and solid equations, which is obtained multiplying eqs (5.2)-(5.4) by the appropriate test functions, integrating in the appropriate space and summing the resulting terms

$$\begin{gathered}\iint_{\Omega_f(t)}\left[\partial_t\mathbf{u}+\nabla\mathbf{u}\cdot(\mathbf{u}-u_g\mathbf{e}_x)-\nabla\cdot\sigma\right]\cdot\psi_u\mathrm{d}\Omega+\rho S\frac{d\mathbf{u}_g}{dt}\cdot\mathbf{V}-\int_{\Gamma_s(t)}(\sigma\cdot\mathbf{n})\mathrm{d}\Gamma\cdot\mathbf{V}-F_d\mathbf{e}_y\cdot\mathbf{V}=0\,,\\ \int_{\Omega_f(t)}\psi_p\cdot(\nabla\cdot\mathbf{u})=0\,.\end{gathered} \tag{5.7}$$

In this combined formulation, the fluid forces acting on the domain borders interface can be further identified through integration by parts of the stress tensor divergence [3]

$$\iint_{\Omega_f(t)}\left[-(\nabla\cdot\sigma)\cdot\psi_u\right]\mathrm{d}\Omega \;=\; \iint_{\Omega_f(t)}\left[\sigma:\nabla\psi_u\right]\mathrm{d}\Omega+\int_{\Gamma_s(t)}[\sigma\cdot\mathbf{n}\cdot\psi_u]\mathrm{d}\Gamma+\int_{\Gamma_w}[\underbrace{\sigma\cdot\mathbf{n}}_{\lambda}\cdot\psi_u]\mathrm{d}\Gamma\,. \tag{5.8}$$

The forces on the external borders of the domain will be further discussed in the final formulation. The imposition of the wall Dirichlet condition, and the determination of the forces in this wall, will be done through the addition of Lagrange multipliers λ degrees of freedom as done by Pfister, Marquet, and Carini (2019). Here we focus on the forces acting on the fluid-solid interface. These will cancel within the combined weak formulation due to the equality of the test functions $\mathbf{V}$ and ψ_u over $\Gamma_s(t)$ on the combined variation space definition and of the forces acting across the fluid-solid interface

$$\begin{gathered}\iint_{\Omega_f(t)}\left[(\partial_t\mathbf{u}+\nabla\mathbf{u}\cdot[(\mathbf{u}-u_g\mathbf{e}_x))\cdot\psi_u+\sigma:\nabla\psi_u\right]\mathrm{d}\Omega+\rho S\left(\frac{d\mathbf{u}_g}{dt}-F_d\mathbf{e}_y\right)\cdot\mathbf{V}=0\,,\\ \int_{\Omega_f(t)}\psi_p\cdot(\nabla\cdot\mathbf{u})=0\,.\end{gathered} \tag{5.9}$$

This combined formulation governs the evolution of the coupled fluid-solid momentum. The mutual compensation of the forces on the fluid-solid interface, from fluid and solid sides, can be seen as a consequence of Newton's third law. These forces being internal to the coupled system, they represent only an exchange between the two media, but not an increase of the coupled system momentum. At this point, the determination of the solid forces calculated on the time-dependent solid boundary has been withdrawn from the system. The fluid domain and the no-slip boundary condition over the solid, however, remain time-dependent. To overcome these issues the fictitious domain formulation will be introduced in the following section.

5.3 FD/DLM formulation

Two steps are going to be taken to overcome the time-dependency of the fluid domain and the moving solid boundary. First, the fluid equations are going to be extended inside the solid, generating a time-independent fictitious domain. Distributed Lagrange multipliers will then

[3] the change of sign in the last two integrals is due to the normal $\mathbf{n}$ being inward rather than outward oriented.

be added to impose the solid velocity no-slip boundary condition inside the fictitious domain, correcting the fluid equations. These two steps lead to the so-called *fictitious domain with distributed Lagrange multipliers formulation* (FD/DLM).

The central idea of a fictitious domain formulation is to avoid the domain time-dependency by extending the fluid equations to a time-independent fictitious domain $\Omega_f \cup \Omega_s$ that includes both solid and fluid domain. To define the weak formulation of the Navier-Stokes equations over this domain, its integral over the solid is simultaneously summed and subtracted from the time-dependent fluid domain as to write

$$\begin{aligned}
&\iint_{\Omega_f(t)} \left[[\partial_t \mathbf{u} + \nabla \mathbf{u} \cdot (\mathbf{u} - u_g \mathbf{e}_x)] \cdot \psi_u + \sigma : \nabla \psi_u \right] \mathrm{d}\Omega = \\
&\iint_{\Omega_f \cup \Omega_s} \left[[\partial_t \mathbf{u} + \nabla \mathbf{u} \cdot (\mathbf{u} - u_g \mathbf{e}_x)] \cdot \psi_u + \sigma : \nabla \psi_u \right] \mathrm{d}\Omega \\
&- \iint_{\Omega_s(t)} \left[[\partial_t \mathbf{u} + \nabla \mathbf{u} \cdot (\mathbf{u} - u_g \mathbf{e}_x)] \cdot \psi_u + \sigma : \nabla \psi_u \right] \mathrm{d}\Omega \,.
\end{aligned} \tag{5.10}$$

The functions enlarged to the solid domain, however, cannot assume an arbitrary value. They need to comply to the physical rigid-body movement of this domain, which is now required in the definition of the modified fictitious combined variation space

$$\tilde{W} = \{(\psi_u, \psi_p, \mathbf{V}) | \psi_u \in (H^1)^2(\Omega_f \cup \Omega_s), \psi_p \in L^2(\Omega_f \cup \Omega_s), \mathbf{V} \in \mathcal{R}^2, \psi_u = \mathbf{V} \, in \, \Omega_s(t), \, \psi_u = 0\}\,, \tag{5.11}$$

where the test function ψ_u should equal $\mathbf{V}$ not only on the border $\Gamma_s(t)$ but throughout the entire solid domain $\Omega_s(t)$. Thanks to this definition it is easy to see that $\nabla \psi_u = 0$ and that the simultaneously added/subtracted momentum inside the solid domain equals in fact the 2nd Newton's law

$$\iint_{\Omega_s(t)} \left[[\partial_t \mathbf{u} + \nabla \mathbf{u} \cdot (\mathbf{u} - u_g \mathbf{e}_x)] \cdot \psi_u + \sigma : \nabla \psi_u \right] \mathrm{d}\Omega = S \frac{d\mathbf{u}_g}{dt} \cdot \mathbf{V} \,. \tag{5.12}$$

Inserting these modifications in eq. (5.9), the fictitious domain combined weak formulation of the system is finally obtained

$$\begin{aligned}
&\int_{\Omega_f \cup \Omega_s} \left[\partial_t \mathbf{u} + \nabla \cdot [(\mathbf{u} - u_g \mathbf{e}_x)\mathbf{u}] + \sigma : \nabla \psi_u \right] \mathrm{d}\Omega \cdot \psi_u + (\rho - 1) S \frac{d\mathbf{u}_g}{dt} \cdot \mathbf{V} - F_d \mathbf{e}_y \cdot \mathbf{V} = 0, \\
&\int_{\Omega_f \cup \Omega_s} \psi_p \cdot (\nabla \cdot \mathbf{u}) = 0.
\end{aligned} \tag{5.13}$$

Note that as the fluid velocity and pressure must coincide between the original and fictitious domain problem the same notation has been kept for both formulations. The incompressibility has been naturally extended to the fictitious domain, since the rigid body is incompressible. [4] In this formulation, we see that the fluid extension to the fictious domain generates a compensation with an "anti-body" of negative mass equal to the fluid inertia in the solid equations. This compensation corrects the solid momentum, taking into account the equivalent acceleration

[4] This formulation can be adapted in the case of compressible solids (Boffi, Hecht, and Pironneau 2018). Their compressibility intervenes modifying the divergence-free fictitious equation.

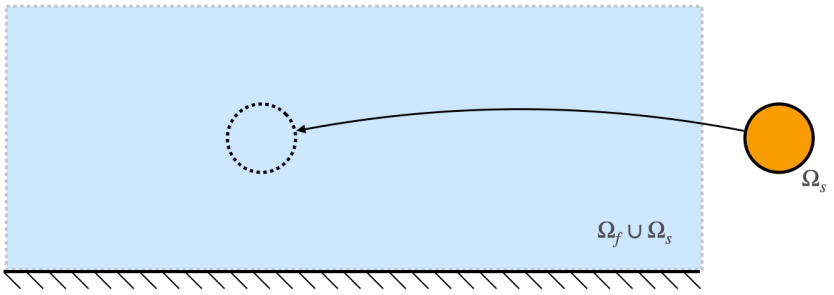

Figure 5.3: Fictitious domain method with distributed Lagrange multipliers sketch applied to the previous configuration. The fluid domain is enlarged to a fictitious one including both solid and fluid $\Omega_f \cup \Omega_s$. Then, to take into account the presence of the solid body Ω_s, distributed Lagrange multipliers are applied over the solid position (dashed line) on the fictitious domain.

existent in the first integral, over the fictitious domain, of the combined weak formulation. However, this compensation is only valid if the equality between fluid and solid velocity is verified over $\Omega_s(t)$. To enforce this, that has until now been supposed in the definition of the combined variational space, we will introduced distributed Lagrange multipliers over the portion of the fictitious domain occupied by the solid. This leads to the the Fictitious Domain with Distributed Lagrange Multipliers (FD-DLM) formulation

$$\begin{aligned} \iint_{\Omega_f \cup \Omega_s} [\partial_t \mathbf{u} \cdot \psi_u] \, \mathrm{d}\Omega \quad = \quad & - \iint_{\Omega_f \cup \Omega_s} \left[[\nabla \mathbf{u} \cdot (\mathbf{u} - u_g \mathbf{e}_x)] \cdot \psi_u + \sigma(p, \mathbf{u}) : \nabla \psi_u \right] \mathrm{d}\Omega \\ & + (\rho - 1) S \frac{d\mathbf{u}_g}{dt} \cdot \mathbf{V} - F_d \mathbf{e}_y \cdot \mathbf{V} + < \mathbf{f}, \psi_u - \mathbf{V} >_{\Omega_s(t)}, \end{aligned} \tag{5.14}$$

which has its principle illustrated in figure 5.3. The volume term of the distributed Lagrange multipliers $< \mathbf{f}, \psi_u - \mathbf{V} >_{\Omega_s(t)}$ ($\langle ., . \rangle_{\Omega_s(t)}$ denoting an appropriate scalar product) is simultaneously used to correct the fictitious Navier-Stokes equations with the solid dynamics and to impose the equality of solid and fluid velocity in $\Omega_s(t)$

$$0 \quad = \quad < \mathbf{u} - \mathbf{u}_g, \psi_f >_{\Omega_s(t)} \ . \tag{5.15}$$

To enforce the remaining no-slip boundary conditions over the domain external boundary Γ_w Lagrange multipliers λ and the weak imposition of the no-slip boundary condition are introduced. Separating the weak formulation within respective variation test functions results in the system weak equations

$$
\begin{aligned}
\iint_{\Omega_f \cup \Omega_s} [\partial_t \mathbf{u} \cdot \psi_u] \, \mathrm{d}\Omega &= -\iint_{\Omega_f \cup \Omega_s} \left[[\nabla \mathbf{u} \cdot (\mathbf{u} - u_g \mathbf{e}_x)] \cdot \psi_u + \sigma(p, \mathbf{u}) : \nabla \psi_u \right] \mathrm{d}\Omega \\
&\quad + < \mathbf{f}, \psi_u >_{\Omega_s(t)} - \int_{\Gamma_w} [\lambda \cdot \psi_u] \, \mathrm{d}\Gamma, \\
0 &= \iint_{\Omega_f \cup \Omega_s} \left[(\nabla \cdot \mathbf{u}) \cdot \psi_p \right] \mathrm{d}\Omega, \\
(\rho - 1) S \frac{d\mathbf{u}_g}{dt} \cdot \mathbf{V} &= - < \mathbf{f}, \mathbf{V} >_{\Omega_s(t)} + F_d \mathbf{e}_y \cdot \mathbf{V}, \\
0 &= < \mathbf{u} - \mathbf{u}_g, \psi_f >_{\Omega_s(t)}, \\
0 &= \int_{\Gamma_w} [\mathbf{u} \cdot \psi_l] \, \mathrm{d}\Gamma,
\end{aligned}
\tag{5.16}
$$

with the the final variation space taking the form

$$
\bar{W} = \{(\psi_u, \psi_f, \psi_p, \psi_l, \mathbf{V}) | \psi_u \in (H^1)^2(\Omega_f \cup \Omega_s), \psi_f \in (L^2)^2(\Omega_s), \psi_p \in L^2(\Omega_f \cup \Omega_s), \psi_l \in (H^{-1/2})^2(\Gamma), \mathbf{V} \in \mathcal{R}^2\} \,. \tag{5.17}
$$

As explained by (Glowinski et al. 1999), the additional Lagrange multiplier $\mathbf{f}$ added in the Navier-Stokes equation can be understood as an additional volumic force required to maintain the rigid-body (alternatively the solid material behaviour) in $\Omega_s(t)$. For the inner product $< \mathbf{f}, \psi_u >_{\Omega_s(t)}$ we have opt for the standard inner product on $L^2(\Omega_s(t))$.

$$
< \mathbf{f}, \psi_u(x(t), t) >_{\Omega_s(t)} = \iint_{\Omega_s(t)} [\mathbf{f}(\mathbf{X}) \cdot \psi_u(\mathbf{x_f})] \mathrm{d}\Omega \,. \tag{5.18}
$$

A discussion of the possible inner products and their physical qualities can be found in (Glowinski et al. 1999). In this work we have opted for the L^2 product since it achieves a rather sharp description of the solid interface, for example than a H^1 product. To achieve an even sharper interface, a more discontinuous product as a collocation method (Bertrand, Tanguy, and Thibault 1997) would be another possible choice. A particular treatment is necessary for the computation of this inner project. In the case of the term present in the Navier-Stokes equations, the operator requires the projection of the Lagrange multiplier $\mathbf{f}$ from the position $\mathbf{X} \in \Omega_s$ of the solid domain to $\mathbf{x}_f \in \Omega_s(t) \subset \Omega_f \cup \Omega_s$ the actual position occupied by the solid in the fictitious domain. Similarly the fluid velocity needs to be evaluated in the solid domain to impose the no-slip boundary condition. The discrete version of this weak formulation will have to face numerical impurities associated to these interpolations, in addition to the non-conformity of the fluid-solid interface. The stress continuity across the fluid-solid interface is thus approximated and not strongly enforced by this formulation. This fact must be particularly kept in mind for fluid-solid linear stability, where the stress continuity is essential (Pfister, Marquet, and Carini 2019).

5.3.1 Numerical method

A continuous Galerkin finite-element method is employed to discretize the equations (5.16) in space. Quadratic elements (P2) are used for the flow velocity and the Lagrange multipliers while linear elements (P1) are used for the pressure. The choice of the Lagrange multipliers

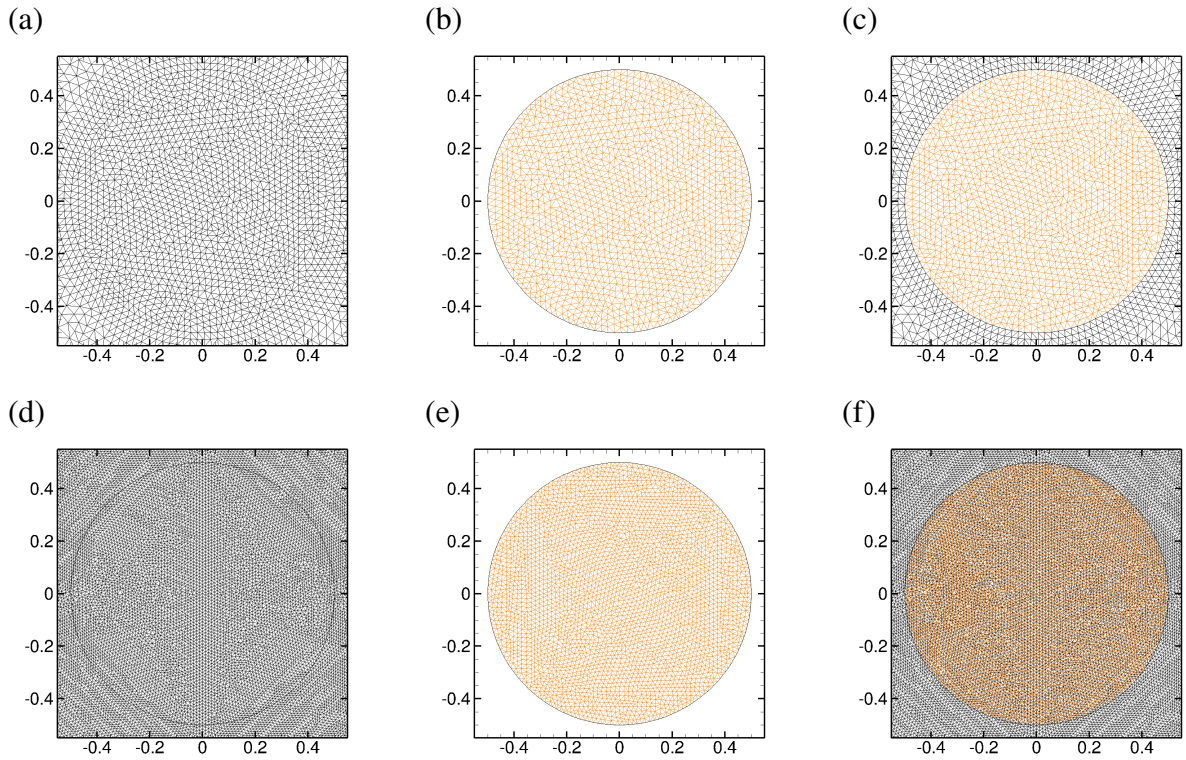

Figure 5.4: Spatial discretization of the (a,d) Fictitious $\Omega_f \cup \Omega_s$ (black mesh), (b,e) solid Ω_s (orange mesh) and (c,f) superposition of the two domains for (a-c) a conforming and (d-f) a non-conforming case.

elements was based on the solver validation for a conforming interface case, detailed in the subsection §5.3.1.1. The implementation is based on the FreeFEM software (Hecht 2012). Two computational domains are discretized, the fictitious $\Omega_f \cup \Omega_s$ and the solid Ω_s ones, as illustrated in figure 5.4. The FD-DLM formulation handles both conforming, when the solid domain discretization conforms to the background mesh (a-c), and non-conforming (d-f) descriptions, where there is no conformity between the solid and the background discretization. The discretization of the solid domain must ensure the stability of the finite element formulation. If polynomial elements of same order are chosen between the fluid velocity and the distributed Lagrange multipliers, the height of the solid domain triangles should be between twice or the same of the background mesh to ensure the formulation stability (Glowinski et al. 1999). For the cases treated in chapter 6. Delaunay triangulation of the fictitious and solid domains results typically in meshes of 1.2×10^4 and 300 triangles. The triangle size is typically of order $O(10^{-2})$ in regions where the solid domain passes going up to $O(10^{-1})$ in regions of near zero out-of-plane vorticity ω_z. The minimum and maximum mesh refinement levels have been set to attend a convergence of order $O(10^{-4})$ of the foil horizontal velocity and the vertical hydrodynamic force. The FD/DLM technique requires the interpolation between Lagrange multiplier from the time-dependent solid domain to the fictitious domain. Normally, the interpolation accuracy is optimal when solid and background fictitious elements are near a conforming description, becoming perfect in the conforming case. To guarantee this accuracy, the present numerical method explore the Hessian-based mesh adaptation functionalities of FreeFEM, adapting the fictitious domain mesh to regenerate the solid frontier after a certain number of iterations (usually 10 times every flapping period) as done by Boffi, Hecht, and Pironneau (2018). The accuracy of the Lagrange multipliers $\mathbf{f}$ projection throughout the simulation is thus enhanced, while avoiding the high computational cost of an uniform mesh refinement.

The unsteady problem (5.16) is discretized in time using a r-order implicit linearized scheme. All terms are implicit. The nonlinear convective term from the Navier Stokes equations is implicit linearized through the r-order extrapolation formula $\sum_{k=1}^{r}\gamma_k[\nabla\mathbf{u}^{n+1}\cdot(\mathbf{u}^{n+1-k}-\mathbf{u}_g^{n+1-k})]$. The resulting matrix formulation takes the form

$$\underbrace{\begin{bmatrix} \mathbf{A}_f & 0 & \mathbf{I}_f & \mathbf{I}_\lambda \\ 0 & \alpha_0/\Delta t & \mathbf{I}_s & 0 \\ \mathbf{I}_f^T & \mathbf{I}_s^T & 0 & 0 \\ \mathbf{I}_\lambda^T & 0 & 0 & 0 \end{bmatrix}}_{\mathbf{A}} \cdot \begin{bmatrix} (\mathbf{u}^{n+1}, p^{n+1})^T \\ u_g^{n+1} \\ \mathbf{f}^{n+1} \\ \lambda^{n+1} \end{bmatrix} = \begin{bmatrix} -\sum_{k=1}^{r}\iint_{\Omega_f\cup\Omega_s}(\alpha_k/\Delta t)\mathbf{u}^{n+1-k}\cdot\psi_u \mathrm{d}\Omega \\ -\sum_{k=1}^{r}(\alpha_k/\Delta t)u_g^{n+1-k} \\ \iint_{\Omega_s(t)} v_g\cdot\mathbf{e}_y\cdot\psi_f \\ 0 \end{bmatrix}. \quad (5.19)$$

where the matrices identified by orange colors need to be assembled in every iteration. Δt is the time step and $(\mathbf{u}^{n+1}, p^{n+1})$ the velocity and pressure at time $t_{n+1} = (n+1)\Delta t$. A first-order scheme ($r = 1$, $\alpha_0 = 1$, $\alpha_1 = -1$ and $\gamma_1 = 1$) is used for the first two temporal iterations ($n \leq 1$), followed by a second-order scheme ($r = 2$, $\alpha_0 = 3/2$, $\alpha_1 = -2$, $\alpha_2 = 1/2$, $\gamma_1 = 2$ and $\gamma_2 = -1$).

The problems treated in this thesis have a great advantage compared to those normally treated by FD/DLM formulations (Boffi and Gastaldi 2017). As the heaving movement is imposed, the non-inertial frame of reference follows the horizontal motion and the solid is rigid, the solid position is completely determined for the time instant $n + 1$. Different than problems

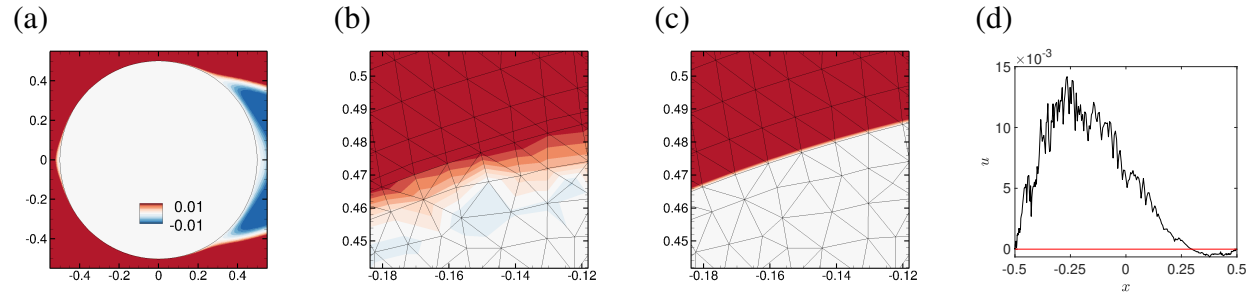

Figure 5.5: (a) Large and close-up (b,c) view of the stream-wise velocity on a cylinder surface for $Re = 40$ over the fictitious domain. (b) P1 and (c) P2 discretization of the distributed Lagrange multipliers. The fictitious and solid domain are conforming (meshes shown in figure 5.4(a-c)). (d) Value of the horizontal velocity on the cylinder wall upper part $y \geq 0$.

with solid deformation, no special scheme is required to implicitly determine the solid position at $n+1$. The equality of fluid and solid velocity can be treated implicitly and severe time-step restrictions induced by an explicit coupling (Causin, Gerbeau, and Nobile 2005) are avoided.

In the present numerical method, the matrix A needs to be factorized at every time iteration, as the three orange identified blocks need to be reconstructed. In the case of the fluid block A_f, the reconstruction is necessary due to the linearized implicit discretization. The interpolation matrices $\mathbf{I}_f$ and $\mathbf{I}_f^T$ of the distributed Lagrange multiplier need to be rebuild due to the movement of the time-dependent solid domain. As the structure moves, the position where the multipliers and the fluid velocity are interpolated change with time. These matrices benefit from specific interpolation functions from FreeFEM used to shift the spatial position of variables and test functions in weak formulations called *mapu* and *mapt* (Boffi, Hecht, and Pironneau 2018) [5]. $\mathbf{I}_f$ is an interpolation matrix that brings the Lagrange multipliers $\mathbf{f}^{n+1}$ of Ω_s to the current position occupied by the solid domain in $\Omega_f \cup \Omega_s$. Equivalently, $\mathbf{I}_f^T$ is an inverse interpolation that brings the fluid velocity $\mathbf{u}^{n+1}$ at the solid position of $\Omega_f \cup \Omega_s$ to Ω_s. Although the implicit discretization guarantees a greater temporal scheme stability, caution is recommended when adopting large time steps. As the Lagrange multipliers are vertically displaced along the domain, they generate fresh cells previously occupied by the solid that return to the fluid domain. To circumvent this issue, we have here limited the time-step by the triangles height nearby the solid interface and the foil vertical velocity. A time step of $\Delta t = 1 \cdot 10^{-3}$ was generally adopted in this work, allowing a good trade-off between the computational cost and the simulation accuracy.

5.3.1.1 Discretization of the distributed Lagrange multipliers

The spatial discretization of the distributed Lagrange multiplier remains an open problem (Boffi, Gastaldi, and Ruggeri 2014). In literature studies (Glowinski et al. 1999; Glowinski, Pan, and Périaux 2006; Boffi and Gastaldi 2017) distributed Lagrange multipliers and fluid velocity are usually discretized with elements of same polynomial order, stability conditions being then imposed over the height of the background and solid domains triangles. However, this stability

[5] The functions *mapu* and *mapt* allow the user to build a variational formulation $\int_\Omega u \cdot t \mathrm{d}\Omega$ with the positions of the variable u or test function t shifted from the domain Ω where they are defined, or at an user defined list of points.

condition is still less precise than, for example, the one that links fluid pressure and velocity. For example Glowinski et al. (1999) uses similar elements for fluid velocity, pressure and Lagrange multipliers. The stability condition imposed for fluid velocity and pressure elements is the use of a twice coarser triangulation for the pressure. In the mean time, the distributed Lagrange multipliers have a more flexible criterion, its discretization being required to be between twice coarser or of the same order of the fluid velocity.

In the present work we have placed ourselves within this range through a simple experiment. In a conform discretization, where no interpolation problems exist, we have typically discretized the fluid velocity and pressure with P2 and P1 elements. The elements of the distributed Lagrange multiplier were then adopted as quadratic (P2) or linear (P1), achieving the discretization limits of Glowinski et al. (1999). Our choice of the distributed Lagrange multipliers discretization was then based on the imposition of the no-slip boundary with the present method. The configuration studied was the steady flow surrounding a cylinder at a Reynolds number $Re = 40$, whose flow is depicted in figure 5.5(a). The distributed Lagrange multipliers were used in the unsteady solver simply to apply the no-slip boundary condition $\mathbf{u} = 0$ over the cylinder surface. For both adopted elements, no instability of the unsteady nonlinear solver was observed. However, the precision achieved to impose the interface velocity was much greater for P2 elements (same order as the fluid velocity) than P1. While P1 elements present oscillations in the level of the interface (see figure 5.5-b), P2 elements manage to perfectly impose the no-slip boundary condition in the fictitious domain, seen in figure 5.5(c). Quantitatively, the oscillations observed in the fictitious domain for P1 elements are reflected in the velocity u over the solid interface, represented in figure 5.5(d) for the cylinder upper surface. While P1 elements present oscillations of $O(10^{-2})$, P2 elements precisely apply the no-slip boundary condition up to order $O(10^{-12})$. This high precision is probably attained because of the use of same order elements and the mesh conformity. These two factors assembled together achieves the effect of a collocation approach, the velocity being precisely imposed at each degree of freedom of the background mesh. Following this observation, both P2 elements and spatial discretization of similar triangle sizes between the fictitious and the solid domain have been used in this work.

5.3.2 Validations

The unsteady nonlinear solver will be validated, as in the first chapter, against three different moving rigid solid body problems (of increasing difficulty) found in the literature. The first two problems are identical to the first chapter: the transitory regime of an impulsively started cylinder towed with a constant velocity and a non-propelled oscillating cylinder. The final problem will be the configuration studied in the next chapter, the self-propelled infinite array of heaving NACA0010 wings confined in a channel. When analysing this problem, mesh and time-step dependency of the present numerical method will be evaluated. Results obtained with our unsteady nonlinear solver are compared to the numerical results of Becker et al. (2015).

5.3.2.1 Impulsed cylinder

The vortex wake dynamics have been tested through the computed streamwise velocity in the nearby wake of an impulsively started cylinder. The cylinder is impulsively started with a constant velocity $u_g = -1$, the Reynolds number based on this velocity and the cylinder

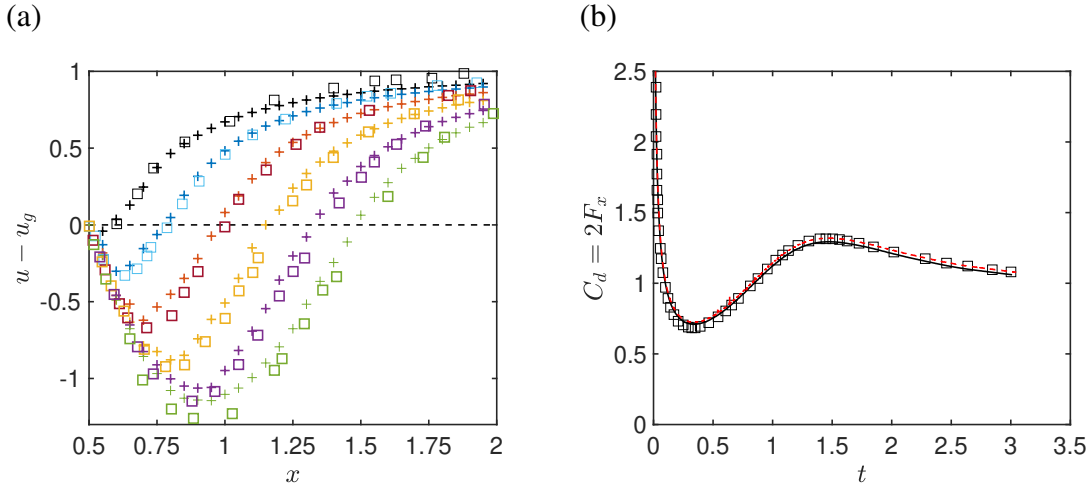

Figure 5.6: Nonlinear solver validation: impulsevily started cylinder with $u_g = -1$ and $Re = 550$. (a) Streamwise velocity u obtained with the present method (crosses) compared to experimental results of Bouard and Coutanceau (1980) (squares - figure 18 of the article) in the wake behind the cylinder for $x \in [0.5, 2]$ at the symmetry plan ($y = 0$). The different coloured markers correspond from top to bottom to time instants starting at $t = 0.5$ in steps of 0.5 up to 3. (b) Drag coefficient for the cylinder for $t \in [0, 3]$ obtained with the present method (red line) compared to the chapter 1 solver (black line) and values extracted from Bergmann and Iollo (2011) (squares - figure 8(a) of the article).

diameter being $Re = 550$ (Re replacing β in the numerical solver). In the previous solver, the solid dynamics are decoupled from the fluid one and the solid velocities are permanently set to $(u_g, v_g) = (-1, 0)$.

A comparison between our numerical and the experimental results of Bouard and Coutanceau (1980), figure 5.6(a), reveals a very good agreement. Our simulations were performed using a square domain of length $30D$ and height $16D$ where D is the cylinder diameter. The mesh is composed of 2.7×10^4 triangles, with mesh refinement being increased to triangles of order $O(10^{-2})$ in a small box of size 5 in the center of the domain around the cylinder. Dirichlet no-slip, two times symmetry and stress-free boundary conditions are respectively applied in the inflow, upper, lower and outflow boundaries of the domain. A time-step of $\Delta t = 10^{-4}$ has been adopted. In all considered time instants, numerical and experimental values present a good agreement of the relative velocity between the fluid and the cylinder in the wake. Similarly to the adoption of a conform method with a non-inertial frame of reference, the wake velocity is well resolved by the numerical method.

Another important validation measure concerns the hydrodynamic forces acting on the solid. These forces are here obtained by a direct integration of the distributed Lagrange multiplier, and it is important to cross-validate this method with the previous forces calculated using velocity and pressure fluid fields. A comparison between the drag coefficient obtained with the FD-DLM formulation, the non-inertial frame of reference and that computed by Bergmann and Iollo (2011) with a different numerical method is presented in figure 5.6(b). The time-evolution of the drag coefficient $C_d = 2F_x$ predicted by all numerical methods presents a perfect agreement

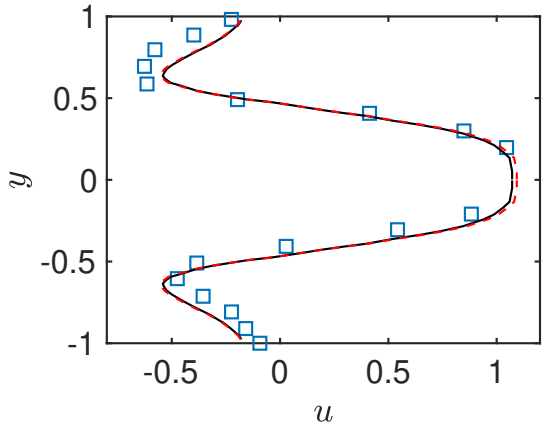

Figure 5.7: Nonlinear solver validation: Comparison of the values of the streamwise velocity in different vertical positions for $x = -0.6$ of the established regime of a non-propelled horizontally oscillating cylinder for $t = 0.5$. Control parameters are $\beta = 20$ and $A = 5/2\pi$ and $x_g = -A\sin(2\pi t)$. Experimental results of Dütsch et al. (1998) (squares - figure 8(a) of the article), method presented in chapter 1 (solid black line) and the present numerical method (red dashed line).

within the time evaluated.

5.3.2.2 Oscillating cylinder

A case where the imposed solid velocity is periodic and not steady is considered. In this case, the cylinder is animated with a sinusoidal horizontal motion of $x_g = -A\sin(2\pi t)$, the amplitude of motion being $A = 5/2\pi$ and the Stokes number $\beta = 20$. As the cylinder is non-propelled, the vertical velocity $v_g = 0$. The solid dynamics are completely imposed and remain uncoupled from the fluid dynamics. The selected flow regime correspond to a two-dimensional flow that does not break any symmetry (Dütsch et al. 1998). To compare the fluid dynamics with the experimentally measured one, we compare the stream-wise velocity at different vertical ($y \in [-1, 1]$) and a fixed horizontal position ($x = -0.6$), figure 5.7. A comparison with the previous results with a non-inertial frame of reference is equally performed. Our simulations were performed with a mesh composed of 1×10^4 triangles, a time-step of $\Delta t = 10^{-3}$ and a circular domain of radius $40D$ with stress-free boundary conditions in its outer surface. The velocity vertical profile predicted by our simulations presents a very good agreement within all methods.

5.3.2.3 Self-propulsion of an infinite array of flapping wings

The nonlinear solver employed in this study has been validated through a comparison with the numerical study of Becker et al. (2015). The adopted configuration will be further described in the next chapter. It consists of a NACA0010 wing and density $\rho_s = 10\rho_f$ confined in a channel of vertical height 3.5 times greater than the foil chord $H = 3.5c$, in a square domain of size $L = 6c$ with periodic boundary conditions applied in the left and right boundaries of the domain. A sinusoidal heaving movement $y_g = -A\cos(2\pi t)$ is applied to the foil, which is

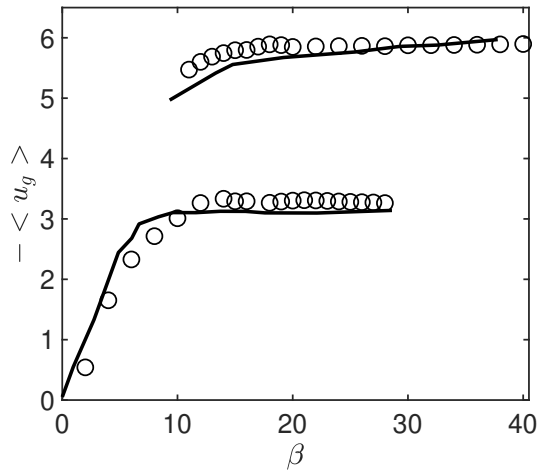

Figure 5.8: (a) Validation between the present numerical method (open circles) and the numerical results of Becker et al. (2015) (solid line). Fixed parameters are $\rho = 10$, $A = 1$, $H = 3.5$ and $L = 6$.

Time step	$- < u_g >$	Mesh nb. of triangles	$- < u_g >$
$\Delta t = 0.005$	3.217	8132	3.324
$\Delta t = 0.001$	3.263	11794	3.263
$\Delta t = 0.0005$	3.263	16532	3.263

Table 5.1: Influence of the time step and of the mesh number of triangles for the solution of Stokes numbers $\beta = 12$ evaluated through the convergence of the time-averaged horizontal velocity $< u_g >$. In the case of time-step convergence a fixed mesh of 11794 triangles was used, whereas in the mesh convergence a fixed time step $\Delta t = 0.001$ was used.

self-propelled in the horizontal direction. Similar to the authors we investigate the evolution of the time-averaged horizontal velocity with the increase of the Stokes number for $\beta \in [2, 40]$. One can see in figure 5.8 that the time-averaged horizontal velocity obtained with the present numerical method compare very well with values found in the reference. In addition the range of coexisting solutions in our study $11 \leq \beta \leq 29$ differs only slightly, fast solutions of $-\langle u_g \rangle \sim 6$ being found up to $\beta = 11$ instead of 10 in our case.

The influence of the spatial and time discretization over the time-averaged horizontal velocity of the array is evaluated. The mesh number of elements and time step are varied in table 5.1 for a case where the Stokes number is $\beta = 12$. Other fixed parameters are $\rho = 10$, $A = 1$, $L = 6$, $H = 3.5$. It is visible from this table that a time step of $\Delta t = 0.001$ and a mesh of 11794 triangles are sufficient to guarantee the convergence of the time-averaged horizontal velocity up to $O(10^{-3})$. The same value was attained for this time step and mesh refinement for all other values of Stokes numbers in the presented thesis. In cases where the gap has been varied, the number of triangles has been increased accordingly, with the same maximum and minimum level of mesh refinement being maintained.

Chapter 6

Stabilizing and destabilizing effect of the hydrodynamic collective interaction

In this final chapter, the effect of the collective interaction in an infinite array of flapping wings is investigated. This work was initiated to assess unstable self-propelled states of the infinite array. Results here reported indicate a route to establish the bifurcation undergone by the fluid-solid system. Characteristics of the unstable states and the stablizing/destabilizing hydrodynamic interaction effect acting on the coupled system are highlighted.

This work investigates the hysteresis in flapping frequency of a horizontally self-propelled infinite array of wings separated by a constant gap confined in a channel heaving heaving with a constant amplitude. Unsteady nonlinear simulations of an array with imposed horizontal velocity and fixed flapping amplitude and frequencies are performed to study how the system evolves inside the hysteresis. Additional intermediary unstable *quasi*-self-propelled solutions are determined by this method. While the two collectively interacting stable solutions of the hysteresis achieve a higher energetic performance than a single non-interacting wing, the unstable state features performance degradation. Constructive (destructive) interactions between flapping foil and incoming wake exhibited by stable (unstable) solutions originate this effect. Results with an imposed horizontal velocity further explain the solutions stability. They reveal the hydrodynamic force alternates between a stabilizing and destabilizing effect respectively for the stable self-propelled and unstable *quasi*-self-propelled solution. Studies of the nonlinear perturbation of unstable solutions highlight the self-propelled array avoids unstable interactions through coupled adaptation of its horizontal velocity and wake. This study is concluded by evaluating the influence of the gap between wings. A discrete set of branches of constant gap/ time-averaged velocity ratio is obtained. Results here presented suggest that control strategies aiming at optimize the horizontal speed of collective swimmers should exploit the hydrodynamic interaction destabilizing effect to achieve faster solutions with reduced cost of transportation.

Contents

6.1 Introduction

Collective dynamics are ubiquitous in nature. In the case of flapping propulsion, natural examples are bird flocks and fish schools (Portugal et al. 2014; Hemelrijk et al. 2015; Ashraf et al. 2016) which are believed to be formed due to group energetic benefits. The matter of how these groups are assembled remains, however, an open question. Elements often invoked to explain group formations are social traits (Sumpter 2006), for example avoiding and misleading predators, sensory mechanisms and active control (Liao and Akanyeti 2017), where animals actively adapt their trajectory to benefit from the unsteady flow shed by neighbors (Liao, Beal, and Lauder 2003), and passive hydrodynamic interactions (Lighthill 1975). From an energetic point of view, the former are of particular interest. As they dispense the need of active control mechanisms to achieve group cohesion, engineering projects can exploit them without complex additional components. The present study is dedicated to a better understanding of how passive flow-mediated interactions can be manipulated to enhance collective systems performance.

It has been long conjectured (Lighthill 1975) that the orderly patterns exhibited in collective dynamics might arise spontaneous and exclusively through flow-mediated interactions. As the study of interacting wings evolved from collective interactions held at fixed separation with an incoming flow (Ristroph and Zhang 2008) towards self-propelled bodies, the "Lighthill conjecture" was progressively verified. Infinite arrays of flapping wings with fixed gaps (Becker et al. 2015), two tandem wings with a non fixed gap (Zhu, He, and Zhang 2014; Ramananarivo et al. 2016; Peng, Huang, and Lu 2018a) and even many wings interactions (Peng, Huang, and Lu 2018b; Park and Sung 2018; Lin et al. 2019) sometimes in complex lattices (Oza, Ristroph, and Shelley 2019) were seen to achieve stable collective dynamics exclusively through passive flow interactions. Nevertheless, the final collective dynamics selected by those interactions are in many cases not unique, depending on initial conditions. An example is the self-propulsion of an infinite array of flapping wings confined in a channel (Becker et al. 2015). This configuration, studied both experimentally (depicted later in figure 6.1(a)) and numerically, consisting of a flat horizontal NACA0010 profile that is heaved vertically and free to rotate around its heaving axis in a cylindrical water tank confined by top and bottom walls. As the wing rotates, it encounters the wake shed by its other half blade. The rotational geometry induces then passive hydrodynamic interaction between the two parts of the wing, this arrange mimicking an infinite array of flapping wings separated by a constant gap equivalent to the half circumference arc separating the wing blades. As this cylindrical configuration presents a good comparison with horizontally translating geometries (Vandenberghe, Zhang, and Childress 2004; Alben and Shelley 2005), the system was investigated numerically as the two-dimensional horizontal locomotion of a heaving NACA0010 profile. The infinite array is mimicked in the numerical simulation by the introduction of periodic boundary conditions. Both experimental and numerical studies revealed that under a fixed flapping amplitude the collective dynamics evolution with the frequency presents a hysteresis, two coexisting solutions being obtained for certain flapping frequencies. As these solutions present power input advantages and a slower or faster velocity than a non-interacting flapping wing, understanding the mechanism that selects stable states is crucial for future engineering applications. In this work we are interested on revisiting this problem, through unsteady numerical simulations, to study the bifurcation at the origin of this hysteretic behaviour in frequency.

The stable self-propelled states appear to be selected by a constructive interaction between the foil horizontal dynamics and the interacting wake. Destructive interactions (Partridge and Pitcher 1979; Usherwood et al. 2011; Kim, Huang, and Sung 2010) are generally not observed for self-propelled flapping foils. Determining them might be an essential step to understand coupled mechanisms responsible for the natural selection of constructive interactions and if these mechanisms can be exploited by control strategies. A possible path towards unstable solutions, thus the study of the bifurcation undergone by the system, is to study how the interacting wake respond to the loss of a fluid-solid degree of freedom that "adapts" the dynamics. For a minimal school of two tandem wings separated by a free gap, Ramananarivo et al. (2016) studied the system evolution if the gap degree of freedom, that allows the foil to adjust its position generating constructive interacts, was to be blocked by an external force acting on the follower wing. As the follower is drifted apart from its equilibrium position the system responds through the evolution of the hydrodynamic force and the foil velocity. The evolution of this hydrodynamic force with the foil position revealed a spring-like stabilizing effect. Moreover, the evolution of this force with the horizontal position of the follower wing in the wake leads to the impression that different stable equilibria are connected, with unstable solutions existing in the middle. These unstable solutions were however not visualized in this study. In the present study, for the infinite array of flapping wings studied by Becker et al. (2015), we will follow a similar approach. Through numerical simulations of an array with imposed horizontal velocity at a fixed flapping amplitude and frequency, we will demonstrate the existence of unstable self-propelled solutions. This result highlights the possibility of a saddle-node bifurcation undergone by fluid-solid the system. The mechanism at the origin of the the self-propelled infinite array hysteresis in frequency is finally addressed. Inspired by the spring-like effect over the foil position of Ramananarivo et al. (2016), we study here the hydrodynamic force evolution while varying the horizontal velocity of the infinite array. As the system does not have the horizontal position but the velocity as a free degree of freedom, we show that in this case a damping-like stabilizing hydrodynamic interaction is obtained. Through the added observation of stabilizing/destabilizing hydrodynamic forces, unstable solutions and nonlinear perturbations (Jallas, Marquet, and Fabre 2017) we will draw commentaries on the existence of fluid-solid instability mechanisms leading to stable flapping states of locomotion and pattern organizations, a role already notorious for fluid instabilities in several natural examples (Gallaire and Brun 2017).

The mechanisms behind the so quoted energetic improvement of collective interactions remains an ongoing research. In this work we will show that, different than the stable self-propelled solutions of the infinite array that benefit from a significant reduction of the heaving power input compared to a single flapping wing (Becker et al. 2015), the unstable solutions require a higher power input. To understand the mechanisms behind performance enhancement and degradation, we revisit the energetic performance of both stable and unstable self-propelled solutions. Using outputs of numerical simulations performed for the infinite array and a non-interacting wing, the hydrodynamic interaction effects are discerned through a decomposition of the total flow and foil velocity in a "single non-interacting" and "wake hydrodynamic interaction" parts. This decomposition allows to correlate interaction effects to previous mechanisms observed in the literature, such as a favourable pressure gradient (Bergmann and Iollo 2011), vortex interception (Verma, Novati, and Koumoutsakos 2018) or suction effect from neighbouring vortex (Lin et al. 2019).

(a)

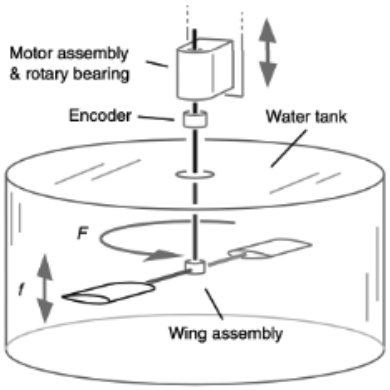

(b)

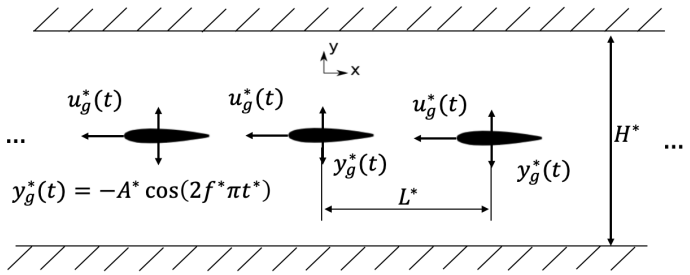

Figure 6.1: Configuration studied: (a) by Becker et al. (2015) and (b) rolled out infinite array used in this study. The system of axis (e_x, e_y) that follows the foil center of gravity g, the heaving motion $y_g^*(t)$, the horizontal velocity $u_g^*(t)$, the fixed gap between wings L^* and the height channel H^* are indicated in (b).

This work starts (§6.2) with the presentation of the governing nonlinear equations and details of the employed numerical methods. Unsteady nonlinear simulations of a self-propelled infinite array are compared to one with an imposed horizontal velocity in §6.3. This section study both stable and unstable solutions of the array, analysing their energetic efficiency and stability. Finally the gap between wings is studied. Conclusions about the stabilizing character of the hydrodynamic interactions in an infinite array of flapping wings and the effects of gap separation and flapping frequency are presented in §6.4.

6.2 Problem formulation, theoretical and numerical methods

We investigate the horizontally constrained self-propulsion of an infinite array of vertically flapping foils separated by a fixed gap L^* confined in a channel of height H^*. The foils are NACA 0010 profiles of chord $c = 1$ and density ρ_s. The adopted configuration, represented in figure 6.1(b) is a two-dimensional approximation of the experimental setup of Becker et al. (2015) 6.1(a). Rotational flow effects of the experiment are thus neglected in our configuration. This infinite array translates in an initially quiescent two-dimensional fluid of density ρ_f and kinematic viscosity ν with a velocity $\mathbf{u}_g = (u_g, v_g)$. The vertical velocity is imposed through a sinusoidal heaving motion

$$y_g^*(t) = -A^* \cos(2\pi f^* t^*), \tag{6.1}$$

the mean position of this heaving motion being attained at the center of the channel $y = 0$. The horizontal velocity u_g is free and determined by the hydrodynamic forces acting on the solid-fluid interface Γ_s. This rigid-body fluid-structure interaction is characterized by five non-dimensional parameters: the frequency-based Stokes number β, the solid-fluid density ratio ρ, and the chord-based flapping amplitude A, gap between wings L and channel height H, defined respectively as

$$\beta = \frac{f^* c^2}{\nu},\ \rho = \frac{\rho_s}{\rho_f},\ A = \frac{A^*}{c},\ L = \frac{L^*}{c} \text{ and } H = \frac{H^*}{c}. \tag{6.2}$$

The characteristic scales for length, mass and time are respectively the foil chord c, the fluid density ρ_f and the flapping period $1/f^*$. The non-dimensional flapping period T is equal to 1 whatever the value of the Stokes number β due to the choice of characteristic time-length, and β encodes the effect of the flapping frequency. In the present study, the channel height, the flapping amplitude and the solid-fluid density ratio are fixed to $H = 3.5$, $A = 1$ and $\rho = 10$ to equal parameters chosen by Becker et al. (2015). This choice was made in the reference to approach experimental conditions. In this work we will study the influence of the Stokes number in the range $1 \leq \beta \leq 50$ as well as the gap $4 \leq L \leq 40$.

6.2.1 Governing non-linear equations

To simulate the self-propulsion of the infinite array we adopt the hypothesis of spatial periodicity along the array. The array is then reduced to a single flapping wing in a domain of size $H \times L$ with inflow and outflow periodic boundary conditions (figure 6.2). The dynamics of the absolute fluid velocity $\mathbf{u} = (u, v)$ and pressure p, coupled to the foil self-propelled horizontal velocity u_g are governed by the system of equations

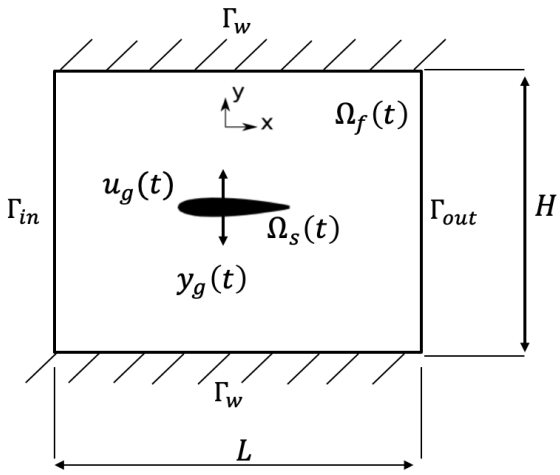

Figure 6.2: Simplification of the infinite array to a single wing in a periodic domain. Inflow (Γ_{in}), outflow (Γ_{out}), wall (Γ_w) boundaries, fluid ($\Omega_f(t)$) and solid domain ($\Omega_s(t)$) are identified in the figure.

$$
\begin{aligned}
\partial_t \mathbf{u} &= -\nabla\mathbf{u}\cdot(\mathbf{u}-u_g\mathbf{e}_x) + \nabla\cdot\sigma(p,\mathbf{u}), && \text{in } \Omega_f(t)\\
0 &= \nabla\cdot\mathbf{u}, && \text{in } \Omega_f(t)\\
\frac{du_g}{dt} &= (\rho S)^{-1}\int_{\Gamma_s}(\sigma(p,\mathbf{u})\cdot\mathbf{n})\cdot\mathbf{e}_\mathbf{x}\mathrm{d}\Gamma, && \text{in } \Omega_s(t)\\
\mathbf{u}(\mathbf{x},t) &= [u_g, v_g]^T, && \text{on } \Omega_s(t)\\
\mathbf{u}(\mathbf{x},t) &= 0, && \text{on } \Gamma_w\\
\mathbf{u}(\Gamma_{in},t) &= \mathbf{u}(\Gamma_{out},t), && \text{on } \Gamma_{in}
\end{aligned}
\tag{6.3}
$$

where $v_g = 2\pi A\sin(2\pi t)$ is the foil imposed vertical velocity and the Cauchy stress tensor $\sigma(p,\mathbf{u})$ of an incompressible Newtonian fluid is

$$\sigma(p,\mathbf{u}) = -p\mathcal{I} + \beta^{-1}(\nabla\mathbf{u} + \nabla\mathbf{u}^T)\,. \tag{6.4}$$

The surrounding flow is governed by the Navier-Stokes equations, first two lines of the system (6.3), written in a non-inertial frame of reference that follows the foil center of mass *g horizontal* motion. This formulation, previously adopted in other fluid-structure interactions studies such as falling and rising bodies in fluids (Jenny, Bouchet, and Dušek 2003; Tchoufag, Fabre, and Magnaudet 2014) and in our previous study (Benetti Ramos et al. 2020), allows to maintain the foil horizontal position fixed in space. As the configuration dealt in this study is confined by channel walls, the non-inertial frame of reference cannot be adopted to follow the vertical motion of the foil as well. The temporal evolution of the foil horizontal velocity u_g is governed by Newton's second law (3rd line of (6.3)) that balances the solid inertia (ρS), its acceleration and the hydrodynamic forces acting over the body. The system of equations is finally closed by three set of boundary conditions, three last lines of (6.3). The first and second

ones are the no-slip boundary condition over the foil surface $\Gamma_s(t)$ and the channel walls Γ_w, while the last one imposes the periodicity of the fluid velocity between the in (Γ_{in}) and outflow (Γ_{out}) boundaries.

6.2.1.1 Unstable *quasi*-self-propelled solutions through imposed horizontal velocity

These equations can be simplified as to obtain the flow around an array towed at a constant horizontal velocity. The advantage of uncoupling the solid from the fluid dynamics is that unstable non self-propelled states can be calculated. The previous governing equations are simplified for a known horizontal velocity. The solid dynamics vanish from the system of equations (6.3) and the boundary condition at the solid surface

$$\mathbf{u}(\mathbf{x}, t) = [u_g, v_g(t)]^T, \text{on}\, \Gamma_s(t), \tag{6.5}$$

is known and imposed for all time instants. Different than the self-propelled case, non-zero time-averaged values of the horizontal force $< F_x >$ are possible. After all, the uncoupled system equilibrium is no longer a cruise solution, where the solid is no longer accelerated $< F_x >= 0$. However, for certain velocities, the time-averaged value of the force is zero. In these cases, the solutions obtained by this uncoupled analysis approach the self-propelled equilibrium. They are here labelled *quasi*-self-propelled solution, since they do not possess the inherent unsteady horizontal velocity character. This approximation is justified for two main reasons. First, when the average force is zero, the fluid and solid system are in equilibrium, with the foil being no longer accelerated. Second, an imposed horizontal velocity might be in fact a good approximation of the self-propelled dynamics if the time-averaged along a flapping period value of the velocity $< u_g >= \int_{t_0}^{t_0+1} u_g(t)\mathrm{d}t$ is much greater than its fluctuations u_g'. In this case the total velocity, which is decomposed as

$$u_g(t) =< u_g > + u_g'(t), \tag{6.6}$$

can be simplified at first order to the averaged velocity $u_g \approx < u_g >$, a constant value as the imposed velocity. An *a posteriori* analysis confirms the similarity between the self-propelled and *quasi*-self-propelled stable solutions (§6.5) time-averaged horizontal velocity. Vorticity contours of both solutions are also remarkably similar.

6.2.2 Fictitious Domain formulation with distributed Lagrange multipliers

A fictitious domain with distributed Lagrange multipliers (FD-DLM) formulation (Glowinski et al. 2001; Boffi, Hecht, and Pironneau 2018) is used to account for the foil heaving motion. To establish a time-independent domain, this formulation extends the fluid equations to a fictitious domain $\Omega_f \cup \Omega_s$ that encloses fluid and solid. To impose the solid velocity in the time-dependent solid domain $\Omega_s(t)$ Lagrange multipliers $\mathbf{f}$ are introduced in the system weak formulation. In the present configuration, Lagrange multipliers λ are also introduced to enforce the no-slip and periodic boundary conditions over the domain external boundaries $\Gamma = \Gamma_w \cup \Gamma_{in} \cup \Gamma_{out}$. The system weak formulation is obtained by multiplying each equation of the system (6.3) with an appropriate test-function (of the same functional space of the related variable) and integrating over space

$$
\begin{aligned}
\iint_{\Omega_f \cup \Omega_s} [\partial_t \mathbf{u} \cdot \psi_u] \, \mathrm{d}\Omega &= -\iint_{\Omega_f \cup \Omega_s} \left[[\nabla \mathbf{u} \cdot (\mathbf{u} - u_g \mathbf{e}_x)] \cdot \psi_u + \sigma(p, \mathbf{u}) : \nabla \psi_u \right] \mathrm{d}\Omega \\
&\quad + < \mathbf{f}, \psi_u >_{\Omega_s(t)} - \int_{\Gamma_w \cup \Gamma_{in}} [\lambda \cdot \psi_u] \, \mathrm{d}\Gamma , \\
0 &= \iint_{\Omega_f \cup \Omega_s} \left[(\nabla \cdot \mathbf{u}) \cdot \psi_p \right] \mathrm{d}\Omega , \\
\frac{du_g}{dt} &= -[(\rho - 1)S]^{-1} < \mathbf{f}, V >_{\Omega_s(t)} \cdot \mathbf{e}_\mathbf{x} , \\
0 &= < \mathbf{u} - \mathbf{u}_g, \psi_f >_{\Omega_s(t)} , \\
0 &= \int_{\Gamma_{in}} [\mathbf{u}(\Gamma_{in}) - \mathbf{u}(\Gamma_{out}) \cdot \psi_l] \, \mathrm{d}\Gamma + \int_{\Gamma_w} [\mathbf{u} \cdot \psi_l] \, \mathrm{d}\Gamma .
\end{aligned}
\tag{6.7}
$$

The combined variation space W of the test-functions ($[\psi_\mathbf{u}, \psi_p, V, \psi_f, \psi_l]$) and variables ($[\mathbf{u}, p, u_g, \mathbf{f}, \lambda]$) is defined as

$$
W = \{\psi_u \in (H^1)^2(\Omega_f \cup \Omega_s), \psi_f \in (L^2)^2(\Omega_s), \psi_p \in L^2(\Omega_f \cup \Omega_s), \psi_l \in (H^{-1/2})^2(\Gamma), V \in \mathbb{R}^2\} . \tag{6.8}
$$

The L_2 scalar product $< \mathbf{f}, \psi_u >_{\Omega_s(t)}$

$$
< \mathbf{f}, \psi_u(x(t), t) >_{\Omega_s(t)} = \iint_{\Omega_s(t)} [\mathbf{f}(\mathbf{X}) \cdot \psi_u(\mathbf{x_f})] \mathrm{d}\Omega , \tag{6.9}
$$

introduced in the above formulation requires a projection between the fictitious and time-dependent solid domain. The Lagrange multiplier $\mathbf{f}$, from the position $\mathbf{X} \in \Omega_s$ of the solid domain, is projected to the instantaneous position $\mathbf{x}_f \in \Omega_s(t) \subset \Omega_f \cup \Omega_s$ occupied by the solid in the fictitious domain (as is the case of the fluid velocity $\mathbf{u}$ in $< \mathbf{u} - \mathbf{u}_g, \psi_f >_{\Omega_s(t)}$). Finally, $< \mathbf{f}, V >_{\Omega_s(t)}$ is equivalent to the hydrodynamic force acting on the foil, figuring thus at the right hand side of the Newton law governing the foil dynamics. A similar formulation is used for the imposed horizontal velocity governing equations. In this case, the solid dynamics scalar equation vanishes from the weak formulation as in the continuous equations.

6.2.3 Numerical Method

A continuous Galerkin finite-element method is employed to discretise the equations (6.7) in space. Quadratic elements (P2) are used for the flow velocity and the Lagrange multipliers and linear elements (P1) are used for the pressure. The implementation is based on the FreeFEM software (Hecht 2012). The computational domains, represented in figure 6.3, consist of a rectangle of (non-dimensional) size $H \times L$ for the fictitious domain $\Omega_f \cup \Omega_s$ and the solid domain Ω_s is a NACA0010 with foil center of mass positioned at the middle length of the rectangle $L/2$. A Delaunay triangulation of these results, respectively, in meshes of 1.2×10^4 and 300 triangles. The triangle size is typically of order $O(10^{-2})$ going up to $O(10^{-1})$ in flow regions of small variation of the out-of-plane vorticity ω_z. The minimum and maximum mesh refinement levels have been set to attend a convergence of order $O(10^{-4})$ of the foil horizontal velocity and the vertical hydrodynamic force. To ensure both the formulation stability and a good interpolation between Lagrange multiplier from the time-dependent solid domain to the

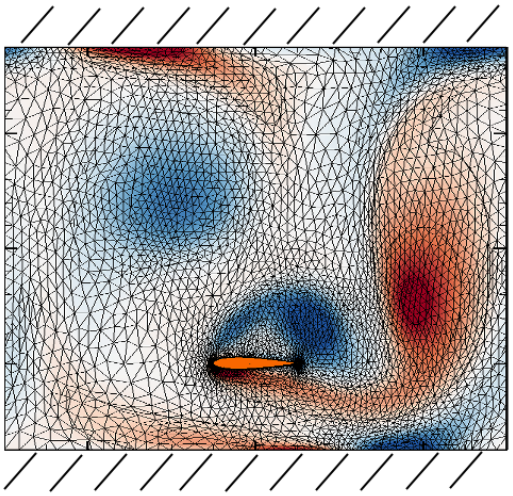

Figure 6.3: Spatial discretisation of the whole $\Omega_f \cup \Omega_s$ (black mesh) and solid computational domains Ω_s (orange mesh).

fictitious domain the height of the solid domain triangles have been kept of same order as the region it overlaps in the background fictitious domain (Glowinski et al. 1999). To guarantee this, the present numerical method explores the Hessian-based mesh adaptation functionalities of FreeFEM, adapting the fictitious domain mesh to regenerate the solid frontier as done by Boffi, Hecht, and Pironneau (2018) every tenth of flapping period. The accuracy of the Lagrange multipliers $\mathbf{f}$ projection throughout the simulation is thus enhanced, while avoiding the high computational cost of an uniform mesh refinement.

The unsteady problem (6.7) is discretised in time using a r-order implicit linearized scheme. All terms are implicit, apart from the nonlinear convective term from the Navier Stokes equations, that is implicit linearized through the r-order extrapolation formula $\sum_{k=1}^{r} \gamma_k [\nabla \mathbf{u}^{n+1} \cdot (\mathbf{u}^{n+1-k} - \mathbf{u}_g^{n+1-k})]$. The resulting matrix formulation takes the form

$$\underbrace{\begin{bmatrix} \mathbf{A}_f & 0 & \mathbf{I}_f & \mathbf{I}_\lambda \\ 0 & \alpha_0/\Delta t & \mathbf{I}_s & 0 \\ \mathbf{I}_f^T & \mathbf{I}_s^T & 0 & 0 \\ \mathbf{I}_\lambda^T & 0 & 0 & 0 \end{bmatrix}}_{\mathbf{A}} \cdot \begin{bmatrix} (\mathbf{u}^{n+1}, p^{n+1})^T \\ u_g^{n+1} \\ \mathbf{f}^{n+1} \\ \lambda^{n+1} \end{bmatrix} = \begin{bmatrix} -\sum_{k=1}^{r} \iint_{\Omega_f \cup \Omega_s} (\alpha_k/\Delta t) \mathbf{u}^{n+1-k} \cdot \psi_u \mathrm{d}\Omega \\ -\sum_{k=1}^{r} (\alpha_k/\Delta t) u_g^{n+1-k} \\ \iint_{\Omega_s(t)} v_g \cdot \mathbf{e}_y \cdot \psi_f \mathrm{d}\Omega \\ 0 \end{bmatrix}, \quad (6.10)$$

where Δt is the time step and $(\mathbf{u}^{n+1}, p^{n+1})$ the velocity and pressure at time $t_{n+1} = (n+1)\Delta t$. A first-order scheme ($r = 1$, $\alpha_0 = 1$, $\alpha_1 = -1$ and $\gamma_1 = 1$) is used for the first two temporal iterations ($n \leq 1$), followed by a second-order scheme ($r = 2$, $\alpha_0 = 3/2$, $\alpha_1 = -2$, $\alpha_2 = 1/2$, $\gamma_1 = 2$ and $\gamma_2 = -1$). The equality of fluid and solid velocity being treated implicitly, severe time-step restrictions induced by an explicit coupling (Causin, Gerbeau, and Nobile 2005) are avoided. However, due to the movement of the solid domain, the time step should be maintained small as to avoid the emergence of freshly cleared cells. A time step of $\Delta t = 1 \cdot 10^{-3}$ allows a

good trade-off between the computational cost and the simulation accuracy. The matrices $\mathbf{I}_f$, $\mathbf{I}_f^T$ and $\mathbf{I}_\lambda^T$ use particular interpolation functionalities from FreeFEM. $\mathbf{I}_f$ interpolates the Lagrange multiplier $\mathbf{f}^{n+1}$ from the solid Ω_s to the fictitious domain. $\mathbf{I}_f^T$ evaluates the fluid velocity $\mathbf{u}^{n+1}$ from the fictitious in the solid domain. Finally, $\mathbf{I}_\lambda^T$ interpolates the outflow velocity $\mathbf{u}^{n+1}(\Gamma_{out})$ in the inflow boundary Γ_{in}. In this last case a particular attention is made to build a mesh with equal discretisation points over the inflow and outflow boundaries. In this way, only a spatial shift of $(\mathbf{x} - (L, 0)^T)$ is needed and no interpolation is made as to build the matrix $\mathbf{I}_\lambda^T$. This system is simplified according to the continuous formulation in the case of the imposed horizontal velocity, with the system matrix $\mathbf{A}$ loosing its second line and column and the known u_g being added to the right hand side. The solver validation is detailed in §6.6.

6.3 Results

Unsteady nonlinear simulations are performed for a self-propelled and an imposed horizontal velocity infinite array. In the first case, the self-propelled dynamics are studied in the Stokes number range $2 \leq \beta \leq 50$. These results were simultaneously compared with those of an array with imposed horizontal velocity $2 \leq -\langle u_g \rangle \leq 7$ for fixed Stokes numbers in the range $5 \leq \beta \leq 35$. In both cases the gap between wings $L = 6$, the density ratio $\rho = 10$, the flapping amplitude $A = 1$ and the channel height $H = 3.5$ were kept fixed. Since the self-propelled behaviour of the array has already been studied by Becker et al. (2015), the goal of these simulations was to compare the self-propelled and imposed velocity analyses, what is done in §6.3.1. The hydrodynamic advantages (disadvantages), based on the power consumption and the cost of transport, of the stable (unstable) collective interactions are then studied in §6.3.2. In §6.3.3 the hydrodynamic force evaluated from imposed velocity simulations is used to assess the solutions stability. The nonlinear perturbations that bring the unstable solution to the two stable self-propelled states are finally discussed. This section is concluded in §6.3.4 by a parametric investigation of the effect of the gap between wings $2 \leq L \leq 40$ for a fixed Stokes number $\beta = 15$.

6.3.1 Stable self-propelled and unstable *quasi*-self-propelled solutions

The infinite array time-averaged horizontal velocity evolution, shown in figure 6.4, is not continuous with the Stokes number β and matches perfectly Becker et al. (2015) numerical results. Its growth follows the one of a single (non-interacting) wing for low Stokes numbers $\beta \leq 10$. Beyond this point, while the non interacting wing velocity grows continuously, the velocity of the array attains a value of $-\langle u_g \rangle \sim 3.2$ that remains constant until $\beta = 29$. A discontinuous jump of the array velocity takes then place, its value climbing up to $-\langle u_g \rangle \sim 6$, value that again remains constant for $30 \leq \beta \leq 50$. When the Stokes number is decreased, a hysteretic behaviour with two coexisting solutions is seen for $11 \leq \beta \leq 29$. These coexisting solutions are hereafter labelled fast and slow solutions, since they present resp. an increase/decrease of the horizontal velocity of the array when compared to a single wing.

Quasi-self-propelled solutions (solutions obtained with an imposed horizontal velocity that achieve nevertheless a zero time-averaged horizontal force) match closely the time-averaged value of stable self-propelled solutions. A slight divergence is observed in the β range where two

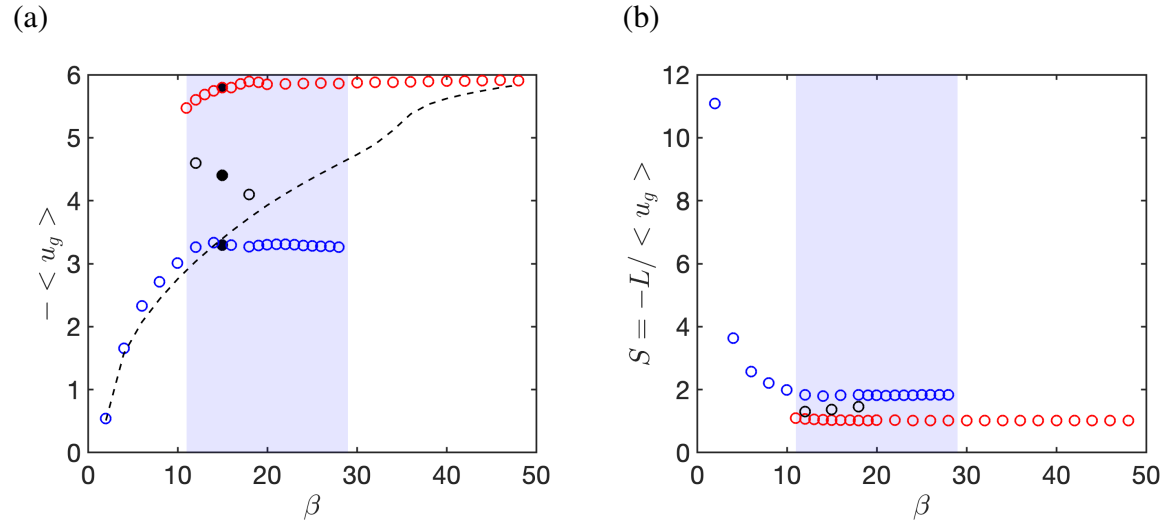

Figure 6.4: Evolution of the (a) time-averaged horizontal velocity and (b) schooling number of the self-propelled infinite array with the Stokes number β. Stable self-propelled fast and slow solutions are identified by red and blue circles, and unstable solutions by black circles. The velocity of a non-interacting wing is represented in (a) by a dashed line. A light blue background identify zones of coexisting stable solutions. Solutions represented by filled circles in (a) are depicted in figure 6.5. Fixed parameters are $L = 6$, $\rho = 10$, $A = 1$, $H = 3.5$.

self-propelled solutions coexist, where this imposed horizontal method predicts a third branch of solutions. The time-averaged velocity of these solutions, results added for $\beta = 12$, 15 and 18 in figure 6.4, placed in the middle of the fast and slow branches. This analysis predicts a continuation of this branch for higher Stokes, but this values have not been here included. In fact, for higher Stokes numbers these solutions become mostly non-periodic and the force time-averaged value is not precisely defined. The additional solutions found by the *quasi*-self-propelled analysis point, nevertheless, to the possibility of a saddle-node bifurcation undergone by the self-propelled system. As remarked by Becker et al. (2015), the self-propelled solutions appear to remain near constants Schooling numbers $S = L/< u_g >\sim 1.25$ or 1.75, the gap distance measured in wavelengths of flapping movements, as seen in figure 6.4(b). The unstable solutions, on the other hand, continuously increase with β not forming any particular constant value of S, similar to the unstable solutions of different lattices predicted by reduced order models in Oza, Ristroph, and Shelley (2019).

Fast and slow stable and unstable solutions present different wake-flapping foil interactions which are depicted in figure 6.5 for a fixed Stokes number $\beta = 15$. The stable self-propelled states, in figure 6.5 (a) and (c), present both constructive wake-flapping foil interactions [1]. In the case of the fast solution a dual interaction takes place. Both the incoming wake and the leading edge vortex (LEV) end up reinforcing the trailing edge vortex (TEV) shed at the end

[1]As a side note, Becker et al. (2015) named fast and slow self-propelled solutions as vortex core destroying and vortex slaloming interactions, based on the foil center of mass trajectory. Here we keep the "destructive" notation for the interaction of different sign vortices, which is not the case of the fast solution.

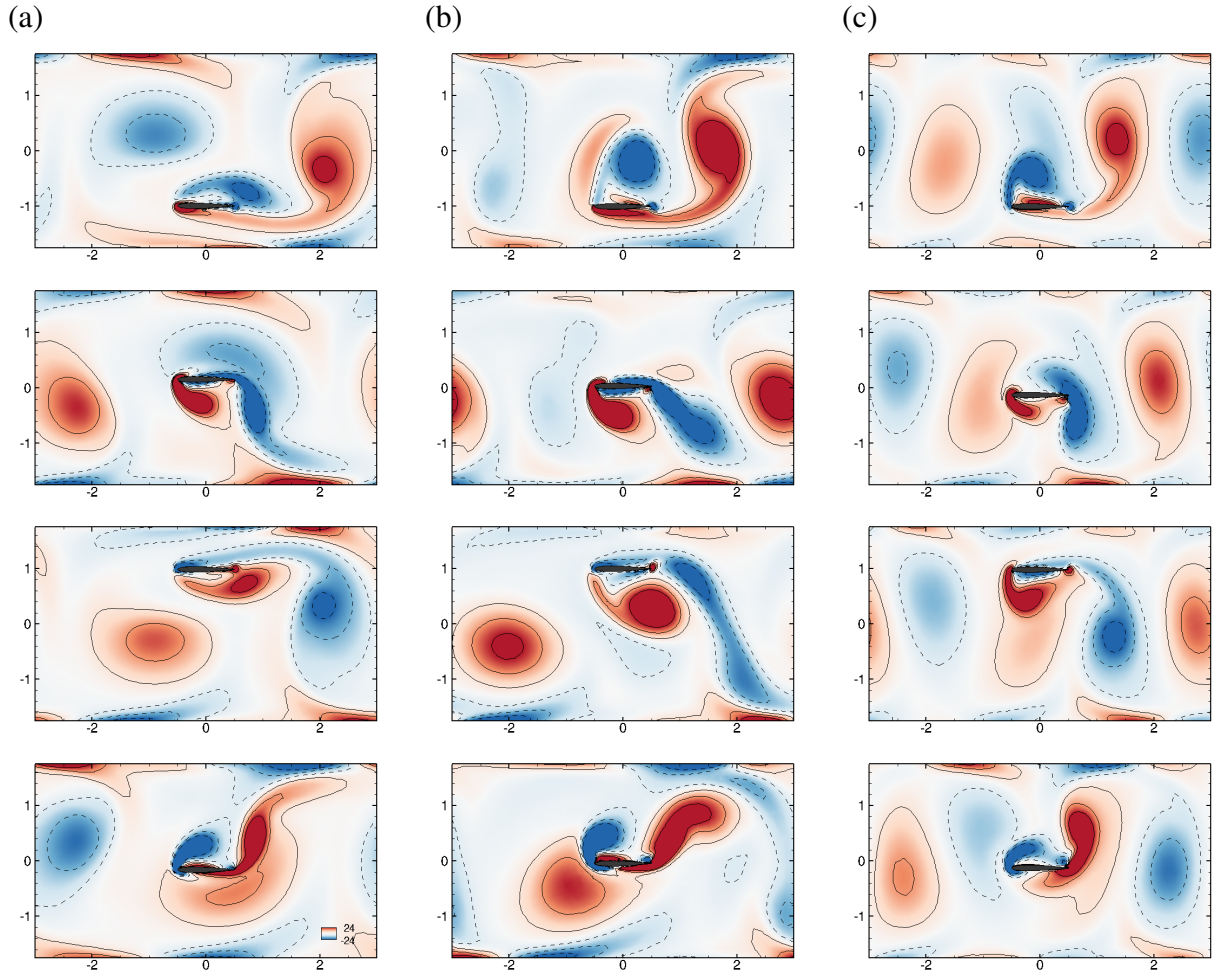

Figure 6.5: Four equally spaced allong a flapping period flow vorticity contours of the self-propelled infinite array of flapping wings. For $\beta = 15$ (a) fast solution with constructive trailing edge wake interaction, (b) unstable intermediary solution and (c) slow solution with constructive leading edge wake interaction. Fixed parameters are $\rho = 10$, $A = 1$, $L = 6$, $H = 3.5$.

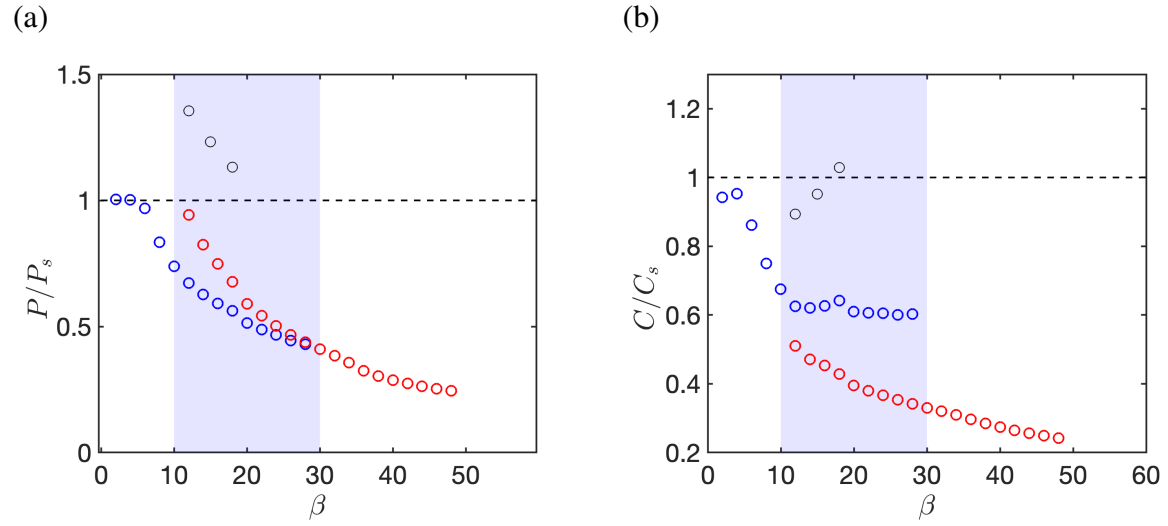

Figure 6.6: Evolution with the Stokes number β of the (a) power input P and of the (b) cost of transport C compared to those of single flapping wing (P_s and C_s). Blue, red and black circles identify again slow, fast and unstable solutions. A dashed line highlight in both figures the unitary value when both quantities equal the one of a single wing.

of the strokes. This can be seen for the negative LEV and wake vortices at the end of the upward stroke in the three first lines of figure 6.5 (a). In the slow solution (6.5-c), the interaction between the wake and the vortex shed by the foil takes place mainly around the foil leading edge. The incoming wake vortex constructively interact with the LEV, that is subsequently crushed by the wing heaving motion. The unstable solution, different than the stable ones, features a destructive interaction with the incoming wake. As seen in column (b) of figure 6.5 the interaction between wake and flapping foil takes place mainly around the leading edge, similarly to the slow solution. At this time, however, the foil LEV has the opposite sign of the incoming one. A vortex dipole is thus formed, affecting the production of the trailing edge vortex. A slight difference is observable between the half-strokes and the upward stroke is seemingly more impacted by this destructive interaction. In both cases, nevertheless, the LEV and the vortex wake end up forming a dipole at the end of each half-stroke, as seen in the third line of (b) for the upward stroke. This dipole then impacts the TEV shed at the end of each stroke, with the TEV even disappearing in the last line of (b).

6.3.2 Wake interaction effect over the flapping foil efficiency

The collective interaction has a significant effect on the energetic aspects of the array. Considering the flapping movement power input, $P = \int_{t_0}^{t_0+1} v_g(t) \times F_y(t) \mathrm{d}t$, and the "gallons-per-mile" cost of transport (COT), $C =< P > /< u_g >$, the stable self-propelled solutions present significant advantages both in power (figure 6.6-a) and COT (6.6-b) when compared to a single non-interacting wing (P_s, C_s). The ratio of these quantities is always below one for both fast and slow solutions. In the range of coexisting solutions, the power consumption is more significantly reduced for the slow solution, attaining a decrease of $\sim 50\%$, whereas the fast solution presents the greatest COT reduction, its ratio always falling below 50%. The unstable solutions, on the

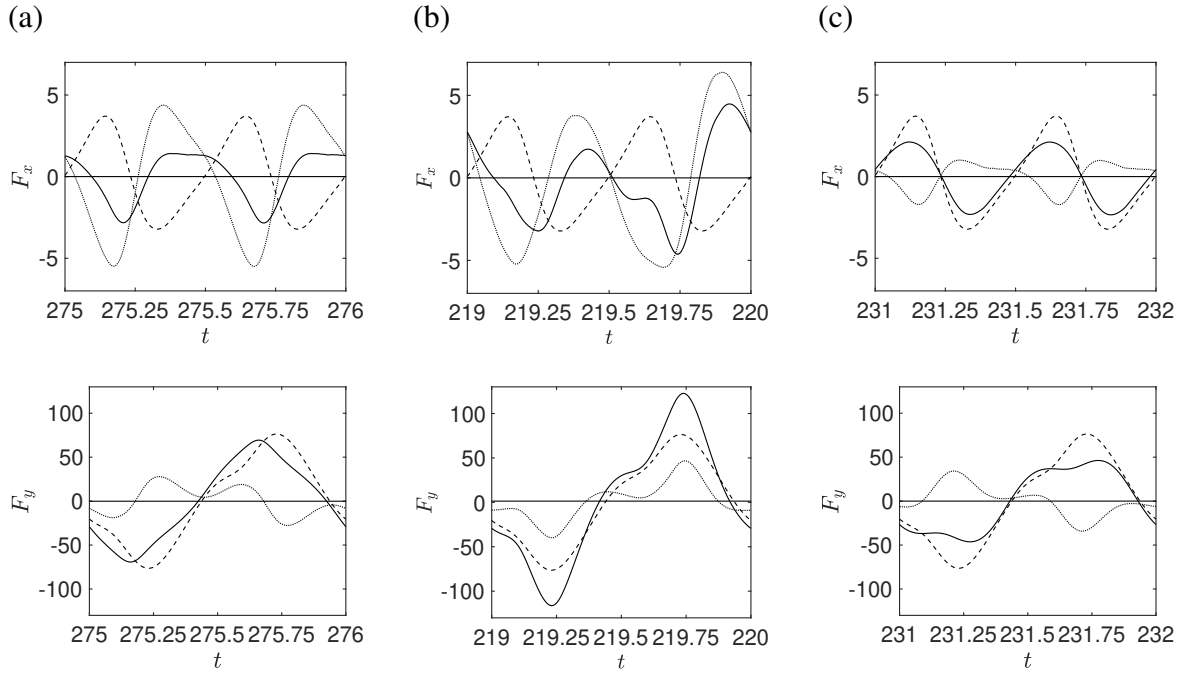

Figure 6.7: Temporal evolution of the horizontal (top) and vertical (bottom) forces acting on the wing decomposed in the single (dashed line), wake interaction (dotted line) and total components (solid line). (a) Fast solution, (b) unstable and (c) slow solution for $\beta = 15$. Fixed parameters are $\rho = 10$, $A = 1$, $L = 6$, $H = 3.5$.

other hand, present an increase of the power consumption. In their case, the power ratio figures always above 1. Only a small gain in COT is achieved for two out of three solutions, due to their velocity increase.

This energetic advantage (disadvantage) observed for the stable (unstable) interacting solutions can be better illustrated through a decomposition of the forces actuating over the foil (as well as the generated flow)

$$\mathbf{F}(\mathbf{u}, p) = \mathbf{F}_s(\mathbf{u}_s, p_s) + \mathbf{F}_i(\mathbf{u}_i, p_i) \tag{6.11}$$

where the effects of the interaction between wings $\mathbf{F}_i(\mathbf{u}_i, p_i)$ are discerned from those of a single non-interacting wing $\mathbf{F}_s(\mathbf{u}_s, p_s)$. This decomposition, depicted in figure 6.7, reveals how the wake interaction effect results in energetic benefits. Seemingly, this effect adapts the foil/wake interaction, using the velocity degree of freedom, through the horizontal force. This adaptation leads then to vortex interception interactions that affect the vertical force. First, let us focus on the modifications of the horizontal force. In the case of fast and slow solutions, the interaction resp. increase and reduce their velocity, which is achieved through the horizontal force. In the case of the fast solution, (6.7-a) the wake accelerate the foil (during negative values since negative velocity) resulting in a total force that is almost out-of-phase with that of a non-interacting wing. This acceleration takes place in instants t = 275-275.25 and 275.5-275.75, where the incoming wake vortex is coming to enter in contact with the foil. The interaction appears then to push the foil forward, generating the TEV interaction that characterizes this solution. In the slow solution the wake interaction decrease the force amplitude of a single wing.

As seen in figure 6.7(c), the horizontal force of a single wing has its deceleration and acceleration reduced in intensity. The deceleration reduction can be associated to the wing collision with its LEV, seen for example between figure 6.5(c) first and second row. The acceleration reduction can be associated to the negative flow faced by the foil when the incoming wake vortex reaches its leading edge that takes place for $t \sim 0.25$-0.5 (second and third rows of 6.5(c)). It seems the foil acceleration is slowed down by the wake to accommodate the positive interaction of the wake and LEVs. The unstable state, figure 6.7(b), features an interaction intermediary between these two solutions. It present, nevertheless, an unique deceleration of great intensity experienced by the foil for $t \sim 219.9$ when the destructive interaction between the LEV and the incoming wake takes place.

For both stable self-propelled solutions the vertical force force is significantly reduced when compared to a single wing. For the slow solution this is true for almost every time instant. The greatest reduction is observed around $t \sim 231.125$ and 231.625, when the lateral surface of the foil interacts with the shed LEV benefiting from a suction effect. The fast solution features a vertical force increase for $t \in (0, 0.125)$. This might be associated to the leading edge vortex driven apart from the foil and convected towards the trailing edge. However, when the foil encounters the wake vortex, $t \in (275.125, 275.25)$, the vertical force is again reduced. For the unstable solution, the interaction effect is completely different, with the vertical force being intensified. This effect is significantly stronger for instants when the foil reaches the middle height of the channel $t \sim 219.25$ and 219.75. It appears that the formation of the vortex dipole in the unstable solution leaves the foil not only without suction effect, neither from LEV or incoming wake vortices, but also erases positive effects from LEV-foil interaction. The vertical force is thus increased while comparing to a single wing, resulting in the degradation of the power input.

The wake interaction flow structures ($\mathbf{u}_i, p_i, \omega_{z,i}$) and their effect over the non-interacting flow are depicted in figure 6.8 to better understand the origin of the previously discussed forces. As the effect of this component over the single wing flow is similar along the flapping period, only an instant when the foil is at its lower position $y_g = -1$ (and t is an integer) is considered here. In all cases, stable and unstable solutions, the action of the wake interaction over the single wing flow (middle column) consists of two different parts. One part is the incoming upstream vortices, which are identical to the total flow since the single wing travels in a quiescent fluid. The second part, that starts at the foil leading edge, is composed of vortex dipoles. The superposition of the wake interaction and single wing flow components in the middle column reveals this interaction mainly tend to displace the non-interacting vortices through dipoles. This is very similar to *so-called* vortex displacement modes (Fabre, Sipp, and Jacquin 2006; Brion, Sipp, and Jacquin 2014). In the case of the fast solution (6.8-a) the vortex displacement shifts the non-interacting vortices further downstream. The leading edge vortex shed by the single wing is simultaneously attenuated (reinforced) in its left (right) portion, resulting in its net displacement towards the trailing edge. The trailing edge vortex of the non-interacting flow is simultaneously displaced downstream, opening space for the constructive interaction of the downward stroke LEV and the upward stroke TEV.

For the (6.8-b) unstable solution, the pair of LEV and TEV shed during the downward stroke are reinforced resp. in their upper and lower parts. These simultaneous reinforcement drifts the LEV afar and degrades the LEV-foil interaction. This results in the loss of suction effects and vertical force degradation. The TEV displacement does not generate any particular constructive interaction as observed for fast and slow solutions. Finally for the slow solution, in the line (c)

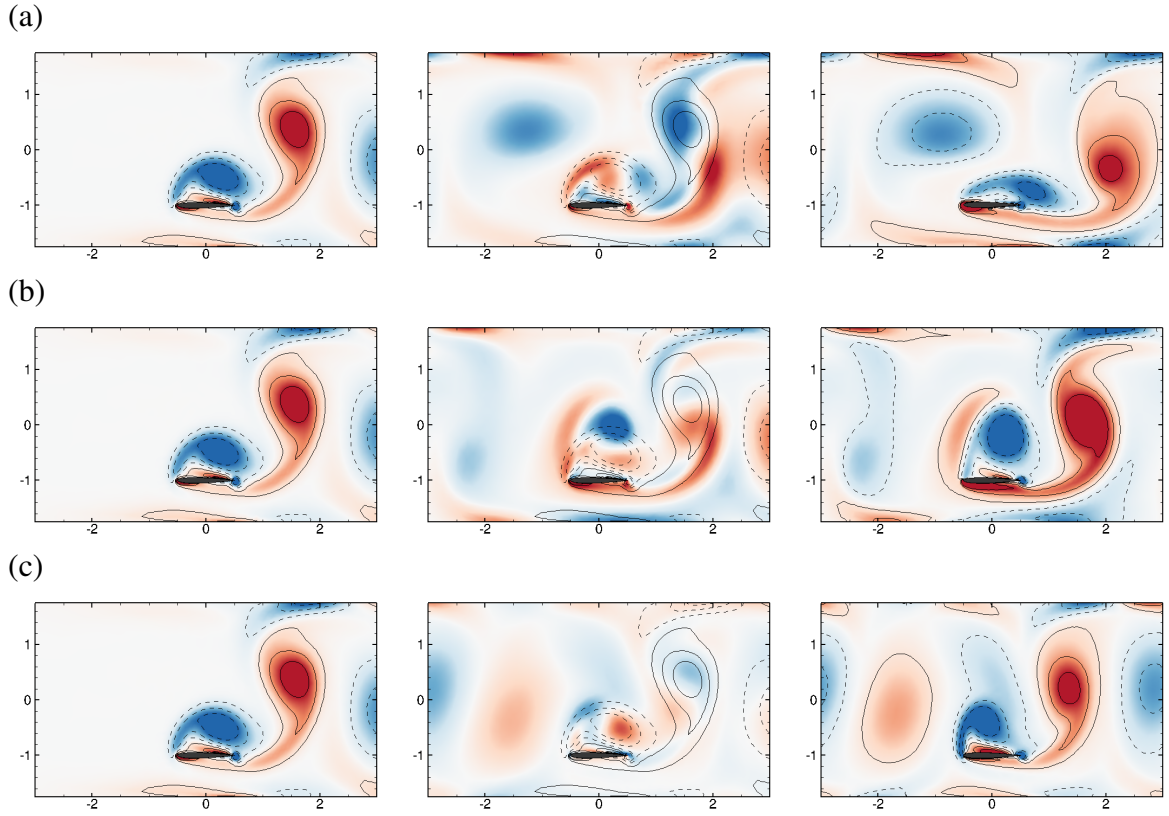

Figure 6.8: Decomposition of the total flow (third column), represented by vorticity contours, in its single wing (first column) and wake interaction (second column) components. For $\beta = 15$ (a) Fast solution, (b) unstable solution and (c) slow solution. In the second column, we superpose single wing and wake interaction components, that are respectively represented by lines and flooded contours. Other fixed parameters are $\rho = 10$, $A = 1$, $L = 6$, $H = 3.5$.

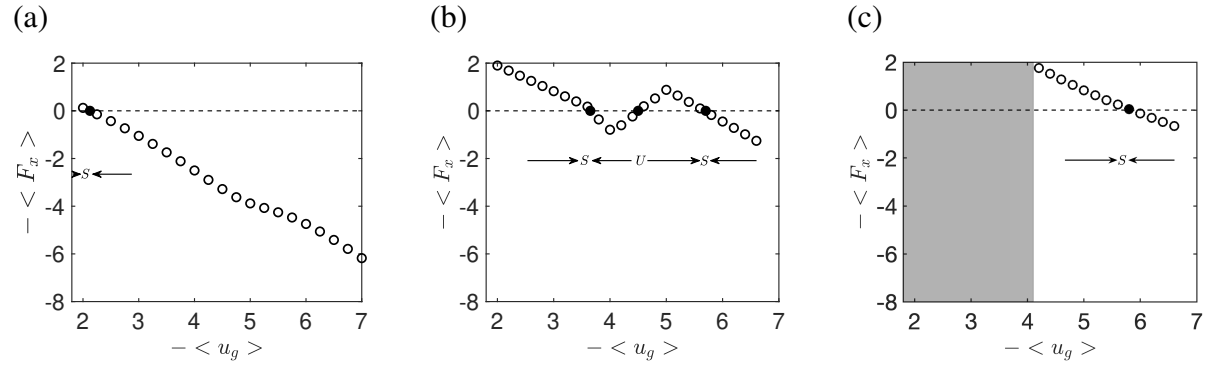

Figure 6.9: Time-averaged horizontal force evolution with the infinite array imposed horizontal velocity u_g for different Stokes numbers. (a) $\beta = 5$, (b) $\beta = 12$ and (c) $\beta = 30$. Arrows indicate the action of the force on the foil velocity, if this one would be free to move. S and U designate respectively stable and unstable points of zero time-averaged force $< F_x >= 0$ with respect to the hydrodynamic tendency. In (c) the grey patch designates a region where solutions are non-periodic. Fixed parameters are $\rho = 10$, $A = 1$, $L = 6$, $H = 3.5$.

of figure 6.8, the interaction effect is lower in amplitude than the other two solutions. Its effect, nevertheless, is visibly opposed to the fast solution, tending to the displace the vortices up rather than downstream. The non-interacting flow is now attenuated (reinforced) in its right (left) portion, resulting in its net displacement towards the leading edge. The trailing edge vortex is simultaneously arranged upstream. This displacement retards the vortex propagation in the channel, what allows the future constructive leading edge interaction of the incoming wake and flapping foil.

6.3.3 Stabilizing and destabilizing effect of hydrodynamic interactions

To understand the emergence of two stable solutions and the existence of the unstable *quasi*-self-propelled state, we study the evolution of the hydrodynamic interaction with the imposed array horizontal velocity. The hydrodynamic interaction effect is characterized by the time-averaged horizontal force. Its evolution with the imposed horizontal speed is depicted for three different characteristic cases in figure 6.9. This evolution is remarkably different for Stokes numbers before, in and after the range of coexisting fast and slow solutions. For low Stokes numbers before the hysteresis, as $\beta = 5$ (6.9-a), the average force monotonously decreases with the increase of the array velocity. The force tends to accelerate the foil ($-\langle F_x \rangle > 0$) for small horizontal velocities, $-u_g \leq 2.2$, passing to a resistive role, where it decelerates the foil, afterwards. Only one *quasi*-self-propelled solution is obtained in this range, with a horizontal velocity similar to the one of the self-propelled case. This panorama changes once the range of coexisting solutions is attained. In this case, exemplified for $\beta = 12$ in (6.9-b), the force variation with the velocity becomes non-monotonous. The force accelerates the foil for velocities $-u_g \leq 3.4$. It becomes then negative, assuming a resistive role for $3.4 \leq -u_g \leq 4.5$. However, after becoming negative, the force does not continuously decrease and inverts its tendency for $-u_g \geq 4$. The force becomes again positive and accelerates the foil for $4.5 \leq -u_g \leq 5.6$. However, the tendency changes again, starting to decay for $-u_g \geq 5$. The force becomes again resistive

for $-u_g \geq 5.6$. Throughout these different variations of accelerating and resistive force, three quasi-self-propelled solutions are found. We will shortly discuss the evolution of the hydrodynamic force action over these equilibria. For higher Stokes numbers $\beta \geq 20$, the force behaviour for small velocities $-u_g \leq 4$ becomes significantly non-periodic. The tendency presented in (6.9-b) when compared to (a) is maintained: the force become more and more positive for a fixed velocity as β increases. Nevertheless, a time-averaged analysis remains dependent of the averaging process. These results are thus not displayed here. In the case of $\beta = 30$, we observe a monotonous behaviour for the periodic solutions $-u_g \geq 4$. The force accelerates the foil for $-u_g \leq 5.7$ and becomes resistive afterwards, with only one quasi-self-propelled equilibrium being found.

Two results are obtained from the previous time-averaged force analysis. The first, already discussed in the previous section, is the existence of *quasi*-self-propelled solutions. Here, however, we are interested at the behaviour of the time-averaged hydrodynamic force around these solutions. Two contrasting behaviours of the hydrodynamic interaction are clearly distinguished: one that surrounds solutions labelled S (stable) and another around U (unstable) solutions. While S solutions are very similar to true self-propelled ones, the U states are not retrieved when the foil dynamics are not imposed. Around the S solutions the hydrodynamic interaction has a stabilizing effect. Provided the wing would be free to move, a small variation of its time-averaged horizontal velocity results in a resistive stabilizing effect of the hydrodynamic interaction. The force obtained for a increase (resp. decrease) of the horizontal velocity is negative (positive) and has the tendency of bringing the foil back to its original time-averaged velocity (see arrows in figure 6.9). For the unstable cases U, on the other hand, the hydrodynamic force has a destabilizing effect. For the case illustrated in (6.9-b), a positive or negative variation of the velocity results in a similar increase from the hydrodynamic interaction. The interaction effect then leads the unstable solution to one of the two unstable solutions.

Although this time-averaged analysis remains, of course, an approximation of self-propelled cases, a similar link between a perturbation time-averaged force and horizontal velocity is a possible linear instability indicator. As shown in one of our past studies, for a non-interacting symmetric self-propelled foil in a quiescent fluid (Benetti Ramos et al. 2020), the existence of a perturbation synchronous to the base solution of same velocity and force sign is an evidence of a linear Floquet instability of the fluid-solid system. More studies to provide an appropriate self-propelled unstable base solution, further studying its fluid-solid Floquet stability could shed more lights into linear mechanisms of the system instability.

An alternative path to access the mechanisms leading the unstable solution towards the two stable self-propelled states is the nonlinear perturbation of the unstable state,

$$(\mathbf{u}", p", \omega_z", u_g") = (\mathbf{u}^{sp}, p^{sp}, \omega_z^{sp}, u_g^{sp}) - (\mathbf{u}^{qsp}, p^{qsp}, \omega_z^{qsp}, u_g^{qsp}), \tag{6.12}$$

defined as the difference between a stable self-propelled (sp) and the unstable *quasi*-self-propelled (qsp) equilibria. Similar to the effect of the wing interaction over the non-interacting flow, the action of the nonlinear perturbations over the unstable solution, depicted in figure 6.10, is mainly constituted of vortex displacement dipoles. In both slow and fast solutions, the dipoles are centered over the leading and trailing edge vortices of resp. negative and positive vorticity. The slow solution nonlinear perturbation (6.10-a) displaces the vortex above the foil towards its

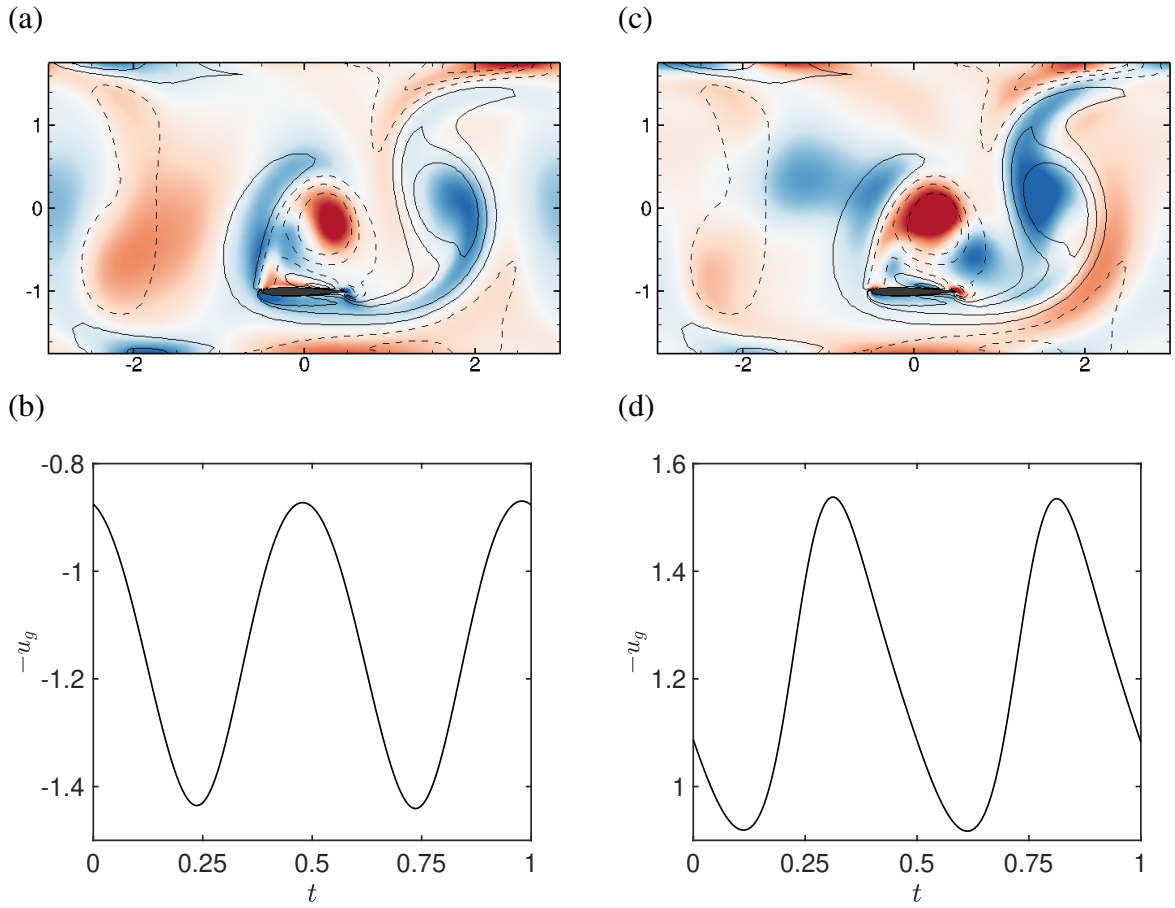

Figure 6.10: Nonlinear perturbation of the unstable *quasi*-self-propelled solution for $\beta = 15$: flow vorticity $\omega"_z$ and horizontal velocity $u"_g$ periodic evolution leading towards the (a,c) fast and (b,d) slow solutions. In (a,b) the middle unstable solution and the nonlinear perturbation are superposed, respectively represented by lines and flooded contours. Fixed parameters are $\rho = 10$, $A = 1$, $L = 6$, $H = 3.5$.

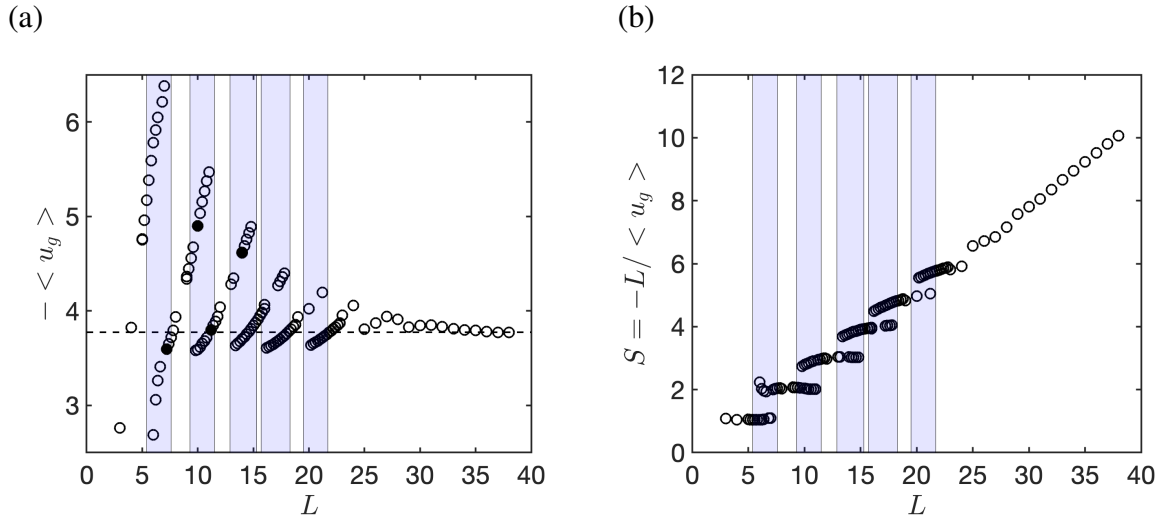

Figure 6.11: (a) Time-averaged horizontal velocity and (b) schooling number $S = -L/< u_g >$ of the self-propelled infinite array evolution with the gap L between the wings. The light blue background again identify ranges where coexisting solutions are obtained. Contours of the solutions represented by filled circles are in figure 6.12. Other fixed parameters are $\beta = 15$, $\rho = 10$, $A = 1$, $H = 3.5$.

lower left and erases the destructive positive vorticity that surrounds it. The trailing edge vortex is mainly weakened in its lower right part, generating its horizontal alignment characteristic of the slow solution. These two vortex displacement are equally followed by the decrease of the foil horizontal velocity (6.10-b). The minima of the velocity perturbation are for the instants $t = 0.25$ and 0.75 that precede the wake-flapping foil leading edge interaction. This intuitively indicates that the foil adjust its velocity to allow a constructive vortex interaction at the leading edge. The perturbation towards the fast solution (6.10-c,d), on the other hand, presents peak increases of the horizontal velocity shortly at these same time instants. This increase is possibly a necessary adjustment to achieve the summed constructive interaction of the wake vortex and the previously shed LEV at the foil trailing edge. The nonlinear perturbation of the flow (6.10-c) indeed acts over the vortex over the foil to displace it towards the trailing edge and to open space to this interaction by moving the trailing edge vortex further downstream. The incoming negative vortex is also displaced and intensified. Apparently, as conceived by Lin et al. (2019) for a finite array of simultaneously heaving and pitching foils separated by a free gap, the self-propelled array is indeed capable of avoiding a destructive wake interaction through the wake and foil velocity adaptation.

6.3.4 Parametric study with the gap L between wings

The effect of the gap between wings $2 \leq L \leq 40$ for a fixed Stokes number $\beta = 15$ is finally investigated. Other parameters as the density ratio $\rho = 10$ and the channel height $H = 3.5$ are kept fixed.

The evolution with the gap L of the array time-averaged horizontal velocity and Schooling number S (figure 6.11) reveals that the interaction effects disappear as the gap is increased. For

very large gaps between the wings, greater than 30 times the chord, interaction effects are no longer present (6.11-a) and the array velocity equals the one of a single wing. For $L \leq 25$, interaction effects results in average velocities either lower or higher than that of a single wing. Two stable solutions, again fast and slow (trailing and leading edge) interactions, are obtained for certain gaps. This phenomenon is identical to that of a fixed gap and increasing frequency. A surprising observation is that the greatest velocity increase is obtained for $L \sim 7$, and not the closest gap $L = 2$. Smaller gaps have not been explored in this study since solutions become very non-periodic.

The Schooling number S evolves in a discrete set of stable orbits as the gap is increased, as seen in figure 6.11 (b). These sets evolve near integer Schooling numbers, such as $S = 1$ or 2. For small gaps $L \leq 10$ and $S = 1{,}2$ they are very flat remaining almost constants as the gap increases. This behaviour is then progressively lost. Beyond the third set $S = 3$ the interaction effects apparently weaken and the Schooling evolution with the gap is more "diagonal". These integer between particle and wake wavelengths adds up to several other observations of hydrodynamic collective interaction, for example flapping swimmers (Ramananarivo et al. 2016; Peng, Huang, and Lu 2018a) and walking droplets (Perrard et al. 2014), where particle dynamics, as flapping wings, seem to be piloted by the particle/wake interaction. An interpretation of this phenomenon might be possible through hydrodynamic pilot-wave theory (Bush 2015), where the infinite array can be seen as particles (individual wings) interacting actively with a (self-produced) wave (wake) whose mutual influence pilots stable interaction states of motion.

Similar to the case of a fixed gap, slower and faster coexisting solutions always feature leading and trailing edge wake-flapping foil interactions. As the gap is increased, solutions evolve from slow to fast interactions, discontinuously falling from the latter to the former as the self-propelled system switch between branches. To observe this effect, solutions identified in the previous figure 6.11 are depicted in figure 6.12. As one can see, starting from a point $L = 7$ at (6.12-a) we see a slow solution, featuring a leading interaction, very similar to the one of $L = 6$ exhibited in figure 6.5. This solution evolves as the gap is increased, with its velocity increasing above the one of a non-interacting wing. As the velocity and gap are simultaneously increased, the slow interaction becomes a fast trailing edge interaction, as shown in (6.5-b) for $L = 10$. This effect is repeated in every branch of stable self-propelled solutions, as it can be again observed for the slow and fast solutions of the branch $S \sim 3$ depicted in figures 6.5(c,d) for $L = 11$ and $L = 14$.

6.4 Conclusions

This work investigated the coexistence of self-propelled states of locomotion of an infinite array of heaving wings confined within a channel with a constant gap between wings. The self-propelled dynamics of an array with NACA0010 wings of density ratio $\rho = 10$, flapping amplitude $A = 1$ and channel height $H = 3.5$ were investigated through unsteady nonlinear simulations, based on the resolution of the coupled self-propelled array-fluid system. The influence of the Stokes number and gap between wings have been analysed.

The self-propelled dynamics for $1 \leq \beta \leq 50$ with a fixed gap of $L = 6$, featuring a range of two coexisting slow and fast solutions $11 \leq \beta \leq 29$, was compared to the dynamics of the array with an imposed the time-averaged velocity. The *quasi*-self-propelled equilibria of the

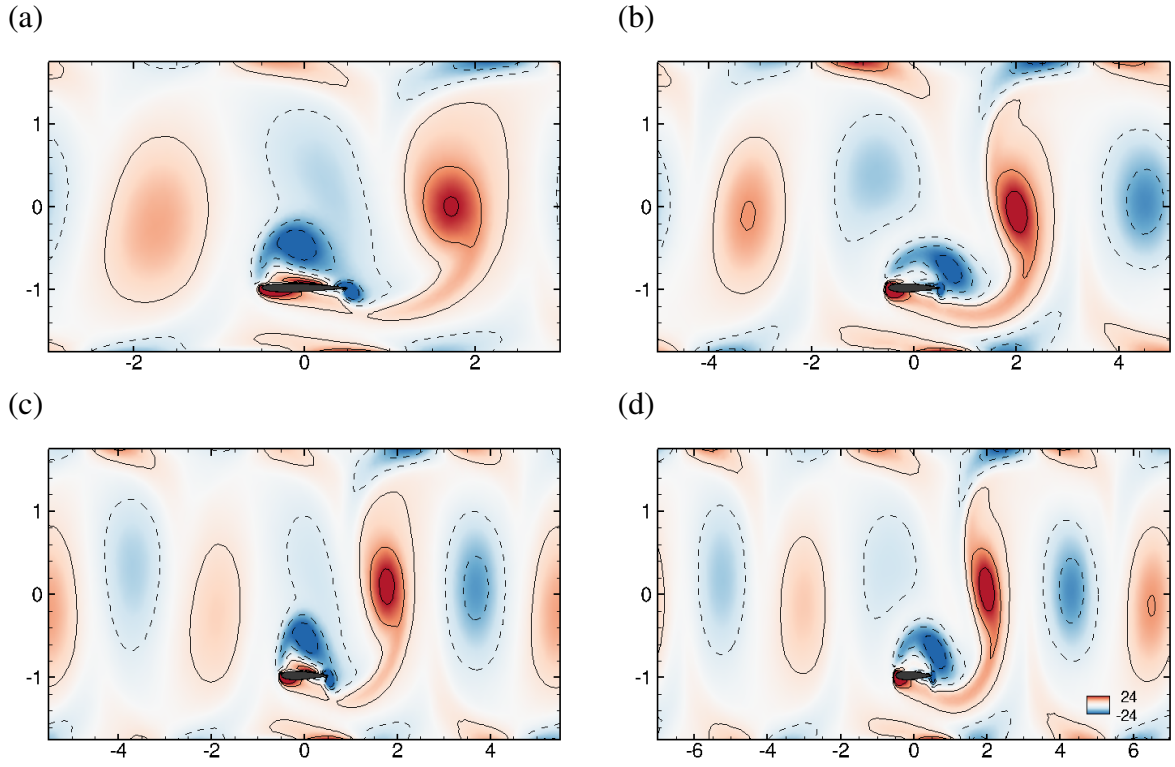

Figure 6.12: Vorticity contours of the self-propelled infinite array of flapping wings for different gaps L between wings. (a) $L = 7$ (LE interaction), (b) $L = 10$ (TE interaction), (c) $L = 11$ (LE interaction) and (d) $L = 14$ (TE interaction). Fixed parameters are $\rho = 10$, $A = 1$, $\beta = 15$, $H = 3.5$.

array, solutions with imposed velocity of zero average horizontal force, revealed the existence of three rather than two solutions in the range of coexisting solutions. These newly established unstable solutions indicate a possible saddle-node bifurcation of the self-propelled system. A comparison of the two stable self-propelled and the unstable *quasi*-self-propelled solutions was then performed. While the two stable solutions present significant energetic benefits for the interacting foils, the unstable solution mostly degrades the system performance. To understand this different positive/negative effect of the wake interaction, the total solutions, flow and forces, have been decomposed into a single wing and wake-foil interaction components. Stable self-propelled solutions present wake-foil fields that favor a constructive interaction between incoming wake and vortices shed by the foil. Unstable solutions, however, drive the leading edge vortex further away from itself while achieving a destructive interaction with the incoming wake.

The evolution of the hydrodynamic force with the array imposed velocity was then addressed. For fixed flapping amplitudes and frequencies, this evolution revealed a stabilizing/destabilizing interaction character associated to the stable/unstable *quasi*-self-propelled solutions of the system. In the case of the unstable solutions, an increase/decrease of the time-averaged horizontal velocity is followed by an equivalent tendency of the horizontal force amplifying velocity perturbations. This behaviour, similar to that of linear perturbations in the onset of flapping locomotion of symmetric foils (Benetti Ramos et al. 2020), is characteristic of the fluid-solid system instability. Nonlinear perturbations of the unstable solutions leading towards fast and slow solutions revealed that, similar to the conception of Lin et al. (2019), the self-propelled array is capable of avoiding destructive wake interactions through adaptation of its flow and foil velocity. The mechanism at play is an inherently coupled fluid-solid one where both wake and foil velocity adapt as to achieve the constructive wake-flapping foil interactions observed for the unsteady solutions.

The effect of the gap between wings was finally analysed. This study revealed the existence of a discrete set of solutions of the self-propelled system, centered around constant Schooling numbers S. The effect of the interaction is progressively lost as the gap increases, with the solution tending for large gaps towards a non-interacting one. Inside a single branch, of fixed Schooling number, the solution transition between fast and slow interactions resp. with trailing and leading edge interactions, as the gap increases. The jump between branches is characterized by a discontinuous transition from a fast to a slow solution.

The results presented in this work highlight the role played by wake-flapping foil interactions in the stability of self-propelled solutions of a flapping wings array. They indicate, for example, that control strategies aiming to optimize the horizontal speed in such a configuration can use the destabilizing interaction thus transitioning to a faster solution without the need of additional energy expenses. To better characterize the fluid-solid system instability, the imposed horizontal velocity approach should be further improved. True unstable self-propelled solutions should be obtained, either via nonlinear bifurcation methods (Dijkstra et al. 2014) or filtering techniques (Sipp and Lebedev 2007; Shaabani-Ardali, Sipp, and Lesshafft 2017), a challenging task for the numerical tools existent so far. Finally, it would be interesting to evaluate how this stabilizing/destabilizing effect evolves for a finite number of elements of the array (Ramananarivo et al. 2016; Peng, Huang, and Lu 2018a; Peng, Huang, and Lu 2018b), for other lattices (Oza, Ristroph, and Shelley 2019) and for uncoordinated flapping swimmers (Newbolt, Zhang, and

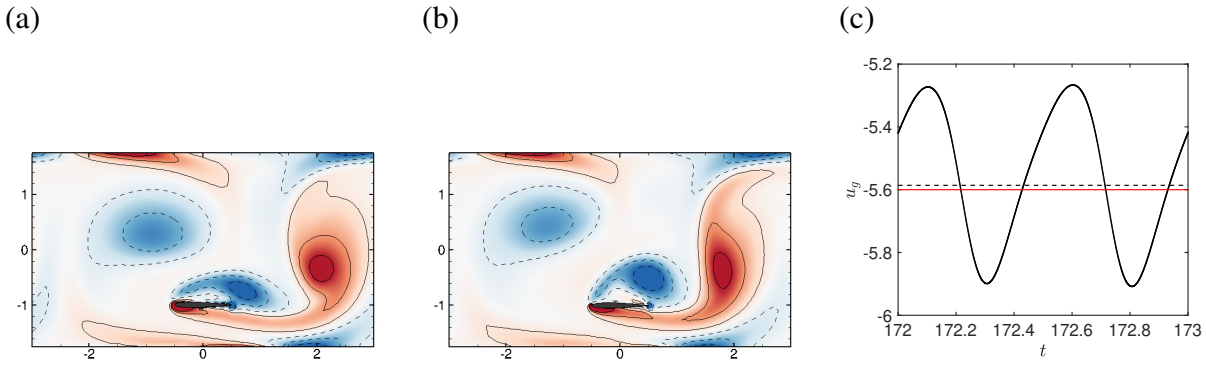

Figure 6.13: Comparison for $\beta = 15$ between (a) self-propelled and (b) *quasi*-self-propelled solution for $- < u_g >= 5.6$. (c) Comparison between the unsteady u_g signal and the self (dashed black line) and *quasi*-self-propelled (red line) time-averaged velocity values. Fixed parameters are $\rho = 10$, $A = 1$, $L = 6$, $H = 3.5$.

Ristroph 2019). To approach more efficient systems, the effect of a passive elasticity could compared to the rigid system. For a non-interacting heaving foil passively pitching around its leading edge (Spagnolie et al. 2010) lumped elasticity provided velocity enhancement for certain flapping frequencies. Passive mechanisms of elastic bodies reacting to the unsteady wake of a neighbour (Beal et al. 2006; Eldredge and Pisani 2008) are capable of resulting in body locomotion. What could be the effect of this supplementary degree of freedom over the coexistent states and the hydrodynamic interaction when the wings are actively flapped? The answer might be surprising, since counter intuitive effects have already been observed for deforming bodies in a tandem arrangement (Ristroph and Zhang 2008).

6.5 Comparison between *quasi*-self-propelled and self-propelled solution

The comparison between self-propelled and *quasi*-self-propelled solutions is supported by two main factors. These can be fairly illustrated by a comparison, figure 6.13, between the self-propelled solution obtained for $\beta = 15$, $\rho = 10$, $A = 1$, $L = 6$, $H = 3.5$ and the similar *quasi*-self-propelled obtained for a fixed horizontal velocity $- < u_g >= 5.6$. The first reason, inherent of the self-propelled solutions, concerns the greater order of magnitude of the horizontal velocity periodic signal time-average than its fluctuations, visible in (6.13-c). The horizontal velocity in fact has a time average of $< u_g >\sim 5.55$ and a fluctuation $u'_g \sim 0.3$ that represents only 5% of the amplitude of the time-average value. It is reasonable to consider thus, that the flow might be fairly represented by a constant horizontal velocity, one hypothesis that is sometimes followed in the literature to simplify the study of fish swim (Li et al. 2019). It is even more evident that this approach remains somehow acceptable when we compare the vorticity contours of both *quasi* and self-propelled solutions, figures 6.13 (b) and (a). Although remarkable differences exist in the shape of the vortex, the overall aspect is fairly similar. Even more, the characteristic interactions between the incoming wake and the flapping foil are

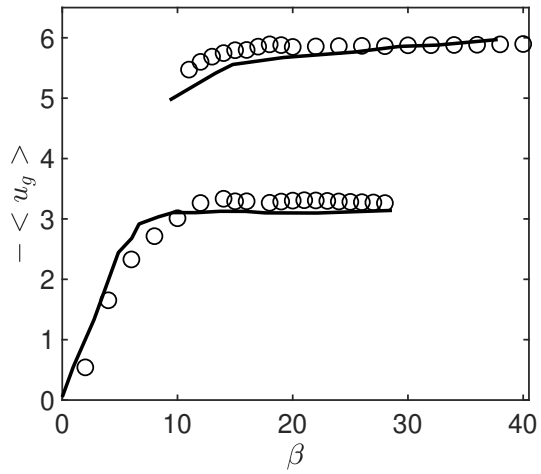

Figure 6.14: (a) Validation between the present numerical method (open circles) and the numerical results of Becker et al. (2015) (solid line). Other Fixed parameters are $\rho = 10$, $A = 1$, $H = 3.5$.

perfectly capture by the *quasi*-self-propelled analysis. This becomes even more evident when the time-averaged velocity of both solutions is compared in figure 6.13(c), the value between both analyses being identical.

6.6 Nonlinear solver validation

The nonlinear solver employed in this study has been validated through a comparison with the numerical study of (Becker et al. 2015). The adopted configuration and control parameters are identical to those chosen by the authors. One can see in figure 6.14 that the time-averaged horizontal velocity obtained with the present numerical method compare very well with values found on the reference. In addition the range of coexisting solutions in our study $11 \leq \beta \leq 29$ differs only slightly with the authors finding fast solutions of $\langle u_g \rangle$ up to $\beta = 10$ instead of 11.

Conclusions & perspectives

Summary and main results

This thesis represents a step towards the prediction and understanding of flapping wings self-propelled dynamics as fluid-solid instabilities. Different methodologies were derived to study single and collective dynamics. For taking into account the foil self-propelled motion, a non-inertial frame of reference was introduced. Considering a rigid foil, this frame of reference can even include the foil flapping motion. In more general situations (confinement, foil deformation, collective interaction with free gaps and others) a non-inertial frame of reference cannot be used. Fictitious domain methods with distributed Lagrange multipliers were then presented. To easily assess periodic cruise regime dynamics and determine unstable periodic solutions (when these exist) a time spectral method coupled to pseudo arc-length continuation was presented. To assess the stability of self-propelled periodic solutions the so-called fluid-solid Floquet stability analysis, that takes into account the inherent coupling between flow and foil dynamics both in the base-solution and perturbation level, was introduced in this work.

These methods allowed to study two different problems, the self-propelled dynamics of a symmetric foil in a quiescent fluid and of an infinite array of wings in a channel. Each problem was addressed in a separated part of the thesis. At the first part, after introducing the specific numerical methods in chapter 1, the self-propelled dynamics at the onset of flapping propulsion, for a fixed flapping amplitude and increasing frequency, were predicted and explained by the fluid-solid Floquet instabilities of symmetric non-propulsive solutions (chapter 2). Attaining higher flapping frequencies (chapter 3), the three new self-propelled propulsive regimes beyond the onset were explained through nonlinear continuation, local and global bifurcations of the fluid-solid system. Finally the last chapter of this part (chapter 4) analysed the thrust of the self-propelled foil in its cruise regime. A decomposition between diffusive and pressure forces identified the existence of a transition between a regime were the former and the latter forces drive the thrust. The last part of this thesis addressed the collective dynamics of self-propelled flapping wings confined in a channel. Fictitious domain methods were first introduced (chapter 5) to address the channel confinement. Coexisting self-propelled solutions over a range of flapping frequencies of an infinite array of heaving wings was then studied. Self-propelled and imposed horizontal velocity simulations revealed a possible saddle-node bifurcation of the coupled fluid-solid system at the origin of the hysteretic behaviour (chapter 6).

Theoretical and numerical methods

Two chapters of this thesis, chapters 1 and 5, were dedicated to numerical methods for determining nonlinear equilibria of self-propelled foils coupled to viscous fluids. The chosen modeling

is capable of following the wing self-propelled motion by adopting a non-inertial frame of reference placed on the wing center of gravity. When the foil is rigid and the fluid domain is not bounded (with solid walls that could become time-dependent in the non-inertial frame) the wing flapping motion can be equally taken into account by this frame of reference. The fluid-solid coupled problem is eased almost to the level of solving an exclusively fluid problem. For more complex setups as elastic foils or closed channels, fictitious domain methods with distributed Lagrange multipliers were implemented. Both methods were demonstrated to achieve a great level of accuracy for describing the foil self-propelled dynamics. In addition to unsteady nonlinear solvers based on these two formulations, specific methods for time-periodic solutions were developed. A so-called fluid-solid Floquet stability analysis that integrates the coupling of the fluid with the foil dynamics both on the base-solution and perturbation level was introduced. Time spectral methods coupled to pseudo arc-length continuation allowing to assess directly periodic cruise solutions even when these are unstable were then presented. All these methods were validated in a significant number of configurations. The unsteady nonlinear solver was cross-validated against the literature. The time-spectral method and arc-length continuation were then validated against this unsteady solver. In the case of the self-propelled fluid-solid Floquet stability analysis, the validation was performed in two steps. As no validation case exist in the literature, the Arnoldi method was validated in the case of a purely hydrodynamic problem. To validate the fluid-solid couple problem then, the linear growth of small amplitude perturbations initiated in the unsteady solver was compared with the growth rate predicted by the Floquet analysis. The ensemble of these methods allowed to systematically study linear and nonlinear fluid-solid instabilities resulting in the emergence of self-propelled flapping foils dynamics in viscous fluids.

The onset of flapping propulsion as a fluid-solid Floquet instability

The propulsion onset of a self-propelled symmetric heaving foil in a quiescent fluid was first addressed. The emergence of a periodic state of unidirectional locomotion and a quasi-periodic state of back & forth motion around a fixed point were studied with nonlinear and linear analyses. Unsteady nonlinear simulations were conducted for a fixed flapping amplitude and an increasing frequency (Stokes number). For smaller Stokes numbers, the flow surrounding the foils remains symmetric and non-propulsive symmetric solutions are retrieved. As the Stokes is increased above a critical threshold the flow breaks symmetry and a periodic state of unidirectional propulsion is reached. Increasing the Stokes numbers leads to a sub-critical transition between propulsive and again non-propulsive solutions. Finally, a back & forth regime is attained for higher Stokes. The established nonlinear transition route was then investigated through fluid-solid Floquet stability analysis of non-propulsive solutions. Unstable synchronous and asynchronous Floquet modes were obtained, respectively in the range of unidirectional propulsion and back & forth motion. The onset of these nonlinear solutions as well as their quasi-periodic frequency (when it is the case) are accurately captured by this coupled stability analysis, different than a purely-hydrodynamic one. The unstable modes have a propulsive character, featuring asymmetric flows with non-zero forces that accelerate a non-zero velocity perturbation. In the case of the asynchronous mode, its associated complex multiplier introduces the slow modulation that leads to the non-coherent back & forth movement. A time-averaged analysis of the velocity and force perturbation allows to establish physical instability criteria. Unstable synchronous modes are determined by same sign time-averaged horizontal forces and

velocities, meaning the flow accelerates velocity perturbations. Unstable asynchronous modes are obtained when the phase between the quasi-periodic perturbations of velocity and force imply in the foil being more accelerated than decelerated along the slow period. The influence of the solid-to-fluid density ratio was finally analysed, revealing that the coupling terms are not erased when this ratio tends to infinity. Two distinct asymptotic behaviours are obtained for synchronous and asynchronous modes. The first ones become marginally unstable, the solid velocity remains non-zero but the effect of the fluid force becomes negligible in the infinite ratio limit. The foil velocity being no longer accelerated, the Floquet mode is only marginally unstable. In the case of asynchronous modes, the solid velocity tends to zero when the density ratio increase. Then, the fluid-solid coupling terms disappear, and the Floquet modes tend to a purely hydrodynamic stability analysis. We conclude that the onset of flapping propulsion is a fluid-solid Floquet instability. The coupled fluid-solid analysis encompasses and improves the literature purely hydrodynamic one.

Local and global bifurcations of self-propelled foils for higher flapping frequencies

Beyond the onset of flapping propulsion, three new unidirectional propulsive solutions follow back & forth quasi-periodic oscillations, as the flapping amplitude is kept the same and the frequency risen. These three propulsive solutions, that appear in the following order, are distinguished by their up and down quasi-periodic wake deviation, a symmetric periodic wake and a deviated periodic wake. The fluid-solid Floquet stability analysis of non-propulsive solutions, employed in the past chapter, was not capable of predicting the onset of these three regimes. We have thus decided to introduce the coupling between fluid and solid not only at the perturbation, but also at the base-solution level, studying the stability of propulsive and not non-propulsive base solutions. Nonlinear bifurcation methods were employed to continuate symmetric periodic wake propulsive solutions. The emergence of deviated quasi-periodic and periodic wake behaviours was explained through local bifurcations of symmetric periodic wake solutions. Unstable symmetric periodic solutions were obtained using time spectral methods and pseudo arc-length continuation. Their fluid-solid Floquet stability revealed the existence of unstable synchronous and asynchronous Floquet modes in the frequency range of deviated periodic and quasi-periodic wake solutions. Unstable synchronous modes feature the periodic wake deviation of nonlinear solutions. Asynchronous modes also feature wake deviation, but the associated complex multiplier generates the quasi-periodic up and down deviation of the wake. The slow frequency introduced by this multiplier matches the quasi-periodic behaviour of nonlinear solutions at the onset. Finally, phase portraits of the nonlinear back & forth and deviated quasi-periodic wake solutions were used to highlight the existence of a *homoclinic* global bifurcation. As the onset of flapping propulsion, transitions between self-propelled dynamics beyond the onset are explained as global and local fluid-solid bifurcations.

Diffusion and pressure-driven thrust regimes

The physical nature of the thrust acting on the cruise regime of self-propelled symmetric heaving foils was analysed for different flapping amplitude, frequencies, density and aspect ratios. In cruise regimes, the time-averaged contribution of diffusion and pressure to the horizontal force distinguished the existence of two different thrust regimes. The first, for low flapping amplitude

and frequencies, is driven by diffusive forces. The thrust is generated by an asymmetric shear on the foil lateral surface. The second, is driven by pressure. Its thrust production relies on the fluid acceleration behind the flapping body and its consequent reduction of the trailing edge suction force. The influence of the thickness-to-chord aspect ratio and flapping amplitude revealed that the diffusive driven thrust regime is enhanced for smaller aspect ratios. The transition between the diffusion and pressure-driven thrust regimes takes place for a fixed product of amplitude and flapping frequency.

The role of hydrodynamic force in collective interactions

The last chapter of this thesis concerned the coexistence of self-propelled locomotion states of an infinite array of heaving wings in a confined channel. Self-propelled and imposed horizontal velocity solutions were compared, revealing a possible saddle-node bifurcation. The two stable coexisting self-propelled solutions are faster and slower than a single flapping wing, featuring constructive interactions with the wake. The unstable solutions interact destructively with the incoming wake, having an intermediary velocity between fast and slow co-existing self-propelled states. Constructive and destructive interactions lead respectively to energetic enhancement and degradation. Energetic enhancement is connected to the exploitation of the leading edge vortex to reduce power input, what is not achieved by the unstable solution. The evolution of the hydrodynamic force acting on the imposed velocity array simulations revealed a stabilizing (destabilizing) damping character of the collective interaction related to stable (unstable) solutions. Nonlinear perturbations of the unstable solution reveal that the array adapts its velocity and fluid flow to avoid destructive interactions. The mechanism at play is an inherently coupled fluid-solid one. The increase of the gap between wings finally revealed the existence of a discrete set of solutions centered around constant gap against distance traveled in a flapping period ratio. Results of this study highlight the role played by wake-flapping foil interaction in the stability of self-propelled arrays. They indicate that control strategies aiming at optimizing horizontal velocity in such configurations should play with destabilizing effect of interactions exploiting this to transition to faster solutions without additional energy expenses.

Perspectives

Insights and numerical tools developed during thesis might be valuable for future works. As a complement to the conclusion, some imagined outlines are here described hoping to provide a basis for future discussions.

Direction reversal of passively pitching self-propelled flapping foils

The elastic deformation of wings and bodies is an essential aspect of living organisms flapping propulsion. In this thesis, rigid wings were adopted to simplify the coupled fluid-solid dynamics up to the wing self-propelled degree of freedom. As the fluid-solid coupling has been highlighted as essential ingredient of self-propelled regimes in this work, the reintroduction of elasticity degrees of freedom might originate new regimes and transitions. To study these, tools developed in this work as the fictitious domain with distributed Lagrange multiplier, the time-spectral method and the fluid-solid Floquet stability analysis can be adapted. A clear case is the self-propelled dynamics of a heaving elliptical foil in a quiescent fluid free to passively pitch around

its leading edge (Spagnolie et al. 2010). This model approximates the passive elasticity of living organisms through a lumped elasticity around the foil leading edge. Numerical and experimental results for a fixed flapping amplitude and varying frequency revealed the existence of a bifurcation for high flapping frequencies where the foil propulsion direction is reversed. As trajectory control is lost in this case, understanding how the foil elasticity leads to this scenario is important for future engineering applications. The branching scenario of Spagnolie et al. (2010) indicates the possibility of a saddle-node of periodic cycles as the one investigated in chapter 3. Such bifurcation could be analyzed with the time spectral method coupled to pseudo arc-length continuation. As the system is not confined and the body is still rigid, the non-inertial frame of reference moving with the foil center of gravity can still be adopted for the fluid-solid coupling. However, due to the foil pitching a projection of the equations in a rotating frame of reference, as done in Jallas, Marquet, and Fabre (2017), needs to be included in the tools developed in chapter 1. Such an adaption would require only modifications of the variational formulation used in the numerical method implemented in FreeFEM. This problem could be investigated thus in a short horizon following this thesis.

Towards three-dimensional self-propelled flapping foils

A simplification made along this thesis was to assume two-dimensional foils and surrounding flow. As wings have finite spans and flow three-dimensional instabilities can appear, modifications generated by withdrawing this hypothesis need to be evaluated. A first step could be the inclusion of a periodic span-wise dimension as done for studying the three dimensional transition in the wake of fixed (Barkley and Henderson 1996) or oscillating cylinders (Leontini, Thompson, and Hourigan 2007) with incoming flows. How would this three-dimensional transition takes place in the case of self-propelled objects? The onset of symmetry breaking of non-propelled oscillating cylinders (Elston, Sheridan, and Blackburn 2004; Elston, Blackburn, and Sheridan 2006) is known to combine both two-dimensional symmetry breaking and the onset of three-dimensionality. However, as shown in chapter 2 predictions from non-propelled systems are substantially different than self-propelled systems. In addition, the onset of flapping propulsion of low aspect ratio foils is very different than cylinders (Deng and Caulfield 2016). The flow generated by the flapping wing in this case, presented in chapter 2, might be more related to the instability of a pair of counter-rotating vortex rings than the instability around the oscillating cylinder. This isolated vortex pair is known to exhibit short and long wavelength helical or Crow instabilities, these instabilities being subsequently affected by the presence of solid walls (Dehtyriov, Hourigan, and Thompson 2019). In the case of self-propelled foils near the onset of flapping propulsion, this problem would be posed in the case of the vortex pair interacting with a flapping rather than steady solid wall. To study this problem, the fluid-solid Floquet stability analysis could be enlarged to periodic perturbations over a wing of infinite span. As shown by Barkley and Henderson (1996), the introduction of spanwise periodic perturbations results in the resolution of a modified two-dimensional problem. Span-wise derivatives are simplified to the inclusion of a wave-number, which can thus be varied to find the least unstable one. This would require a minimal modification of the fluid-solid Floquet stability analysis introduced in this work.

Adjoint-based sensitivity of fluid-solid Floquet modes & flapping wings optimization

Throughout this thesis, we have consistently highlighted that the onset of different flapping wings self-propelled regimes can be predicted and explained by a fluid-solid Floquet stability. Although linearly unstable mechanisms are characterized through the direct Floquet modes, a greater physical understanding of these can be obtained by identifying the spatial region and even time instants, in the case of periodic solutions, that drive the instability. Such idea is formalized in hydrodynamics by the concept of *sensitivity*, posed in the case of the primary and secondary instability of circular cylinders by resp. (Giannetti and Luchini 2007; Giannetti, Camarri, and Luchini 2010) for perturbation and (Marquet, Sipp, and Jacquin 2008; Giannetti, Camarri, and Citro 2019) base-flow modifications. These works identify specific regions (and time instants in Giannetti, Camarri, and Luchini (2010) and Giannetti, Camarri, and Citro (2019)) in the flow field that drive the instability, giving hints on how these can be optimally perturbed. An essential ingredient for this analysis are adjoint equations. Adjoint equations, commonly employed for purely hydrodynamics problems, could be thus enlarged for the specific case of coupled fluid - self-propelled foils. This analysis could then discuss on the onset of flapping propulsion, or the dynamics beyond this, either instabilities are driven by the fluid or solid dynamics and how to optimally perturb them. Adjoint-based optimization approaches are also very interesting for flapping propulsion due to its large space of control parameters (Xu and Wei 2016). As the adjoint problem obtain simultaneously the sensitivity with respect to several control parameters, its computational cost is independent of the number of variables. The large control space of flapping propulsion could then be easily explored.

Stability of collective interactions self-propelled solutions

The problem started in chapter 6 indicates a possible saddle-node bifurcation over the infinite array time-averaged velocity evolution with the Stokes number. However, the unstable self-propelled solution was only approximated by a *quasi*-self-propelled solution that eliminates both fluid-solid coupling and the unsteady character of the real unstable solution. A proper stability study of this problem would require the actual calculation of the unstable base-solution, followed by its fluid-solid Floquet stability analysis. Concerning the fluid-solid Floquet stability analysis, the algorithm written in chapter 1 could be easily adapted to the fictitious domain with distributed Lagrange multiplier method used in chapters 5 and 6. The calculation of unstable base-solutions, on the other hand, would be a greater challenge. An adaptation of the time-spectral method to fictitious domain with distributed Lagrange multipliers method was started in this thesis. However it ended up revealing that (1) the time-averaged preconditionner introduced in chapter 1 is not robust to attain great fluctuation amplitudes, which is the case of the problem treated in chapter 6. (2) The convergence of the TSM Newton algorithm using the FD/DLM method is sensitive to the error committed on the interface description. To overcome these issues, mesh adaptation for each time instant and direct factorization of the TSM Jacobian rather than iterative methods were used. However, this method attains a very large computational requirement before attaining harmonic and mesh convergence. Numerical developments as a fluctuation amplitude / harmonic content robust preconditionner are still needed for attaining the unstable base-solutions and investigating this bifurcation. Another alternative would be to adopt unsteady filtering techniques (Shaabani-Ardali, Sipp, and Lesshafft 2019) instead of the

TSM.

An interesting path that could be taken towards unstable states is the implementation of reduced-order models. During this thesis, a reduced order model to study the infinite array of flapping wings was developed during the internship of Gaétan Raynaud. This model, inspired by the one of Facchinetti, Langre, and Biolley (2004) in the study of vortex-induced vibration of cylinders, couples the solid equation to a Van der Pool oscillator that models the fluid forces. A delay term is added to this oscillator to take into account the wake interaction. A similar reduced order model was proposed by Oza, Ristroph, and Shelley (2019) for flapping swimmers to study several lattices of flapping swimmers. As these models allow both to isolate/model physical phenomena and are very computationally efficient, they could be employed to study different lattices and stability of self-propelled solutions. However, the full resolution of the fluid equations might remain essential to understand flow phenomena associated to the system stability/instability and conceive control strategies.

The effect of passive elasticity in collective interactions

As flapping swimmers can swim exclusively through passive deformations of their elastic body (Beal et al. 2006), a final interesting problem would be to introduce elastic or passively-pitching wings in the chapter 6 problem to study the evolution with frequency of the self-propelled array velocity. Spagnolie et al. (2010) have shown that a self-propelled heaving and passively pitching elliptical foil has a mean horizontal velocity evolution with the Stokes number very different than a rigid purely heaving foil. For some flapping frequencies, the velocity is severely increased, while for others it is decreased. For very high frequencies, direction reversal with discontinuous branch switching (as previously invoked in this conclusion) is observed and trajectory control is lost. How would a similar lumped passive elasticity model affect the locomotion of the self-propelled array studied in chapter 6? To answer this question, the fictitious domain method with distributed Lagrange multipliers could be easily adapted to take into account the passive pitching (and even an elastic structure in the future). Would elasticity enhance the observed hysteresis or promote a continuous evolution of the array velocity? The answer to these questions would be of utmost importance for the design of elastic wings of flapping propulsion based devices.

Concluding remarks

Throughout this thesis, the self-propelled dynamics of a single and an infinite array of flapping wings in a viscous fluid have been predicted and explained through stability analysis of the coupled fluid-solid system. As many directions are still possible and flourishing around this topic, oncoming studies of this propulsion strategy can possibly benefit of the awareness of this coupling. Future works can probably go deeper in the last questions raised, and we hope the description of coupled fluid-solid mechanisms will improve our understanding of this form of locomotion.

Bibliography

Alben, Silas and Michael Shelley (2005). "Coherent locomotion as an attracting state for a free flapping body." In: *Proceedings of the National Academy of Sciences of the United States of America* 102.32, pp. 11163–11166. ISSN: 0027-8424. DOI: 10.1073/pnas.0505064102. URL: http://www.pnas.org/content/102/32/11163{\%}5Cnhttp://www.ncbi.nlm.nih.gov/pubmed/16055551{\%}5Cnhttp://www.pnas.org/content/102/32/11163.full{\%}5Cnhttp://www.pnas.org/content/102/32/11163.full.pdf.

Andersen, A. et al. (2017). "Wake structure and thrust generation of a flapping foil in two-dimensional flow". In: *Journal of Fluid Mechanics* 812, R4. ISSN: 14697645. DOI: 10.1017/jfm.2016.808.

Angot, Philippe, Charles Henri Bruneau, and Pierre Fabrie (1999). "A penalization method to take into account obstacles in incompressible viscous flows". In: *Numerische Mathematik* 81.4, pp. 497–520. ISSN: 0029599X. DOI: 10.1007/s002110050401.

Arbie, M. Rizqie, Uwe Ehrenstein, and Christophe Eloy (2016). "Stability of momentumless wakes". In: *Journal of Fluid Mechanics* 808, pp. 316–336. ISSN: 14697645. DOI: 10.1017/jfm.2016.645.

Ashraf, I. et al. (2016). "Synchronization and collective swimming patterns in fish (Hemigrammus bleheri)". In: *Journal of the Royal Society Interface* 13.123. ISSN: 17425662. DOI: 10.1098/rsif.2016.0734.

Balay, Satish et al. (2015). *PETSc Web page*. http://www.mcs.anl.gov/petsc. URL: http://www.mcs.anl.gov/petsc.

Barkley, D (2006). "Linear analysis of the cylinder wake mean flow". In: *Europhysics Letters* 75.5, pp. 750–756. DOI: 10.1209/epl/i2006-10168-7.

Barkley, Dwight and Ronald D. Henderson (1996). "Three-dimensional Floquet stability analysis of the wake of a circular cylinder". In: *Journal of Fluid Mechanics* 322, pp. 215–241. ISSN: 00221120. DOI: 10.1017/S0022112096002777.

Barrett, David Scott (1996). *Propulsive Efficiency of a Flexible Hull Underwater Vehicle*.

Beal, D. N. et al. (2006). "Passive propulsion in vortex wakes". In: *Journal of Fluid Mechanics* 549, pp. 385–402. ISSN: 00221120. DOI: 10.1017/S0022112005007925.

Becker, Alexander D. et al. (2015). "Hydrodynamic schooling of flapping swimmers". In: *Nature Communications* 6.May, pp. 1–8. ISSN: 20411723. DOI: 10.1038/ncomms9514. URL: http://dx.doi.org/10.1038/ncomms9514.

Benetti Ramos, Luis et al. (2020). "Fluid-solid Floquet stability analysis of self-propelled heaving foils". In: *submitted to Journal of Fluid Mechanics*. URL: https://w3.onera.fr/erc-aeroflex/sites/w3.onera.fr.erc-aeroflex/files/docs/paper/benettiramos-etal-jfm2020.pdf.

Bergmann, M and A Iollo (2011). "Modeling and simulation of fish-like swimming". In: *Journal of Computational Physics* 230.2, pp. 329–348. ISSN: 10902716. DOI: 10.1016/j.jcp.2010.09.017. URL: http://dx.doi.org/10.1016/j.jcp.2010.09.017.

Bergmann, M., A. Iollo, and R. Mittal (2014). "Effect of caudal fin flexibility on the propulsive efficiency of a fish-like swimmer". In: *Bioinspiration and Biomimetics* 9.4. ISSN: 17483190. DOI: 10.1088/1748-3182/9/4/046001.

Bergmann, Michel and Angelo Iollo (2016). "Bioinspired swimming simulations". In: *Journal of Computational Physics* 323, pp. 310–321. ISSN: 10902716. DOI: 10.1016/j.jcp.2016.07.022.

Bertrand, F., P. A. Tanguy, and F. Thibault (1997). "A three-dimensional fictitious domain method for incompressible fluid flow problems". In: *International Journal for Numerical Methods in Fluids* 25.6, pp. 719–736. ISSN: 02712091. DOI: 10.1002/(sici)1097-0363(19970930)25:6<719::aid-fld585>3.0.co;2-k.

Boffi, Daniele and Lucia Gastaldi (2017). "A fictitious domain approach with Lagrange multiplier for fluid-structure interactions". In: *Numerische Mathematik* 135.3, pp. 711–732. ISSN: 0029599X. DOI: 10.1007/s00211-016-0814-1.

Boffi, Daniele, Lucia Gastaldi, and Michele Ruggeri (Dec. 2014). "Mixed Formulation for Interface Problems with Distributed Lagrange Multiplier". In: *Comput. Math. Appl.* 68.12, 2151–2166. ISSN: 0898-1221. DOI: 10.1016/j.camwa.2014.07.020. URL: https://doi.org/10.1016/j.camwa.2014.07.020.

Boffi, Daniele, Frédéric Hecht, and Olivier Pironneau (2018). "Distributed Lagrange Multiplier for Fluid-Structure Interactions". In: *Numerical Methods for PDEs: State of the Art Techniques*. 1. Springer. Chap. 5, pp. 129–145. ISBN: 9783319946764.

Bouard, Roger and Madeleine Coutanceau (1980). "The early stage of development of the wake behind an impulsively started cylinder for 40 < Re < 104". In: *Journal of Fluid Mechanics* 101.3, pp. 583–607. ISSN: 14697645. DOI: 10.1017/S0022112080001814.

Brion, V., D. Sipp, and L. Jacquin (2014). "Linear dynamics of the lamb-chaplygin dipole in the two-dimensional limit". In: *Physics of Fluids* 26.6. ISSN: 10897666. DOI: 10.1063/1.4881375.

Bush, John W.M. (2015). "Pilot-wave hydrodynamics". In: *Annual Review of Fluid Mechanics* 47, pp. 269–292. ISSN: 00664189. DOI: 10.1146/annurev-fluid-010814-014506.

Cahouet, J. and J. -P Chabard (1988). "Some fast 3D finite element solvers for the generalized Stokes problem". In: *International Journal for Numerical Methods in Fluids* 8.8, pp. 869–895. ISSN: 10970363. DOI: 10.1002/fld.1650080802.

Candelier, Fabien, Frederic Boyer, and Alban Leroyer (2011). "Three-dimensional extension of Lighthill's large-amplitude elongated-body theory of fish locomotion". In: *Journal of Fluid Mechanics* 674, pp. 196–226. ISSN: 00221120. DOI: 10.1017/S002211201000649X.

Causin, P., J. F. Gerbeau, and Fabio Nobile (2005). "Added-mass effect in the design of partitioned algorithms for fluid-structure problems". In: *Computer Methods in Applied Mechanics and Engineering* 194.42-44, pp. 4506–4527. ISSN: 00457825. DOI: 10.1016/j.cma.2004.12.005.

Chen, Yufeng et al. (2017). "A biologically inspired , flapping-wing , hybrid aerial-aquatic microrobot". In: *Science Robotics* 5619.October, pp. 1–12.

Chen, Yufeng et al. (2019). "Controlled flight of a microrobot powered by soft artificial muscles". In: *Nature* 575.7782, pp. 324–329. ISSN: 14764687. DOI: 10.1038/s41586-019-1737-7. URL: http://dx.doi.org/10.1038/s41586-019-1737-7.

Childress, Stephen and Robert Dudley (2004). "Transition from ciliary to flapping mode in a swimming mollusc: Flapping flight as a bifurcation in Reω". In: *Journal of Fluid Mechanics* 498.498, pp. 257–288. ISSN: 00221120. DOI: 10.1017/S002211200300689X.

Cossu, C and L Morino (2000). "On the instability of a spring-mounted circular cylinder in a viscous flow at low Reynolds number". In: *Journal of Fluids and Structures* 14, pp. 183–196. DOI: 10.1006/j.

Dehtyriov, Daniel, Kerry Hourigan, and Mark C. Thompson (2019). "Direct numerical simulation of a counter-rotating vortex pair interacting with a wall". In: *Journal of Fluid Mechanics*. ISSN: 14697645. DOI: 10.1017/jfm.2019.816.

Deng, Jian and C. P. Caulfield (2016). "Dependence on aspect ratio of symmetry breaking for oscillating foils: Implications for flapping flight". In: *Journal of Fluid Mechanics* 787, pp. 16–49. ISSN: 14697645. DOI: 10.1017/jfm.2015.661.

— (2018a). "Horizontal locomotion of a vertically flapping oblate spheroid". In: *Journal of Fluid Mechanics* 840, pp. 688–708. ISSN: 14697645. DOI: 10.1017/jfm.2018.62.

— (2018b). "Horizontal locomotion of a vertically flapping oblate spheroid". In: *Journal of Fluid Mechanics* 840, pp. 688–708. ISSN: 14697645. DOI: 10.1017/jfm.2018.62.

Deng, Jian et al. (2016). "Instabilities of interacting vortex rings generated by an oscillating disk". In: *Physical Review E* 94.3, pp. 1–7. ISSN: 24700053. DOI: 10.1103/PhysRevE.94.033107.

Deng, Jian et al. (2017). "Coherent structures in interacting vortex rings". In: *Physical Review Fluids* 2.2, pp. 15–18. ISSN: 2469990X. DOI: 10.1103/PhysRevFluids.2.022701.

Deng, Shuanghou, Mustafa Percin, and Bas Van Oudheusden (2015). "Aerodynamic Characterization of 'DelFly Micro' in Forward Flight Configuration by Force Measurements and Flow Field Visualization". In: *Procedia Engineering* 99, pp. 925–929. ISSN: 18777058. DOI: 10.1016/j.proeng.2014.12.623. URL: http://dx.doi.org/10.1016/j.proeng.2014.12.623.

Deparis, Simone et al. (2016). "FaCSI: A block parallel preconditioner for fluid–structure interaction in hemodynamics". In: *Journal of Computational Physics* 327, pp. 700–718. ISSN: 10902716. DOI: 10.1016/j.jcp.2016.10.005. URL: http://dx.doi.org/10.1016/j.jcp.2016.10.005.

Dijkstra, Henk A. et al. (2014). "Numerical bifurcation methods and their application to fluid dynamics: Analysis beyond simulation". In: *Communications in Computational Physics* 15.1, pp. 1–45. ISSN: 18152406. DOI: 10.4208/cicp.240912.180613a.

Dowell, E. H. et al. (1989). *A modern course in aeroelasticity*. Vol. 3. Springer.

Dudley, R. and C. P. Ellington (1990). "Mechanics of forward flight in bumblebees". In: *Journal of Experimental Biology* 148, pp. 19–52. ISSN: 00220949.

Dütsch, H. et al. (1998). "Low-Reynolds-number flow around an oscillating circular cylinder at low Keulegan–Carpenter numbers". In: *Journal of Fluid Mechanics* 360, 249–271. DOI: 10.1017/S002211209800860X.

Ehrenstein, Uwe (2019). "Thrust and drag scaling of a rigid low-aspect-ratio pitching plate". In: *Journal of Fluids and Structures* 87, pp. 39–57. ISSN: 10958622. DOI: 10.1016/j.jfluidstructs.2019.03.013. URL: https://doi.org/10.1016/j.jfluidstructs.2019.03.013.

Ehrenstein, Uwe and Christophe Eloy (2013). "Skin friction on a moving wall and its implications for swimming animals". In: *Journal of Fluid Mechanics* 718, pp. 321–346. ISSN: 00221120. DOI: 10.1017/jfm.2012.613.

Eldredge, Jeff D. and David Pisani (2008). "Passive locomotion of a simple articulated fish-like system in the wake of an obstacle". In: *Journal of Fluid Mechanics* 607, pp. 279–288. ISSN: 00221120. DOI: 10.1017/S0022112008002218.

Eloy, Christophe (2013). "On the best design for undulatory swimming". In: *Journal of Fluid Mechanics* 717, pp. 48–89. ISSN: 00221120. DOI: 10.1017/jfm.2012.561.

Elston, John R., H. M. Blackburn, and John Sheridan (2006). "The primary and secondary instabilities of flow generated by an oscillating circular cylinder". In: *Journal of Fluid Mechanics* 550, pp. 359–389. ISSN: 00221120. DOI: 10.1017/S0022112005008372.

Elston, John R., John Sheridan, and H. M. Blackburn (2004). "Two-dimensional floquet stability analysis of the flow produced by an oscillating circular cylinder in quiescent fluid". In: *European Journal of Mechanics, B/Fluids* 23, pp. 99–106. ISSN: 09977546. DOI: 10.1016/j.euromechflu.2003.05.002.

Engels, T. et al. (2016). "Bumblebee Flight in Heavy Turbulence". In: *Physical Review Letters* 116.2, pp. 1–5. ISSN: 10797114. DOI: 10.1103/PhysRevLett.116.028103. arXiv: 1512.07614.

Ern, Patricia et al. (2012). "Wake-Induced Oscillatory Paths of Bodies Freely Rising or Falling in Fluids". In: *Annual Review of Fluid Mechanics* 44.1, pp. 97–121. ISSN: 0066-4189. DOI: 10.1146/annurev-fluid-120710-101250.

Fabre, D. et al. (2018). "A Practical Review on Linear and Nonlinear Global Approaches to Flow Instabilities". In: *Applied Mechanics Reviews* 70.6. ISSN: 00036900. DOI: 10.1115/1.4042737.

Fabre, D Ã, P Assemat, and J Magnaudet (2011). "A quasi-static approach to the stability of the path of heavy bodies falling within a viscous fluid". In: 27, pp. 758–767. DOI: 10.1016/j.jfluidsstructs.2011.03.013.

Fabre, David, Denis Sipp, and Laurent Jacquin (2006). "Kelvin waves and the singular modes of the Lamb-Oseen vortex". In: *Journal of Fluid Mechanics* 551, pp. 235–274. ISSN: 00221120. DOI: 10.1017/S0022112005008463.

Facchinetti, M. L., E. de Langre, and F. Biolley (2004). "Coupling of structure and wake oscillators in vortex-induced vibrations". In: *Journal of Fluids and Structures* 19.2, pp. 123–140. ISSN: 08899746. DOI: 10.1016/j.jfluidstructs.2003.12.004.

Faux, D. et al. (2018). "Two modes resonant combined motion for insect wings kinematics reproduction and lift generation". In: *Epl* 121.6. ISSN: 12864854. DOI: 10.1209/0295-5075/121/66001.

Fernandez, Miguel Angel and Patrick Le Tallec (2003). "Linear stability analysis in fluid-structure interaction with transpiration. Part I: Formulation and mathematical analysis". In: *Computer Methods in Applied Mechanics and Engineering* 192.43, pp. 4805–4835. ISSN: 00457825. DOI: 10.1016/j.cma.2003.07.001.

Fernández-Prats, Rafael et al. (2015). "Large-amplitude undulatory swimming near a wall". In: *Bioinspiration and Biomimetics* 10.1. ISSN: 17483190. DOI: 10.1088/1748-3190/10/1/016003. arXiv: 1412.2932.

Filella, Audrey et al. (2018). "Model of Collective Fish Behavior with Hydrodynamic Interactions". In: *Physical Review Letters* 120.19, pp. 1–6. ISSN: 10797114. DOI: 10.1103/PhysRevLett.120.198101. arXiv: 1705.07821.

Floquet, G (1883). "Sur les équations différentielles linéaires à coefficients périodiques". In: *Annales scientifiques de l'É.N.S. 2e série* 12, pp. 47–88.

Floryan, Daniel et al. (2017). "Scaling the propulsive performance of heaving and pitching foils". In: *Journal of Fluid Mechanics* 822, pp. 386–397. ISSN: 14697645. DOI: 10.1017/jfm.2017.302. arXiv: arXiv:1704.07478v1.

Gaissert, Nina et al. (2011). "Inventing a Micro Aerial Vehicle inspired by the mechanics of dragonfly flight". In: *Bionic Learning Network*.

Gallaire, François and P. T. Brun (2017). "Fluid dynamic instabilities: Theory & application to pattern forming in complex media". In: *Philosophical Transactions of the Royal Society A: Mathematical, Physical and Engineering Sciences* 375.2093. ISSN: 1364503X. DOI: 10.1098/rsta.2016.0155.

Garrick, I. E. (1936). "Propulsion of a flapping and oscillating airfoil". In: *NACA Report n.567*, pp. 1–14.

Gazzola, Mattia, Médéric Argentina, and L. Mahadevan (2014a). "Scaling macroscopic aquatic locomotion". In: *Nature Physics* 10.10, pp. 758–761. ISSN: 17452481. DOI: 10.1038/nphys3078.

— (2014b). "Scaling macroscopic aquatic locomotion - Supplementary information". In: *Nature Physics* 10.10, pp. 758–761. ISSN: 17452481. DOI: 10.1038/nphys3078.

Gazzola, Mattia et al. (2011). "Simulations of single and multiple swimmers with non-divergence free deforming geometries". In: *Journal of Computational Physics* 230.19, pp. 7093–7114. ISSN: 00219991. DOI: 10.1016/j.jcp.2011.04.025.

Giannetti, F., S. Camarri, and V. Citro (2019). "Sensitivity analysis and passive control of the secondary instability in the wake of a cylinder". In: *Journal of Fluid Mechanics* 864, 45–72. DOI: 10.1017/jfm.2019.17.

Giannetti, Flavio, Simone Camarri, and Paolo Luchini (2010). "Structural sensitivity of the secondary instability in the wake of a circular cylinder". In: *Journal of Fluid Mechanics* 651, pp. 319–337. ISSN: 00221120. DOI: 10.1017/S0022112009993946.

Giannetti, Flavio and Paolo Luchini (2007). "Structural sensitivity of the first instability of the cylinder wake". In: *Journal of Fluid Mechanics* 581, pp. 167–197. ISSN: 00221120. DOI: 10.1017/S0022112007005654.

Gilmore, Rowan J. and Michael B. Steer (1991). "Nonlinear circuit analysis using the method of harmonic balance—a review of the art. II. Advanced concepts". In: *International Journal of Microwave and Millimeter-Wave Computer-Aided Engineering* 1.2, pp. 159–180. ISSN: 15226301. DOI: 10.1002/mmce.4570010205.

Glowinski, R et al. (1999). "A distributed Lagrange multiplier/fictitious domain method for particulate flows". In: *International Journal of Multiphase Flow* 25, pp. 755–794.

Glowinski, R. et al. (2001). "A Fictitious Domain Approach to the Direct Numerical Simulation of Incompressible Viscous Flow past Moving Rigid Bodies: Application to Particulate Flow". In: *Journal of Computational Physics* 169.2, pp. 363–426. ISSN: 00219991. DOI: 10.1006/jcph.2000.6542.

Glowinski, Roland, Tsorng Whay Pan, and Jacques Périaux (2006). "Numerical simulation of a multi-store separation phenomenon: A fictitious domain approach". In: *Computer Methods in Applied Mechanics and Engineering* 195.41-43, pp. 5566–5581. ISSN: 00457825. DOI: 10.1016/j.cma.2005.09.018.

Godoy-Diana, Ramiro et al. (2009). "A model for the symmetry breaking of the reverse Bénard-von Kármán vortex street produced by a flapping foil". In: *Journal of Fluid Mechanics*. ISSN: 00221120. DOI: 10.1017/S0022112008005727. arXiv: 0812.4137.

Gopinath, Arathi et al. (2007). "Three-Dimensional Unsteady Multi-stage Turbomachinery Simulations Using the Harmonic Balance Technique". In: *45th AIAA Aerospace Sciences Meeting and Exhibit* January 2017. ISSN: 0338-1684. DOI: 10.2514/6.2007-892. URL: http://arc.aiaa.org/doi/10.2514/6.2007-892.

Gopinath, Arathi K and Antony Jameson (2005). "Time Spectral Method for Periodic Unsteady Computations over Two-and Three-Dimensional Bodies". In: *43rd AIAA Aerospace Sciences Meeting and Exhibit*, pp. 1–14. ISBN: 978-1-62410-064-2. DOI: 10.2514/6.2005-1220. URL: https://arc-aiaa-org.ezaccess.libraries.psu.edu/doi/pdf/10.2514/6.2005-1220.

Govaerts, Willy J. F. (2000). *Numerical methods for bifurcations of dynamical equilibria*. Society for Industrial and Applied Mathematics.

Goza, Andres, Tim Colonius, and John E. Sader (2018). "Global modes and nonlinear analysis of inverted-flag flapping". In: *Journal of Fluid Mechanics* 857, pp. 312–344. ISSN: 14697645. DOI: 10.1017/jfm.2018.728. arXiv: 1709.09745.

Goza, Andres, Daniel Floryan, and Clarence Rowley (2020). "Connections between resonance and nonlinearity in swimming performance of a flexible heaving plate". In: *Journal of Fluid Mechanics* 888. ISSN: 14697645. DOI: 10.1017/jfm.2020.60. arXiv: 1908.05704.

Goza, Andres et al. (2016). "Accurate computation of surface stresses and forces with immersed boundary methods". In: *Journal of Computational Physics* 321, pp. 860–873. ISSN: 10902716. DOI: 10.1016/j.jcp.2016.06.014. arXiv: 1603.02306. URL: http://dx.doi.org/10.1016/j.jcp.2016.06.014.

Gray, J (1933). "The movement of fish with special reference to the eel". In: *Journal of Experimental Biology* 10.3, pp. 88–104.

Griffith, Martin D. and Justin S. Leontini (2017). "Sharp interface immersed boundary methods and their application to vortex-induced vibration of a cylinder". In: *Journal of Fluids and Structures* 72, pp. 38–58. ISSN: 10958622. DOI: 10.1016/j.jfluidstructs.2017.04.008. URL: http://dx.doi.org/10.1016/j.jfluidstructs.2017.04.008.

Hall, Kenneth C., Jeffrey P. Thomas, and W. S. Clark (2002). "Computation of unsteady nonlinear flows in cascades using a harmonic balance technique". In: *AIAA Journal* 40.5, pp. 879–886. ISSN: 00011452. DOI: 10.2514/2.1754.

Hecht, Frédéric (2012). "New development in freefem ++ Frédéric Hecht To cite this version : HAL Id : hal-01476313". In: *Journal of Numerical Mathematics* 20.3, pp. 1–14.

Hemelrijk, C. K. et al. (2015). "The increased efficiency of fish swimming in a school". In: *Fish and Fisheries* 16.3, pp. 511–521. ISSN: 14672979. DOI: 10.1111/faf.12072. arXiv: 1307.7282.

Iooss, Gerard and Daniel D. Joseph (1997). *Elementary Stability and Bifurcation Theory (Undergraduate Texts in Mathematics)*. URL: http://www.amazon.com/Elementary-Stability-Bifurcation-Undergraduate-Mathematics/dp/0387970681.

Jallas, Damien, Olivier Marquet, and David Fabre (2017). "Linear and nonlinear perturbation analysis of the symmetry breaking in time-periodic propulsive wakes". In: *Physical Review E* 95.6, pp. 1–15. ISSN: 24700053. DOI: 10.1103/PhysRevE.95.063111.

Jenny, Mathieu, Gilles Bouchet, and Jan Dušek (2003). "Nonvertical ascension or fall of a free sphere in a Newtonian fluid". In: *Physics of Fluids* 15.1, pp. L9–L12. ISSN: 10706631. DOI: 10.1063/1.1529179.

Jenny, Mathieu and Jan Dušek (2004). "Efficient numerical method for the direct numerical simulation of the flow past a single light moving spherical body in transitional regimes". In:

Journal of Computational Physics 194.1, pp. 215–232. ISSN: 00219991. DOI: 10.1016/j.jcp.2003.09.004.

Karásek, Matěj et al. (2019). "Accurate position control of a flapping-wing robot enabling free-flight flow visualisation in a wind tunnel". In: *International Journal of Micro Air Vehicles* 11. ISSN: 17568307. DOI: 10.1177/1756829319833683. URL: https://doi.org/10.1177/1756829319833683.

Kessler, A. E. et al. (2013). "Satellite telemetry reveals long-distance migration in the Asian great bustard Otis tarda dybowskii". In: *Journal of Avian Biology* 44.4, pp. 311–320. ISSN: 09088857. DOI: 10.1111/j.1600-048X.2013.00072.x.

Kim, Sohae, Wei Xi Huang, and Hyung Jin Sung (2010). "Constructive and destructive interaction modes between two tandem flexible flags in viscous flow". In: *Journal of Fluid Mechanics* 661, pp. 511–521. ISSN: 00221120. DOI: 10.1017/S0022112010003514.

Kress, Wendy and Per Lötstedt (2006). "Time step restrictions using semi-explicit methods for the incompressible Navier-Stokes equations". In: *Computer Methods in Applied Mechanics and Engineering* 195.33-36, pp. 4433–4447. ISSN: 00457825. DOI: 10.1016/j.cma.2005.09.009.

Lauga, Eric (2011). "Life around the scallop theorem". In: *Soft Matter* 7.7, pp. 3060–3065. ISSN: 1744683X. DOI: 10.1039/c0sm00953a. arXiv: 1011.3051.

Leontini, Justin S., M. C. Thompson, and K. Hourigan (2007). "Three-dimensional transition in the wake of a transversely oscillating cylinder". In: *Journal of Fluid Mechanics* 577, pp. 79–104. ISSN: 00221120. DOI: 10.1017/S0022112006004320.

Lewin, G. C. and H. Haj-Hariri (2003). "Modelling thrust generation of a two-dimensional heaving airfoil in a viscous flow". In: *Journal of Fluid Mechanics* 492.492, pp. 339–362. ISSN: 00221120. DOI: 10.1017/S0022112003005743.

Li, Gen et al. (2019). "On the energetics and stability of a minimal fish school". In: *PLoS ONE* 14.8, pp. 1–20. ISSN: 19326203. DOI: 10.1371/journal.pone.0215265.

Lian, Q. X. and Z. Huang (1989). "Starting flow and structures of the starting vortex behind bluff bodies with sharp edges". In: *Experiments in Fluids* 8.1-2, pp. 95–103. ISSN: 07234864. DOI: 10.1007/BF00203070.

Liao, James C. and Otar Akanyeti (2017). "Fish swimming in a Kármán vortex street: kinematics, sensory biology and energetics". In: *Marine Technology Society Journal* 51.5, pp. 48–55. ISSN: 0025-3324. DOI: 10.4031/MTSJ.51.5.8.

Liao, James C, David N Beal, and George V Lauder (2003). "Fish Exploiting Vortices Decrease Muscle Activity". In: *Science* 302.November, pp. 1566–1569. DOI: 10.1126/science.1088295.

Lighthill, James (1975). *Mathematical Biofluiddynamics*. Society for Industrial and Applied Mathematics. ISBN: 0898710146.

Lighthill, M J (1969). "Hydromechanics of aquatic animal propulsion". In: *Annual Review of Fluid Mechanics* 1.1, pp. 413–446. DOI: 10.1146/annurev.fl.01.010169.002213.

Lighthill, M. J. (1971). "Large-Amplitude Elongated-Body Theory of Fish Locomotion". In: *Proceedings of the Royal Society B: Biological Sciences* 179.1055, pp. 125–138. ISSN: 0962-8452. DOI: 10.1098/rspb.1971.0085. URL: http://rspb.royalsocietypublishing.org/cgi/doi/10.1098/rspb.1971.0085.

Lin, Xingjian et al. (2019). "Self-organization of multiple self-propelling flapping foils: Energy saving and increased speed". In: *Journal of Fluid Mechanics* 884, pp. 1–14. ISSN: 14697645. DOI: 10.1017/jfm.2019.954.

Lu, Xi Y. and Qin Liao (2006). "Dynamic responses of a two-dimensional flapping foil motion". In: *Physics of Fluids* 18.9. ISSN: 10706631. DOI: 10.1063/1.2357733.

Lucas, Kelsey N. et al. (2014). "Bending rules for animal propulsion". In: *Nature Communications* 5.May 2013, pp. 1–7. ISSN: 20411723. DOI: 10.1038/ncomms4293. URL: http://dx.doi.org/10.1038/ncomms4293.

Marquet, O., D. Sipp, and L. Jacquin (2008). "Sensitivity analysis and passive control of cylinder flow". In: *Journal of Fluid Mechanics* 615, 221–252. DOI: 10.1017/S0022112008003662.

Moored, K. W. et al. (2012). "Hydrodynamic wake resonance as an underlying principle of efficient unsteady propulsion". In: *Journal of Fluid Mechanics* 708.February 2015, pp. 329–348. ISSN: 0022-1120. DOI: 10.1017/jfm.2012.313. URL: http://www.journals.cambridge.org/abstract{_}S0022112012003138.

Moored, K. W. et al. (2014). "Linear instability mechanisms leading to optimally efficient locomotion with flexible propulsors". In: *Physics of Fluids* 26.4. ISSN: 10897666. DOI: 10.1063/1.4872221.

Mougin, G. and J. Magnaudet (2003). "The generalized Kirchhoff equations and their application to the interaction between a rigid body and an arbitrary time-dependent viscous flow". In: *International Journal of Multiphase Flow* 28, pp. 1837–1851. ISSN: 03019322. DOI: 10.1016/S0301-9322(02)00078-2.

Mougin, Guillaume and Jacques Magnaudet (2002). "Path Instability of a Rising Bubble". In: *Physical Review Letters* 88.1, p. 4. ISSN: 10797114. DOI: 10.1103/PhysRevLett.88.014502.

Moulin, Johann (2020). *On the flutter bifurcation in laminar flows: linear and nonlinear modal methods*. PhD thesis, Institut Polytechnique de Paris.

Mueller, Thomas J (2001). *Fixed and Flapping Wing Aerodynamics for Micro Air Vehicle Applications*. AIAA. ISBN: 1563475170.

Mueller, Thomas J and James D Delaurier (2003). "Aerodynamics of small vehicles". In: *Annual Review Fluid Mechanics* 35, pp. 89–111. DOI: 10.1146/annurev.fluid.35.101101.161102.

Muller, U. K. (2004). "Swimming of larval zebrafish: ontogeny of body waves and implications for locomotory development". In: *Journal of Experimental Biology* 207.5, pp. 853–868. ISSN: 0022-0949. DOI: 10.1242/jeb.00821. URL: http://jeb.biologists.org/cgi/doi/10.1242/jeb.00821.

Mundis, Nathan L. and Dimitri J. Mavriplis (2017). "Toward an optimal solver for time-spectral fluid-dynamic and aeroelastic solutions on unstructured meshes". In: *Journal of Computational Physics* 345, pp. 132–161. ISSN: 10902716. DOI: 10.1016/j.jcp.2017.04.067. URL: http://dx.doi.org/10.1016/j.jcp.2017.04.067.

Mundis, N.L. and D.J. Mavriplis (2013). "GMRES applied to the time-spectral and quasi-periodic time-spectral methods". In: *21st AIAA Computational Fluid Dynamics Conference*, pp. 1–20.

Murphy, David W. et al. (2016). "Underwater flight by the planktonic sea butterfly". In: *Journal of Experimental Biology* 219.4, pp. 535–543. ISSN: 00220949. DOI: 10.1242/jeb.129205.

Navrose, N. and Sanjay Mittal (2016). "Lock-in in vortex-induced vibration". In: *Journal of Fluid Mechanics* 794, pp. 565–594. ISSN: 14697645. DOI: 10.1017/jfm.2016.157.

Negi, Prabal S, Ardeshir Hanifi, and Dan S Henningson (2019). "Global stability of rigid-body-motion fluid-structure-interaction problems". In: *arXiv preprint arXiv:1910.09605*.

Newbolt, Joel W., Jun Zhang, and Leif Ristroph (2019). "Flow interactions between uncoordinated flapping swimmers give rise to group cohesion". In: *Proceedings of the National Academy of Sciences of the United States of America* 116.7, pp. 2419–2424. ISSN: 10916490. DOI: 10.1073/pnas.1816098116.

Oza, Anand U, Leif Ristroph, and Michael J Shelley (2019). "Lattices of Hydrodynamically Interacting Flapping Swimmers". In: *Physical Review X* 9.4, p. 41024. ISSN: 2160-3308. DOI: 10.1103/PhysRevX.9.041024. URL: https://doi.org/10.1103/PhysRevX.9.041024.

Païdoussis, Michael P., Stuart J. Price, and Emmanuel De Langre (2010). *Fluid-structure interactions: Cross-flow-induced instabilities*. Vol. 9780521119, pp. 1–402. ISBN: 9780511760792. DOI: 10.1017/CBO9780511760792. arXiv: arXiv:1011.1669v3.

Park, Sung Goon and Hyung Jin Sung (2018). "Hydrodynamics of flexible fins propelled in tandem, diagonal, triangular and diamond configurations". In: *Journal of Fluid Mechanics* 840, pp. 154–189. ISSN: 14697645. DOI: 10.1017/jfm.2018.64.

Partridge, B. L. and T. J. Pitcher (1979). "Evidence against a hydrodynamic function for fish schools [12]". In: *Nature* 279.5712, pp. 418–419. ISSN: 00280836. DOI: 10.1038/279418a0.

Peng, Ze Rui, Haibo Huang, and Xi Yun Lu (2018a). "Collective locomotion of two closely spaced self-propelled flapping plates". In: *Journal of Fluid Mechanics* 849, pp. 1068–1095. ISSN: 14697645. DOI: 10.1017/jfm.2018.447.

— (2018b). "Hydrodynamic schooling of multiple self-propelled flapping plates". In: *Journal of Fluid Mechanics* 853, pp. 587–600. ISSN: 14697645. DOI: 10.1017/jfm.2018.634.

Perrard, Stéphane et al. (2014). "Self-organization into quantized eigenstates of a classical wave-driven particle". In: *Nature Communications* 5, pp. 1–8. ISSN: 20411723. DOI: 10.1038/ncomms4219.

Peskin, Charles S. (1972). "Flow patterns around heart valves: A numerical method". In: *Journal of Computational Physics* 10.2, pp. 252–271. ISSN: 10902716. DOI: 10.1016/0021-9991(72)90065-4.

Pfister, J.-L. and O. Marquet (2020). "Fluid structure stability analyses and nonlinear dynamics of flexible splitter plates interacting with a circular cylinder flow". In: *Journal of Fluid Mechanics* 896, pp. 1–38. ISSN: 0022-1120. DOI: 10.1017/jfm.2020.284.

Pfister, J.-L. et al. (2020). "Symmetry breaking of flexible splitter plates: experiments and quasi-steady stability analysis". In: *in preparation to Journal of Fluid Mechanics*.

Pfister, Jean Lou, Olivier Marquet, and M. Carini (2019). "Linear stability analysis of strongly coupled fluid–structure problems with the Arbitrary Lagrangian Eulerian method". In: *Computer Methods in Applied Mechanics and Engineering* 355, pp. 663–689. ISSN: 00457825. DOI: 10.1016/j.cma.2019.06.024. URL: https://doi.org/10.1016/j.cma.2019.06.024.

Piñeirua, M., R. Godoy-Diana, and B. Thiria (2015). "Resistive thrust production can be as crucial as added mass mechanisms for inertial undulatory swimmers". In: *Physical Review E - Statistical, Nonlinear, and Soft Matter Physics* 92.2, pp. 1–6. ISSN: 15502376. DOI: 10.1103/PhysRevE.92.021001. arXiv: 1507.04952.

Portugal, Steven J. et al. (2014). "Upwash exploitation and downwash avoidance by flap phasing in ibis formation flight". In: *Nature* 505.7483, pp. 399–402. ISSN: 00280836. DOI: 10.1038/nature12939. URL: http://dx.doi.org/10.1038/nature12939.

Purcell, E. M. (1977). "Life at low Reynolds number". In: *American Journal of Physics* 45.1, pp. 3–11. ISSN: 0002-9505. DOI: 10.1119/1.10903. arXiv: arXiv:1011.1669v3. URL: http://aapt.scitation.org/doi/10.1119/1.10903.

Quinn, Daniel B., George V. Lauder, and Alexander J. Smits (2014). "Flexible propulsors in ground effect". In: *Bioinspiration and Biomimetics* 9.3. ISSN: 17483190. DOI: 10.1088/1748-3182/9/3/036008.

Ramananarivo, Sophie, Ramiro Godoy-Diana, and Benjamin Thiria (2010). "Rather than resonance, flapping wing flyers may play on aerodynamics to improve performance". In: *Proceedings of the National Academy of Sciences of the United States of America* 108.15. ISSN: 0027-8424. DOI: 10.1073/pnas.1017910108. arXiv: 1011.4688. URL: http://arxiv.org/abs/1011.4688{\%}0Ahttp://dx.doi.org/10.1073/pnas.1017910108.

— (2013). "Passive elastic mechanism to mimic fish-muscle action in anguilliform swimming". In: *Journal of the Royal Society Interface* 10.88. ISSN: 17425662. DOI: 10.1098/rsif.2013.0667.

— (2014). "Propagating waves in bounded elastic media: Transition from standing waves to anguilliform kinematics". In: *Epl* 105.5. ISSN: 12864854. DOI: 10.1209/0295-5075/105/54003.

Ramananarivo, Sophie et al. (2016). "Flow interactions lead to orderly formations of flapping wings in forward flight". In: *Physical Review Fluids* 1.7. ISSN: 2469990X. DOI: 10.1103/PhysRevFluids.1.071201.

Raspa, V. et al. (2014). "Vortex-induced drag and the role of aspect ratio in undulatory swimmers". In: *Physics of Fluids* 26.4. ISSN: 10897666. DOI: 10.1063/1.4870254.

Reigh, Shang Yik et al. (2017). "Swimming with a cage: Low-Reynolds-number locomotion inside a droplet". In: *Soft Matter* 13.17, pp. 3161–3173. ISSN: 17446848. DOI: 10.1039/c6sm01636g.

Rigas, Georgios, Denis Sipp, and Tim Colonius (2020). "Non-linear input/output analysis: application to boundary layer transition". In: 1.2008, pp. 1–30. arXiv: 2001.09440. URL: http://arxiv.org/abs/2001.09440.

Ristroph, Leif and Stephen Childress (2014). "Stable hovering of a jellyfish-like flying machine". In: *Journal of the Royal Society Interface* 11.92. ISSN: 17425662. DOI: 10.1098/rsif.2013.0992.

Ristroph, Leif and Jun Zhang (2008). "Anomalous hydrodynamic drafting of interacting flapping flags". In: *Physical Review Letters* 101.19, pp. 1–4. ISSN: 00319007. DOI: 10.1103/PhysRevLett.101.194502. arXiv: 0905.1159.

Rubino, A. et al. (2018). "Adjoint-based fluid dynamic design optimization in quasi-periodic unsteady flow problems using a harmonic balance method". In: *Journal of Computational Physics* 372, pp. 220–235. ISSN: 10902716. DOI: 10.1016/j.jcp.2018.06.023. URL: https://doi.org/10.1016/j.jcp.2018.06.023.

Saad, Yousef (2011). *Numerical Methods for Large Eigenvalue Problems*. Society for Industrial and Applied Mathematics.

Sane, Sanjay P. (2003). "The aerodynamics of insect flight". In: *Journal of Experimental Biology* 206.23, pp. 4191–4208. ISSN: 00220949. DOI: 10.1242/jeb.00663.

Santhanakrishnan, Arvind et al. (2018). "Flow structure and force generation on flapping wings at low Reynolds numbers relevant to the flight of tiny insects". In: *Fluids* 3.3. ISSN: 23115521. DOI: 10.3390/fluids3030045.

Schaeffer, David G. and John W. Cain (2016). *Ordinary Differential Equations: Basics and Beyond*. Vol. 65, p. 542. ISBN: 978-1-4939-6387-4. DOI: 10.1007/978-1-4939-6389-8. URL: http://link.springer.com/10.1007/978-1-4939-6389-8.

Schmid, Peter J., Miguel Fosas De Pando, and N. Peake (2017). "Stability analysis for n -periodic arrays of fluid systems". In: *Physical Review Fluids* 2.11, pp. 1–25. ISSN: 2469990X. DOI: 10.1103/PhysRevFluids.2.113902.

Schmid, Peter J. and Dan S. Henningson (2001). *Stability and Transition in Shear Flows*. Springer. ISBN: 9781461265641.

Send, Wolfgang et al. (2012). "Artificial hinged-wing bird with active torsion and partially linear kinematics". In: *28th Congress of the International Council of the Aeronautical Sciences 2012, ICAS 2012* 2, pp. 1148–1157.

Shaabani-Ardali, Léopold, Denis Sipp, and Lutz Lesshafft (2017). "Time-delayed feedback technique for suppressing instabilities in time-periodic flow". In: *PHYSICAL REVIEW FLUIDS* 2.113904. DOI: 10.1103/PhysRevFluids.2.113904.

— (2019). "Vortex pairing in jets as a global Floquet instability: Modal and transient dynamics". In: *Journal of Fluid Mechanics* 862, pp. 951–989. ISSN: 14697645. DOI: 10.1017/jfm.2018.977.

Shyy, W. et al. (2010). "Recent progress in flapping wing aerodynamics and aeroelasticity". In: *Progress in Aerospace Sciences* 46.7, pp. 284–327. ISSN: 03760421. DOI: 10.1016/j.paerosci.2010.01.001. arXiv: 0602423 [astro-ph]. URL: http://dx.doi.org/10.1016/j.paerosci.2010.01.001.

Sicot, F., G. Puigt, and M. Montagnac (2008). "Block-Jacobi Implicit Algorithms for the Time Spectral Method". In: *AIAA Journal* 46.12, pp. 3080–3089. ISSN: 0001-1452. DOI: 10.2514/1.36792. URL: http://arc.aiaa.org/doi/10.2514/1.36792.

Sipp, Denis and Anton Lebedev (2007). "Global stability of base and mean flows: A general approach and its applications to cylinder and open cavity flows". In: *Journal of Fluid Mechanics* 593, pp. 333–358. ISSN: 00221120. DOI: 10.1017/S0022112007008907.

Smits, Alexander J (2019). "Undulatory and oscillatory swimming". In: *Journal of Fluid Mechanics* 874.

Spagnolie, Saverio E. et al. (2010). "Surprising behaviors in flapping locomotion with passive pitching". In: *Physics of Fluids* 22.4, pp. 1–20. ISSN: 10706631. DOI: 10.1063/1.3383215.

Sumpter, D. J.T. (2006). "The principles of collective animal behaviour". In: *Philosophical Transactions of the Royal Society B: Biological Sciences* 361.1465, pp. 5–22. ISSN: 09628436. DOI: 10.1098/rstb.2005.1733.

Tammisola, O., F. Lundell, and L. D. Söderberg (2012). "Surface tension-induced global instability of planar jets and wakes". In: *Journal of Fluid Mechanics* 713, pp. 632–658.

Taylor, G. (1952). "Analysis of the Swimming of Long and Narrow Animals". In: *Proceedings of the Royal Society A: Mathematical, Physical and Engineering Sciences* 214.1117, pp. 158–183. ISSN: 1364-5021. DOI: 10.1098/rspa.1952.0159. arXiv: 0912.1431. URL: http://rspa.royalsocietypublishing.org/cgi/doi/10.1098/rspa.1952.0159.

Tchoufag, Joël, David Fabre, and Jacques Magnaudet (2014). "Global linear stability analysis of the wake and path of buoyancy-driven disks and thin cylinders". In: *Journal of Fluid Mechanics*. ISSN: 14697645. DOI: 10.1017/jfm.2013.642.

Tchoufag, Joël, Jacques Magnaudet, and David Fabre (2014). "Linear instability of the path of a freely rising spheroidal bubble". In: *Journal of Fluid Mechanics* 751, pp. 1–12. ISSN: 14697645. DOI: 10.1017/jfm.2014.340.

Triantafyllou, G.S., M.S. Triantafyllou, and M.A. Grosenbaugh (1993). *Optimal Thrust Development in Oscillating Foils with Application to Fish Propulsion*. DOI: 10.1006/jfls.1993.1012. URL: http://linkinghub.elsevier.com/retrieve/pii/S0889974683710121.

Triantafyllou, M. S., G. S. Triantafyllou, and R. Gopalkrishnan (1991). "Wake mechanics for thrust generation in oscillating foils". In: *Physics of Fluids A* 3.12, pp. 2835–2837. ISSN: 08998213. DOI: 10.1063/1.858173.

Usherwood, James R. et al. (2011). "Flying in a flock comes at a cost in pigeons". In: *Nature* 474.7352, pp. 494–497. ISSN: 00280836. DOI: 10.1038/nature10164.

Vandenberghe, Nicolas, Stephen Childress, and Jun Zhang (2006). "On unidirectional flight of a free flapping wing". In: *Physics of Fluids* 18.1, pp. 1–8. ISSN: 10706631. DOI: 10.1063/1.2148989.

Vandenberghe, Nicolas, Jun Zhang, and Stephen Childress (2004). "Symmetry breaking leads to forward flapping flight". In: *Journal of Fluid Mechanics* 506.506, pp. 147–155. ISSN: 00221120. DOI: 10.1017/S0022112004008468.

Verma, Siddhartha, Guido Novati, and Petros Koumoutsakos (2018). "Efficient collective swimming by harnessing vortices through deep reinforcement learning". In: ISSN: 0027-8424. DOI: 10.1073/pnas.1800923115. arXiv: 1802.02674. URL: http://arxiv.org/abs/1802.02674.

Wang, Z. Jane (2000). "Vortex shedding and frequency selection in flapping flight". In: *Journal of Fluid Mechanics* 410, pp. 323–341. ISSN: 00221120. DOI: 10.1017/S0022112099008071.

Weide, Edwin van der, Arathi Gopinath, and Antony Jameson (2005). "Turbomachinery Applications with the Time Spectral Method". In: *35th AIAA Fluid Dynamics Conference and Exhibit*, pp. 1–12. ISSN: 0002-7863. DOI: 10.2514/6.2005-4905. URL: http://arc.aiaa.org/doi/10.2514/6.2005-4905.

Weis-Fogh, T. (1973). "Quick Estimates of Flight Fitness in Hovering Animals, Including Novel Mechanisms for Lift Production". In: *Journal of Experimental Biology* 59.1, pp. 169–230. ISSN: 0022-0949. eprint: https://jeb.biologists.org/content/59/1/169.full.pdf. URL: https://jeb.biologists.org/content/59/1/169.

Wiggins, Stephen (1988). *Global Bifurcations and Chaos - Analytical Methods*. Vol. 73. 1. ISBN: 9788578110796. DOI: 10.1017/CBO9781107415324.004. arXiv: arXiv:1011.1669v3.

Williams, Brian J. et al. (2014). "A self-propelled biohybrid swimmer at low Reynolds number". In: *Nature Communications* 5, pp. 1–8. ISSN: 20411723. DOI: 10.1038/ncomms4081.

Wu, Theodore Yaotsu (2010). "A Review on Fish Swimming and Bird/Insect Flight". In: *Annual Review of Fluid Mechanics* 43.1, pp. 25–58. ISSN: 0066-4189. DOI: 10.1146/annurev-fluid-122109-160648. arXiv: 1006.1927. URL: http://arxiv.org/abs/1006.1927.

Xu, Min and Mingjun Wei (2016). "Using adjoint-based optimization to study kinematics and deformation of flapping wings". In: *Journal of Fluid Mechanics* 799, pp. 56–99. ISSN: 14697645. DOI: 10.1017/jfm.2016.351.

Young, John, Joseph C.S. Lai, and Max F. Platzer (2014). "A review of progress and challenges in flapping foil power generation". In: *Progress in Aerospace Sciences* 67, pp. 2–28. ISSN: 03760421. DOI: 10.1016/j.paerosci.2013.11.001. URL: http://dx.doi.org/10.1016/j.paerosci.2013.11.001.

Zhang, Jun (2017). "Footprints of a flapping wing". In: *Journal of Fluid Mechanics* 818, pp. 1–4. ISSN: 14697645. DOI: 10.1017/jfm.2017.173.

Zhang, Xing et al. (2009). “Effects of geometric shape on the hydrodynamics of a self-propelled flapping foil”. In: *Physics of Fluids* 21.10. ISSN: 10706631. DOI: 10.1063/1.3251045.

Zhu, J. et al. (2019). “Tuna robotics: A high-frequency experimental platform exploring the performance space of swimming fishes”. In: *Science Robotics* 4.34. ISSN: 24709476. DOI: 10.1126/scirobotics.aax4615.

Zhu, Xiaojue, Guowei He, and Xing Zhang (2014). “Flow-Mediated Interactions between Two Self-Propelled Flapping Filaments in Tandem Configuration”. In: *Physical Review Letters* 113.23. ISSN: 10797114. DOI: 10.1103/PhysRevLett.113.238105.

Luis H. Benetti Ramos
Contact information: luisbenettiramos@gmail.com

Doctoral student
18/09/2017 – 10/11/2020
Institut de Mathématiques de Bordeaux
UMR 5251 Université de Bordeaux, F-33400 Talence, France
&
ONERA, The French Aerospace Lab
8, Rue des Vertugadins, F-92190 Meudon, France.